



Scuola Internazionale Superiore di Studi Avanzati - Trieste

ASTROPHYSICS SECTOR

A physical model for the evolution of galaxies and active galactic nuclei through cosmic times

Thesis submitted for the degree of Doctor Philosophiaæ
Academic Year 2012/2013

CANDIDATE

Zhen-Yi Cai

SUPERVISORS

Prof. Luigi Danese

Prof. Gianfranco De Zotti

Dr. Andrea Lapi

Prof. Ju-Fu Lu

October 2013

SISSA - Via Bonomea 265 - 34136 TRIESTE - ITALY

To my family

Abstract

A comprehensive investigation of the cosmological evolution of the luminosity function (LF) of galaxies and active galactic nuclei (AGNs) in the infrared (IR) has been presented. Based on the observed dichotomy in the ages of stellar populations of early-type galaxies on one side and late-type galaxies on the other, the model interprets the epoch-dependent LFs at $z \gtrsim 1$ using a physical approach for the evolution of proto-spheroidal galaxies and of the associated AGNs, while IR galaxies at $z \lesssim 2$ are interpreted as being mostly late-type “cold” (normal) and “warm” (starburst) galaxies.

As for proto-spheroids, in addition to the epoch-dependent LFs of stellar and AGN components separately, we have worked out, for the first time, the evolving LFs of these objects as a whole (stellar plus AGN component), taking into account in a self-consistent way the variation with galactic age of the global spectral energy distribution (SED). This high- z model provides a physical explanation for the observed positive evolution of both galaxies and AGNs up to $z \simeq 2.5$ and for the negative evolution at higher z , for the sharp transition from Euclidean to extremely steep counts at (sub-)millimeter wavelengths, as well as the (sub-)millimeter counts of strongly lensed galaxies that are hard to account for by alternative, physical or phenomenological approach.

The evolution of late-type galaxies and $z \lesssim 2$ AGNs is described using a parametric phenomenological approach complemented with empirical/observed SED. The “cold” population has a mild luminosity evolution and no density evolution, while the “warm” population evolves significantly in luminosity and negligible in density. Type 1 AGNs has similar evolutions in luminosity and density, while the type 2 AGNs only evolves in density.

This “hybrid” model provides a good fit to the multi-wavelength (from the mid-IR to millimeter waves) data on LFs at different redshifts and on number counts (both global and per redshift slices). The modeled total AGN contributions to the counts and to the cosmic infrared background (CIB) are always sub-dominant. They are maximal at mid-IR wavelengths: the contribution to the 15 and 24 μm counts reaches 20% above 10 and 2 mJy, respectively, while the contributions to the CIB are of 8.6% and of 8.1% at 15 and 24 μm , respectively. A prediction of the present model, useful to test it, is a systematic variation with wavelength of the populations dominating the counts and the contributions to the CIB intensity. This implies a specific trend for cross-wavelength CIB power spectra, which is found to be in good agreement with the data.

Updated predictions for the number counts and the redshift distributions of star-forming galaxies spectroscopically detectable by future mission, e.g., the SPace Infrared telescope for Cosmology and

Astrophysics (SPICA), have been obtained exploiting this “hybrid” model for the evolution of the dusty star-forming galaxies. Preliminary radio counts of star-forming galaxies, resulting from a combination of the “hybrid” model and the well-known IR-radio correlation, are also made to explain the sub-mJy excess of radio source counts that will be determined precisely by future Square Kilometer Array (SKA) surveys.

To understand the role played by star-forming galaxies at $z \gtrsim 6$ on the cosmic re-ionization, the high- z physical model has been tentatively extended to very small halos for the evolution of ultraviolet (UV) LF of high- z star-forming galaxies taking into account in a self-consistent way their chemical evolution and the associated evolution of dust extinction. The model yields good fits of the UV and Ly α LFs at all redshifts ($z \gtrsim 2$) at which they have been measured, providing a simple explanation for the weak evolution observed between $z = 2$ and $z = 6$. The observed range of UV luminosities at high- z implies a minimum halo mass capable of hosting active star formation $M_{\text{crit}} \lesssim 10^{9.8} M_{\odot}$, consistent with the constraints from hydrodynamical simulations. We show that the escape fraction of ionizing photons is higher in less massive galaxies, where it can reach values substantially higher than frequently assumed. As a consequence, galaxies already represented in the UV LF ($M_{\text{UV}} \leq -18$) can keep the universe fully ionized up to $z \simeq 7.5$. On one side this implies a more extended ionized phase than indicated by some (uncertain) data, pointing to a rapid drop of the ionization degree above $z \simeq 6.5$. On the other side, the electron scattering optical depth inferred from Cosmic Microwave Background experiments favor an even more extended ionized phase. Since all these constraints on the re-ionization history are affected by substantial uncertainties, better data are needed for further firm conclusions.

Publications

The major contents of this thesis have already appeared in some of the following papers:

- Bonato, M.; Negrello, M.; **Cai, Z.-Y.**; Bressan, A.; De Zotti, G.; Lapi, A.; Gruppioni, C.; Spinoglio, L.; Danese, L.,
Exploring the early dust-obscured phase of galaxy formation with future mid-/far-infrared spectroscopic surveys,
2013, MNRAS, in preparation
- **Cai, Z.-Y.**; Lapi, A.; Bressan, A.; De Zotti, G.; Negrello, M.; Danese, L.,
A physical model for the evolving UV luminosity function of high-redshift galaxies and their contribution to the cosmic reionization,
2013, ApJ, submitted
- Feretti, L.; Prandoni, I.; Brunetti, G.; Burigana, C.; Capetti, A.; Della Valle, M.; Ferrara, A.; Ghirlanda, G.; Govoni, F.; Molinari, S.; Possenti, A.; Scaramella, R.; Testi, L.; Tozzi, P.; Umana, G.; Wolter, A.; and 78 coauthors,
Italian SKA White Book,
2013, June 28, Version 4.0
- PRISM Collaboration; Andre, P.; Baccigalupi, C.; Barbosa, D.; Bartlett, J.; Bartolo, N.; Battistelli, E.; Battye, R.; Bendo, G.; Bernard, J. P.; and 94 coauthors,
PRISM (Polarized Radiation Imaging and Spectroscopy Mission): A White Paper on the Ultimate Polarimetric Spectro-Imaging of the Microwave and Far-Infrared Sky,
2013, arXiv:1306.2259 [astro-ph.CO]
- **Cai, Z.-Y.**; Lapi, A.; Xia, J.-Q.; De Zotti, G.; Negrello, M.; Gruppioni, C.; Rigby, E.; Castex, G.; Delabrouille, J.; Danese, L.,
A hybrid model for the evolution of galaxies and Active Galactic Nuclei in the Infrared,
2013, ApJ, 768, 21
- Lapi, A.; Negrello, M.; González-Nuevo, J.; **Cai, Z.-Y.**; De Zotti, G.; Danese, L.,
Effective Models for Statistical Studies of Galaxy-scale Gravitational Lensing,
2012, ApJ, 755, 46
- González-Nuevo, J.; Lapi, A.; Fleuren, S.; Bressan, S.; Danese, L.; De Zotti, G.; Negrello, M.; **Cai, Z.-Y.**; Fan, L.; Sutherland, W.; and 32 coauthors,
Herschel-ATLAS: Toward a Sample of \sim 1000 Strongly Lensed Galaxies,
2012, ApJ, 749, 65

Acknowledgments

First and foremost I would like to acknowledge the support from the joint PhD project between Xiamen University (XMU) and SISSA, without which there would not be the thesis, and to thank all my supervisors: Ju-Fu Lu and Wei-Min Gu in XMU; Luigi Danese, Gianfranco De Zotti, and Andrea Lapi in SISSA. After having been introduced into astrophysics by Wei-Min Gu and trusted to perform the joint PhD project by Ju-Fu Lu, I started my study in SISSA four years ago and thereafter I have been benefiting from the unforeseen physical insight illuminated by Gigi, the questions explained scrupulously by Gianfranco with great patience, and the explicit modeling of galaxy evolution introduced by Andrea. Furthermore, I am grateful to Gianfranco and Andrea for reading and revising my manuscript exhaustively. I also thank Joaquin González-Nuevo for introducing me to many useful astrophysical tools and the lensing project. I am indebted to the student secretariats, Riccardo Iancer and Federica Tuniz, for helping me living easily in the peaceful Trieste of lovely Italy. Special thanks to all knowledgeable researchers, teaching me the knowledge of nature, and all my forever friends, experiencing with me in our spacetime, in XMU, PKU, and SISSA. Last but not least, ... I am missing my parents far away.

Contents

Abstract	i
Publications	iii
Acknowledgments	v
Contents	vii
1 Introduction	1
2 The cosmological framework	5
2.1 Homogeneous and isotropic cosmology	5
2.1.1 Geometry and metric $g_{\mu\nu}$	5
2.1.2 Dynamical evolution of $a(t)$ and $\rho(t)$	7
2.2 Virialization of dark matter halos	10
2.2.1 Linear growth theory	10
2.2.2 Non-linear collapse	12
2.2.3 Statistics of Gaussian fluctuation field	14
2.2.4 Statistics of virialized halos	15
2.2.5 Properties of virialized halos	18
2.3 Baryon evolution within virialized dark matter halos	18
3 An “hybrid” galaxy evolution model	21
3.1 High- z star-forming galaxies and associated AGNs ($z \gtrsim 1$)	21
3.1.1 Self-regulated evolution of high- z proto-spheroidal galaxies	22
3.1.2 SEDs of high- z populations	28
3.1.3 Parameters of the physical model	31
3.1.4 Luminosity function and its evolution	32
3.2 Low- z star-forming galaxies and associated AGNs ($z \lesssim 2$)	34
3.2.1 Phenomenological backward evolution	34
3.2.2 SEDs of low- z populations	35
3.2.3 Parameters of the empirical model	39
3.3 Observables	40

3.3.1	Number counts and contributions to the background	41
3.3.2	Galaxy-galaxy lensing	42
3.3.3	Power spectrum of the cosmic infrared background anisotropy	47
4	Obscured star formation and black hole growth	51
4.1	Luminosity functions and redshift distributions	51
4.1.1	IR (8–1000 μm) luminosity functions	52
4.1.2	Optical and near-IR AGN luminosity functions	53
4.1.3	Monochromatic luminosity functions from IR to radio wavelengths	55
4.1.4	High- z luminosity functions including strongly lensed galaxies	62
4.1.5	Redshift distributions	67
4.2	Number counts	70
4.2.1	IR/(sub-)millimeter counts	70
4.2.2	Mid-IR AGN counts	74
4.2.3	(Sub-)millimeter lensed counts	75
4.2.4	Radio counts of star-forming galaxies	75
4.3	The cosmic infrared background (CIB)	79
4.3.1	CIB intensity	79
4.3.2	Clustering properties of dusty galaxies and CIB power spectrum	80
4.4	IR line luminosity functions	83
4.4.1	Correlations between line and continuum IR luminosity	83
4.4.2	Simulations of line and continuum IR luminosity	86
4.4.3	Predictions for the SPICA reference survey	90
5	Early UV–bright star formation and reionization	95
5.1	Ingredients of the model	95
5.2	Non-ionizing UV photons and cosmic star formation rate history	96
5.2.1	Luminosity functions of Lyman break galaxies	96
5.2.2	Cosmic star formation rate history	101
5.3	Ionizing photons and cosmic reionization	101
5.3.1	Luminosity functions of Lyman alpha emitters	101
5.3.2	Cosmic reionization	106
6	Conclusions	113
	Bibliography	119

Chapter 1

Introduction

The huge amount of panchromatic data that has been accumulating over the last several years has not yet led to a fully coherent, established picture of the cosmic star formation history, of the evolution of active galactic nuclei (AGNs), and of the interrelations between star formation and nuclear activity. This thesis is aimed at investigating the formation and evolution of galaxies and associated AGNs by means of the infrared/(sub-)millimeter and ultraviolet (UV) data.

Many, increasingly sophisticated, phenomenological models for the cosmological evolution of the galaxy and AGN luminosity functions (LFs) over a broad wavelength range have been worked out (e.g., Béthermin et al. 2012a, 2011; Gruppioni et al. 2011; Rahmati & van der Werf 2011; Marsden et al. 2011; Franceschini et al. 2010; Valiante et al. 2009; Le Borgne et al. 2009; Rowan-Robinson 2009). These models generally include multiple galaxy populations, with different spectral energy distributions (SEDs) and different evolutionary properties, described by simple analytic formulae. In some cases also AGNs are taken into account. All of them, however, admittedly have limitations.

The complex combination of source properties (both in terms of the mixture of SEDs and of evolutionary properties), called for by the richness of data, results in a large number of parameters, implying substantial degeneracies that hamper the interpretation of the results. The lack of constraints coming from the understanding of the astrophysical processes controlling the evolution and the SEDs limits the predictive capabilities of these models. In fact, predictions of pre-*Herschel* phenomenological models, matching the data then available, yielded predictions for *Herschel* counts quite discrepant from each other and with the data.

The final goal is a physical model linking the galaxy and AGN formation and evolution to primordial density perturbations. In this thesis we make a step in this direction presenting a comprehensive “hybrid” approach, combining a physical, forward model for spheroidal galaxies and the early evolution of the associated AGNs with a phenomenological backward model for late-type galaxies and for the later AGN evolution. We start from the consideration of the observed dichotomy in the ages of stellar populations of early-type galaxies on one side and late-type galaxies on the other. Early-type galaxies and massive bulges of Sa galaxies are composed of relatively old stellar populations with mass-weighted ages of $\gtrsim 8\text{--}9$ Gyr (corresponding to formation redshifts $z \gtrsim 1\text{--}1.5$), while the disc components of spiral and irregular

galaxies are characterized by significantly younger stellar populations. For instance, the luminosity-weighted age for most of Sb or later-type spirals is $\lesssim 7$ Gyr (cf. [Bernardi et al. 2010](#), their Figure 10), corresponding to a formation redshift $z \lesssim 1$. Thus proto-spheroidal galaxies are the dominant star-forming population at $z \geq 1.5$, while IR galaxies at $z < 1.5$ are mostly late-type “cold” (normal) and “warm” (starburst) galaxies.

Fuller hierarchical galaxy formation models, whereby the mass assembly of galaxies is related to structure formation in the dark matter and the star formation and merger histories of galaxies of all morphological types are calculated based on physical prescriptions have been recently presented by several groups ([Lacey et al. 2008](#); [Fontanot et al. 2009](#); [Narayanan et al. 2010](#); [Shimizu et al. 2012](#)). However, the predictions for the IR evolution of galaxies are limited to a small set of wavelengths and frequently highlight serious difficulties with accounting for observational data ([Lacey et al. 2010](#); [Niemi et al. 2012](#); [Hayward et al. 2013](#)).

While the evolution of dark matter halos in the framework of the “concordance” Λ CDM cosmology is reasonably well understood thanks to N -body simulations such as the Millennium, the Millennium-XXL and the Bolshoi simulations ([Springel et al. 2005](#); [Boylan-Kolchin et al. 2009](#); [Angulo et al. 2012](#); [Klypin et al. 2011](#)), establishing a clear connection between dark matter halos and visible objects proved to be quite challenging, especially at (sub-)millimeter wavelengths. The early predictions of the currently favored scenario, whereby both the star formation and the nuclear activity are driven by mergers, were more than one order of magnitude below the observed SCUBA 850 μm counts ([Kaviani et al. 2003](#); [Baugh et al. 2005](#)). The basic problem is that the duration of the star formation activity triggered by mergers is too short, requiring non-standard assumptions either on the initial mass function (IMF) or on dust properties to account for the measured source counts. The problem is more clearly illustrated in terms of redshift-dependent far-IR/submillimeter LF, estimated on the basis of *Herschel* data ([Eales et al. 2010](#); [Gruppioni et al. 2010](#); [Lapi et al. 2011](#); [Gruppioni et al. 2013](#)). These estimates consistently show that $z \simeq 2$ galaxies with Star Formation Rates (SFRs) $\text{SFR} \simeq 300 M_{\odot} \text{ yr}^{-1}$ have comoving densities $\Phi_{300} \sim 10^{-4} \text{ Mpc}^{-3} \text{ dex}^{-1}$. The comoving density of the corresponding halos is $n(M_{\text{vir}}) \sim \Phi_{300} (t_{\text{exp}}/\tau_{\text{SFR}})$, where M_{vir} is the total virial mass (mostly dark matter), τ_{SFR} is the lifetime of the star-forming phase and t_{exp} is the expansion timescale. For the fiducial lifetime $\tau_{\text{SFR}} \simeq 0.7$ Gyr advocated by [Lapi et al. \(2011\)](#), $\log(M_{\text{vir}}/M_{\odot}) \simeq 12.92$, while for $\tau_{\text{SFR}} \simeq 0.1$ Gyr, typical of a merger-driven starburst, $\log(M_{\text{vir}}/M_{\odot}) \simeq 12.12$. Thus while the [Lapi et al. \(2011\)](#) model implies a $\text{SFR}/M_{\text{vir}}$ ratio easily accounted for on the basis of standard IMFs and dust properties, the latter scenario requires a $\text{SFR}/M_{\text{vir}}$ ratio more than a factor of 6 higher.

To reach the required values of $\text{SFR}/M_{\text{vir}}$ or, equivalently, of $L_{\text{IR}}/M_{\text{vir}}$, [Baugh et al. \(2005\)](#) resorted to a top-heavy IMF while [Kaviani et al. \(2003\)](#) assumed that the bulk of the submillimeter emission comes from a huge amount of cool dust. But even tweaking with the IMF and with dust properties, fits of the sub-mm counts obtained within the merger-driven scenario ([Lacey et al. 2010](#); [Niemi et al. 2012](#)) are generally unsatisfactory. Further constraints on physical models come from the clustering properties of submillimeter galaxies that are determined by their effective halo masses. As shown by [Xia et al. \(2012\)](#), both the angular correlation function of detected submillimeter galaxies and the power spectrum

of fluctuations of the cosmic infrared background (CIB) indicate halo masses larger than implied by the major mergers plus top-heavy initial stellar mass function scenario (Kim et al. 2012) and smaller than implied by cold flow models but consistent with the self-regulated baryon collapse scenario (Granato et al. 2004; Lapi et al. 2006, 2011).

As is well known, the strongly negative K -correction emphasizes high- z sources at (sub-)millimeter wavelengths. The data show that the steeply rising portion of the (sub-)millimeter counts is indeed dominated by ultra-luminous star-forming galaxies with a redshift distribution peaking at $z \simeq 2.5$ (Chapman et al. 2005; Aretxaga et al. 2007; Yun et al. 2012; Smolčić et al. 2012). As shown by Lapi et al. (2011), the self-regulated baryon collapse scenario provides a good fit of the (sub-)millimeter data (counts, redshift-dependent LFs) as well as of the stellar mass functions at different redshifts. Moreover, the counts of strongly lensed galaxies were predicted with remarkable accuracy (Negrello et al. 2007, 2010; Lapi et al. 2012; González-Nuevo et al. 2012). Further considering that this scenario accounts for the clustering properties of submillimeter galaxies (Xia et al. 2012), we conclude that it is well grounded, and we adopt it for the present analysis. However, we upgrade this model in two respects. First, while on one side, the model envisages a co-evolution of spheroidal galaxies and active nuclei at their centers, the emissions of the two components have so far been treated independently of each other. This is not a problem in the wavelength ranges where one of the two components dominates, as in the (sub-)millimeter region where the emission is dominated by star formation, but is no longer adequate at mid-IR wavelengths, where the AGN contribution may be substantial. In this thesis, we present and exploit a consistent treatment of proto-spheroidal galaxies including both components. Second, while the steeply rising portion of (sub-)millimeter counts is fully accounted for by proto-spheroidal galaxies, late-type (normal and starburst) galaxies dominate both at brighter and fainter flux densities and over broad flux density ranges at mid-IR wavelengths. At these wavelengths, AGNs not associated to proto-spheroidal galaxies but either to evolved early-type galaxies or to late-type galaxies are also important. Since we do not have a physical evolutionary model for late-type galaxies and the associated AGNs, these source populations have been dealt with adopting a phenomenological approach. This “hybrid” model for the cosmological evolution of the LF of galaxies and AGNs is described in Chapter 3 after having introduced the cosmological framework for the virialization of dark matter halos in Chapter 2. The dust obscured cosmic evolution of galaxies and AGNs at mid-IR to millimeter wavelengths are presented in Chapter 4, within which predictions for future SSpace Infrared telescope for Cosmology and Astrophysics (SPICA) spectroscopic surveys are presented to investigate the complex physics ruling the dust-enshrouded active star-forming phase of galaxy evolution and the relationship with nuclear activity using the rich suite of spectral lines in the mid- to far-IR wavelength region.

Perhaps you may add a sentence in the Introduction explaining that our model gives an alternative explanation of the main sequence and off-sequence galaxies. The former are the most massive objects, forming stars for a short time at very high rates, the latter are less massive objects, with longer star formation times. (I don't understand this point) Perhaps Andrea can help you in writing a short paragraph on that?

Adopting the ratio of total IR luminosity (8–1000 μm) to 8 μm luminosity, IR8 ($\equiv L_{\text{IR}}/L_8$), Elbaz

et al. (2011) defined an IR main sequence for star-forming galaxies independent of redshift and luminosity. Our model gives an alternative explanation of the main sequence and off-sequence galaxies. The former are the galaxies with longer star formation times ($\gtrsim 0.1$ Gyr), while the latter are the galaxies with enhanced star formation triggered by interactions/mergers and shorter star formation times (~ 0.1 Gyr). With shorter star formation times, the hot stars do not have the time to leave their birth clouds and to migrate to less dense regions, where they would ionize the interstellar medium (ISM) and enhance the emissions of polycyclic aromatic hydrocarbon (PAH), therefore their IR8 values tend to be larger.

One of the frontiers of present day astrophysical/cosmological research is the understanding of the transition from the “dark ages”, when the hydrogen was almost fully neutral, to the epoch when stars and galaxies began to shine and the intergalactic hydrogen was almost fully re-ionized. Recent, ultra-deep observations with the Wide Field Camera 3 (WFC-3) on the Hubble Space Telescope (HST, Ellis et al. 2013; Robertson et al. 2013) have substantially improved the observational constraints on the abundance and properties of galaxies at cosmic ages of less than 1 Gyr. Determinations of the UV LF of galaxies at $z = 7\text{--}8$ have been obtained by Schenker et al. (2013) and McLure et al. (2013), with the latter authors providing first estimates over a small luminosity range, also at $z = 9$. Constraints on the UV luminosity density at redshifts up to 12 have been presented by Ellis et al. (2013). Since galaxies at $z \gtrsim 6$ are the most likely sources of the UV photons capable of ionizing the intergalactic hydrogen, the study of the early evolution of the UV luminosity density is directly connected with the understanding of the cosmic re-ionization. Therefore, Chapter 5 exhibits the earliest phases of galaxy evolution, before the ISM is strongly metal enriched and large amounts of dust could form, in the UV wavelength range based on the extended high- z physical model for proto-spheroidal galaxies. The high- z observed UV LFs ($z \simeq 2\text{--}10$) are very well reproduced with the SFRs yielded by the model incorporated the extinction law derived by Mao et al. (2007) and a Chabrier (2003) IMF, while similarly good fits are obtained for the Ly α LFs that provide constraints on the production rate of ionizing photons adopted to reconstruct the cosmic reionization history of the universe.

Finally, Chapter 6 contains a summary of the thesis and our main conclusions. Tabulations of multi-frequency model counts, redshift distributions, SEDs, redshift-dependent LFs at several wavelengths, and a large set of figures comparing model predictions with the data are available at the Web site http://people.sissa.it/~zcai/galaxy_agn/. When writing this thesis, I benefited greatly from the previous PhD theses by Lapi (2004), Shankar (2005), Mao (2006), Negrello (2006), and Fan (2011).

Chapter 2

The cosmological framework

The early galaxy redshift surveys carried out in the 1980s ([Coleman et al. 1988; Tucker et al. 1997; Lahav & Suto 2004](#), for a review) have established that the universe is nearly homogeneous and isotropic on scales $\gtrsim 200h^{-1}$ Mpc. On smaller scales structures are observed over a broad range of sizes, from super-clusters, to galaxy clusters and groups, to individual galaxies, etc.. As shown in Section 2.1, the global evolution of the Universe is described under the assumption of its homogeneity and isotropy, known as the *cosmological principle*, and of the validity of Einstein's *general relativity*. Due to the gravitational instability, the overdensities grew up from the initial quantum fluctuations into the present day structures, as described in Section 2.2. Crucial for galaxy formation theories are the evolution with cosmic time of the *mass function* and of the *formation rate* of virialized dark matter halos within which visible galaxies are believed to form and live ([White & Rees 1978](#)).

2.1 Homogeneous and isotropic cosmology

2.1.1 Geometry and metric $g_{\mu\nu}$

The cosmological principle leads to the *Robertson-Walker* metric ([Robertson 1935; Weinberg 2008](#)) whereby the space-time line element writes

$$ds^2 = -g_{\mu\nu}dx^\mu dx^\nu = c^2dt^2 - a^2(t)\left[d\vec{x}^2 + K\frac{(\vec{x}\cdot d\vec{x})^2}{1-K\vec{x}^2}\right] = c^2dt^2 - a^2(t)\left[\frac{dr^2}{1-Kr^2} + r^2(d\theta^2 + \sin^2\theta d\phi^2)\right], \quad (2.1)$$

where K is the curvature parameter that can be positive, negative, or 0. The metric tensor is then $g_{\mu\nu} = \text{diag}[-c^2, a^2/(1-Kr^2), (ar)^2, (ar\sin\theta)^2]$. The proper distance between the three-dimensional space position \vec{x} and its neighborhood $\vec{x} + d\vec{x}$ over an isochronous surface is solely scaled by the time-dependent function $a(t)$, named the *scale factor*. This kind of space coordinates are known as the *comoving coordinates*. Since there is nothing special with our position, we can safely put ourself at the origin of the selected coordinates. Consequently, we can infer at time t the proper distance of a distant object at radial coordinate r traced by a photon emitted at the previous time $t_e (\leq t)$ coming toward us along the

radial direction as

$$d_P(r, t) = \int_{t_e}^t c dt' = -a(t) \int_r^0 \frac{dr'}{\sqrt{1 - Kr'^2}} = a(t) d_C(r) = a(t) \begin{cases} \frac{\sin^{-1}(\sqrt{|K|} r)}{\sqrt{|K|}}, & K > 0 \\ r, & K = 0 \\ \frac{\sinh^{-1}(\sqrt{|K|} r)}{\sqrt{|K|}}, & K < 0 \end{cases} \quad (2.2)$$

where the minus sign is selected so that $a(t) \geq 0$ and $d_C(r)$ is the line-of-sight time-independent comoving distance from r to the origin. The scale factor $a(t)$ is related to an observable quantity z inferred from the shift of spectral lines in the observer frame compared to the source frame. Suppose that we have a photon emitted at the time t_e in a time interval δt_e (emitted frequency $\nu_e \propto 1/\delta t_e$) at a radial coordinate r and observed at the time t_o in a time interval δt_o (observed frequency $\nu_o \propto 1/\delta t_o$) at the origin. The relation between the emitted interval δt_e and the observed interval δt_o follows directly from Equation (2.1) as

$$d_C(r) \equiv \int_0^r \frac{dr'}{\sqrt{1 - Kr'^2}} = \int_{t_e}^{t_o} \frac{cdt'}{a(t')} = \int_{t_e + \delta t_e}^{t_o + \delta t_o} \frac{cdt'}{a(t')}, \quad (2.3)$$

which results in $\delta t_o/\delta t_e = a(t_o)/a(t_e) = \nu_e/\nu_o \equiv 1 + z$ as long as $\delta t_o \ll t_o$ and $\delta t_e \ll t_e$. This is valid nearly over the whole evolutionary history of the Universe. Observations tell us that the ratio ν_e/ν_o increases with source distance, implying that $a(t_e)$ decreases with increasing distance, i.e., that *the Universe is expanding* (Hubble 1929). The expansion rate at time t is $H(t) \equiv \dot{a}(t)/a(t)$ and the current value, known as the *Hubble constant*, is usually written as $H_0 \equiv \dot{a}(t_0)/a(t_0) = 100h \text{ km s}^{-1} \text{ Mpc}^{-1}$. In our work we have used $h = 0.71$ (see Table 2.1).

The comoving radial distance, Equation (2.3), can now be expressed as

$$d_C(z) = \int_t^{t_o} \frac{cdt'}{a(t')} = \frac{1}{a_0} \int_0^z \frac{cdz'}{\dot{a}(t')/a(t')} = \frac{1}{a_0} \int_0^z \frac{cdz'}{H(z')} \quad \text{and} \quad r(z) = S_K[d_C(z)], \quad (2.4)$$

where the function $S_K[x] = \sin(\sqrt{|K|} x)/\sqrt{|K|}$, $x, \sinh(\sqrt{|K|} x)/\sqrt{|K|}$ for $K > 0, = 0, < 0$, respectively. The proper distance (or physical distance) of a source at redshift z to an observer at the origin is related to the comoving distance by $d_P(z, t) = a(t)d_C(z)$. To relate the observed bolometric flux S or the angular size θ of a source at redshift z to its bolometric luminosity L or to its linear size l in analogy to what is done in Euclidean space, the *luminosity distance* $d_L(z)$ or the *angular diameter distance* $d_A(z)$ are defined so that $L = 4\pi d_L^2 S$ or $l = \theta d_A$, respectively. They are related to the radial coordinate $r(z)$, and through it, to the comoving distance $d_C(z)$, by

$$d_L(z) = a^2(t_0)r(z)/a[t(z)] = a_0r(z)(1+z) \quad \text{and} \quad d_A(z) = r(z)a[t(z)] = a_0r(z)/(1+z). \quad (2.5)$$

Another useful quantity is the *comoving volume* V_C at redshift z , the corresponding element d^2V_C within the redshift interval dz and the solid angle $d\Omega$ is given as

$$d^2V_C(z) = \frac{dr}{\sqrt{1 - Kr^2}} \cdot rd\theta \cdot r \sin \theta d\phi = \frac{dd_C(z)}{dz} dz \cdot r^2(z) d\Omega = \frac{cr^2(z)}{a_0 H(z)} dz d\Omega, \quad (2.6)$$

where the solid angle $d\Omega = \sin \theta d\theta d\phi$. Furthermore, the age of the Universe $t(z)$ at redshift z is

$$t(z) = \int_z^\infty \frac{a[t(z')]}{c} \frac{dd_C(z')}{dz'} dz' = \int_z^\infty \frac{dz'}{(1+z')H(z')}.$$
 (2.7)

Finally, the *Hubble distance* (also named *curvature scale* or even *Hubble horizon*), characterizing the expansion rate and beyond which the general relativistic effect on the growth of cosmological perturbations is significant at given cosmic epoch, reads

$$d_H(z) \equiv \frac{c}{H(z)},$$
 (2.8)

(see, e.g., Hogg 1999; Padmanabhan 2002; Mukhanov 2005; Schneider 2006; Weinberg 2008; Mo et al. 2010, for more details).

2.1.2 Dynamical evolution of $a(t)$ and $\rho(t)$

According to Einstein's *general relativity* (Einstein 1916), the geometry of space-time is entirely determined by its energy/matter contents, according to the Einstein field equations

$$R_{\mu\nu} - \frac{1}{2}g_{\mu\nu}R = -\frac{8\pi G}{c^2}T_{\mu\nu},$$
 (2.9)

where the *Ricci tensor* $R_{\mu\nu}$ and the *Ricci scalar* R are linked to the metric tensor $g_{\mu\nu}$ and the energy/matter contents are described by the energy-momentum tensor $T_{\mu\nu}$. $T_{\mu\nu}$ is constructed assuming that the contents of the universe can be modeled as uniform ideal fluids, consistent with the *cosmological principle*. This gives

$$T_{\mu\nu} = (\rho + p/c^2)u_\mu u_\nu - g_{\mu\nu}p/c^2,$$
 (2.10)

where $u_\mu = [-c, 0, 0, 0]$ is the four velocity of the ideal fluid. The total density $\rho = \rho(t)$ and the total pressure $p = p(t)$ are only a function of time or of $a(t)$ and include any kind of matter/energy components under the additivity assumption, i.e., $\rho \equiv \sum_w \rho_w$ and $p \equiv \sum_w p_w$, where the ρ_w and p_w are the density and the pressure of w constituent, respectively.

The known constituents are the radiation, with density $\rho_r \propto a^{-4}$, including hot relativistic particles with $\bar{v} \simeq c$, and the matter, with density $\rho_m \propto a^{-3}$ (cold non-relativistic particles with $\bar{v} \ll c$ and then insignificant pressure), and the “dark energy” that may be represented by the cosmological constant Λ or by the *vacuum energy* $\rho_\Lambda \propto a^0$. This assumes that the cosmological constant is a kind of energy density (on the right hand side of Equation (2.9)) instead of the modification of geometry (on the left hand side of Equation (2.9)).

In the following, we will also mention other kinds of energy density such as the curvature energy density¹ $\rho_K' \propto a^{-2}$ and the scale energy density² $\rho_L \propto a^{-1}$.

¹The reason why we indicate the curvature energy density with a prime is to distinguish it from the curvature K and to draw attention to the difference with its usual definition with a minus sign.

²Named from its inverse dependence on the *scale factor*.

Recasting the Einstein's field equations with these choices of $g_{\mu\nu}$ and $T_{\mu\nu}$ (Weinberg 2008), we end up with the *Friedmann equations*

$$\frac{Kc^2}{a^2} + \left(\frac{\dot{a}}{a}\right)^2 = \frac{8\pi G}{3}\rho \quad (2.11)$$

$$\ddot{a} = -\frac{4\pi G}{3}\left(\rho + 3\frac{p}{c^2}\right), \quad (2.12)$$

to which we can add the energy conservation equation $T^{0\nu}_{;\nu} = 0$

$$0 = \frac{d\rho}{dt} + 3\frac{\dot{a}}{a}\left(\rho + \frac{p}{c^2}\right) = \frac{1}{c^2 a^3} \left[\frac{d(\rho c^2 a^3)}{dt} + p \frac{d(a^3)}{dt} \right]. \quad (2.13)$$

Adding the cosmological constant term $\Lambda g_{\mu\nu}$ to the geometry part of Equation (2.9) is equivalent to introducing a kind of constant energy constituent with $\rho_\Lambda \equiv \Lambda c^2/8\pi G$ and $\rho_\Lambda + 3p_\Lambda/c^2 \equiv -\Lambda c^2/4\pi G$ ($\Lambda > 0$), i.e., with an *equation of state* of $p_\Lambda = -\rho_\Lambda c^2$.

With these five possible energy kinds, we rewrite Equation (2.11) as

$$\frac{3Kc^2}{8\pi Ga^2} + \frac{3\dot{a}^2}{8\pi Ga^2} = \rho_r + \rho_m + \rho_{K'} + \rho_L + \rho_\Lambda. \quad (2.14)$$

If the energy density of the w constituent scales as $\rho_w \propto a^{-\alpha_w}$ and its *equation of state* is $p_w = w\rho_w c^2$, we have $\alpha \equiv 3(1+w)$. Defining the present critical density $\rho_{c,0} \equiv 3H_0^2/8\pi G$ and the present dimensionless density of the w energy kind in units of the present critical density as $\Omega_{w,0} \equiv \rho_{w,0}/\rho_{c,0}$, we can obtain $1 = \Omega_{r,0} + \Omega_{m,0} + \Omega_{L,0} + \Omega_{\Lambda,0}$ and the evolution of the Hubble constant

$$H^2(z) = H_0^2[\Omega_{r,0}(1+z)^4 + \Omega_{m,0}(1+z)^3 + \Omega_{L,0}(1+z) + \Omega_{\Lambda,0}] = H_0^2 E^2(z), \quad (2.15)$$

where $E(z) \equiv \sqrt{\Omega_{r,0}(1+z)^4 + \Omega_{m,0}(1+z)^3 + \Omega_{L,0}(1+z) + \Omega_{\Lambda,0}}$. The dimensionless density of the w constituent at redshift z is $\Omega_w(z) \equiv \Omega_{w,0}(1+z)^{\alpha_w}/E^2(z)$. Note that the curvature energy density, $\rho_{K'} \equiv 3Kc^2/8\pi Ga^2$, has been excluded in the definition of the critical density, i.e., the critical density corresponds to a zero-curvature ("flat") universe.

Since the radiation density is very small at present and only significant beyond the radiation-matter equi-density epoch at $1+z_{\text{eq}} \simeq \Omega_{m,0}/\Omega_{r,0} \sim 3300(\Omega_{m,0}h^2/0.143)$, it is usually neglected in the evolution of the Universe after the epoch of last scattering or decoupling between photons and electrons at around $z_{\text{dec}} \sim 1100$. In current cosmological models the $\Omega_{L,0}$ term is not generally included and the accelerated expansion is entirely attributed to $\Omega_{\Lambda,0}$. However, this $\Omega_{L,0}$ -kind energy could be a simple case of the speculated time-varying vacuum energy called *quintessence* (Peebles & Ratra 2003).

A summary of current estimates of the main cosmological parameters is given in Table 2.1 where we also list the values used in our work on galaxy formation and evolution.

Although our adopted values are slightly different from the best fit values obtained from *WMAP-9* or *Planck* data, the differences are not significant for the present purposes as illustrated in the left panel of Figure 2.1, which shows the distance modulus of Type Ia SNe as a function of redshift. The SNe

Table 2.1: The present main cosmic energy constituents and the cosmological parameters

Contents/Parameters	$\rho_w \propto a^{-\alpha}$	w	Adopted ^a	WMAP-9 ^b	Planck ^c
Relativistic species ^d $\Omega_{r,0}$	4	1/3	0	-	$4.327 \times 10^{-5} / h^2$
Total matter $\Omega_{m,0}$	3	$\simeq 0$	0.27	0.2865	0.314 ± 0.020
Cold dark matter $\Omega_{CDM,0}$	3	0	0.226	0.2402 ± 0.0088	0.263 ± 0.007
Baryons $\Omega_{b,0}$	3	$\simeq 0$	0.044	0.04628 ± 0.00093	0.0486 ± 0.0007
Curvature energy ^e $\Omega_{K',0}$	2	-1/3	0	-0.0027 ± 0.0039	-0.0010 ± 0.0065
Scale energy $\Omega_{L,0}$	1	-2/3	-	?	?
Dark energy $\Omega_{\Lambda,0}$	0	-1	0.73	0.7135 ± 0.0096	0.686 ± 0.020
Hubble constant h	-	-	0.71	0.6932 ± 0.0080	0.674 ± 0.014
Scalar spectral index n_s	-	-	1	0.9608 ± 0.0080	0.9616 ± 0.0094
RMS matter fluctuation today ^f σ_8	-	-	0.81	0.820 ± 0.014	0.834 ± 0.027
Optical depth of electron scattering τ_e	-	-	-	0.081 ± 0.012	0.097 ± 0.038

^a Values of the cosmological parameters adopted in our work on galaxy formation and evolution.

^b Values taken from Table 4 of Hinshaw et al. (2012), obtained using a six-parameter Λ CDM model fit to WMAP nine-year data combined with external data sets (i.e., eCMB, BAO, and H_0), except Ω_K from their Table 9.

^c Values from Table 2 of Planck collaboration et al. (2013b) for the six-parameter base Λ CDM model using the Planck temperature power spectrum data alone, except Ω_K determined using multiple data sets (i.e., Planck temperature power spectrum, Planck lensing, WMAP-9 low- l polarization, high-resolution CMB data, and BAO) from their Section 6.2.3.

^d The present density of relativistic particles, i.e., photons, neutrinos, and “extra radiation species”, is parameterized as $\rho_{r,0} = \rho_{\gamma,0}[1 + (7/8)(4/11)^{4/3}N_{\text{eff}}] = 8.126 \times 10^{-34} \text{ g cm}^{-3}$ using the current photon density $\rho_{\gamma,0} = (\pi^2/15)(k_B T_{\gamma,0})^4/(\hbar c)^3/c^2 = \alpha_r T_{\gamma,0}^4/c^2 = 4.645 \times 10^{-34} \text{ g cm}^{-3}$ with the radiation energy constant $\alpha_r = 7.56577 \times 10^{-15} \text{ erg cm}^{-3} \text{ K}^{-4}$, the current CMB temperature $T_{\gamma,0} = 2.72548 \pm 0.00057 \text{ K}$ (Fixsen 2009), and the effective number of neutrino species $N_{\text{eff}} = 3.30 \pm 0.27$ from Section 6.3.2 of Planck collaboration et al. (2013b).

^e Dimensionless curvature energy density $\Omega_{K',0} \equiv \rho_{K',0}/\rho_{c,0} = K(c/a_0 H_0)^2$. It is negative because of our sign convention.

^f Present-day mass variance on the $8h^{-1}$ Mpc scale, see Section 2.2.

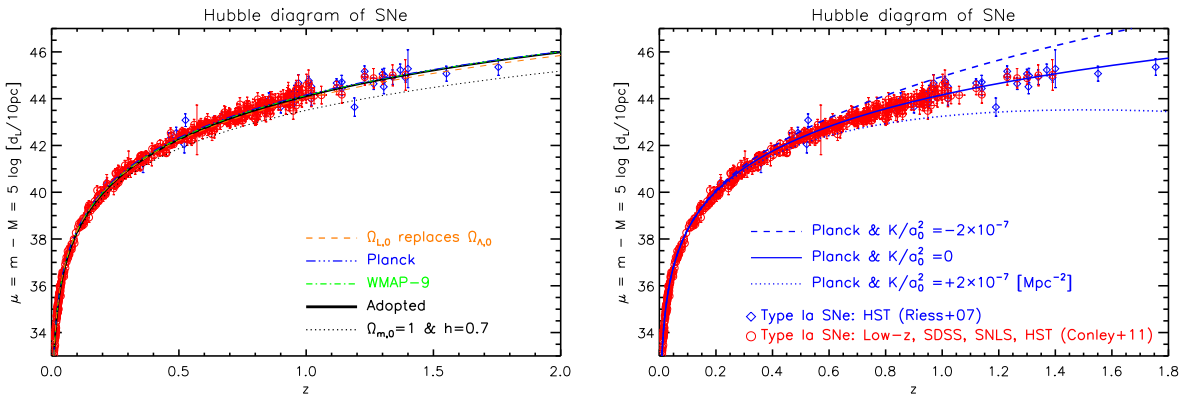


Figure 2.1: *Left:* Distance modulus of Type Ia SNe as a function of redshift. The dotted black line corresponds to a flat cosmology with $\Omega_{m,0} = 1$ and $h = 0.7$ and is shown to illustrate that data require cosmic acceleration. The solid black line correspond to the cosmological model adopted in our work while the dot-dashed green line and the triple-dot-dashed blue line correspond to the best fit WMAP-9 and Planck flat cosmologies, respectively, with the parameters listed in Table 2.1. The 3 lines are indistinguishable from each other. Adopting the Planck parameters except for replacing $\Omega_{\Lambda,0}$ with $\Omega_{L,0}$ yields a curve (dashed orange line) only slightly below those for models with the cosmological constant. Red circles refer to the collection of Type Ia SNe by Conley et al. (2011) including 123 low- z , 93 SDSS, 242 SNLS, and 14 HST SNe , while the open blue diamonds refer to the HST SNe by Riess et al. (2007). *Right:* Constraints on the curvature of the universe from SN data are illustrated by the dependence on redshift of the distance modulus for the best fit values of parameters determined by Planck except for curvature values of $|K|/a_0^2 = 2 \times 10^{-7} \text{ Mpc}^{-2}$.

data at high- z prefer an accelerating universe compared to the matter-dominated non-accelerating one (black dotted line) with matter density $\Omega_{m,0} = 1$ and $h = 0.7$. Results for an alternative cosmology with acceleration driven by the scale energy density (orange line) rather than by a cosmological constant are also shown. Although the possibility of alternative cosmologies should be kept in mind, in the following we will adhere to the standard flat cosmology with cosmological constant.

2.2 Virialization of dark matter halos

The aim of this section is to briefly describe the derivation of the *halo mass function*, $n(M_{\text{vir}}, z) \equiv d^2N(M_{\text{vir}}, z)/dM_{\text{vir}}dV_C$, which gives the average comoving number density of virialized halos in the mass range $M_{\text{vir}} \pm dM_{\text{vir}}/2$ at redshift z , and of the *halo formation rate*, $\dot{n}(M_{\text{vir}}, z) \equiv d^3N'(M_{\text{vir}}, z)/dM_{\text{vir}}dV_Cdt$, which is, in general, different from the time derivative of the halo mass function ([Sasaki 1994](#)).

The halo mass function is a statistical property of the density fluctuation field whose overdense regions above some density threshold are identified as virialized objects. Its derivation relies on a combination of the linear growth theory and of the spherical or ellipsoidal collapse for non-linear growth.

2.2.1 Linear growth theory

After the postulated *big bang*, the expansion history $a(t)$ of the Universe can be divided into three distinct eras according to the different dominant energy content: a radiation-dominated era at $z \gtrsim z_{\text{eq}} \simeq \Omega_{\text{m},0}/\Omega_{\text{r},0} \sim 3300(\Omega_{\text{m},0}h^2/0.143)$ with $a(t) \propto t^{1/2}$, a matter-dominated decelerating era during $z_{\text{da}} \lesssim z \lesssim z_{\text{eq}}$ with $a(t) \propto t^{2/3}$, and a dark-energy-dominated accelerating era at $z \lesssim z_{\text{da}} \simeq (2\Omega_{\Lambda,0}/\Omega_{\text{m},0})^{1/3} - 1 \sim 0.6$ with $a(t) \propto e^t$.

The cosmic evolution of the density fluctuation field $\rho(t, \vec{x})$ at any position \vec{x} is generally described by the perturbation theory of gravitational instability in general relativity ([Mukhanov 2005; Weinberg 2008](#)). For the astrophysical scales $\lesssim 100h^{-1}$ Mpc of interest here, which have already entered the Hubble horizon in the radiation dominated epochs, the hydrodynamical equations in the Newtonian limit with a special relativistic source term p/c^2 are a good approximation to follow the growth of perturbations of each energy constituent, especially that of dark matter. It is convenient to follow the peculiar evolution of perturbations after having removed the global cosmic evolution, working in the comoving frame. In this coordinate frame, (t, \vec{x}) , the growth of perturbations of the w constituent (density field ρ_w , pressure field p_w , velocity field \vec{v}_w) is given by the continuity equation, the Euler equation, and the Poisson equation, under the gravitational potential $\phi(t, \vec{x})$. Further assuming that the equation of state is $p_w = p_w(\rho_w) = w\rho_w c^2$, these equations can be expressed in terms of the *density contrast* $\delta_w(t, \vec{x}) = (\rho_w - \bar{\rho}_w)/\bar{\rho}_w = (p_w - \bar{p}_w)/\bar{p}_w$ as

$$\forall w, \quad \frac{\partial \delta_w}{\partial t} + \frac{1+w}{a} \vec{\nabla}_x \cdot [(1+\delta_w) \vec{v}_w] = 0, \quad (2.16)$$

$$\frac{\partial \vec{v}_w}{\partial t} + \frac{\vec{v}_w \cdot \vec{\nabla}_x}{a} \vec{v}_w + \frac{\dot{a}}{a} \vec{v}_w = -\frac{c_{s,w}^2 \vec{\nabla}_x \delta_w}{(1+w)(1+\delta_w)a} - \frac{1}{a} \vec{\nabla}_x \phi, \quad (2.17)$$

$$\nabla_x^2 \phi = 4\pi G a^2 \sum_{w'}^{w'} (1+3w') \bar{\rho}_{w'} \delta_{w'}, \quad (2.18)$$

where the sound velocity of the w constituent is $c_{s,w}^2 = dp_w/d\rho_w = wc^2$ (see Table 2.1 for w values). Exact solutions of the above equations can only be obtained numerically. However, in the linear regime when $\delta_w \ll 1$ ([Peebles 1980; Padmanabhan 2002; Bernardeau et al. 2002](#)), the above equations can be recast as a second-order differential equation describing the evolution of the density contrast $\delta_w(t, \vec{x})$ in

comoving real space:

$$\forall w, \quad \frac{\partial^2 \delta_w}{\partial t^2} + 2 \frac{\dot{a}}{a} \frac{\partial \delta_w}{\partial t} \simeq \frac{c_{s,w}^2}{a^2} \nabla_x^2 \delta_w + (1+w) 4\pi G \sum_{w'}^{w'} (1+3w') \bar{\rho}_{w'} \delta_{w'}, \quad (2.19)$$

and the corresponding evolution of the \vec{k} -mode perturbation $\tilde{\delta}_w^{\vec{k}}(t)$ in Fourier space:

$$\forall w \& \vec{k}, \quad \frac{d^2 \tilde{\delta}_w^{\vec{k}}}{dt^2} + 2 \frac{\dot{a}}{a} \frac{d \tilde{\delta}_w^{\vec{k}}}{dt} + \left[\frac{c_{s,w}^2 k^2}{a^2} - (1+w)(1+3w) 4\pi G \bar{\rho}_w \right] \tilde{\delta}_w^{\vec{k}} \simeq (1+w) 4\pi G \sum_{w' \neq w}^{w'} (1+3w') \bar{\rho}_{w'} \tilde{\delta}_{w'}^{\vec{k}}, \quad (2.20)$$

showing that different Fourier modes evolve independently in linear theory.

In the radiation-dominated era all δ_w remained nearly constant. The dark matter over-densities δ_{DM} began to grow and set up gravitational potential wells in the matter-dominated era, while the baryons were tightly coupled to photons and were oscillating in and out the dark matter potential wells. Therefore the baryon over-densities did not grow much until the recombination epoch. After decoupling, the baryons fell into the dark matter potential wells inducing the growth of small modes of baryonic perturbations toward the overdensity of dark matter on large scale, i.e., $\tilde{\delta}_b^{\vec{k}} \lesssim \tilde{\delta}_{\text{DM}}^{\vec{k}}$ for small \vec{k} . The growth of small scales, large \vec{k} , over-densities was still suppressed by pressure support, i.e., $\tilde{\delta}_b^{\vec{k}} \ll \tilde{\delta}_{\text{DM}}^{\vec{k}}$ for large \vec{k} . Further considering that $\bar{\rho}_{\text{DM}} = \Omega_{\text{DM},0} \bar{\rho}_b / \Omega_{b,0} \simeq 5 \bar{\rho}_b$, we have $\bar{\rho}_{\text{DM}} \delta_{\text{DM}} \gg \bar{\rho}_b \delta_b$ so that the baryon effect on the growth of dark matter over-densities is small. We know from CMB anisotropy measurements that in the matter-dominated era the radiation over-densities δ_r are very small and for a cosmological constant δ_Λ is always zero. Consequently, the equation governing the evolution of dark matter over-densities, $\delta_{\text{DM}}(t, \vec{x})$, Equation (2.19), simplifies to

$$\frac{\partial^2 \delta_{\text{DM}}}{\partial t^2} + 2 \frac{\dot{a}}{a} \frac{\partial \delta_{\text{DM}}}{\partial t} \simeq 4\pi G (\bar{\rho}_{\text{DM}} \delta_{\text{DM}} + \bar{\rho}_b \delta_b + 2\bar{\rho}_r \delta_r - 2\bar{\rho}_\Lambda \delta_\Lambda) \simeq 4\pi G \bar{\rho}_{\text{DM}} \delta_{\text{DM}} \simeq \frac{3}{2} \Omega_{m,0} \left(\frac{\dot{a}}{a} \right)^2 \delta_{\text{DM}}, \quad (2.21)$$

where the last approximation is obtained using the Friedmann equation (Equation (2.11)) in a flat Universe and replacing $\Omega_{\text{DM},0}$ with $\Omega_{m,0}$ to include the effect of baryons in deepening the gravitational potential wells. Noting that the above equation implies a position independent evolution, one can factorize $\delta_{\text{DM}}(t, \vec{x}) = D(t) \delta'_{\text{DM}}(\vec{x})$ where the time dependent function, $D(t)$, is called the *growth factor*. This linear growth factor can be analytically obtained from the above equation as

$$D(z) = \frac{5\Omega_{m,0} H_0^2}{2} H(z) \int_z^\infty \frac{(1+z') dz'}{H^3(z')} \simeq \frac{5\Omega_m(z)}{2(1+z)} / \left[\frac{1}{70} + \frac{209}{140} \Omega_m(z) - \frac{1}{140} \Omega_m^2(z) + \Omega_m^{4/7}(z) \right], \quad (2.22)$$

where the normalization constant is such that $\lim_{z \rightarrow \infty} D(z) = 1/(1+z)$ and $\Omega_m(z) = \Omega_{m,0}(1+z)^3 [H_0/H(z)]^2$ (Lahav et al. 1991; Carroll et al. 1992). In the Einstein-de Sitter Universe ($\Omega_{m,0} = 1$ and $\Omega_{\Lambda,0} = 0$), the linear growth factor is $D(z) = 1/(1+z) = a(z)/a_0 = [t(z)/t_0]^{2/3}$ with $t_0 = 2/3H_0$.

Now having the linear growth of density fluctuation field in hand, we will introduce next when a region of this density fluctuation field can be identified as a virialized object. The above equations are obviously no longer valid when the density fluctuation field enters the non-linear regime, that will be discussed in the next sub-section.

2.2.2 Non-linear collapse

An over-dense region first expands more slowly than the unperturbed background thus increasing its density contrast, and at some time collapses as the result of the gravitational instability. Its evolution of this region becomes non-linear at some redshift z_{nl} , reaches its turn-around epoch at z_{ta} , and finally collapses to a virialized object at z_{vir} .

The main features of non-linear growth and the critical density threshold are most easily illustrated in the Einstein-de Sitter universe using the spherical collapse model (Peebles 1980; Cooray & Sheth 2002; Mo et al. 2010). In this case a slightly over-dense region (fractional over-density δ_i) of physical radius r_i at the initial cosmic time t_i (scale factor a_i) contains a mass $M = (1 + \delta_i)\bar{\rho}(t_i)\frac{4}{3}\pi r_i^3$, where $\bar{\rho}(t_i)$ is the background average matter density. The fractional over-density $\delta(t)$ evolves as

$$1 + \delta(t) \equiv \frac{\rho(t)}{\bar{\rho}(t)} = \frac{3M/4\pi r^3(t)}{\rho_{c,0}[a_0/a(t)]^3} = \frac{9GM}{2} \frac{t^2}{r^3(t)}, \quad (2.23)$$

where $a(t)/a_0 = (t/t_0)^{2/3}$, $t_0 = 2/3H_0$, and $\rho_{c,0} = 3H_0^2/8\pi G$. The evolution of its radius $r(t)$ is governed by $d^2r/dt^2 = -GM/r^2$. This equation has a parametric solution: $r(\theta) = A(1 - \cos \theta)$ and $t(\theta) = B(\theta - \sin \theta)$ with $A^3 = GM B^2$. A Taylor expansion of $r(\theta)$ and $t(\theta)$ up to second order gives the initial values $\delta_i \simeq 3\theta_i^2/20$, $A \simeq 2r_i/\theta_i^2 \simeq 3r_i/10\delta_i$ and $B \simeq 6t_i/\theta_i^3 \simeq (3/5)^{2/3}(3/4)t_i/\delta_i^{2/3}$. The evolution of the over-density is then given by

$$1 + \delta[t(\theta)] = \frac{9}{2} \frac{(\theta - \sin \theta)^2}{(1 - \cos \theta)^3}, \quad (2.24)$$

and the evolution of the scale factor by

$$\frac{a[t(\theta)]}{a_i} = \left[\frac{t(\theta)}{t_i} \right]^{2/3} = \left(\frac{3}{5} \right) \left(\frac{3}{4} \right)^{2/3} \frac{1}{\delta_i} (\theta - \sin \theta)^{2/3}. \quad (2.25)$$

Equation (2.24) shows that the evolution of this region becomes non-linear ($\delta_{\text{nl}} \simeq 1$) at $\theta_{\text{nl}} \simeq 2.086 \simeq 2\pi/3$, reaches its maximum radius r_{max} with zero expansion velocity zero (turn-around epoch) at $\theta_{\text{ta}} = \pi$ ($\delta_{\text{ta}} = 9\pi^2/2^4 - 1 \simeq 4.552$), and finally collapses to a point at $\theta_{\text{vir}} = 2\pi$.

In reality the region will not collapse to a singularity but will reach the virial equilibrium in a time essentially corresponding to $\theta_{\text{vir}} = 2\pi$. The virial theorem gives an equilibrium (virial) radius $r_{\text{vir}} = r_{\text{max}}/2$. The overdensity at virialization is $1 + \Delta_{\text{vir}} = 18\pi^2$, independently of the initial radius r_i and of the initial over-density δ_i ; the latter quantity however determines the virialization redshift as shown below.

According to Equation (2.25) the *linear* evolution of the over-density goes as

$$\delta^{\text{lin}}[t(\theta)] = \frac{D(t)}{D(t_i)} \delta_i = \frac{a[t(\theta)]}{a_i} \delta_i = \left(\frac{3}{5} \right) \left(\frac{3}{4} \right)^{2/3} (\theta - \sin \theta)^{2/3}. \quad (2.26)$$

The density contrast extrapolated linearly to the virialization time, i.e., to θ_{vir} , is $\delta_{\text{vir}}^{\text{lin}} = \frac{3(12\pi)^{2/3}}{20} \simeq 1.686$.

Combining Equations (2.25) and (2.26), we find

$$1 + z = \frac{a_0}{a(\theta)} = \frac{a_0 \delta_i/a_i}{\delta^{\text{lin}}(\theta)} = \frac{\delta_0^{\text{lin}}}{\delta^{\text{lin}}(\theta)}, \quad (2.27)$$

where $\delta_0^{\text{lin}} \equiv a_0 \delta_i/a_i = D(z=0) \delta_i/D(z_i)$ is the present-day over-density, extrapolated linearly from initial over-density. The critical value of the initial over-density that is required for spherical collapse at redshift z is then

$$\delta_{\text{sc}}(z) \equiv (1+z) \delta^{\text{lin}}(\theta_{\text{vir}}) = \frac{D(z=0)}{D(z)} \delta_{\text{vir}}^{\text{lin}} = \frac{D(z=0)}{D(z)} \delta_0, \quad (2.28)$$

where $\delta_0 \equiv \delta_{\text{vir}}^{\text{lin}} = 3(12\pi)^{2/3}/20$ is the critical over-density required for spherical collapse at $z_{\text{vir}} = 0$. A region with a larger initial over-density virializes at higher redshift.

In a flat universe with cosmological constant the linear growth factor can be approximated by Equation (2.22) and the critical over-density for spherical collapse δ^{lin} by Nakamura & Suto (1997)

$$\delta_0 \simeq \frac{3(12\pi)^{2/3}}{20} [1 + 0.0123 \log \Omega_m(z)]. \quad (2.29)$$

A good approximation for the fractional over-density Δ_{vir} at the virialization redshift z is (Eke et al. 1996; Bryan & Norman 1998)

$$\Delta_{\text{vir}}(z) \simeq \{18\pi^2 + 82[\Omega_m(z) - 1] - 39[\Omega_m(z) - 1]^2\}/\Omega_m(z). \quad (2.30)$$

The virialized halo mass M_{vir} and the virial radius r_{vir} at z are related by

$$M_{\text{vir}}(z) = \frac{4\pi}{3} \Delta_{\text{vir}}(z) \bar{\rho}_m(z) r_{\text{vir}}^3 = \frac{4\pi}{3} \Delta_{\text{vir}}(z) \Omega_m(z) \bar{\rho}_c(z) r_{\text{vir}}^3, \quad (2.31)$$

where $\bar{\rho}_c(z)$ is the critical density ($\bar{\rho}_c(z) \equiv 3H^2(z)/8\pi G$).

The over-density threshold for ellipsoidal collapse was derived by Sheth & Tormen (1999, 2002) and Sheth et al. (2001) as

$$\delta_{\text{ec}}(R, z) \simeq \delta_{\text{sc}}(z) \left\{ 1 + \beta \left[\frac{\sigma^2(R, z=0)}{\delta_{\text{sc}}^2(z)} \right]^\gamma \right\}, \quad (2.32)$$

where $\sigma(R, z=0)$ (defined in the following) is the mass variance of the present density fluctuation field, extrapolated linearly from the initial density fluctuation field, smoothed on a scale R containing the mass M , $\beta \approx 0.47$ and $\gamma \approx 0.615$. These values were determined considering the evolution of an ellipsoidal density fluctuations (Sheth et al. 2001; Zentner 2007). The introduction of this scale dependent critical threshold can substantially reduce the discrepancy on the halo mass function between theoretical predictions based on spherical collapse model (Press & Schechter 1974; Bond et al. 1991) and numerical simulations (Kauffmann et al. 1999).

2.2.3 Statistics of Gaussian fluctuation field

The Fourier transform of any fluctuation field $\delta(t, \vec{x})$ and its inverse transform are given by, respectively, (e.g., [Bracewell 2000](#))

$$\tilde{\delta}(t, \vec{k}) = \int_{\vec{x}} \delta(t, \vec{x}) e^{i\vec{k} \cdot \vec{x}} d^3 \vec{x} \quad \text{and} \quad \delta(t, \vec{x}) = \frac{1}{(2\pi)^3} \int_{\vec{k}} \tilde{\delta}(t, \vec{k}) e^{-i\vec{k} \cdot \vec{x}} d^3 \vec{k}. \quad (2.33)$$

An important assumption is that the initial density fluctuation field $\delta(t_i, \vec{x})$ was a Gaussian random field and that fluctuations were small as inferred from CMB observations. For a Gaussian random field, the *power spectrum*, $P(t, \vec{k}) \equiv |\tilde{\delta}(t, \vec{k})|^2/V$ averaged over a fair sample of the universe with volume $V = \int_{\vec{x}} d^3 \vec{x}$ in real space, contains its complete statistical information and is the Fourier transform of the two-point correlation function of the field. The cosmological principle further implies that the power spectrum is only a function of the wave number $k (= |\vec{k}|)$, i.e., $P(t, \vec{k}) = P(t, k) = |\tilde{\delta}(t, k)|^2/V$. The evolution of density fluctuation field can then be traced back to the evolution of the power spectrum.

The initial power spectrum predicted by inflation models tends to be nearly scale free, i.e., of the form $P(t_i, k) \propto k^{n_s}$, where n_s is the primordial spectral index (see Table 2.1), although the so-called “running” spectral index $n_s = 0.93 + 0.5(-0.03) \ln(k/0.05/h)$ provides an even better description of the flatter shape on small scales. The power spectrum observed after decoupling has a peak around the comoving wave number $k \sim 0.02h \text{ Mpc}^{-1}$ (physical scale $R = 2\pi/k \sim 300h^{-1} \text{ Mpc}$) due to different growth rate of perturbations before and after the radiation-matter equi-density epoch (e.g., [Mo et al. 2010](#)). The evolution of the primordial power spectrum prior to decoupling can be accurately followed only using the relativistic treatment. The result is described by the linear *transfer function*, approximations of which have been worked out by [Bardeen et al. \(1986\)](#) and [Eisenstein & Hu \(1998\)](#).

For the standard scenario adopted here (adiabatic perturbations in a cold dark matter cosmology) we adopt the analytic approximation of the linear transfer function for $\Omega_{b,0} \ll \Omega_{m,0}$ by [Bardeen et al. \(1986\)](#)

$$T[q(k)] = \frac{\ln(1 + 2.34q)}{2.34q} [1 + 3.89q + (16.1q)^2 + (5.46q)^3 + (6.71q)^4]^{-1/4}, \quad (2.34)$$

where $q \equiv k/h\Gamma$ with k in units of Mpc^{-1} and $\Gamma = \Omega_{m,0}h \exp(-\Omega_{b,0} - \sqrt{2h}\Omega_{b,0}/\Omega_{m,0})$ instead of $\Omega_{m,0}h$ to take into account the effect of baryons ([Sugiyama 1995](#)). The power spectrum after decoupling ($z \lesssim z_{\text{dec}}$) is then

$$P^{\text{lin}}(z, k) = A k^{n_s} T^2(k) \left[\frac{D(z)}{D(z=0)} \right]^2, \quad (2.35)$$

where the normalization factor A is fixed by the present-day mass variance of the matter density field smoothed on a scale of $8h^{-1} \text{ Mpc}$, called $\sigma_8 \equiv \sigma(R = 8h^{-1} \text{ Mpc}, z = 0)$.

Observationally, we can measure the density fluctuation field $\delta(t, \vec{x}; R)$ smoothed with some filter (window function) W with scale resolution R

$$\delta(t, \vec{x}; R) = \int_{\vec{x}'} d^3 \vec{x}' W(\vec{x}' - \vec{x}; R) \delta(t, \vec{x}'). \quad (2.36)$$

The mass variance of the smoothed density field is

$$\sigma^2(R, z) = \langle \delta^2(z, \vec{x}; R) \rangle_{\vec{x}} = \int_{\vec{k}} \frac{P^{\text{lin}}(z, \vec{k})}{(2\pi)^3} |\tilde{W}(\vec{k}; R)|^2 d^3 \vec{k} = \int_k \frac{k^3 P^{\text{lin}}(z, k)}{2\pi^2} |\tilde{W}(k; R)|^2 d \ln k, \quad (2.37)$$

where $\tilde{W}(\vec{k}; R)$ is the Fourier transform of the window function. Three different kinds of window functions are usually adopted: real-space top-hat window, Fourier-space top-hat window, and Gaussian window (e.g., [Zentner 2007](#)). Here, we adopt the Fourier-space top-hat window,

$$\tilde{W}(k; R) = \begin{cases} 1 & k \leq k_s(R) \\ 0 & k > k_s(R) \end{cases}, \quad (2.38)$$

where $k_s(R) \simeq (9\pi/2)^{1/3}/R$ corresponding to enclosed mass $M = 4\pi \bar{\rho}_{m,0} R^3/3 \simeq 6\pi^2 \bar{\rho}_{m,0} k_s^{-3}$ ([Lacey & Cole 1993](#)). Now we can link the previously mentioned normalization factor A to σ_8 as

$$\sigma_8^2 = \sigma^2(R = 8h^{-1} \text{ Mpc}, z = 0) = \frac{A}{2\pi^2} \int_0^{k_s(8h^{-1})} k^{n_s+2} T^2(k) dk. \quad (2.39)$$

Finally, the normalized mass variance $\sigma(M_{\text{vir}})$ (in short for $\sigma(M_{\text{vir}}, z = 0)$ unless specified otherwise) of the density fluctuation field, extrapolated linearly from the primordial perturbation field and smoothed on a scale containing a mass M_{vir} , is

$$\sigma^2(M_{\text{vir}}) = \sigma_8^2 \int_0^{k_s(M_{\text{vir}})} k^{n_s+2} T^2(k) dk / \int_0^{k_s(8h^{-1})} k^{n_s+2} T^2(k) dk, \quad (2.40)$$

which is accurately approximated (error < 1% over a broad range of M_{vir} , $10^6 < M_{\text{vir}}/M_\odot < 10^{16}$, for our choice of cosmological parameters (see Table 2.1)) by

$$\sigma(M_{\text{vir}}) = \frac{\sigma_8}{0.84} [14.110393 - 1.1605397x - 0.0022104939x^2 + 0.0013317476x^3 - 2.1049631 \times 10^{-6}x^4], \quad (2.41)$$

where $x \equiv \log(M_{\text{vir}}/M_\odot)$.

2.2.4 Statistics of virialized halos

Given the mass variance $\sigma(M_{\text{vir}})$ of the present density fluctuation field, smoothed on scale R ($M_{\text{vir}} \propto R^3$), and the critical density threshold $\delta_c(M_{\text{vir}}, z)$ required for virialization of a region with mass M_{vir} at redshift z , the comoving number density of halos virialized at redshift z is given by

$$n(M_{\text{vir}}, z) = \frac{\bar{\rho}_{m,0}}{M_{\text{vir}}} \left| \frac{dF(\geq M_{\text{vir}}, z)}{dM_{\text{vir}}} \right| \quad \text{or} \quad M_{\text{vir}}^2 \frac{n(M_{\text{vir}}, z)}{\bar{\rho}_{m,0}} \frac{d \ln M_{\text{vir}}}{d \ln \nu} = \left| \frac{dF(\geq M_{\text{vir}}, z)}{d \ln \nu} \right|, \quad (2.42)$$

where $\nu \equiv [\delta_c(M_{\text{vir}}, z)/\sigma(M_{\text{vir}})]^2$ and $F(\geq M_{\text{vir}}, z)$ is the fractional volume that would be occupied by virialized halos containing masses larger than M_{vir} at redshift z . If a region has a density contrast larger than the critical one, it is identified as a virialized halo. If, instead, its density contrast is lower than

the critical one, this region could either be non-virialized or could be a “diffuse” region belonging to a larger virialized halo. Thus the mass of this “diffuse” region should be included when counting the total virialized mass beyond the critical density threshold. Therefore, the fractional volume is represented by

$$F(\geq M_{\text{vir}}, z) = 1 - \int_{-\infty}^{\delta_c(M_{\text{vir}}, z)} P[\delta; \sigma(M_{\text{vir}}), \delta_c(M_{\text{vir}}, z)] d\delta, \quad (2.43)$$

where $P[\delta; \sigma(M_{\text{vir}}), \delta_c(M_{\text{vir}}, z)]$ is the probability that, given the mass variance $\sigma(M_{\text{vir}})$ of a fluctuation field smoothed on scale R , a region of the same scale not only has density contrast δ but also does not belong to a larger virialized region ($R' > R$) that has density contrast larger than the critical one.

In their pioneering work [Press & Schechter \(1974\)](#) derived the halo mass function based on the assumptions of a scale independent critical density $\delta_c(M_{\text{vir}}, z) = \delta_{\text{sc}}(z)$, given by the spherical collapse model, and of a Gaussian probability distribution,

$$P[\delta; \sigma(M_{\text{vir}})] d\delta = \frac{1}{\sqrt{2\pi}\sigma^2} e^{-\delta^2/2\sigma^2} d\delta, \quad (2.44)$$

for a region of scale $\propto M_{\text{vir}}^{1/3}$ having density contrast δ . This approach missed the mass of the aforementioned “diffuse” regions (half of the total mass) when counting all the virialized mass. This was empirically remedied adding a factor of 2 to the mass function. About fifteen years later this deficiency was resolved by [Bond et al. \(1991\)](#) using the excursion set theory to derive the correct probability distribution,

$$P[\delta; \sigma(M_{\text{vir}}), \delta_{\text{sc}}(z)] d\delta = \frac{1}{\sqrt{2\pi}\sigma^2} \left[e^{-\delta^2/2\sigma^2} - e^{-(2\delta_{\text{sc}}-\delta)^2/2\sigma^2} \right] d\delta, \quad (2.45)$$

where the first term is just the probability that a region has density contrast δ and the second term is the probability that this region is enclosed in a larger region with density contrast larger than the critical one $\delta_{\text{sc}}(z)$. The final [Press & Schechter \(1974\)](#) halo mass function is then

$$M_{\text{vir}}^2 \frac{n_{\text{PS}}(M_{\text{vir}}, z)}{\bar{\rho}_{\text{m},0}} \frac{d \ln M_{\text{vir}}}{d \ln \nu} = \left(\frac{\nu}{2} \right)^{1/2} \frac{e^{-\nu/2}}{\sqrt{\pi}}, \quad (2.46)$$

where $\nu(M_{\text{vir}}, z) \equiv [\delta_{\text{sc}}(z)/\sigma(M_{\text{vir}})]^2$. However this function was found to over-predict (under-predict) the less (more) massive halo density found by N -body simulations of hierarchical clustering ([Kauffmann et al. 1999](#); [Sheth & Tormen 1999](#)).

The further improvement was introduced by [Sheth et al. \(2001\)](#) assuming that the virialized objects form from an ellipsoidal, rather than a spherical, collapse. As a result of this, the critical density threshold for ellipsoidal collapse is scale dependent (Equation (2.32)) and this results in a smaller density of less massive halos. The fact that the less massive objects typically exhibit larger ellipticity and are more easily disrupted by tidal interactions implies a larger critical density threshold for virialization and a lower density. Unfortunately, it is difficult to get analytically the aforementioned probability for the ellipsoidal collapse. Instead, [Sheth et al. \(2001\)](#) simulated a large number of random walks and computed the function $|dF(\geq M_{\text{vir}}, z)/d \ln \nu|$, which was then fitted with a functional form motivated by

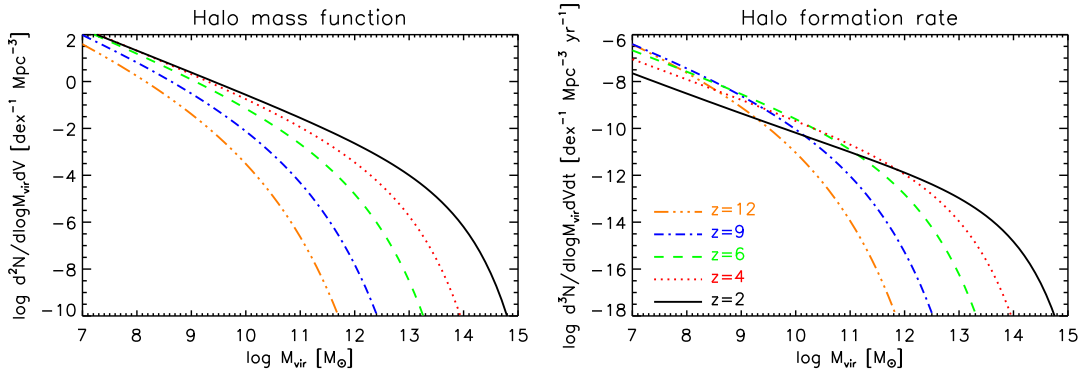


Figure 2.2: Evolution with redshift of the halo mass function (left panel) and of the halo formation rate (right panel).

consideration of ellipsoidal collapse. The resulting halo mass function is given by

$$M_{\text{vir}}^2 \frac{n_{\text{ST}}(M_{\text{vir}}, z)}{\bar{\rho}_{\text{m},0}} \frac{d \ln M_{\text{vir}}}{d \ln \nu} = A [1 + (a\nu)^{-p}] \left(\frac{a\nu}{2}\right)^{1/2} \frac{e^{-a\nu/2}}{\sqrt{\pi}} \equiv f_{\text{ST}}(\nu), \quad (2.47)$$

where $\nu(M_{\text{vir}}, z) \equiv [\delta_{\text{sc}}(z)/\sigma(M_{\text{vir}})]^2$, $A = 0.322$, $p = 0.3$, and $a = 0.707$. This improved halo mass function will be adopted in the following.

The derivative of the halo mass function with respect of the cosmic time has two terms: a positive term giving the formation rate of new halos by mergers of lower mass halos (\dot{n}_{form}) and a negative term corresponding to the disappearance of halos incorporated in more massive ones (\dot{n}_{destr}), i.e., (Sasaki 1994)

$$\frac{dn(M_{\text{vir}}, t)}{dt} = \dot{n}_{\text{form}}(M_{\text{vir}}, t) - \dot{n}_{\text{destr}}(M_{\text{vir}}, t). \quad (2.48)$$

Although the halo formation rate is generally different from $dn(M_{\text{vir}}, t)/dt$, it can be well approximated, for $z \gtrsim 1.5$, by the positive term of the time derivative of the halo mass function (Haehnelt & Rees 1993; Sasaki 1994; Peacock 1999). Lapi et al. (2013), using an excursion set approach, also showed that is a good approximation and pointed out that the survival time, t_{destr} , of the halos that are subject to merging into larger halos is difficult to define unambiguously. In the following the halo formation rate at $z \gtrsim 1.5$ will be assumed to be

$$\begin{aligned} \frac{dn_{\text{ST}}(M_{\text{vir}}, z)}{dt} &= n_{\text{ST}}(M_{\text{vir}}, z) \frac{d \ln f_{\text{ST}}(\nu)}{dt} = -n_{\text{ST}}(M_{\text{vir}}, z) \left[\frac{a\delta_c}{\sigma^2} + \frac{2p}{\delta_c} \frac{\sigma^{2p}}{\sigma^{2p} + a^p \delta_c^{2p}} - \frac{1}{\delta_c} \right] \frac{d\delta_c}{dz} \frac{dz}{dt} \\ &\simeq n_{\text{ST}}(M_{\text{vir}}, z) \left[\frac{a\nu}{2} + \frac{p}{1 + (a\nu)^p} \right] \frac{d \ln \nu}{dz} \left| \frac{dz}{dt} \right| \simeq \dot{n}_{\text{ST}}(M_{\text{vir}}, z). \end{aligned} \quad (2.49)$$

Figure 2.2 shows the evolution with redshift of the halo mass function (Equation 2.47) and of the halo formation rate (Equation 2.49).

2.2.5 Properties of virialized halos

After Equation (2.31), the virial radius of a halo of mass M_{vir} is

$$R_{\text{vir}} \simeq 100 \left(\frac{M_{\text{vir}}}{10^{12} M_{\odot}} \right)^{1/3} \left[\frac{\Delta_{\text{vir}}(z) h^2 \Omega_{\text{m},0}}{18\pi^2 \times 0.7^2 \times 0.3} \right]^{-1/3} \left(\frac{1+z}{3} \right)^{-1} \text{kpc}, \quad (2.50)$$

and the rotational velocity of the dark matter halo at its virial radius is

$$V_{\text{vir}} = \left(\frac{GM_{\text{vir}}}{R_{\text{vir}}} \right)^{1/2} \simeq 200 \left(\frac{M_{\text{vir}}}{10^{12} M_{\odot}} \right)^{1/3} \left[\frac{\Delta_{\text{vir}}(z) h^2 \Omega_{\text{m},0}}{18\pi^2 \times 0.7^2 \times 0.3} \right]^{1/6} \left(\frac{1+z}{3} \right)^{1/2} \text{km s}^{-1}. \quad (2.51)$$

The baryons falling into the newly created potential wells are shock-heated to the virial temperature given by

$$T_{\text{vir}} = \mu m_{\text{p}} V_{\text{vir}}^2 / 2k_{\text{B}} \simeq 1.4 \times 10^6 \left(\frac{M_{\text{vir}}}{10^{12} M_{\odot}} \right)^{2/3} \left[\frac{\Delta_{\text{vir}}(z) h^2 \Omega_{\text{m},0}}{18\pi^2 \times 0.7^2 \times 0.3} \right]^{1/3} \left(\frac{1+z}{3} \right) \text{K}, \quad (2.52)$$

where m_{p} is the proton mass, k_{B} is the Boltzmann constant, and $\mu \simeq 2/(1+3X+Y/2) \simeq 0.59$ is the mean molecular weight of a completely ionized gas with primordial mass fraction of hydrogen $X = 0.75$ and helium $Y = 1 - X$. Using high-resolution N -body simulations for hierarchical structure formation, [Navarro et al. \(1997\)](#) found that the equilibrium density profiles of dark matter halos exhibit a universal shape, independent of the halo mass, of the initial density fluctuation field and of cosmological parameters. Such a universal density profile is described by

$$\rho(r) = \frac{\rho_s}{cx(1+cx)^2}, \quad (2.53)$$

where $x \equiv r/R_{\text{vir}}$, $c \sim 4$ is the concentration parameter, and the characteristic density ρ_s is linked to the halo mass through $\rho_s = \frac{M_{\text{vir}}}{4\pi R_{\text{vir}}^3} \frac{c^3}{\ln(1+c) - c/(1+c)}$.

2.3 Baryon evolution within virialized dark matter halos

Following the virialization of host dark matter halos, the shock-heated baryons begin to fall toward the halo centers as they loose energy via radiative cooling (see [Sutherland & Dopita 1993](#) for an exhaustive discussion of cooling processes) and condense into molecular clouds where stars form. Evolved galaxies show a variety of morphologies and are broadly classified as “early-type” (elliptical/S0 galaxies), “late-type” (disk galaxies with/without a central bulge or bars), and irregulars (see [van den Bergh 1998](#); and [Buta 2011](#) for a recent review on galaxy morphology). The first galaxy formation models ([Eggen et al. 1962](#)) envisaged a *monolithic collapse* of proto-galactic gas clouds while N-body simulations in the framework of the cold dark matter cosmology fostered the *hierarchical merger* scenario ([White & Rees 1978](#); [Steinmetz & Navarro 2002](#); [Di Matteo et al. 2005](#); [Benson 2010](#); [Wilman et al. 2013](#)). In the real universe, both processes must have had a role in building galaxies in different epochs and/or halos. Our model is based on the consideration of the following facts.

1. *Age of stellar populations:* Locally a dichotomy in the ages of stellar populations of early-type galaxies on one side and late-type galaxies on the other is observed. Early-type galaxies and massive bulges of S0 and Sa galaxies are composed of relatively old stellar populations with mass-weighted ages of $\gtrsim 8\text{--}9$ Gyr (corresponding to formation redshifts $z \gtrsim 1\text{--}1.5$), while the disk components of spiral and irregular galaxies are characterized by significantly younger stellar populations. For instance, the luminosity-weighted age for most of Sb or later-type spirals is $\lesssim 7$ Gyr (cf. [Bernardi et al. 2010](#), their Figure 10), corresponding to a formation redshift $z \lesssim 1$. In general, the old stellar populations feature low specific angular momentum as opposed to the larger specific angular momentum of the younger ones (e.g., [Lapi et al. 2011](#)).
2. *Stellar mass function of galaxies:* A comparison of the K -band luminosity function or of the stellar mass function at $z \gtrsim 1.5$ with the local ones shows that most local massive elliptical galaxies were already present at $z \sim 1.5$ and since then have undergone essentially passive evolution with little or modest additional growth through minor mergers ([Kaviraj et al. 2008](#); [Mancone et al. 2010](#); [Fan et al. 2010](#)).
3. *Star formation history:* The duration of star formation in the massive early-type galaxies can be constrained by the observed α -enhancement (higher α/Fe element ratios) and by the (sub-)millimeter counts and redshift distributions. Although the duration inferred from the α -enhancement depends on the assumed initial mass function, an upper limit of $\lesssim 1$ Gyr is generally derived ([Matteucci 1994](#); [Thomas et al. 1999](#)). The (sub-)millimeter data requires that extreme star formation (at rates of thousands $M_\odot \text{ yr}^{-1}$, [Chapman et al. 2005](#)) are sustained for $\gtrsim 0.5$ Gyr in massive galaxies at $z \sim 2\text{--}3$ ([Lapi et al. 2011](#)). In merger-driven galaxy formation models star formation typically does not truncate after 1 Gyr ([Thomas & Kauffmann 1999](#); however, see [Arrigoni et al. 2010](#); [Khochfar & Silk 2011](#)), while the timescale of a merger-induced starburst is of the order of the dynamical time (~ 0.1 Gyr for massive early-type galaxies, [Benson 2010](#)).
4. *Tight correlations:* There are many tight correlations for elliptical galaxies: the fundamental plane ([Renzini & Ciotti 1993](#)), the color-magnitude relation ([Bower et al. 1992](#)), and the luminosity-size relation ([Nair et al. 2010](#)). These correlations are tight enough to allow little room for merger scenarios that would show larger scatter due to the diverse star formation histories of merging progenitors (apart from small mass additions through minor mergers at late epochs; see [Kaviraj et al. 2008](#)). They have been known for a long time and have been recently confirmed with very large samples, and also shown to persist up to substantial redshifts ([Stanford et al. 1998](#); [Renzini 2006](#); [Clemens et al. 2009](#); [Thomas et al. 2010](#); [Rogers et al. 2010](#); [Peebles & Nusser 2010](#), and references therein). In addition, early-type galaxies were found to host supermassive black holes whose mass is proportional to the bulge and the halo mass of the host galaxy (see [Magorrian et al. 1998](#); also [Ferrarese & Ford 2005](#) for a review). All that indicates that the formation and evolution of early-type galaxies is almost independent of environment, and driven mainly by self-regulated processes and intrinsic galaxy properties such as mass. This is further supported by the current high-resolution numerical simulations on the dark matter halos formation.

5. *Build-up of dark matter halos:* High-resolution N -body simulations have been performed to study the assembly history of galactic dark matter halos ([Zhao et al. 2003](#); [Wang et al. 2011](#); [Lapi & Cavaliere 2011](#)). [Wang et al. \(2011\)](#) confirmed the earlier work regarding the inside-out growth of halos. The halo's inner regions containing the visible galaxies are stable since early times when a few major mergers quickly set up the halo bulk, while the later minor mergers and diffuse accretion only slowly affect the halo outskirts with little effect on the inner regions.

All the above supports the view that massive elliptical galaxies and bulges of disk galaxies formed in a fast collapse phase at high- z ($z \gtrsim 1$) while the formation of disk galaxies mostly occurs at lower redshift ($z \lesssim 2$) with a longer star formation duration. Another important feature included in the modern galaxy evolution models is the feedback from supernova explosions and from nuclear activity. The latter is linked to the growth of supermassive black holes at the centers of galaxies and can account for the so-called “downsizing” (see [Fontanot et al. 2009](#) for a review). Stemming from these ingredients, a comprehensive “hybrid” model for the cosmological evolution of galaxies and associated AGNs is presented in next Chapter.

Chapter 3

An “hybrid” galaxy evolution model

We have worked out a comprehensive investigation of the cosmological evolution of the luminosity function (LF) of galaxies and active galactic nuclei (AGN) in the infrared (IR) by means of a “hybrid” model. The model interprets the epoch-dependent LFs at $z \gtrsim 1$ using a physical model for the evolution of proto-spheroidal galaxies and of the associated AGNs, while IR galaxies at $z \lesssim 2$ are interpreted as being mostly late-type “cold” (normal) and “warm” (starburst) galaxies whose evolution, and that of $z \lesssim 2$ AGNs, is described using a parametric phenomenological approach.

3.1 High- z star-forming galaxies and associated AGNs ($z \gtrsim 1$)

We adopt the model by Granato et al. (2004; see also Lapi et al. 2006, 2011; Mao et al. 2007) that interprets powerful high- z submillimeter galaxies as massive proto-spheroidal galaxies in the process of forming most of their stellar mass. It hinges upon high resolution numerical simulations showing that dark matter halos form in two stages (Zhao et al. 2003; Wang et al. 2011; Lapi & Cavaliere 2011). An early fast collapse of the halo bulk, including a few major merger events, reshuffles the gravitational potential and causes the dark matter and stellar components to undergo (incomplete) dynamical relaxation. A slow growth of the halo outskirts in the form of many minor mergers and diffuse accretion follows; this second stage has little effect on the inner potential well where the visible galaxy resides.

The star formation is triggered by the fast collapse/merger phase of the halo and is controlled by self-regulated baryonic processes. It is driven by the rapid cooling of the gas within a region with radius $\approx 30\%$ of the halo virial radius, i.e., of $\simeq 70(M_{\text{vir}}/10^{13} M_{\odot})^{1/3}[(1+z_{\text{vir}})/3]^{-1}$ kpc, where M_{vir} is the halo mass and z_{vir} is the virialization redshift, encompassing about 40% of the total mass (dark matter plus baryons). The star formation and the growth of the central black-hole, which are regulated by the energy feedback from supernovae (SNe) and from the active nucleus, are very soon obscured by dust and are quenched by quasar feedback. The AGN feedback is relevant especially in the most massive galaxies and is responsible for their shorter duration ($5 - 7 \times 10^8$ yr) of the active star-forming phase. In less massive proto-spheroidal galaxies the star formation rate is mostly regulated by SN feedback and continues for a few Gyr. Only a minor fraction of the gas initially associated with the dark matter halo is converted

into stars. The rest is ejected by feedback processes.

The equations governing the evolution of the baryonic matter in dark matter halos and the adopted values for the parameters are given in the following subsections where some examples of the evolution with galactic age (from the virialization time) of quantities related to the stellar and to the AGN component are also shown. This model has been adopted to explain observational results and also to make predictions at a variety of redshifts and wavelengths (Silva et al. 2004a,b, 2005; Cirasuolo et al. 2005; Granato et al. 2006; Shankar et al. 2006; Lapi et al. 2006, 2008, 2011; Mao et al. 2007; Negrello et al. 2007, 2010; Fan et al. 2008, 2010; Cook et al. 2009; González-Nuevo et al. 2012; Xia et al. 2012).

As shown by Lapi et al. (2011), the self-regulated baryon collapse scenario provides a good fit of the (sub-)millimeter data (counts, redshift-dependent LFs) as well as of the stellar mass functions at different redshifts. Moreover, the counts of strongly lensed galaxies were predicted with remarkable accuracy (Negrello et al. 2007, 2010; Lapi et al. 2012; González-Nuevo et al. 2012). Further considering that this scenario accounts for the clustering properties of submillimeter galaxies (Xia et al. 2012), we conclude that it is well grounded, and we adopt it for the present analysis. However, we upgrade this model in two respects. First, while on one side, the model envisages a co-evolution of spheroidal galaxies and active nuclei at their centers, the emissions of the two components have so far been treated independently of each other. This is not a problem in the wavelength ranges where one of the two components dominates, as in the (sub-)millimeter region where the emission is dominated by star formation, but is no longer adequate at mid-IR wavelengths, where the AGN contribution may be substantial. Consequently, we present and exploit a consistent treatment of proto-spheroidal galaxies including both components. Second, while the steeply rising portion of (sub-)millimeter counts is fully accounted for by proto-spheroidal galaxies, late-type (normal and starburst) galaxies dominate both at brighter and fainter flux densities and over broad flux density ranges at mid-IR wavelengths. At these wavelengths, AGNs not associated with proto-spheroidal galaxies but either to evolved early-type galaxies or to late-type galaxies are also important (see Section 3.2).

3.1.1 Self-regulated evolution of high- z proto-spheroidal galaxies

The gas initially associated to a galactic halo of mass M_{vir} , with a cosmological mass fraction $f_b = M_{\text{gas}}/M_{\text{vir}} = 0.165$ is heated to the virial temperature at the virialization redshift, z_{vir} . Its subsequent evolution partitions it in three phases: a hot diffuse medium with mass M_{inf} infalling and/or cooling toward the center; cold gas with mass M_{cold} condensing into stars; low-angular momentum gas with mass M_{res} stored in a reservoir around the central supermassive black hole, and eventually viscously accreting onto it. In addition, two condensed phases appear and grow, namely, stars with a total mass M_{\star} and the black hole with mass M_{\bullet} . Figure 3.1 illustrates these processes of baryon evolution. Unless otherwise specified, we will restrict ourselves to the ranges $11.3 \lesssim \log(M_{\text{vir}}/M_{\odot}) \lesssim 13.3$ and $z_{\text{vir}} \gtrsim 1.5$. The redshift and the lower mass limit are crudely meant to single out galactic halos associated with individual spheroidal galaxies. Disk-dominated (and irregular) galaxies are primarily associated with halos virialized at $z_{\text{vir}} \lesssim 1.5$, which may have incorporated halos less massive than $10^{11.3} M_{\odot}$ virialized at earlier times, that form their bulges. The upper mass limit to individual galaxy halos comes from weak-

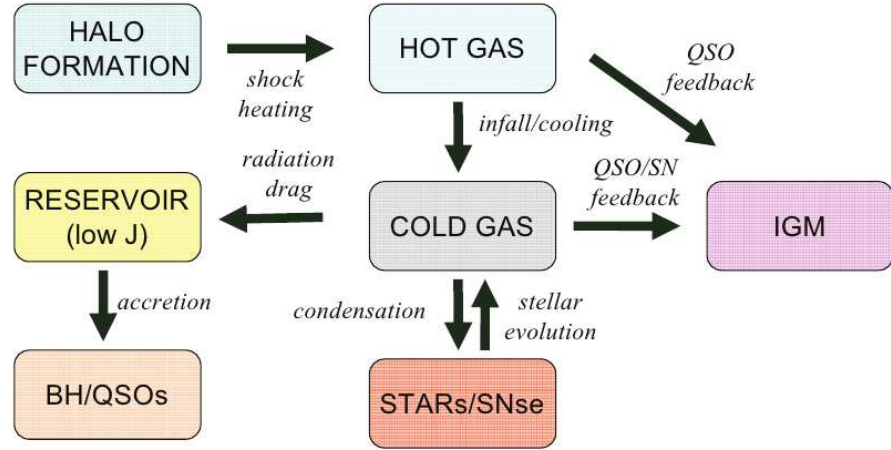


Figure 3.1: Scheme of baryon evolution proposed by Granato et al. (2004) for high- z proto-spheroidal galaxies (Figure kindly provided by A. Lapi).

lensing observations (e.g., Kochanek & White 2001; Kleinheinrich et al. 2005), kinematic measurements (e.g., Kronawitter et al. 2000; Gerhard et al. 2001), and from a theoretical analysis on the velocity dispersion function of spheroidal galaxies (Cirasuolo et al. 2005). The same limit is also suggested by modeling of the spheroids mass function (Granato et al. 2004), of the quasar LFs (Lapi et al. 2006), and of the submillimeter galaxy number counts (Lapi et al. 2011).

The evolution of the three gas phases is governed by the following equations:

$$\begin{aligned}\dot{M}_{\text{inf}} &= -\dot{M}_{\text{cond}} - \dot{M}_{\text{inf}}^{\text{QSO}}, \\ \dot{M}_{\text{cold}} &= \dot{M}_{\text{cond}} - [1 - \mathcal{R}(t)]\dot{M}_{\star} - \dot{M}_{\text{cold}}^{\text{SN}} - \dot{M}_{\text{cold}}^{\text{QSO}}, \\ \dot{M}_{\text{res}} &= \dot{M}_{\text{inflow}} - \dot{M}_{\text{BH}},\end{aligned}\quad (3.1)$$

which link the gas mass infall rate, \dot{M}_{inf} , the variation of the cold gas mass, \dot{M}_{cold} , and the variation of the reservoir mass, \dot{M}_{res} , to the condensation rate of the cold gas, \dot{M}_{cond} , to the star formation rate, \dot{M}_{\star} , to the cold gas removal by SN and AGN feedback, $\dot{M}_{\text{cold}}^{\text{SN}}$ and $\dot{M}_{\text{cold}}^{\text{QSO}}$, respectively, to the fraction of gas restituted to the cold component by the evolved stars, $\mathcal{R}(t)$, to the inflow rate of cold gas into the reservoir around the central supermassive black hole, \dot{M}_{inflow} , and to the back hole accretion rate, \dot{M}_{BH} .

Inflowing hot gas \dot{M}_{cond}

The hot gas cools and flows toward the central region at a rate

$$\dot{M}_{\text{cond}} \simeq \frac{\dot{M}_{\text{inf}}}{t_{\text{cond}}} \quad (3.2)$$

with $M_{\text{inf}}^0 = f_b M_{\text{vir}}$, over the condensation timescale $t_{\text{cond}} = \max[t_{\text{dyn}}(R_{\text{vir}}), t_{\text{cool}}(R_{\text{vir}})]$, namely, the maximum between the dynamical and cooling time at the halo virial radius R_{vir} . At the virialization epoch, the dynamical time and the cooling time are given by, respectively, $t_{\text{dyn}}(r) = \left[\frac{3\pi}{32G\rho_m(r)} \right]^{1/2}$ and

$t_{\text{cool}}(r) = \frac{3}{2} \frac{\rho_{\text{gas}}(r)}{\mu m_p} \frac{k_B T_{\text{vir}}}{C n_e^2(r) \Lambda(T_{\text{vir}})}$, where the ρ_m is the total matter density, ρ_{gas} is the gas density, μ is the effective molecular weight, $n_e \simeq \rho_{\text{gas}}/\mu e m_p$ is the electron density, $\Lambda(T)$ is the cooling function (Sutherland & Dopita 1993), and $C \equiv \langle n_e^2(r) \rangle / \langle n_e(r) \rangle^2 \sim 7$ is the clumping factor (Lapi et al. 2006). The gas has been shock-heated to the virial temperature T_{vir} , and is therefore fully ionized, so that $\mu_e \simeq 2/(1+X)$, $X = 0.75$ being the hydrogen mass fraction. Its density profile is assumed to follow that of dark matter (see Equations 2.52 and 2.53). Including all these ingredients, the condensation timescale is well approximated by (Fan et al. 2010)

$$t_{\text{cond}} \simeq 8 \times 10^8 \left(\frac{1+z}{4} \right)^{-1.5} \left(\frac{M_{\text{vir}}}{10^{12} M_\odot} \right)^{0.2} \text{yr}, \quad (3.3)$$

where the coefficient is 10% smaller than the value used by Fan et al. (2010). Note that the cooling and inflowing gas we are dealing with is the one already present within the halo at virialization. In this respect it is useful to keep in mind that the virial radius of the halo ($R_{\text{vir}} \simeq 220(M_{\text{vir}}/10^{13} M_\odot)^{1/3}[3/(1+z_{\text{vir}})]$ kpc, see Equation 2.50) is more than 30 times larger than the size of the luminous galaxy, and that only a minor fraction of the gas within the halo condenses into stars. Indeed, we need strong feedback processes, capable of removing most of the halo gas, to avoid an overproduction of stars. This implies that any gas infalling from outside the halo must also be swept out by feedback; it could however become important for the formation of a disk-like structure surrounding the preformed spheroid once it enters the passive evolution phase, with little feedback (Cook et al. 2009). As mentioned previously, the additional material (stars, gas, dark matter) infalling after the fast collapse phase that creates the potential well, i.e., during the slow-accretion phase, mostly produces a growth of the halo outskirts, and has little effect on the inner part where the visible galaxy resides.

Star formation rate \dot{M}_\star

The star formation rate is given by

$$\dot{M}_\star \simeq \frac{M_{\text{cold}}}{t_\star}, \quad (3.4)$$

where the star formation timescale is $t_\star \simeq t_{\text{cond}}/s$. The quantity s , i.e., the ratio between the large-scale condensation timescale and the star formation timescale in the central region, is found to be $\simeq 5$ both for an isothermal and for an NFW density profile with a standard value of the concentration parameter (see Equation 2.53; Fan et al. 2010). The fraction of mass restituted by stars at the end of their life per unit mass of formed stars is represented by

$$\mathcal{R}(t) = \frac{1}{\dot{M}_\star(t)} \int_{m(t)}^{m_{\text{max}}} (m - m_{\text{rem}}) \phi(m) \dot{M}_\star[t - \tau(m)] dm, \quad (3.5)$$

where the $m \equiv m_\star/M_\odot$ is the mass of a single star in solar units, m_{rem} is the mass retained by the star at the end of its life, $\phi(m)$ is the initial mass function (IMF), $\tau(m) \propto m^{-2.5}$ is the lifetime of a star of mass m , m_{max} is the assumed maximum mass of formed stars, and $m(\tau)$ is the mass of a star whose lifetime is τ . For a Chabrier (2003) IMF of the form $\phi(m) = m^{-x}$ with $x = 1.4$ for $0.1 \leq m \leq 1$ and $x = 2.35$ for

$m > 1$ we find $\mathcal{R} \simeq 0.54$ under the instantaneous recycling approximation.

The infrared luminosity (8–1000 μm) associated with dust enshrouded star formation is

$$L_{\star,\text{IR}}(t) = k_{\star,\text{IR}} \times 10^{43} \left(\frac{\dot{M}_{\star}}{M_{\odot} \text{ yr}^{-1}} \right) \text{ erg s}^{-1}, \quad (3.6)$$

where the coefficient $k_{\star,\text{IR}}$ depends on the SED. We adopt $k_{\star,\text{IR}} \sim 3$ (Lapi et al. 2011; Kennicutt 1998). Note that this relation assumes that all the radiation of newborn stars is absorbed by dust. Whenever this is not the case, the determination of the SFR requires both IR and optical/UV data. However for the intense star formation phases of interest here, Equation (3.6) holds.

SN feedback $\dot{M}_{\text{cold}}^{\text{SN}}$

The gas mass loss due to the SN feedback is

$$\dot{M}_{\text{cold}}^{\text{SN}} = \beta_{\text{SN}} \dot{M}_{\star}, \quad (3.7)$$

with

$$\beta_{\text{SN}} = \frac{N_{\text{SN}} \epsilon_{\text{SN}} E_{\text{SN}}}{E_{\text{bind}}} \simeq 0.6 \left(\frac{N_{\text{SN}}}{8 \times 10^{-3}/M_{\odot}} \right) \left(\frac{\epsilon_{\text{SN}}}{0.05} \right) \left(\frac{E_{\text{SN}}}{10^{51} \text{ erg}} \right) \left(\frac{M_{\text{vir}}}{10^{12} M_{\odot}} \right)^{-2/3} \left(\frac{1+z}{4} \right)^{-1}. \quad (3.8)$$

We adopt the following values: number of SNe per unit solar mass of condensed stars $N_{\text{SN}} \simeq 1.4 \times 10^{-2}/M_{\odot}$; fraction of the released energy used to heat the gas $\epsilon_{\text{SN}} = 0.05$; kinetic energy released per SN $E_{\text{SN}} \simeq 10^{51}$ erg; halo binding energy $E_{\text{bind}} \simeq 3.2 \times 10^{14} (M_{\text{vir}}/10^{12} M_{\odot})^{2/3} [(1+z)/4] \text{ cm}^2 \text{ s}^{-2}$ (Mo & Mao 2004).

Chemical evolution Z_{gas}

The model also follows the evolution of the cold gas metallicity, $Z_{\text{gas}}(t)$, in presence of the inflow and outflow. An approximate solution of the equations governing the chemical evolution is (A. Lapi et al., in preparation)

$$Z_{\text{gas}}(t) = Z_{\text{inf}}^0 + \frac{s}{s\gamma - 1} \mathcal{E}_Z(t) - \frac{st/t_{\text{cond}}}{e^{(s\gamma-1)t/t_{\text{cond}}} - 1} \cdot \left\{ \mathcal{E}_Z(t) + B_Z \sum_{i=2}^{\infty} \frac{1}{i \cdot i!} \left[(s\gamma - 1) \frac{\min(t, t_Z)}{t_{\text{cond}}} \right]^{i-1} \right\}, \quad (3.9)$$

where $\gamma = 1 - \mathcal{R} - \beta_{\text{SN}}$, the metallicity of the primordial infalling gas is $Z_{\text{inf}}^0 = 10^{-5}$, and the mass fraction of newly formed metals ejected from stars, $\mathcal{E}_Z(t)$, is given by

$$\mathcal{E}_Z(t) \simeq A_Z + B_Z \ln \left[\frac{\min(t, t_{\text{saturation}})}{t_Z} \right] \quad (3.10)$$

with $A_Z = 0.03$, $B_Z = 0.02$, $t_Z = 20$ Myr, and $t_{\text{saturation}} = 40$ Myr for the Chabrier's IMF ($Z_{\odot} \simeq 0.02$). Equation (3.10) accounts for the fact that, soon after the onset of star formation, the metal yield, mainly contributed by stars with large masses ($\geq 20 M_{\odot}$) and short lifetimes ($t_Z \leq 20$ Myr), is a relatively large

fraction of the initial stellar mass ($f_{\text{metal}} \geq 0.12$) while, as the star formation proceeds, it progressively lowers to $f_{\text{metal}} \sim 0.06$ as the main contribution shifts to stars with intermediate masses $\sim 9 - 20 M_{\odot}$ and lifetimes $t_Z \sim 20 - 40$ Myr, and finally saturates to values $f_{\text{metal}} \sim 0.013$ as stars with masses $\leq 9 M_{\odot}$ and long lifetimes ($t_{\text{saturation}} \geq 40$ Myr) take over (Bressan et al. 1998). The two parameters A_Z and B_Z depend mainly on the IMF.

The reservoir around supermassive black holes

The cold gas inflow rate into the reservoir around the super-massive black hole, driven by radiation drag (Kawakatu & Umemura 2002; Kawakatu et al. 2003), is given by

$$\dot{M}_{\text{inflow}} \simeq \frac{L_{\star}}{c^2} (1 - e^{-\tau_{\text{RD}}}) \simeq \alpha_{\text{RD}} \times 10^{-3} \dot{M}_{\star} (1 - e^{-\tau_{\text{RD}}}), \quad (3.11)$$

with

$$\tau_{\text{RD}}(t) = \tau_{\text{RD}}^0 \left(\frac{Z_{\text{gas}}(t)}{Z_{\odot}} \right) \left(\frac{M_{\text{cold}}}{10^{12} M_{\odot}} \right) \left(\frac{M_{\text{vir}}}{10^{13} M_{\odot}} \right)^{-2/3}. \quad (3.12)$$

For the strength of the radiation drag we adopt $\alpha_{\text{RD}} = 2.5$ and set $\tau_{\text{RD}}^0 = 3.0$.

Black hole accretion

The accretion rate into the central black hole obeys the equation

$$\dot{M}_{\text{BH}} = \min(\dot{M}_{\text{BH}}^{\text{visc}}, \lambda_{\text{Edd}} \dot{M}_{\text{Edd}}), \quad (3.13)$$

where $\dot{M}_{\text{BH}}^{\text{visc}}$ is the accretion rate allowed by the viscous dissipation of the angular momentum of the gas in the reservoir

$$\dot{M}_{\text{BH}}^{\text{visc}} = \frac{M_{\text{res}}}{\tau_{\text{visc}}} = \kappa_{\text{accr}} 5 \times 10^3 \left(\frac{V_{\text{vir}}}{500 \text{ km s}^{-1}} \right)^3 \left(\frac{M_{\text{res}}}{M_{\bullet}} \right)^{3/2} \left(1 + \frac{M_{\bullet}}{M_{\text{res}}} \right)^{1/2} \quad (3.14)$$

with $\kappa_{\text{accr}} \simeq 10^{-2}$. $\dot{M}_{\text{Edd}} \equiv M_{\bullet}/\epsilon t_{\text{Edd}}$ is the accretion rate corresponding to the Eddington luminosity given the mass to light conversion efficiency ϵ (we set $\epsilon = 0.1$ so that the Salpeter time $\epsilon t_{\text{Edd}} = 4.5 \times 10^7$ yr) and $\lambda_{\text{Edd}}(z)$ is the Eddington ratio that we assume to slightly increase with redshift for $z \gtrsim 1.5$

$$\lambda_{\text{Edd}}(z) \simeq 0.1(z - 1.5)^2 + 1.0 \quad (3.15)$$

up to a maximum value $\lambda_{\text{Edd,max}} = 4$. The growth rate of the black hole mass is

$$\dot{M}_{\bullet}(t) = (1 - \epsilon) \dot{M}_{\text{BH}} \quad (3.16)$$

starting from a seed mass $M_{\bullet}^{\text{seed}} = 10^2 M_{\odot}$.

AGN feedback

The bolometric AGN luminosity is

$$L_{\bullet} = \epsilon \dot{M}_{\text{BH}} c^2 = 5.67 \times 10^{45} \left(\frac{\epsilon}{0.1} \right) \left(\frac{\dot{M}_{\text{BH}}}{M_{\odot} \text{ yr}^{-1}} \right) \text{ erg s}^{-1}. \quad (3.17)$$

A minor fraction of it couples with the interstellar medium of the host galaxy giving rise to an outflow at a rate

$$\dot{M}_{\text{inf,cold}}^{\text{QSO}} = \dot{M}_{\text{wind}} \frac{M_{\text{inf,cold}}}{M_{\text{inf}} + M_{\text{cold}}}, \quad (3.18)$$

with

$$\dot{M}_{\text{wind}} = \frac{L_{\text{QSO}}^{\text{ISM}}}{E_{\text{bind}}}, \quad (3.19)$$

and

$$L_{\text{QSO}}^{\text{ISM}} \simeq 2 \times 10^{44} \epsilon_{\text{QSO}} \left(\frac{\dot{M}_{\text{BH}}}{M_{\odot} \text{ yr}^{-1}} \right)^{3/2} \text{ erg s}^{-1}. \quad (3.20)$$

$L_{\text{QSO}}^{\text{ISM}}$ is the mechanical AGN luminosity, used to unbind the gas. The coefficient quantifying the strength of the QSO feedback is chosen to be $\epsilon_{\text{QSO}} = 3$. The ratio of the mechanical to the total AGN luminosity

$$L_{\text{QSO}}^{\text{ISM}}/L_{\bullet} \simeq 3.5 \times 10^{-3} \frac{\epsilon_{\text{QSO}}}{\epsilon} \left(\frac{\dot{M}_{\text{BH}}}{M_{\odot} \text{ yr}^{-1}} \right)^{1/2}, \quad (3.21)$$

is constrained to be in the range 0.006–0.15.

Evolutionary sequence of high- z galaxies

Examples of the resulting evolution with galactic age of properties of the stellar and of the AGN component are shown in the left part of Figure 3.2 for three values of the virial mass and $z_{\text{vir}} = 3$. The figure illustrates the different evolutionary histories of galaxies associated to different halo masses. The star formation proceeds at very high rates in massive halos and is quenched after $5\text{--}7 \times 10^8$ yr by the strong AGN feedback; the evolution is essentially passive afterwards. In less massive halos the evolution proceeds at a lower pace in less massive halos, where SN feedback is relatively more effective in slowing down the star formation. On the other hand, the AGN feedback is less strong and lets the star formation continue for longer times (a few Gyr). The combined effect of SN and AGN feedback thus accounts for the observed “downsizing”.

Figure 3.2 shows that the evolutionary history of massive spheroidal galaxies can be roughly divided in four phases. In the first phase, the gas metallicity is low and the galaxy is UV bright. The duration of this phase is different for different halo masses (it last longer for less massive galaxies) but is generally short ($\sim 2 - 3 \times 10^7$ yr for the more massive galaxies; [Mao et al. 2007](#)). A longer period of dust-enshrouded star formation and obscured AGN activity (submillimeter bright, $\sim 5\text{--}7 \times 10^8$ yr) follows. After the interstellar medium is swept out by the AGN feedback we have a brief QSO phase ($\sim 5 \times 10^7$ yr; [Lapi et al. 2006](#)) followed by passive evolution. This evolutionary sequence is indicated by the colored bar in the right-most column of Figure 3.2. This scenario links a variety of high- z galaxy populations selected by

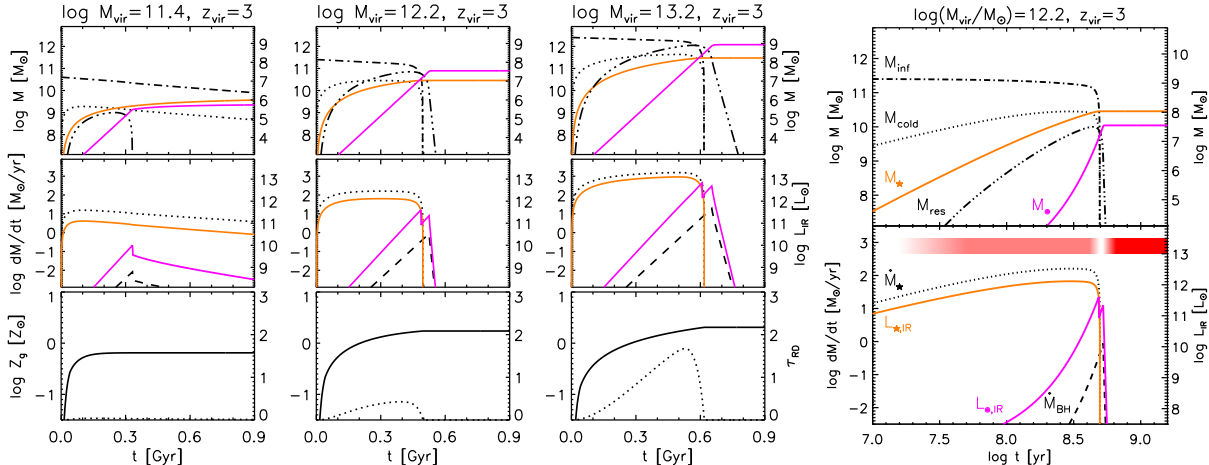


Figure 3.2: *First 3 columns:* Evolution with galactic age of properties of the stellar and of the AGN component of protospheroidal galaxies virialized at $z_{\text{vir}} = 3$ for three choices of the virial (mostly dark matter) mass: $\log(M_{\text{vir}}/M_{\odot}) = 11.4$ (left-hand column), 12.2 (central column), and 13.2 (right-hand column). In the first row, the left y -axis scale refers to masses related to the stellar component (infalling hot gas mass (M_{inf} , dot-dashed line), cold gas mass (M_{cold} , dotted line), stellar mass (M_{\star} , solid orange line)) while the right-hand scale refers to quantities related to the AGN component (reservoir mass (M_{res} , triple-dot-dashed line) and black hole mass (M_{\bullet} , solid magenta line)). In the second row the left-hand scale refers to the SFR (\dot{M}_{\star} , dotted line) and to the BH accretion rate (\dot{M}_{BH} , dashed black line), while the right-hand scale refer to the IR (8–1000 μm) luminosity of the stellar ($L_{\star,\text{IR}}$, solid orange line) and of the AGN ($L_{\bullet,\text{IR}}$, solid magenta line); the zigzag around the evolution peak indicates the transition from obscured to unobscured AGN activity, see Section 3.1.2 for more details) component. In the third row the left-hand scale refers to the gas metallicity (solid line) while the right-hand scale refers to the optical depth of individual gas clouds (dotted line). *Right-most column:* The different evolutionary phases, i.e., dust-free UV bright phase, dust-enshrouded sub-mm bright phase, QSO phase, and passively evolving phase, are indicated by the white, pink, white, and red colors in the bar at the top of the lower panel.

different techniques: Ly α emitters, Lyman break galaxies, submillimeter galaxies, and passively evolving galaxies. In the following chapters, we will compare the model predictions with observations of these different kinds of galaxies.

3.1.2 SEDs of high- z populations

Although there is evidence that the galaxy SEDs vary with luminosity (e.g., Smith et al. 2012), Lapi et al. (2011) have shown that the submillimeter data can be accurately reproduced using a single SED for proto-spheroidal galaxies, i.e., the SED of the strongly lensed $z \simeq 2.3$ galaxy SMM J2135-0102 (Swinbank et al. 2010; Ivison et al. 2010), modeled using GRASIL (Silva et al. 1998). The basic reason for the higher uniformity of the SEDs of high- z active star-forming galaxies compared to galaxies at low- z is that the far-IR emission of the former objects comes almost entirely from dust in molecular clouds, heated by newly formed stars, while in low- z galaxies there are important additional contributions from colder “cirrus” heated by older stellar populations.

This SED worked very well at submillimeter wavelengths but yielded millimeter-wave counts in excess of the observed ones. To overcome this problem the submillimeter slope of the SED has been made somewhat steeper, preserving the consistency with the photometric data on SMM J2135-0102 (see Figure 3.3). Moreover, the SED used by Lapi et al. has a ratio between the total (8–1000 μm) IR and the 8 μm luminosity ($\text{IR8} \equiv L_{\text{IR}}/L_8$) of $\simeq 30$, far higher than the mean value for $z \simeq 2$ galaxies ($\text{IR8} \simeq 9$; Elbaz et al. 2011; Reddy et al. 2012). We have therefore modified the near- and mid-IR portions of the

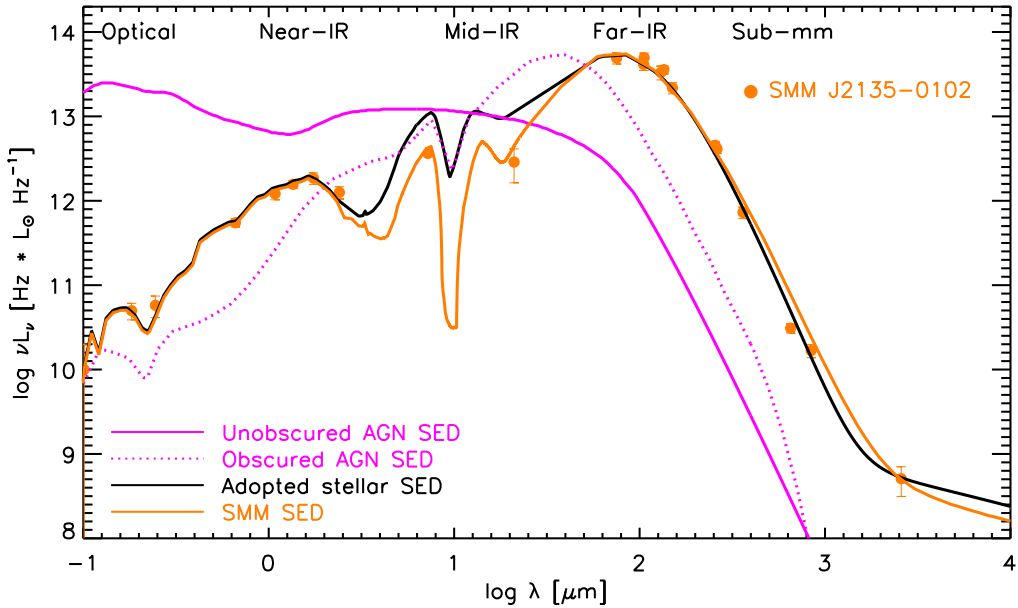


Figure 3.3: SEDs of stellar and AGN components of proto-spheroidal galaxies. The solid black line shows the adopted SED for the stellar component, obtained modifying that of the $z \simeq 2.3$ galaxy SMM J2135-0102, also shown for comparison (solid orange line; the photometric data are from [Swinbank et al. \(2010\)](#) and [Ivison et al. \(2010\)](#)). The dotted magenta line represents the SED adopted for the dust obscured phase of the AGN evolution and is taken from the AGN SED library by [Granato & Danese \(1994\)](#). For unobscured AGNs, we have adopted the mean QSO SED of [Richards et al. \(2006\)](#); solid magenta line). The original SMM J2135-0102 SED and the two AGN SEDs are normalized to $\log(L_{\text{IR}}/L_{\odot}) = 13.85$ while the modified SED is normalized to $\log(L_{\text{IR}}/L_{\odot}) = 13.92$ to facilitate the comparison with the original SED. Except in the rare cases in which the AGN bolometric luminosity is much larger than that of the starburst, the AGN contribution is small at (sub-)millimeter wavelengths, while it is important and may be dominant in the mid-IR.

SED adopting a shape similar to that of Arp 220. The contribution of the passive evolution phase of early-type galaxies is small in the frequency range of interest here and will be neglected.

As mentioned previously, the model follows the AGN evolution through two phases (a third phase, reactivation, will be considered in Section 3.2.1). For the first phase, when the black-hole growth is enshrouded by the abundant, dusty interstellar medium (ISM) of the host galaxy, we adopt the SED of a heavily absorbed AGN taken from the AGN SED library by [Granato & Danese \(1994\)](#). Note that these objects differ from the classical type 2 AGNs because they are not obscured by a circumnuclear torus but by the more widely distributed dust in the host galaxy. They will be referred to as type 3 AGNs. In the second phase the AGN shines after having swept out the galaxy ISM. For this phase, we adopted the mean QSO SED by [Richards et al. \(2006\)](#) extended to submillimeter wavelengths assuming a graybody emission with dust temperature $T_{\text{dust}} = 80$ K and emissivity index $\beta = 1.8$. These SEDs imply that the IR (8–1000 μm) band comprises 92% of the bolometric luminosity of obscured AGNs and 19% of that of the unobscured ones. As illustrated by Figure 3.3, except in the rare cases in which the AGN bolometric luminosity is much larger than that of the starburst, the AGN contribution is small at (sub-)millimeter wavelengths, while it is important and may be dominant in the mid-IR. This implies that the statistics discussed here are insensitive to the parameters describing the extrapolation of the Richards et al. SED to (sub-)millimeter wavelengths.

Figure 3.4 shows the global SEDs and the contributions of the stellar and AGN components for two galaxy ages and three host halo masses virialized at $z_{\text{vir}} = 3$. The shorter evolution timescale of the AGNs

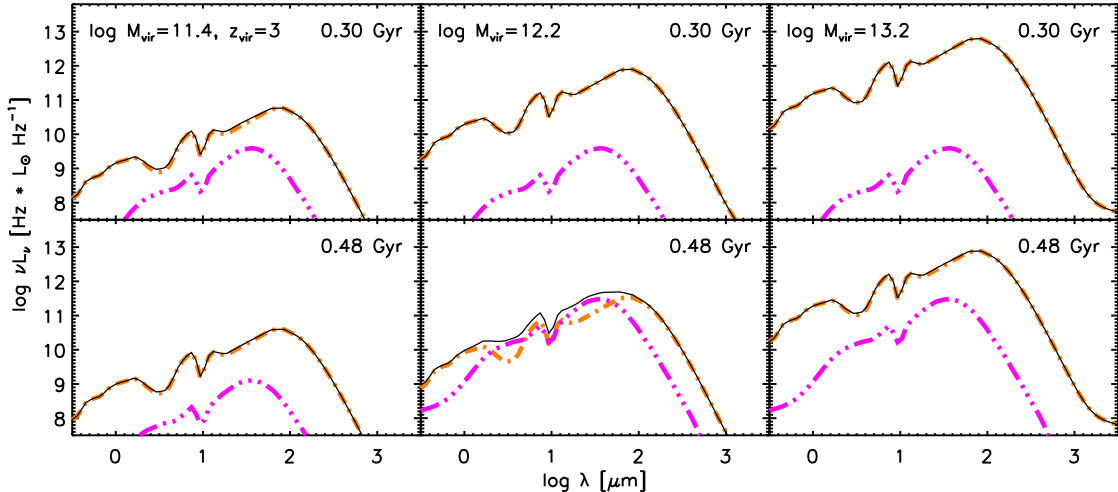


Figure 3.4: Global SEDs (solid black lines) for two galactic ages (0.3 and 0.48 Gyr) and three host halo masses ($\log(M_{\text{vir}}/M_{\odot}) = 11.4, 12.2, \text{ and } 13.2$, from left to right), virialized at $z_{\text{vir}} = 3$. The dot-dashed orange line (overlaid by the solid black line in some panels) and the triple-dot-dashed magenta line show the stellar and the AGN component, respectively. The shorter evolution timescale of the AGNs is clearly visible. The effect of feedback as a function of halo mass on the SFR is very different from that on accretion onto the super-massive black-hole (see the text).

is clearly visible. It is worth noticing that the effect of feedback as a function of halo mass on the SFR is very different from that on accretion onto the supermassive black hole. In the less massive halos the AGN feedback has only a moderate effect on the evolution of the SFR and of the accretion rate, which are mostly controlled by the SN feedback. With reference to the figure, for $\log(M_{\text{vir}}/M_{\odot}) = 11.4$, the star formation continues at an almost constant rate for a few Gyr. On the other hand, the accretion rate onto the central black hole is at the Eddington limit only up to an age of $\simeq 0.3$ Gyr and afterward drops to a strongly sub-Eddington regime. This is because the growth rate of the reservoir is approximately proportional to the SFR (and therefore slowly varying for few Gyr), while the accretion rate grows exponentially until the mass contained in the reservoir is exhausted. From this moment on the accretion rate is essentially equal to the (strongly sub-Eddington) inflow rate. For more massive halos the quenching of both the SFR and of the accretion occurs more or less simultaneously at ages of $\simeq 0.5\text{--}0.7$ Gyr, but while the SFR stops very rapidly, the AGN activity continues until the flow of the matter accumulated in the reservoir runs out. At ages $\gtrsim 0.6$ Gyr, the more massive galaxies are in passive evolution and therefore very weak in the far-IR, while star formation and the dust emission are still present in lower-mass galaxies.

Since the model cannot follow in detail the evolution of the AGN SEDs during the short phase when they shine unobstructed by the interstellar medium of the host galaxy, the distinction between obscured and unobscured AGNs in the model is made in two ways. First, following Lapi et al. (2006), we choose a fixed optical (*B*-band) “visibility time”, $\Delta t_{\text{vis}} = 5 \times 10^7$ yr, consistent with current estimates of the optically bright QSO phase. Alternatively, we set the beginning of the optical bright phase at the moment when the gas mass fraction is low enough to yield a low optical depth. We estimate that this corresponds to a gas fraction within the dark matter potential well $f_{\text{gas}} = M_{\text{gas}}/M_{\text{vir}} \lesssim f_{\text{gas,crit}} = 0.03$. The two approaches give very similar results and we have chosen the criterion $f_{\text{gas}} \lesssim f_{\text{gas,crit}}$ to compute the LFs at optical wavelengths.

Table 3.1: Parameters of the physical model for the evolution of proto-spheroidal galaxies and of the associated AGNs

Parameter	Value	Plausible range	Description
τ_{RD}^0	3.0	1 - 10 ^a	Normalization of optical depth of gas cloud (Equation (3.12))
ϵ	0.10	0.06 - 0.42	Black hole accretion radiative efficiency (Equation (3.17))
λ_{Edd}	1 - 4	\lesssim a few ^b	Redshift-dependent Eddington ratio (Equation (3.15))
ϵ_{QSO}	3.0	1 - 10 ^a	Strength of QSO feedback (Equation (3.20))
$k_{*,\text{IR}}$	3.1	2 - 4 ^c	Conversion factor from of SFR to IR luminosity (Equation (3.6))
σ_*	0.10	\lesssim 0.5	Dispersion of mean stellar luminosity (Equation (3.24))
σ_\bullet	0.35	\lesssim 0.5 ^b	Dispersion of mean AGN luminosity (Equation (3.24))
$f_{\text{gas,crit}}$	0.03	\lesssim 0.165	Gas mass fraction at transition from obscured to unobscured AGNs (Section 3.1.2)
ϵ_{SN}	0.05	0.01 - 0.1 ^d	Strength of SN feedback (Equation (3.8))
α_{RD}	2.5	1 - 10 ^e	Strength of radiation drag (Equation (3.11))

Notes. The values of the first eight parameters used here are somewhat different from those used in previous papers, but still well within the plausible ranges listed in column 3 and discussed in the references given in the footnotes.

^a Granato et al. (2004); ^b Lapi et al. (2006); ^c Lapi et al. (2011); ^d Shankar et al. (2006); ^e A. Lapi et al. (in preparation).

3.1.3 Parameters of the physical model

A minimum χ^2 approach for estimating the optimum values of the parameters of the physical model for proto-spheroidal galaxies and associated AGNs is unfeasible because of the lengthy calculations required. Some small adjustments compared to earlier versions (Granato et al. 2004; Lapi et al. 2006; Mao et al. 2007) were made, by trial and error, to improve the agreement with observational estimates of LFs at $z \gtrsim 1.5$. The chosen values listed in Table 3.1 are still within their plausible ranges.

The impact of these parameters on the derived LFs (see Section 3.1.4) can be more easily understood with reference to the time lag between the halo virialization and the peak in black hole accretion rate, Δt_{peak} (Lapi et al. 2006). The duration of star formation is $\Delta t_{\text{SF}} \lesssim \Delta t_{\text{peak}}$ (see Figure 3.2) due to the drastic effect of QSO feedback in massive halos which dominate the bright end of the LFs. Note that longer Δt_{peak} (or Δt_{SF}) imply higher bright tails of the LFs. The final black hole mass increases with increasing the coefficient, τ_{RD}^0 , of the optical depth of gas clouds (Equation (3.12)) because it implies a higher efficiency of the radiation drag driving the gas into the reservoir. There is a degeneracy, to some extent, between τ_{RD}^0 and the gas metallicity Z_{gas} , implying that τ_{RD}^0 cannot be tightly constrained (see Granato et al. 2004). The value of Δt_{peak} grows substantially in response to a small increase of the radiative efficiency ϵ that yields a slower growth of the black hole mass and a weaker QSO feedback. Higher values of the Eddington ratio, λ_{Edd} , result in lower values of both Δt_{peak} and of the final black hole mass. A rise of λ_{Edd} at high- z is required to account for the observed space density of very luminous QSOs (Lapi et al. 2006). A higher QSO feedback efficiency (higher ϵ_{QSO}) shortens the duration of star formation, Δt_{SF} , but has a minor effect on Δt_{peak} and on the final black hole mass. Finally, the coefficient relating the SFR to the IR luminosity, $k_{*,\text{IR}}$, varies with age mix of stellar populations, chemical composition, and IMF. Increasing it we shift the LFs toward higher luminosities. For additional details and discussions of physically plausible ranges for each parameter we refer to Granato et al. (2004), Cirasuolo et al. (2005), Lapi et al. (2006), Shankar et al. (2006), Mao et al. (2007), Cook et al. (2009), and Fan et al. (2010).

3.1.4 Luminosity function and its evolution

The bolometric LF of proto-spheroids is obtained convolving the halo formation rate $\dot{n}_{\text{ST}}(M_{\text{vir}}, z) = d^3 N_{\text{ST}} / dM_{\text{vir}} dV_C dt$, i.e., Equation (2.49), with the galaxy luminosity distribution, $P(\log L, z; M_{\text{vir}}, z_{\text{vir}})$. The comoving differential LF $\Phi(\log L, z)$, i.e., the number density of galaxies per unit $\log L$ interval at redshift z , is given by

$$\Phi(\log L, z) = \int_{M_{\text{vir}}^{\min}}^{M_{\text{vir}}^{\max}} dM_{\text{vir}} \int_z^{z_{\text{vir}}^{\max}} dz_{\text{vir}} \left| \frac{dt_{\text{vir}}}{dz_{\text{vir}}} \right| \frac{d^3 N_{\text{ST}}}{dM_{\text{vir}} dV_C dt_{\text{vir}}} (M_{\text{vir}}, z_{\text{vir}}) \cdot P(\log L, z; M_{\text{vir}}, z_{\text{vir}}), \quad (3.22)$$

where $P(\log L, z; M_{\text{vir}}, z_{\text{vir}})$ is the luminosity distribution of galaxies at redshift z inside a halo of mass M_{vir} virialized at redshift z_{vir} . We set $z_{\text{vir}}^{\min} = 1.5$ and $z_{\text{vir}}^{\max} = 16$.

The total luminosity of a galaxy is the sum of those of the stellar component and of the active nucleus. For each component we assume a log-normal luminosity distribution

$$P[\log L | \log \bar{L}] d\log L = \frac{\exp[-\log^2(L/\bar{L})/2\sigma^2]}{\sqrt{2\pi\sigma^2}} d\log L, \quad (3.23)$$

with dispersion $\sigma_* = 0.10$ around the mean stellar luminosity $\bar{L}_*(z; M_{\text{vir}}, z_{\text{vir}})$ and $\sigma_\bullet = 0.35$ around the mean AGN luminosity $\bar{L}_\bullet(z; M_{\text{vir}}, z_{\text{vir}})$. The mean luminosities are computed solving the equations detailed in Section 3.1.1. The higher luminosity dispersion for the AGN component reflects its less direct relationship, compared to the stellar component, with M_{vir} and z_{vir} . The distribution of the total luminosity, $L_{\text{tot}} = L_* + L_\bullet$, is then (Dufresne 2004)

$$P[\log L_{\text{tot}} | \log \bar{L}_*, \log \bar{L}_\bullet] d\log L_{\text{tot}} = d\log L_{\text{tot}} \times \int_{-\infty}^{\log L_{\text{tot}}} \frac{dx}{2\pi\sigma_*\sigma_\bullet} \frac{L_{\text{tot}}}{L_{\text{tot}} - 10^x} \exp \left\{ -\frac{(x - \log \bar{L}_*)^2}{2\sigma_*^2} - \frac{[\log(L_{\text{tot}} - 10^x) - \log \bar{L}_\bullet]^2}{2\sigma_\bullet^2} \right\}. \quad (3.24)$$

In the upper left panel of Figure 3.5 we show, as an example, the bolometric LFs at $z = 1.5$ of the stellar and of the AGN components, as well as the LF of the objects as a whole. As shown in Equation (3.24), the latter is different from the sum of the first two, although in this case the difference is difficult to perceive. The bright end is dominated by QSOs shining unobstructed after having swept away the interstellar medium of the host galaxy. In this phase the QSOs reach their maximum luminosity. Around $\log(L_{\text{bol}}/L_\odot) \simeq 13$ the AGNs and the starbursts give similar contributions to the bolometric LF. The inflection at $\log(L_{\text{IR}}/L_\odot) \simeq 11.7$ corresponds to the transition from the regime where the feedback is dominated by supernovae (lower halo masses) to the regime where it is dominated by AGNs. While the star formation in massive halos is abruptly stopped by the AGN feedback after 0.5–0.7 Gyr, it lasts much longer in smaller galaxies, implying a fast increase of their number density.

The upper right panel of the same figure illustrates the evolution with cosmic time of the global LF. The cooling and free-fall timescales shorten with increasing redshift because of the increase of the matter density and this drives a positive luminosity evolution, thwarted by the decrease in the comoving density of massive halos. The two competing factors result, for both the starburst and the AGN component (see the lower panels of the figure), in a positive evolution up to $z \simeq 2.5$ followed by a decline at higher z ,

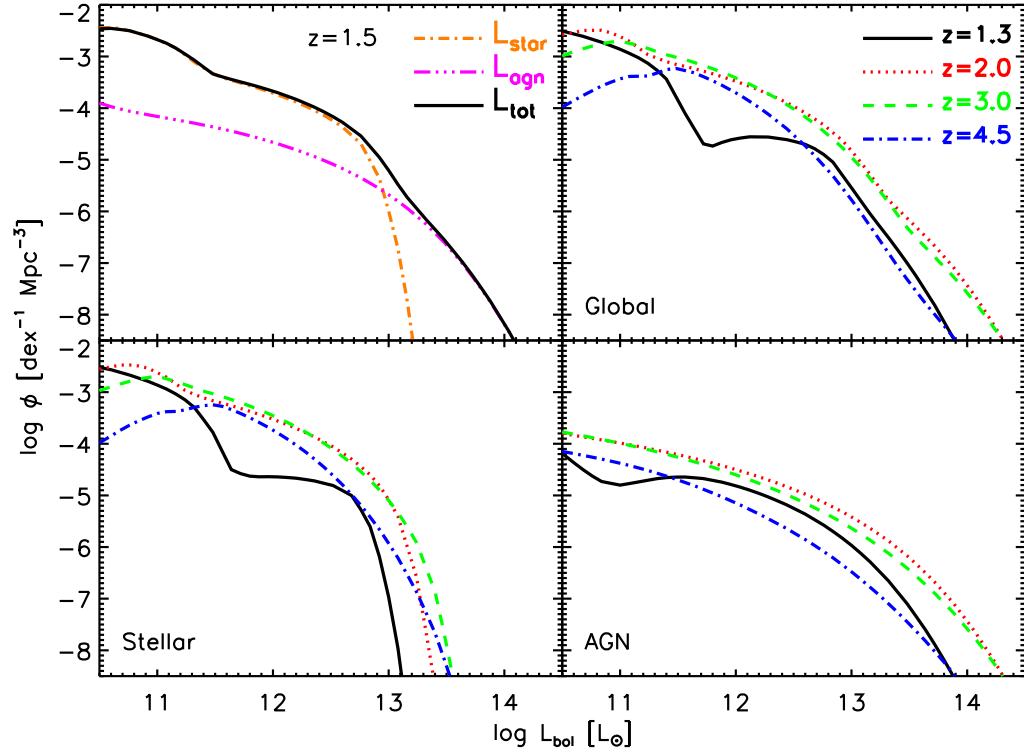


Figure 3.5: Bolometric luminosity functions of proto-spheroidal galaxies. The upper left panel shows the luminosity functions at $z = 1.5$ of the stellar (dot-dashed orange line) and of the AGN component luminosity (triple-dot-dashed magenta line), as well as the global luminosity function (solid black line). Note that, as discussed in Section 3.1.4, the latter is *not* the sum of the two components although in this case is very close to it. The upper right panel illustrates the evolution of the global luminosity function from $z = 1.3$ to $z = 4.5$, while the lower panels show the evolution of each component separately. The decline at low luminosities is an artifact due to the adopted lower limit to the proto-spheroid halo masses. The figure highlights the different shapes of the stellar and AGN bolometric luminosity function, with the latter having a more extended high luminosity tail, while the former sinks down exponentially above $\sim 10^{13} L_\odot$. The evolutionary behaviour of the two components is qualitatively similar and cannot be described as simple luminosity or density evolution; downsizing effects are visible in both cases. On the other hand there are also clear differences.

consistent with the observational determinations by Gruppioni et al. (2010) and Lapi et al. (2011) for the starburst component and by Assef et al. (2011) and Brown et al. (2006) for AGNs. The decrease of the LF at low luminosities, more clearly visible at the higher redshifts, is an artifact due to the adopted lower limit for the considered halo masses. This part of the LF, however, does not contribute significantly to the observed statistics and therefore is essentially irrelevant here. Below the minimum virialization redshift, $z_{\text{vir}}^{\min} = 1.5$, the bolometric LF of proto-spheroidal galaxies rapidly declines as they evolve toward the “passive” phase. The decline is faster at the bright end (above $\log(L_{\text{bol}}/L_\odot) \simeq 12$) since the switching off of the star formation for the more massive halos occurs on a shorter timescale.

The monochromatic LFs of each component or of objects as a whole can obviously be computed using the same formalism, given the respective SEDs. We define $\bar{\mathcal{L}}_{*,\nu} \equiv \nu \bar{L}_{*,\nu} = \nu f_*(\nu) \bar{L}_{*,\text{IR}}$, $\bar{\mathcal{L}}_{\bullet,\nu} \equiv \nu \bar{L}_{\bullet,\nu} = \nu f_\bullet(\nu) \bar{L}_{\bullet,\text{IR}}$, and $\bar{\mathcal{L}}_\nu \equiv \bar{\mathcal{L}}_{*,\nu} + \bar{\mathcal{L}}_{\bullet,\nu}$, where $f(\nu)$ is the SED normalized to $\int_{8\mu\text{m}}^{1000\mu\text{m}} d\nu f(\nu) = 1$. The IR luminosity of AGNs, $\bar{L}_{\bullet,\text{IR}}$, is converted from their bolometric luminosity ($\bar{L}_{\bullet,\text{bol}}$; Equation (3.17)) by a factor of 0.92 and 0.19 for obscured and unobscured phase, respectively (see Section 3.1.2).

3.2 Low- z star-forming galaxies and associated AGNs ($z \lesssim 2$)

Since we do not have a physical evolutionary model for late-type galaxies and the associated AGNs, these source populations have been dealt with adopting a phenomenological approach. Generally, this kind of model interprets the observed LF and its evolution with some empirical functional forms to simulate that derived using a more physical approach. Although it only describes the evolution of LF and contains little physics, it is still useful because it serves as a guide to interpret the observations and to refine the physical models.

3.2.1 Phenomenological backward evolution

Late-type and starburst galaxies

We consider two $z \lesssim 1.5$ galaxy populations: “warm” starburst galaxies and “cold” (normal) late-type galaxies. For the IR LF of both populations, we adopt the functional form advocated by [Saunders et al. \(1990\)](#):

$$\Phi(\log L_{\text{IR}}, z) d\log L_{\text{IR}} = \Phi^* \left(\frac{L_{\text{IR}}}{L^*} \right)^{1-\alpha} \times \exp \left[-\frac{\log^2(1 + L_{\text{IR}}/L^*)}{2\sigma^2} \right] d\log L_{\text{IR}}, \quad (3.25)$$

where the characteristic density Φ^* and luminosity L^* , the low-luminosity slope α , and the dispersion σ of each population are, in principle, free parameters. However, the low-luminosity portion of the LF is dominated by “cold” late-type galaxies and, as a consequence, the value of α of the warm population is largely unconstrained; we have fixed it at $\alpha_{\text{warm}} = 0.01$. In turn, the “warm” population dominates at high luminosities so that the data only imply an upper limit to σ_{cold} . We have set $\sigma_{\text{cold}} = 0.3$.

For the “warm” population, we have assumed power-law density and luminosity evolution [$\Phi^*(z) = \Phi_0^*(1+z)^{\alpha_\Phi}$; $L^*(z) = L_0^*(1+z)^{\alpha_L}$] up to $z_{\text{break}} = 1$, α_Φ and α_L being free parameters. The “cold” population comprises normal disk galaxies for which chemo/spectrophotometric evolution models ([Mazzei et al. 1992](#); [Colavitti et al. 2008](#)) indicate a mild (a factor $\simeq 2$ from $z = 0$ to $z = 1$) increase in the star formation rate, hence of IR luminosity, with look-back time. Based on these results we take, for this population, $\alpha_L = 1$ and no density evolution. At $z > z_{\text{break}}$ both $\Phi^*(z)$ and $L^*(z)$ are kept to the values at z_{break} multiplied by the smooth cut-off function $\{1 - \text{erf}[(z - z_{\text{cutoff}})/\Delta z]\}/2$, with $z_{\text{cutoff}} = 2$ and $\Delta z = 0.5$. The choice of the redshift cutoff for both populations of late-type galaxies is motivated by the fact that the disk component of spirals and the irregular galaxies are characterized by relatively young stellar populations (formation redshift $z \lesssim 1\text{--}1.5$). Above $z = 1.5$, proto-spheroidal galaxies (including bulges of disk galaxies) dominate the contribution to the LF, at least in the observationally constrained luminosity range. The other parameters are determined by minimum χ^2 fits to selected data sets, as described in Section 3.2.3. Their best fit values and the associated uncertainties are listed in Table 3.2.

Reactivated AGNs

In the framework of our reference galaxy and AGN evolutionary scenario, most of the growth of supermassive black holes is associated with the star forming phase of spheroidal components of galaxies at $z \gtrsim 1.5$ when the great abundance of interstellar medium favors high accretion rates, at, or even slightly above,

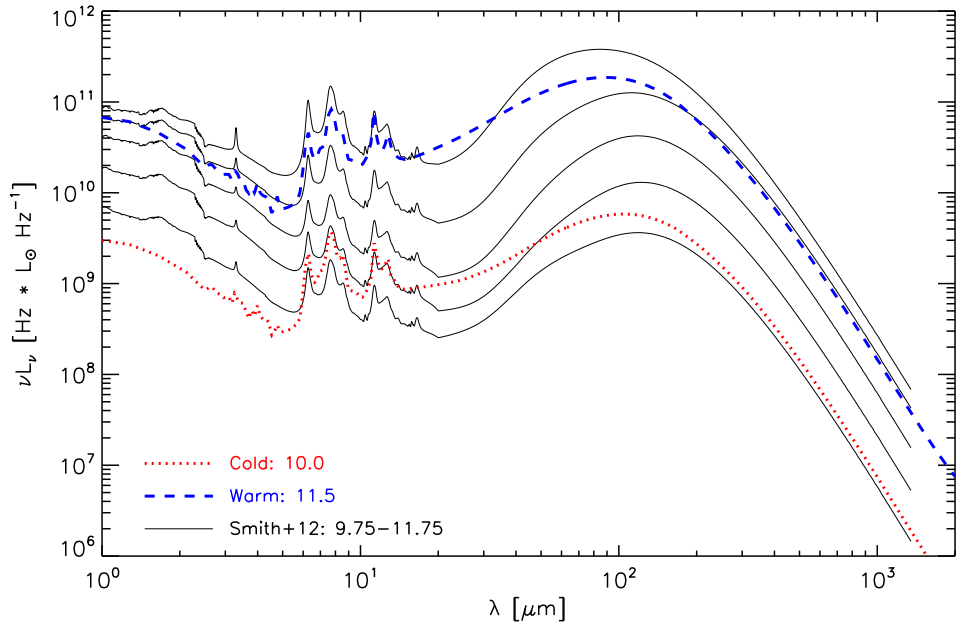


Figure 3.6: SEDs of Smith et al. (2012; black solid lines) for IR luminosities, $\log(L_{\text{IR}}/L_{\odot}) = 9.75, 10.25, 10.75, 11.25$ and 11.75 , from bottom to top. The empirical SEDs for “warm” (blue dashed line) and “cold” (red dotted line) populations are shown for comparison; they are normalized to $\log(L_{\text{IR}}/L_{\odot}) = 11.5$ and 10.0 , respectively.

the Eddington limit. At later cosmic times the nuclei can be reactivated by, e.g., interactions, mergers, or dynamical instabilities. The accretion rates are generally strongly sub-Eddington. Our evolutionary scenario cannot predict their amplitudes and duty cycles. We therefore also adopted for these objects a phenomenological backward evolution model analogous to that used for the “warm” galaxy population, i.e., LFs of the same form of Equation (3.25) and power-law density and luminosity evolution with the same break and cutoff redshifts. However the parameters of the LFs refer to $12 \mu\text{m}$ (see Section 3.2.3 and Table 3.2). The data do not allow a determination of the slopes, α , of the faint portions of the LFs. We have set $\alpha = 1.1$ for type 1 AGNs and $\alpha = 1.5$ for type 2. The steeper slope for type 2 was chosen on account of the fact that these dominate over type 1 at low luminosities. As in the case of normal late-type and of starburst galaxies, the other parameters are obtained by minimum χ^2 fits, as detailed in Section 3.2.3, and the best fit values are listed, with their uncertainties, in Table 3.2. For type 2 AGNs pure density evolution was found to be sufficient to account for the data.

3.2.2 SEDs of low- z populations

Late-type and starburst galaxies

At the very beginning of work to construct our evolutionary model we adopted the luminosity-dependent SEDs of Smith et al. (2012), based on a sample of 1402 $250 \mu\text{m}$ selected galaxies at $z < 0.5$ from the H-ATLAS survey ($100\text{--}500 \mu\text{m}$ *Herschel* data). In Figure 3.6 these SEDs are compared with the empirical SEDs we converged on. We first tried to build a model adopting for all galaxies the same evolutionary law, but no satisfactory fit of the multi-wavelength counts could be found (see Section 3.3.1 for the formalism to compute the source counts). The main discrepancy between the model and the

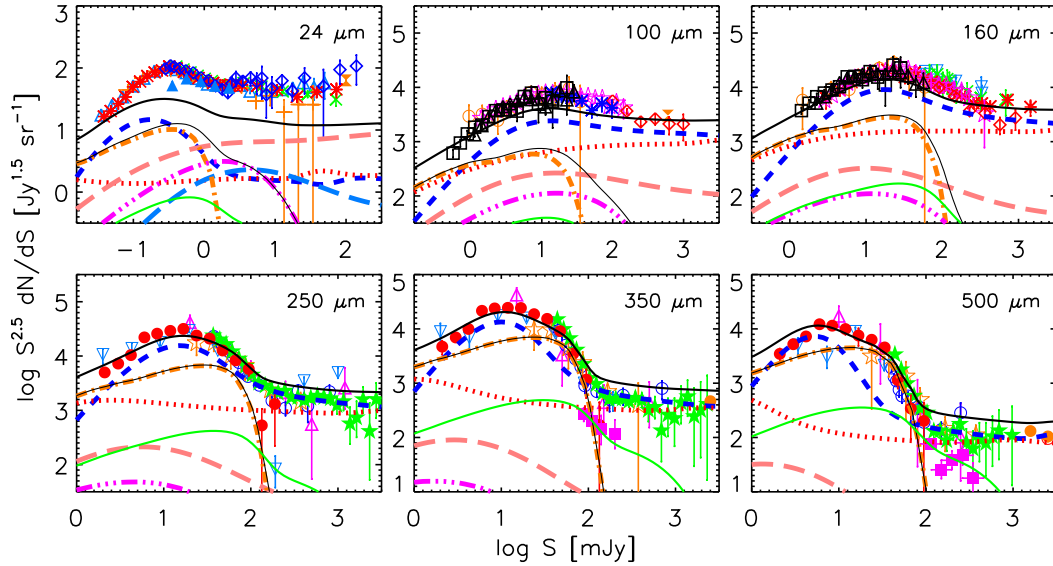


Figure 3.7: Adopting the luminosity-dependent SEDs of Smith et al. (2012) for late-type galaxies leads to a strong under-prediction of the mid-IR counts, as illustrated by the figure. The thick solid lines are the sum of contributions from: “cold” late-type galaxies (dotted red lines), “warm” (starburst) late-type galaxies (dashed blue lines), type 1 AGNs (long-dashed light-blue lines), type 2 AGNs (long-dashed pink lines), stellar component of proto-spheroids (dot-dashed orange lines), AGN component of proto-spheroids (triple-dot-dashed magenta lines), strongly lensed ($\mu \geq 2$) proto-spheroids (solid green lines). The thin solid black lines show the counts of unlensed proto-spheroids, including both the stellar and the AGN components; at $\lambda \geq 250 \mu\text{m}$ these counts essentially coincide with the counts of the stellar component only. References for all the data are given in Table 4.2.

data was that evolutionary laws fitting the submillimeter data strongly under-predicted the mid-/far-IR counts. The next attempt was to consider two populations of late-type galaxies (normal and starburst) with different evolutionary laws, both having the luminosity-dependent SEDs of Smith et al. (2012). The previously noted problem was only slightly attenuated. Figure 3.7 shows an example of this problem with the same luminosity and density evolution behavior as our reference model listed in Table 3.2 but with a slightly different parametrization of the local IR LFs ($\log(\Phi_0^*/\text{Mpc}^{-3}) = -2.665$, $\log(L_0^*/L_\odot) = 9.800$, and $\sigma = 0.343$ for the “warm” population; $\log(\Phi_0^*/\text{Mpc}^{-3}) = -1.752$, $\log(L_0^*/L_\odot) = 9.621$, and $\alpha = 1.283$ for the “cold” population). The new parameters were obtained by simultaneously fitting the *Planck* local LFs of Negrello et al. 2013 (2013; 350, 500, and 850 μm) and the *Herschel* SPIRE counts of Béthermin et al. 2012b (2012b; 250, 350, and 500 μm).

We thus concluded that the SEDs of Smith et al. (2012), which are mostly based on submillimeter data, are not adequate at shorter wavelengths. This conclusion was supported by the comparison of the ratios between submillimeter and mid-IR luminosities obtained from the Smith et al. (2012) SEDs with those obtained from the local LFs at the same wavelengths considering the luminosities that correspond to the same source densities. For example, the ratios $\nu L_\nu(250 \mu\text{m})/\nu L_\nu(24 \mu\text{m})$ obtained from the SEDs are 4.22, 8.24, 10.28, 6.96, and 2.57, for $\log(L_{\text{IR}}/L_\odot)$ increasing from 9.75 to 11.75, while the ratio inferred from the local LFs is $\simeq 1$. This means that the Smith et al. (2012) SEDs are under-luminous at mid-IR wavelengths for given submillimeter luminosity.

Note that the Dale & Helou (2002) SEDs, some of which are illustrated in Figure 3.8, were best determined at mid-IR wavelengths based on *IRAS* and *ISO* 3–100 μm observations of nearby normal

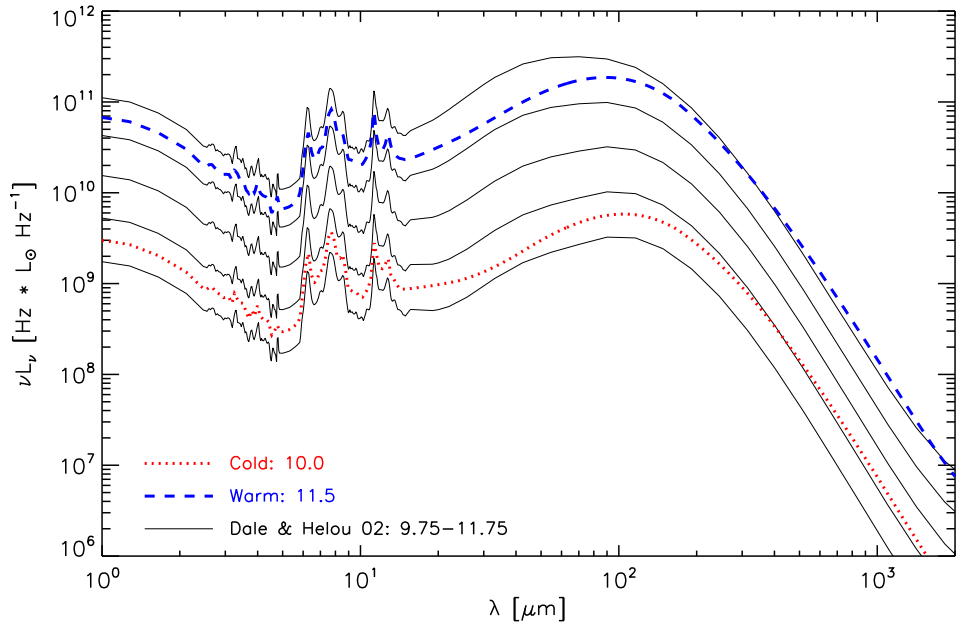


Figure 3.8: SEDs of Dale & Helou (2002; black solid lines) for $\log(L_{\text{IR}}/L_{\odot}) = 9.75, 10.25, 10.75, 11.25$ and 11.75 , from bottom to top. The IR luminosities L_{IR} are estimated from the $60\text{--}100\text{ }\mu\text{m}$ flux density ratios given by Dale & Helou (2002, see Section 3.2.2). The empirical SEDs for the “warm” (blue dashed line) and the “cold” (red dotted line) populations are shown for comparison and are normalized to $\log(L_{\text{IR}}/L_{\odot}) = 11.5$ and 10.0 , respectively.

star-forming galaxies (Dale et al. 2001) and then extended to submillimeter wavelengths based on far-IR ISO and submillimeter SCUBA data (Dale & Helou 2002; and see Shi et al. 2013 for the discussion on merits and disadvantages of these SEDs). Dale & Helou (2002) give SED templates for several values of the $60\text{--}100\text{ }\mu\text{m}$ flux density ratio, $\log[f_{\nu}(60\text{ }\mu\text{m})/f_{\nu}(100\text{ }\mu\text{m})]$. Using the relation between this ratio and the $3\text{--}1100\text{ }\mu\text{m}$ luminosity, L_{TIR} , given by Chapman et al. (2003), we established a correspondence between their SEDs and those by Smith et al., labeled by the values of $\log(L_{\text{IR}}/L_{\odot})$.

Figure 3.9 shows the predicted number counts for two populations of late-type galaxies with the same evolution of our reference model but with slightly different fitting formulae for the local IR LFs ($\log(\Phi_0^*/\text{Mpc}^{-3}) = -2.457$, $\log(L_0^*/L_{\odot}) = 9.755$, and $\sigma = 0.370$ for “warm” population; $\log(\Phi_0^*/\text{Mpc}^{-3}) = -1.617$, $\log(L_0^*/L_{\odot}) = 9.334$, and $\alpha = 1.233$ for “cold” population). The new parameters were obtained by simultaneously fitting the $24\text{ }\mu\text{m}$ local LF of (Rujopakarn et al. 2010), the $60\text{ }\mu\text{m}$ local LF of (Soifer & Neugebauer 1991), and the Spitzer MIPS $24\text{ }\mu\text{m}$ number counts of Béthermin et al. (2010), using the Dale & Helou (2002) SEDs. The fits of the counts are better than those obtained previously, but still not satisfactory. The ratios $\nu L_{\nu}(250\text{ }\mu\text{m})/\nu L_{\nu}(24\text{ }\mu\text{m})$ are now $1.06, 0.94, 0.78, 0.56$, and 0.38 , for $\log(L_{\text{IR}}/L_{\odot})$ increasing from 9.75 to 11.75 , showing that these SEDs are generally under-luminous in the submillimeter, for given mid-IR luminosity.

Considering merits and disadvantages of the above two SED template libraries, we generated composite SEDs at the five mentioned IR luminosities adopting the Smith et al. (2012) SEDs at submillimeter wavelengths and raising them at mid-IR wavelengths, making them close to those by Dale & Helou (2002). Although there is clear evidence of systematic variations of the IR SEDs of low- z galaxies with luminosity (e.g., Smith et al. 2012), we checked whether it would be enough to adopt a single SED for

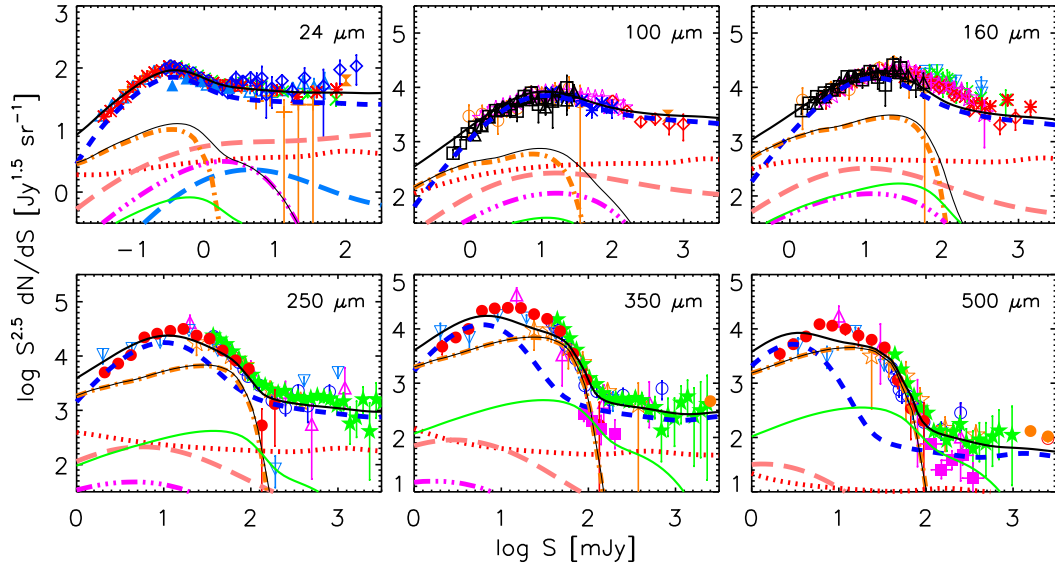


Figure 3.9: Best fit multi-wavelength source counts obtained adopting the SEDs of Dale & Helou (2002) for the two populations of late-type galaxies, with different luminosity and density evolution. At mid- to far-IR wavelengths the fit is much better than was obtained using the Smith et al. (2012) SEDs, but the submillimeter counts are under-predicted. The lines have the same definition as in Figure 3.7. References for all the data are given in Table 4.2.

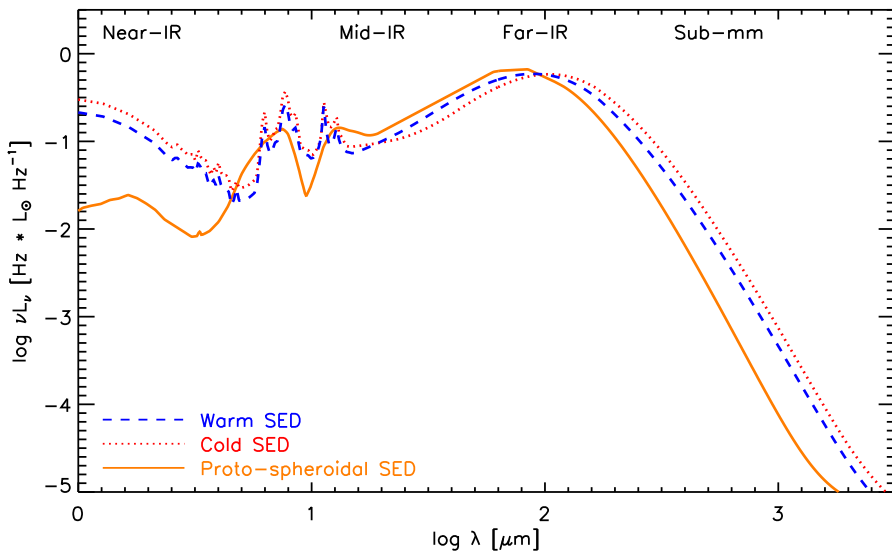


Figure 3.10: Adopted SEDs for the “warm” (dashed blue line) and “cold” (dotted red line) low- z star-forming galaxies. They were generated combining SEDs of Dale & Helou (2002) and Smith et al. (2012), as described in the text. The solid orange line shows, for comparison, the SED of proto-spheroidal galaxies. The three SEDs are normalized to the same total IR luminosity $\log(L_{\text{IR}}/L_{\odot}) = 1$.

each of the two populations of late-type galaxies in order to keep the model as simple as possible. By trial and error we found that the data can be well fitted using for the “cold” population the SED corresponding to $\log(L_{\text{IR}}/L_{\odot}) = 9.75$ and for the “warm” population the SED corresponding to $\log(L_{\text{IR}}/L_{\odot}) = 11.25$. These two empirical SEDs are shown in Figures 3.6 and 3.8 where they are compared with those of Smith et al. (2012) and Dale & Helou (2002), respectively. The empirical SEDs have ratios $\nu L_{\nu}(250 \mu\text{m})/\nu L_{\nu}(24 \mu\text{m})$ of 1.45 and 0.83 for the “cold” and the “warm” population, respectively. The multi-wavelength number counts obtained adopting these SEDs and the parameters listed in Table 3.2

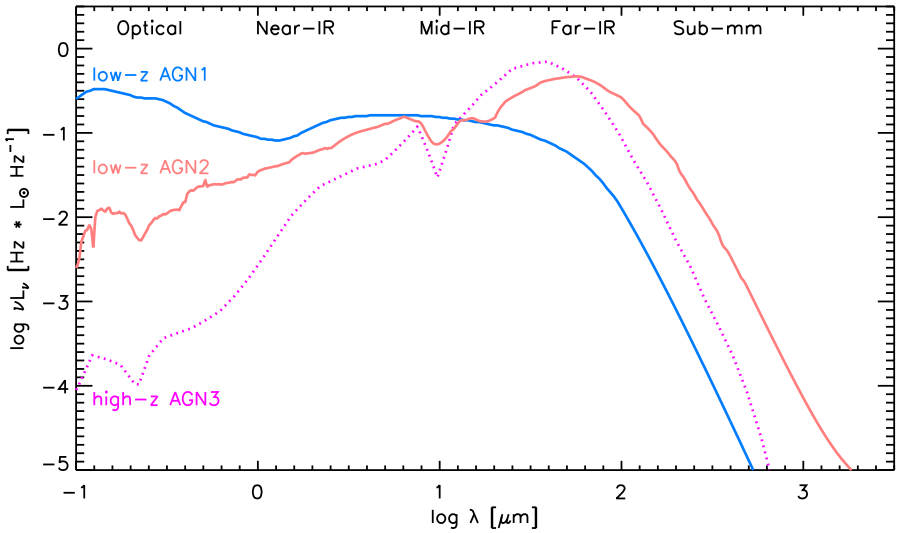


Figure 3.11: SEDs of low- z type 1 AGNs (solid light-blue line) and type 2 AGNs (solid pink line). The dotted magenta line shows, for comparison, the adopted SED of AGNs associated with dusty proto-spheroidal galaxies (type 3 AGNs). The SEDs are normalized to the same, arbitrary, bolometric luminosity.

are shown in Figure 4.18. The agreement with the data is quite good. These two SEDs are also displayed to be compared with that of proto-spheroidal galaxies in Figure 3.10.

Reactivated AGNs

For type 1 AGNs we adopted the mean QSO SED by Richards et al. (2006), extended to millimeter wavelengths as described in Section 3.1.2, while for type-2 AGNs we adopted the SED of the local AGN-dominated ULIRG Mrk 231, taken from the SWIRE library (Polletta et al. 2007). These SEDs are shown in Figure 3.11, where the SED of type 3 AGNs associated with dusty star-forming proto-spheroidal galaxies is also plotted for comparison. The SED of type 3 AGNs is the most obscured at optical/near-IR wavelengths due to the effect of the dense, dusty interstellar medium of the high- z host galaxies. This means that the counts at optical/near-IR wavelengths are dominated by type 1 AGNs with type 2 AGNs becoming increasingly important in the mid-IR. The three AGN populations have approximately the same ratio between the rest-frame 12 μm and the bolometric luminosity, as first pointed out by Spinoglio & Malkan (1989).

3.2.3 Parameters of the empirical model

The minimum χ^2 approach was applied to late-type/starburst galaxies and to reactivated AGNs. The χ^2 minimization was performed using the routine *MPFIT*¹ exploiting the Levenberg-Marquardt least-squares method (Moré 1978; Markwardt 2009).

The huge amount of observational data in the frequency range of interest here and the large number of parameters coming into play forced us to deal with subsets of parameters at a time using specific data for each subset. The parameters of the evolving AGN LFs were obtained using:

¹<http://purl.com/net/mpfit>

Table 3.2: Parameters for low-z AGNs and for “Warm” and “Cold” galaxy populations

	AGN 1 (12 μm)	AGN 2 (12 μm)	Warm (IR)	Cold (IR)
$\log(\Phi_0^*/\text{Mpc}^{-3})$	-5.409 \pm 0.098	-4.770 \pm 0.122	-2.538 \pm 0.051	-1.929 \pm 0.112
$\log(L_0^*/L_\odot)$	9.561 \pm 0.084	10.013 \pm 0.093	10.002 \pm 0.076	9.825 \pm 0.087
α	1.1	1.5	0.01	1.372 \pm 0.121
σ	0.627 \pm 0.017	0.568 \pm 0.021	0.328 \pm 0.014	0.3
α_Φ	2.014 \pm 0.400	4.499 \pm 0.317	0.060 \pm 0.200	0.0
α_L	2.829 \pm 0.297	0.0	3.625 \pm 0.097	1.0
z_{break}	1.0	1.0	1.0	1.0
z_{cutoff}	2.0	2.0	2.0	2.0

Notes. The parameters of the AGN luminosity functions refer to 12 μm (νL_ν) while those for galaxies refer to IR (8–1000 μm) luminosities. Values without error were kept fixed.

- the B -band local QSO LF of [Hartwick & Schade \(1990\)](#);
- the g -band QSO LFs at $z = 0.55$ and 0.85 of [Croom et al. \(2009\)](#);
- the $z \lesssim 0.75, 1.24 \mu\text{m}$ AGN LFs of [Assef et al. \(2011\)](#);
- the bright end [$\log(L_{60}/L_\odot) \geq 12$] of the local 60 μm LF of [Takeuchi et al. \(2003\)](#);
- the *Spitzer* AGN counts at 8 and 24 μm of [Treister et al. \(2006\)](#).

The B - and g -band LFs were used to constrain the parameters of type 1 AGNs (type 2 being important only at the low luminosity end) while the 1.24 μm LFs were regarded as made by a combination of type 1 and type 2 AGNs, the latter being dominant at low luminosities.

As for the evolving LFs of “warm” and “cold” galaxy populations we used the following data sets:

- the *IRAS* 60 μm local LF of [Soifer & Neugebauer \(1991\)](#);
- the *Planck* 350, 550, and 850 μm local LFs of [Negrello et al. \(2013\)](#);
- the *Spitzer* MIPS counts at 24, 70, and 160 μm of [Béthermin et al. \(2010\)](#);
- the *Herschel* PACS counts at 160 μm of [Berta et al. \(2011\)](#);
- the *Herschel* SPIRE counts at 250, 350, and 500 μm of [Béthermin et al. \(2012b\)](#).

The fits of the counts were made after having subtracted the contributions of proto-spheroidal galaxies, which are only important at wavelengths $\geq 160 \mu\text{m}$. The best-fit values of the parameters are listed in Table 3.2, where values without errors denote parameters that were kept fixed, as mentioned in Section 3.2.1.

3.3 Observables

The previous Sections 3.1 and 3.2 have dealt with the cosmic evolution of the LF of galaxies and AGNs. The LFs are basic quantities linked to many other observable quantities such as redshift distributions, number counts, cosmic background light, clustering properties of galaxies and AGNs, cosmic reionization,

and so on. This section describes the formalism for these quantities while the corresponding results will be presented in the following chapters.

To better compare model results with observational data, the instrumental spectral responses were taken into account. This is especially important in the mid-IR because of the complexity of the SEDs due to the PAH emission lines and the strong silicate absorption. The monochromatic luminosity at the effective frequency ν_{eff} in the observer's frame is given by

$$L(\nu_{\text{eff}}) \equiv \int T(\nu') L_{\nu'(1+z)} d\nu' / \int T(\nu') d\nu', \quad (3.26)$$

where $T(\nu)$ is spectral response function and the integration is carried out over the instrumental band-pass. When the model is compared with LF data at frequency ν_i (in the source frame) coming from different instruments for sources at redshift z , we use the response function of the instrument for which ν_{eff} is closest to $\nu_i/(1+z)$. In the case of source counts, we use the response function appropriate for the most accurate data.

3.3.1 Number counts and contributions to the background

The surface density of sources per unit flux density and redshift interval is

$$\frac{d^3N}{dS_\nu dz d\Omega}(S_\nu, z) = \frac{\Phi(\log L_{\nu'}, z)}{L_{\nu'} \ln 10} \frac{dL_{\nu'}}{dS_\nu} \frac{d^2V_C}{dz d\Omega}, \quad (3.27)$$

where $\nu' = \nu(1+z)$ and flux $S_\nu = (1+z)L_{\nu'}/4\pi d_L^2(z)$. The differential number counts, i.e., the number of galaxies with flux density in the interval $S_\nu \pm dS_\nu/2$ at an observed frequency ν per unit solid angle, are then

$$\frac{d^2N}{dS_\nu d\Omega}(S_\nu) = \int_{z_{\min}}^{z_{\max}} dz \frac{\Phi(\log L_{\nu'}, z)}{L_{\nu'} \ln 10} \frac{dL_{\nu'}}{dS_\nu} \frac{d^2V_C}{dz d\Omega}. \quad (3.28)$$

The integral number counts, i.e., the number of galaxies with flux density $S_\nu > S_{\nu,\text{inf}}$ at frequency ν per unit solid angle, are given by

$$\frac{dN}{d\Omega}(S_\nu \geq S_{\nu,\text{inf}}) = \int_{z_{\min}}^{z_{\max}} dz \frac{d^2V_C}{dz d\Omega} \int_{\log L_{\nu',\text{inf}}}^{\infty} \Phi(\log L_{\nu'}, z) d\log L_{\nu'}, \quad (3.29)$$

where $\nu' = (1+z)\nu$ and $L_{\nu',\text{inf}}$ is the monochromatic luminosity of a source at the redshift z observed to have a flux density $S_{\nu,\text{inf}}$. Counts (per steradian) dominated by local objects ($z \ll 1$) can be approximated as

$$S_\nu^{2.5} \frac{d^2N}{dS_\nu d\Omega} \simeq \frac{1}{4\pi} \frac{1}{4\sqrt{\pi}} \int_0^\infty \Phi(\log L_\nu, z \simeq 0) L_\nu^{3/2} d\log L_\nu. \quad (3.30)$$

The redshift distribution, i.e., the surface density of sources with observed flux densities greater than a chosen limit $S_{\nu,\text{inf}}$ per unit redshift interval, is

$$\frac{d^2N}{dz d\Omega}(z, S_\nu \geq S_{\nu,\text{inf}}) = \int_{S_{\nu,\text{inf}}}^\infty \frac{d^3N}{dS'_\nu dz d\Omega} dS'_\nu. \quad (3.31)$$

The contribution of a source population to the extragalactic background at the frequency ν is

$$I_\nu = \int_0^\infty \frac{d^2 N}{dS_\nu d\Omega} S_\nu dS_\nu. \quad (3.32)$$

Interesting constraints on the halo masses of proto-spheroidal galaxies come from the auto- and cross-correlation functions of intensity fluctuations. A key quantity in this respect is the flux function, $d^2 S_\nu / dz d\Omega$, i.e., the redshift distribution of the cumulative flux density of sources below the detection limit $S_{\nu, \text{lim}}$

$$\frac{d^2 S_\nu}{dz d\Omega} = \int_0^{S_{\nu, \text{lim}}} \frac{d^3 N}{dS'_\nu dz d\Omega} S'_\nu dS'_\nu. \quad (3.33)$$

3.3.2 Galaxy-galaxy lensing

The steepness of the (sub-)millimeter counts of proto-spheroidal galaxies and their substantial redshifts imply that their counts are strongly affected by the magnification bias due to gravitational lensing (Blain 1996; Perrotta et al. 2002, 2003; Negrello et al. 2007):

$$\frac{d^3 N_{\text{lensed}}}{dS_\nu dz d\Omega}(S_\nu, z) = \int_\mu d\mu \frac{d^3 N}{dS_\nu dz d\Omega} \left(\frac{S_\nu}{\mu}, z \right) \frac{dP}{d\mu}(\mu|z), \quad (3.34)$$

where $dP/d\mu$ is the amplification distribution that describes the probability for a source at redshift z to be amplified by factor μ . Here we have approximated to unity the factor $1/\langle \mu \rangle$ that would have appeared on the right-hand side, as appropriate for large-area surveys (see Jain & Lima 2011). The amplification distribution stems from the lens model and cross section as in the following.

Mass density profile of lens

We focus here on galaxy-scale lensing, i.e., on those lensing events where the deflector is a single/isolated early-type galaxy and we assume that the lens galaxy at redshift z_ℓ is associated with a dark matter (DM) halo of mass M_H in the range $10^{11.4} - 10^{13.5} M_\odot$ virialized at redshift $z_{\ell, \text{vir}} \gtrsim 1.5$.

The total mass distribution of the lens galaxy is the sum of two components, made of a stellar component plus a DM halo: $\rho(r) = \rho_H(r) + \rho_\star(r)$. The standard NFW profile, i.e., Equation (2.53), is adopted for the DM halo with the concentration c depending on halo mass and redshift as (Prada et al. 2012) $c \approx 5 \left(\frac{M_H}{10^{13} M_\odot} \right)^{-0.074} \left(\frac{1+z_\ell}{1.7} \right)^{-1}$. For the stellar component we adopt the three-dimensional Sérsic profile (Prugniel & Simien 1997)

$$\rho_\star(r) = \frac{M_\star}{4\pi R_e^3} \frac{b_n^{2n}}{n\Gamma(2n)} \left(\frac{r}{R_e} \right)^{-\alpha_n} e^{-b_n(r/R_e)^{1/n}}, \quad (3.35)$$

where R_e is the effective radius, n is the Sérsic index, $b_n \equiv 2n - 1/3 + 0.009876/n$, and $\alpha_n \equiv 1 - 1.188/2n + 0.22/4n^2$.

The DM to baryon ratio M_H/M_\star in early-type galaxies is generally in the range $10 - 70$. In fact, this quantity can be roughly bounded from below by the cosmological DM to baryon mass ratio (see Komatsu

et al. 2011) that takes on values around 6, and from above by the DM to stellar mass ratio that statistical arguments (see Shankar et al. 2006; Lagattuta et al. 2010; Moster et al. 2010) estimate to be around 70. We take $M_{\mathrm{H}}/M_{\star} = 30$ as our fiducial value. The effective radius R_e is related to the stellar mass by (Shen et al. 2003; Hyde & Bernardi 2009)

$$R_e \approx 1.28 \left(\frac{M_{\star}}{10^{10} M_{\odot}} \right)^{0.55} \text{kpc}, \quad (3.36)$$

found to hold (with a $\approx 30\%$ scatter) for $z_{\ell} \lesssim 1$. Values of the Sérsic index for massive early-type galaxies are in the range $n \approx 3 - 10$, with a tendency for more massive systems to feature higher values (e.g., Kormendy et al. 2009). Early-type galaxies with $n = 2$ generally are either dwarf spheroidals or contain a substantial disk component and do not obey Equation (3.36). We will consider a fiducial value $n = 4$, corresponding to the classical de Vaucouleurs (1948) profile.

The classic singular isothermal sphere (SIS) density profile is

$$\rho_{\mathrm{SIS}}(r) = \frac{\sigma_{\mathrm{SIS}}^2}{2\pi G} \frac{1}{r^2} = \frac{M_{\mathrm{H}}}{4\pi R_{\mathrm{H}}^3} \left(\frac{r}{R_{\mathrm{H}}} \right)^{-2}, \quad (3.37)$$

where σ_{SIS} is the one-dimensional velocity dispersion of the overall mass. The second equality follows from the commonly used assumption $\sigma_{\mathrm{SIS}} \approx V_{\mathrm{H}}/\sqrt{2}$, in terms of the halo circular velocity $V_{\mathrm{H}}^2 = G M_{\mathrm{H}}/R_{\mathrm{H}}$ ($R_{\mathrm{H}} = R_{\mathrm{vir}}$ as Equation (2.50)).

The surface density writes

$$\Sigma(s) = \int dr \frac{r}{\sqrt{r^2 - s^2}} \rho(r), \quad (3.38)$$

where s being the radial coordinate projected on the plane of the sky. It is important to remember that the surface density becomes effective for *strong* lensing when it exceeds the critical threshold

$$\Sigma_c = \frac{c^2}{4\pi G} \frac{(1 + z_{\ell}) D_s}{D_{\ell} D_{\ell s}} \quad (3.39)$$

corresponding to a convergence $\kappa = 1$ for a thin lens. Here D_s , D_{ℓ} , and $D_{\ell s} = D_s - D_{\ell}$ are the *comoving* angular distances (also called proper motion distances; see Kochanek 2006) from the source at z_s to the observer at $z = 0$, from the lens at z_{ℓ} to the observer at $z = 0$, and from the source at z_s to the lens at z_{ℓ} , respectively. In a flat Universe the comoving angular distances are defined as $D_{ij} \equiv (c/H_0) \int_{z_i}^{z_j} dz [\Omega_{\mathrm{m},0} (1+z)^3 + 1 - \Omega_{\mathrm{m},0}]^{-1/2}$.

In the radial range $-2.5 \lesssim \log(s/R_{\mathrm{H}}) \lesssim -1$, which generally contributes most to the gravitational deflection, the combination of the stellar and DM components to the total surface density closely mimics a power law

$$\Sigma(s) = \Sigma_0 \left(\frac{s}{s_0} \right)^{-\eta}. \quad (3.40)$$

At fixed halo mass, M_{H} , both the normalization Σ_0 at the reference radius $s_0 \approx 10^{-2} R_{\mathrm{H}}$, and the power-law index $\eta \approx 0.8 - 0.9$ are only weakly dependent on the parameters of the mass distribution. For the SIS density profile, $\eta = 1$.

Lens equation

Considering circular lens and point-like source, the relation between the position of the source, β , and of its (possibly multiple) lensed image(s), θ , relative to the observer is described by the lens equation

$$\beta = \theta - \frac{\theta}{|\theta|} \alpha(|\theta|). \quad (3.41)$$

Here β and θ are the angles formed by the source and by its images with the optical axis, i.e., with the imaginary line connecting the observer and the center of the lens mass distribution. The light rays coming from a distant, point-like source are deflected by an angle

$$\alpha(\theta|z_\ell, z_s) = \frac{2}{\theta} \int_0^\theta d\vartheta \vartheta \frac{\Sigma(s)}{\Sigma_c} = \frac{4G M(< \xi)}{c^2 \xi} \frac{D_{\ell s}}{D_s}, \quad (3.42)$$

where $s = \vartheta D_\ell / (1 + z_\ell)$ and $M(< \xi) \equiv 2\pi \int_0^\xi ds s \Sigma(s)$ is the mass within the projected radius $\xi = \theta D_\ell / (1 + z_\ell)$. Solving the lens equation means finding all the positions θ of the images for a given source position β .

The amplification of the images can be computed as:

$$\mu = \frac{1}{\lambda_+ \lambda_-} \text{ with } \lambda_+ \equiv 1 - \frac{d\alpha}{d\theta} \text{ and } \lambda_- \equiv 1 - \frac{\alpha}{\theta}. \quad (3.43)$$

If either of the two quantities λ_\pm vanishes, the magnification formally diverges. Thus the condition $\lambda_\pm = 0$ defines *critical* curves in the lens plane and corresponding *caustics* in the source plane. The magnification can be positive or negative, implying that the image has positive or negative parity or, equivalently, is direct or reversed. The total magnification μ_{tot} is the sum of the absolute values of the magnifications for all the images, i.e., ignoring parity.

Under the power law approximation the deflection angle due to the lens potential within a circle of angular radius θ is

$$\bar{\alpha}(\theta) = |\bar{\theta}|^{1-\eta}, \quad (3.44)$$

where $\bar{\alpha} \equiv \alpha/\theta_E$ and $\bar{\theta} \equiv \theta/\theta_E$ normalized to the Einstein radius

$$\theta_E = \theta_0 \left(\frac{2}{2-\eta} \frac{\Sigma_0}{\Sigma_c} \right)^{1/\eta}, \quad (3.45)$$

with $\theta_0 \equiv s_0 (1 + z_\ell)/D_\ell$. The magnification of an image is

$$\mu \equiv \frac{1}{\lambda_+ \lambda_-} = \frac{1}{[1 - |\bar{\theta}|^{-\eta}] [1 - (1 - \eta) |\bar{\theta}|^{-\eta}]} \cdot \quad (3.46)$$

This equation highlights that, in addition to the critical curve corresponding to the Einstein ring ($\theta = \theta_E$), for $\eta < 1$ there is also an inner ring at

$$\theta_I = \theta_E (1 - \eta)^{1/\eta}. \quad (3.47)$$

For the SIS model ($\eta = 1$) this gives a constant deflection $\alpha = \theta_E$, and no radial critical curve. For $\bar{\beta} > 1$, i.e., outside θ_E , the lens equation yields only one image at $\bar{\theta} = 1 + \bar{\beta}$ with magnification $\mu = 1 + 1/\bar{\beta}$. On the other hand, for $\bar{\beta} \lesssim 1$, i.e., inside θ_E , it gives the two images $\bar{\theta}_{\pm} = \bar{\beta} \pm 1$, and related magnifications $\mu_{\pm} = 1 \pm 1/\bar{\beta}$; thus the total magnification amounts to $\mu = |\mu_+| + |\mu_-| = \mu_+ - \mu_- = 2/\bar{\beta}$.

For a generic $\eta < 1$ it is not possible to solve the lens equation analytically but we find that the numerical solutions can be well approximated, over the amplification range $1 \lesssim \mu \lesssim 30$ and over the range of parameters explored, by the expressions ($\bar{\beta} = \beta/\theta_E$)

$$\bar{\beta} = 1/(\mu - 1)^{\eta} \quad \text{for } \bar{\beta} \geq \bar{\beta}_I \quad (3.48)$$

$$\bar{\beta} = (2/\mu)^{\eta} \quad \text{for } \bar{\beta} \leq \bar{\beta}_I, \quad (3.49)$$

that recover the SIS solutions for $\eta = 1$. The value $\bar{\beta}_I = \beta_I/\theta_E = \eta(1 - \eta)^{-1+1/\eta}$ corresponds to the location of the inner critical curve θ_I .

Lensing cross section

Given the relation between the source position β and the total magnification of the images μ , the cumulative cross section for lensing magnification, as a function of the lens halo mass M_H and of the lens and source redshifts z_ℓ and z_s , simply writes

$$\sigma(> \mu, M_H, z_s, z_\ell) = \pi \beta^2(\mu). \quad (3.50)$$

The above results apply to the idealized case of a point-like source. What about extended sources? The problem can be solved via the ray-tracing technique (e.g., Schneider et al. 1992, p. 304), i.e., by applying the $\beta - \theta$ and $\beta - \mu$ relations to every point of the unlensed light distribution of the source. This analysis provides an useful way to estimate the maximum amplification μ_{\max} to be expected from extended sources, when their multiple images in the lens plane are not resolved (e.g., Peacock 1982). We compute the quantity μ_{\max} as the ratio between the total flux of the lensed images to that of the unlensed source over the image plane (see Perrotta et al. 2002 for details). For the spherical lenses considered here and fixed source size, μ_{\max} increases monotonically with decreasing offset between the center of the source and the optical axis, while for fixed offset, μ_{\max} depends inversely on the source size, i.e., the half stellar mass radius, R_e , of the source. The values of μ_{\max} for close alignments between the source and the lens decrease from ≈ 50 – 20 for source size $R_e \approx 1$ – 5 kpc to ≈ 10 for $R_e \approx 10$ kpc.

Lensing probability

We computed the lensing optical depth as

$$\tau(z_s | > \mu) = \int_0^{z_s} dz_\ell \int dM_H \frac{d^2N}{dM_H dV} \frac{d^2V}{dz_\ell d\Omega} \sigma(> \mu, M_H, z_s, z_\ell), \quad (3.51)$$

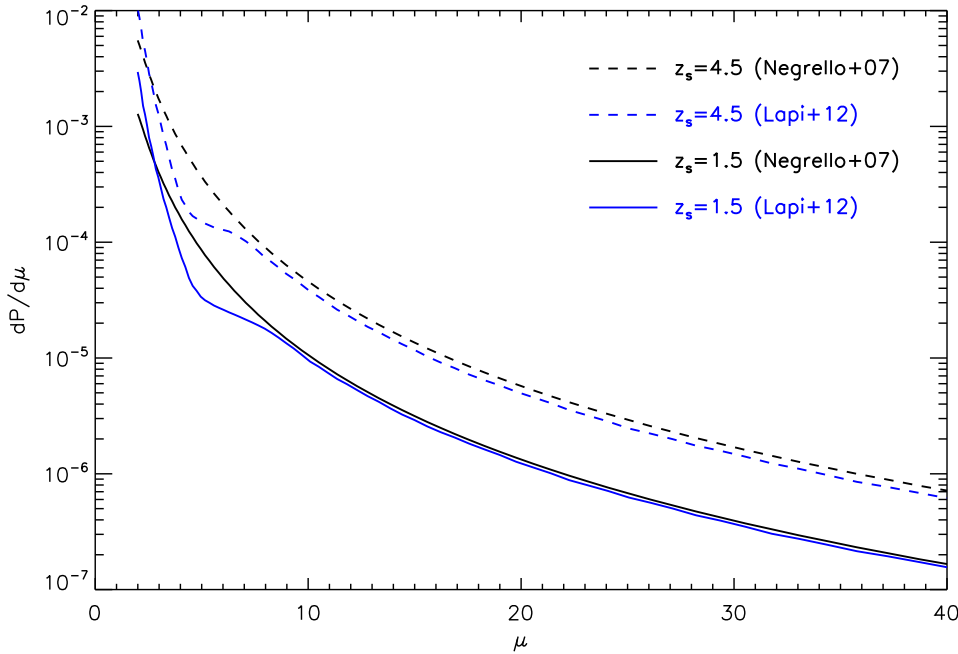


Figure 3.12: Amplification distributions yield by Negrello et al. (2007, black lines) and Lapi et al. (2012, blue lines) for $z_s = 1.5$ (solid lines) and 4.5 (dashed lines). The distributions by Lapi et al. (2012) correspond to the DM concentration $c = 4$, the Sérsic index $n = 4$, the DM to stellar mass ratio $M_H/M_\star = 30$, the lens virialization redshift $z_{\ell,\text{vir}} = 3$, and the maximum halo mass $M_H^{\max} = 10^{13.5} M_\odot$.

where $d^2V/dzd\Omega$ is the comoving volume per unit z -interval and solid angle, while $d^2N/dM_H dV$ is the galaxy halo mass function (see Shankar et al. 2006 for details), i.e., the statistics of halos containing one single galaxy. As in Lapi et al. (2006) the galaxy halo mass function is computed from the standard Sheth & Tormen (1999, 2002) halo mass function by (1) accounting for the possibility that a DM halo contains multiple subhalos each hosting a galaxy and (2) removing halos corresponding to galaxy systems rather than to individual galaxies. We deal with (2) by simply cutting off the halo mass function at a mass of $10^{13.5} M_\odot$ beyond which the probability of having multiple galaxies within a halo quickly becomes very high (e.g., Magliocchetti & Porciani 2003). As for (1), we add the subhalo mass function, following the procedure described by Vale & Ostriker (2004, 2006) and Shankar et al. (2006), and using the fit to the subhalo mass function at various redshifts provided by van den Bosch et al. (2005). However, we have checked that for the masses and redshifts relevant here ($z_{\ell,\text{v}} \gtrsim 1.5$ and $11.4 \lesssim \log(M_H/M_\odot) \lesssim 13.5$), the total (halo + subhalo) mass function differs from the halo mass function by less than 5%.

The differentiation of Equation (3.51) with respect to μ yields (minus) the differential magnification distribution $dP(\mu|z_s)/d\mu$:

$$\frac{dP}{d\mu}(\mu|z_s) = -\frac{d[\tau(z_s) > \mu]}{d\mu}, \quad (3.52)$$

illustrated in Figure 3.12 showing the amplification distributions yielded by Lapi et al. (2012) for the DM concentration $c = 4$, the Sérsic index $n = 4$, the DM to stellar mass ratio $M_H/M_\star = 30$, the lens virialization redshift $z_{\ell,\text{vir}} = 3$, and the maximum halo mass $M_H^{\max} = 10^{13.5} M_\odot$. Higher values of the concentration parameter c of the host DM halo yield higher probabilities of large amplifications (coming from the gravitational field in the inner regions of the lens) compensated by a tiny decrease of the

probability of small amplifications. The effect of varying the Sérsic index of the stellar component is small for $n \gtrsim 4$. Lower M_{H}/M_{\star} ratios, i.e., larger amounts of stellar mass, yield higher probability of large amplifications. The probability of large amplifications increases with increasing virialization redshift, $z_{\ell,\mathrm{vir}}$, of the lens, as expected since, for given mass, both the halo radius and the stellar effective radius decrease; correspondingly, the surface density increases. Increasing the maximum halo mass increases the amplification probability. As visualized in Figure 3.12, increasing z_s increases the normalization of the amplification distribution, reflecting the increase in the lensing optical depth, without substantially affecting its shape. In the same figure, the amplification distributions yielded by Negrello et al. (2007) using the Perrotta et al. (2002) lensing model are shown for comparison.

We have adopted the $dP/d\mu$ of SISSA model worked out by Lapi et al. (2012) and $\mu_{\max} = 30$ to calculate the lensed counts (see Sections 4.1.1, 4.1.3, 4.2.1 and 4.2.3). The differential counts including the effect of lensing can be computed integrating Equation (3.34) over z . The effect of lensing on counts of other source populations and on proto-spheroidal counts at shorter wavelengths is small.

3.3.3 Power spectrum of the cosmic infrared background anisotropy

All the relevant details on the formalism used are given by Xia et al. (2012), while the results are presented in Section 4.3.2. We summarize here, for clarity, the main points. Briefly, the power spectrum of the galaxy distribution was parameterized as the sum of the one-halo term that dominates on small scales and depends on the distribution of galaxies within the same halo, and the two-halo term that dominates on large scales and is related to correlations among different halos.

Halo model formalism

To compare the clustering properties expected from our model with observational data, we adopted the halo model formalism (Cooray & Sheth 2002). The two contributions (one- and two-halo) to the power spectrum write:

$$P_{\mathrm{gal}}(k, z) = P_{\mathrm{gal}}^{\mathrm{1h}}(k, z) + P_{\mathrm{gal}}^{\mathrm{2h}}(k, z), \quad (3.53)$$

$$P_{\mathrm{gal}}^{\mathrm{1h}}(k, z) = \int_M dM \cdot n_{\mathrm{ST}}(M, z) \frac{\langle N_{\mathrm{gal}}(N_{\mathrm{gal}} - 1) \rangle}{\bar{n}_{\mathrm{gal}}^2} |u_{\mathrm{gal}}(k, M, z)|^s, \quad (3.54)$$

$$P_{\mathrm{gal}}^{\mathrm{2h}}(k, z) = P^{\mathrm{lin}}(k, z) \left[\int_M dM \cdot n_{\mathrm{ST}}(M, z) \frac{\langle N_{\mathrm{gal}} \rangle}{\bar{n}_{\mathrm{gal}}} b(M, z) u_{\mathrm{gal}}(k, M, z) \right]^2, \quad (3.55)$$

where $n_{\mathrm{ST}}(M, z)$ is the halo mass function (Sheth & Tormen 1999, see Equation (2.47)), the linear matter power spectrum, $P^{\mathrm{lin}}(k, z)$, has been computed using the CAMB code² (Lewis et al. 2000, see also Equation (2.35)), and the halo bias, $b(M, z)$, is computed following Sheth & Tormen (1999, see also Mo & White 1996; Lapi et al. 2013).

Here, $u_{\mathrm{gal}}(k, M, z)$ denotes the Fourier transform of the mass density profile of the galaxy distribution within the dark matter halo, that we assume to be approximately the same as that of the dark matter,

²<http://camb.info/>

i.e., we take $u_{\text{gal}}(k, M, z) \simeq u_{\text{dm}}(k, M, z)$. The normalized Fourier transform of mean mass density profile of halos (Navarro et al. 1996, 1997, see Equation (2.53)), $u_{\text{dm}}(k, M, z)$, is

$$u_{\text{dm}}(k, M, z) = \frac{4\pi\rho_s r_s^3}{M} \left\{ \sin(kr_s) [Si([1+c]kr_s) - Si(kr_s)] + \cos(kr_s) [Ci([1+c]kr_s) - Ci(kr_s)] - \frac{\sin(cckr_s)}{(1+c)kr_s} \right\}, \quad (3.56)$$

where $r_s = R_{\text{vir}}/c$. The Si and Ci are the sine and cosine integrals, respectively:

$$Si(x) = \int_0^x \frac{\sin(t)}{t} dt, \quad Ci(x) = - \int_x^\infty \frac{\cos(t)}{t} dt. \quad (3.57)$$

Following Bullock et al. (2001), we approximate the dependence of the concentration c on M and z as

$$c(M, z) = \frac{9}{1+z} \left(\frac{M}{M_*} \right)^{-0.13}, \quad (3.58)$$

where $M_*(z)$ is the characteristic mass scale at which $\nu(M, z) = 1$; $M_*(z=0) \simeq 5 \times 10^{12} h^{-1} M_\odot$.

$\langle N_{\text{gal}} \rangle(M)$ is the mean number of galaxies in a halo of mass M , subdivided in “central” and “satellite” galaxies ($\langle N_{\text{gal}} \rangle = \langle N_{\text{cen}} \rangle + \langle N_{\text{sat}} \rangle$), while \bar{n}_{gal} is the mean number density of galaxies:

$$\bar{n}_{\text{gal}}(z) = \int_M dM \cdot n_{\text{ST}}(M, z) \cdot \langle N_{\text{gal}} \rangle(M) = \int_{\ln \nu} d \ln \nu \cdot f_{\text{ST}}(\nu) \frac{\bar{\rho}_{\text{m},0}}{M} \cdot \langle N_{\text{gal}} \rangle(M). \quad (3.59)$$

We model the Halo Occupation Distribution (HOD) using a central-satellite formalism (see, e.g., Zheng et al. 2005): this assumes that the first galaxy to be hosted by a halo lies at its center, while any remaining galaxies are classified as satellites and are distributed in proportion to the halo mass profile. Following Tinker & Wetzel (2010), the mean occupation functions of central and satellite galaxies are parameterized as:

$$\langle N_{\text{cen}} \rangle = \frac{1}{2} \left\{ 1 + \text{erf} \left[\frac{\log(M/M_{\min})}{\sigma_{\log M}} \right] \right\}, \quad (3.60)$$

$$\langle N_{\text{sat}} \rangle = \frac{1}{2} \left\{ 1 + \text{erf} \left[\frac{\log(M/2M_{\min})}{\sigma_{\log M}} \right] \right\} \left(\frac{M}{M_{\text{sat}}} \right)^{\alpha_{\text{sat}}}, \quad (3.61)$$

where M_{\min} , α_{sat} , M_{sat} , and $\sigma_{\log M}$ are free parameters assumed to be redshift independent. In this formalism halos below M_{\min} do not contain galaxies while halos above this threshold contain a central galaxy plus a number of satellite galaxies with a power-law mass function with slope α_{sat} . As for the halo model, we have considered two distinct populations, i.e., proto-spheroidal galaxies and late-type galaxies, both quiescent and starbursting. Taking into account the constraints on clustering of late-type galaxies coming from *IRAS* data (Hawkins et al. 2001), we find that the contribution of these sources is always sub-dominant and, correspondingly, their halo model parameters are very poorly constrained. Moreover the values of M_{sat} and $\sigma_{\log M}$ are poorly constrained also for proto-spheroidal galaxies (Planck Collaboration et al. 2011). We have therefore fixed $M_{\text{sat}} = 20M_{\min}$ and $\sigma_{\log M} = 0.6$ (within the ranges found by Tinker & Wetzel (2010) from clustering studies of optical galaxies). We are then left with only two free parameters, i.e., M_{\min} and α_{sat} , for each population.

In the one-halo term, i.e., Equation (3.54), we set $s = 2$, in analogy with the corresponding term for

the dark matter power spectrum, if $\langle N_{\text{gal}}(N_{\text{gal}} - 1) \rangle > 1$. Otherwise we set $s = 1$ since if the halo contains only one galaxy, it will sit at the center. Taking into account that $\langle N_{\text{gal}}(N_{\text{gal}} - 1) \rangle \simeq 2\langle N_{\text{cen}} \rangle \langle N_{\text{sat}} \rangle + \langle N_{\text{sat}} \rangle^2$ and that only the galaxies that are not at the center get factors of $u_{\text{gal}}(k, M) \simeq u_{\text{dm}}(k, M)$, we have

$$P_{\text{gal}}^{1h}(k, z) \simeq \frac{1}{\bar{n}_{\text{gal}}^2} \int_M dM \cdot n_{\text{ST}}(M, z) \left[2\langle N_{\text{cen}} \rangle \langle N_{\text{sat}} \rangle u_{\text{dm}}(k, M, z) + \langle N_{\text{sat}} \rangle^2 u_{\text{dm}}^2(k, M, z) \right]. \quad (3.62)$$

We also define the effective large-scale bias, $b_{\text{eff}}(z)$, as

$$b_{\text{eff}}(z) = \int_M dM \cdot n_{\text{ST}}(M, z) \frac{\langle N_{\text{gal}} \rangle}{\bar{n}_{\text{gal}}} b(M, z), \quad (3.63)$$

and the effective mass of the halo, M_{eff} ,

$$M_{\text{eff}}(z) = \int_M dM \cdot n_{\text{ST}}(M, z) \frac{\langle N_{\text{gal}} \rangle}{\bar{n}_{\text{gal}}} M. \quad (3.64)$$

Angular power spectrum

The angular power spectrum $P(k_\theta)$ of intensity fluctuations due to clustering of sources fainter than some flux density limit $S_{\nu, \text{lim}}$ is a projection of the spatial power spectrum of such sources at different redshifts z , $P_{\text{gal}}(k, z)$. In the Limber approximation, valid if the angular scale is not too large (i.e., $2\pi k_\theta \geq 10$ with k_θ ³ in units of rad⁻¹), the relation between $P_{\text{gal}}(k, z)$ and $P(k_\theta)$ is:

$$P^{\nu_1 \times \nu_2}(k_\theta) = \int_{z_{\min}}^{z_{\max}} dz P_{\text{gal}} \left[k = \frac{2\pi k_\theta + 1/2}{d_C(z)}, z \right] \left(\frac{d^2 S_{\nu_1}}{dz d\Omega} \cdot \frac{d^2 S_{\nu_2}}{dz d\Omega} \right) \frac{dz d\Omega}{d^2 V_C}, \quad (3.65)$$

where $d^2 S_\nu / dz d\Omega$ is the redshift distribution of the cumulative flux of sources with $S_\nu \leq S_{\nu, \text{lim}}$ (see Equation (3.33)), $d_C(z)$ is the comoving radial distance (see Equation (2.4)), and $d^2 V_C / dz d\Omega$ is the comoving volume (see Equation 2.6)).

Poisson fluctuations add a white noise contribution to the power spectrum of fluctuations

$$P_{\text{shot}}(\nu) = \int_0^{S_{\nu, \text{lim}}} \frac{d^2 N}{dS_\nu d\Omega} S_\nu^2 dS_\nu. \quad (3.66)$$

The cross-wavelength correlations are defined by (Equation (14) of Viero et al. 2013)

$$C_{A \times B}(k_\theta) = \frac{P_{k_\theta}^{A \times B}}{\sqrt{P_{k_\theta}^A \cdot P_{k_\theta}^B}}. \quad (3.67)$$

³Conversion among multipole ℓ , angle θ , and wave number k_θ : $\ell = \frac{180^\circ}{\theta} = 2\pi \frac{k_\theta}{\text{rad}^{-1}} = 21600 \frac{k_\theta}{\text{arcmin}^{-1}}$.

Chapter 4

Obscured star formation and black hole growth

The “hybrid” model described in the previous chapter deals with the dust obscured cosmic evolution of galaxies and AGNs, most directly investigated at mid-IR to millimeter wavelengths where the light absorbed by dust is re-emitted. In this chapter we compare its predictions with multi-wavelengths estimates of the luminosity functions (LFs) at different redshifts and of redshift distributions (Section 4.1), with number counts (Section 4.2) and with the cosmic infrared background (CIB; Section 4.3). The CIB anisotropy due to the clustering of dusty galaxies is analyzed in Section 4.3.2. A selection of these results were presented in [Cai et al. \(2013\)](#).

4.1 Luminosity functions and redshift distributions

The most direct predictions of the *physical model* for proto-spheroidal galaxies are the redshift-dependent SFRs and accretion rates onto the supermassive black holes as a function of halo mass. During the dust enshrouded evolutionary phase essentially all the luminosity produced by young stars is reprocessed by dust so that the SFRs can be immediately translated into the IR (8–1000 μm) LFs of galaxies. As mentioned in Section 3.1, according to our model, the transition from the dust obscured to the passive evolution phase is almost instantaneous and we neglect the contribution of passive galaxies to the IR LFs. In turn, the accretion rates translate into bolometric luminosities of AGNs given the mass-to-light conversion efficiency for which we adopt the standard value $\epsilon = 0.1$. The SEDs then allow us to compute the galaxy and AGN LFs at any wavelength (see Section 3.1.4).

In contrast, the *phenomenological model* for late-type/starburst galaxies yields directly the redshift-dependent IR LFs and that for reactivated AGNs yields the 12 μm LFs. Again these can be translated to any wavelength using the SEDs described in Section 3.2.2.

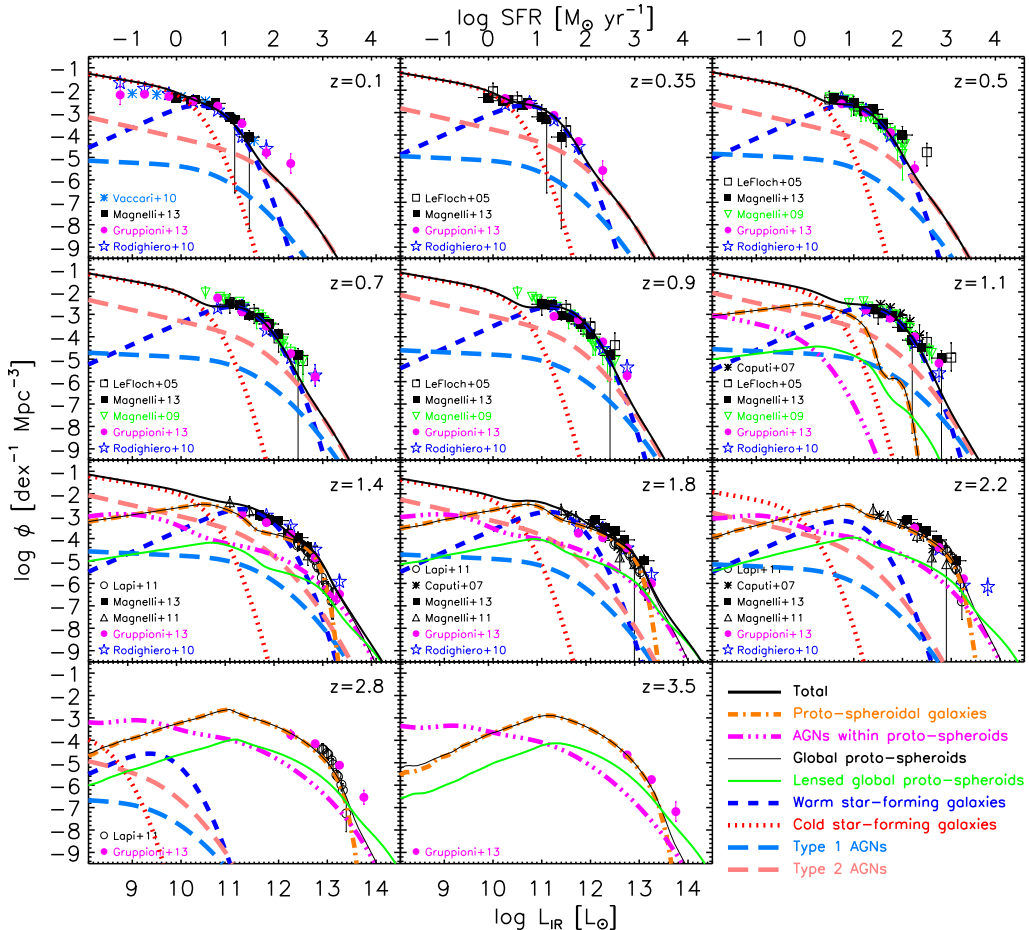


Figure 4.1: Comparison between model and observational determinations of the IR (8–1000 μm) luminosity functions at several redshifts. At $z > 1.0$ we have contributions from proto-spheroidal galaxies (dot-dashed orange lines) and from the associated AGNs (both obscured and unobscured; triple-dot-dashed magenta lines). The thin solid black lines (that are generally superimposed to the dot-dashed orange lines) are the combination of the two components, whose lensed contribution are presented as the green lines detailed in Section 4.1.4. These contributions fade at lower redshifts and essentially disappear at $z < 1$. At $z \lesssim 1.5$ the dominant contributions come from “warm” (short-dashed blue lines) and “cold” (dotted red lines) star-forming galaxies. Type 2 AGNs (long-dashed pink lines) or type 3 AGNs associated with dusty proto-spheroids (triple-dot-dashed magenta lines) dominate at the highest IR luminosities, while type 1 AGNs (long-dashed light-blue lines) are always sub-dominant (in the IR). The thick solid black lines show the sum of all contributions. The upper horizontal scale gives an estimate of the SFRs corresponding to IR luminosities. These estimates are only indicative (see Section 4.1). Data points are from Le Floc'h et al. (2005), Caputi et al. (2007), Magnelli et al. (2009, 2011, 2013), Rodighiero et al. (2010), Vaccari et al. (2010), Gruppioni et al. (2010, 2013), and Lapi et al. (2011).

4.1.1 IR (8–1000 μm) luminosity functions

In Figure 4.1 the model IR LFs are compared with observational determinations at different redshifts. At $z \gtrsim 1.5$, the dominant contributions come from the stellar and AGN components of proto-spheroidal galaxies. These contributions fade at lower redshifts and essentially disappear at $z < 1$. The model implies that AGNs associated with proto-spheroidal galaxies are important only at luminosities higher than those covered by the Lapi et al. (2011) LFs which therefore have been converted to IR LFs using their galaxy SED, i.e., neglecting the AGN contribution, so that $\log(L_{\text{IR}}/L_\odot) = \log(L_{100}/L_\odot) + 0.21$ and $\log(L_{\text{IR}}/L_\odot) = \log(L_{250}/L_\odot) + 1.24$, where L_{100} or L_{250} are νL_ν at the frequencies corresponding to $\lambda = 100$ or $250 \mu\text{m}$, respectively. At $z \lesssim 1.5$ “warm” and “cold” star-forming galaxies take over, “cold” galaxies being important only at low luminosities. Type 2 AGNs (long-dashed pink lines) may dominate

at the highest IR luminosities, while type 1 AGNs (long-dashed light-blue lines) are always sub-dominant (in the IR). The scale on the top x -axis in Figure 4.1 gives the star formation rates corresponding to the IR luminosities

$$\log\left(\frac{L_{\text{IR}}}{L_{\odot}}\right) = \log\left(\frac{\text{SFR}}{M_{\odot} \text{ yr}^{-1}}\right) + 9.892, \quad (4.1)$$

and is therefore meaningful only to the extent that the AGN contribution is negligible. Moreover, the normalization constant applies to high- z proto-spheroidal galaxies whose IR luminosity comes almost entirely from star-forming regions. For more evolved galaxies, older stellar populations can contribute significantly to the dust heating (da Cunha et al. 2012); therefore L_{IR} is no longer a direct measure of the star formation rate and therefore the upper scale has to be taken as purely indicative.

At $z \lesssim 1.5$, the observed evolution of IR LFs is fully accounted for by the combined empirical evolution of late-type galaxies and associated AGNs. Positive luminosity and/or density evolution is required by the data for each low- z population. At $L_{\text{IR}} < 10^{11} L_{\odot}$ most of the infrared galaxies are identified as ‘normal’ spirals with moderate to low SFR. Their dust is heated both by young stars and by older star populations. The intensity of the interstellar radiation field is relatively low and correspondingly the dust is relatively cold (“cold” population). The higher luminosity population is dominated by ‘starburst’ galaxies, including interacting/merging systems, whose emission comes from warmer dust. Dust-enshrouded (type 2) AGNs dominate at the highest luminosities (see Sanders & Mirabel 1996).

The sub-dominance of the contribution of type 1 AGNs to the local far-IR LF follows directly from their optical LF (we have used the B -band local LF of (Hartwick & Schade 1990; see Figure 4.2) and from their mean SED (Richards et al. 2006). On the contrary, type 2 AGNs can dominate at the highest IR luminosities. The evolutions of type 1 and type 2 AGNs are mainly constrained by the g - and J -band data presented in Section 4.1.2. After having fixed the evolutions of the low- z AGNs (type 1 + type 2) and of the cold population, taking into account the chemo/spectrophotometric evolution models (Mazzei et al. 1992; Colavitti et al. 2008), we determined the evolution of the warm population by a minimum χ^2 fit of the data. Interestingly, the values of the parameter α_L , characterizing the luminosity evolution (see Table 3.2), are found to be similar for type 1 AGNs and for “warm” galaxies, implying that the triggers of both the star formation and of the AGN activity could be the same (e.g., interactions).

4.1.2 Optical and near-IR AGN luminosity functions

The comparison between the model and the observed g -band ($0.467 \mu\text{m}$) AGN LFs at several redshifts is presented in Figure 4.2, while the comparison in the J -band ($1.24 \mu\text{m}$) is shown in Figure 4.3. The conversion from monochromatic absolute AB magnitude $M_{\lambda, \text{AB}}$ to the corresponding monochromatic luminosity $\nu L_{\nu}(\lambda)$ is given by $\log(\nu L_{\nu}/[L_{\odot}]) = -0.4M_{\lambda, \text{AB}} - \log(\lambda/\text{\AA}) + 5.530$.

At $z \gtrsim 1.5$, the physical model describes the AGN evolution or black hole growth from the obscured to the unobscured QSO phase, i.e. from the long optically dim phase to the relatively short optically bright phase, co-evolving with its host proto-spheroidal galaxy. The inferred AGN LFs shown as triple-dot-dashed magenta lines in Figures 4.2 and 4.3 include both contributions. The bright end of both the g - and the J -band AGN LFs are dominated by unobscured AGNs, while the turnover points and

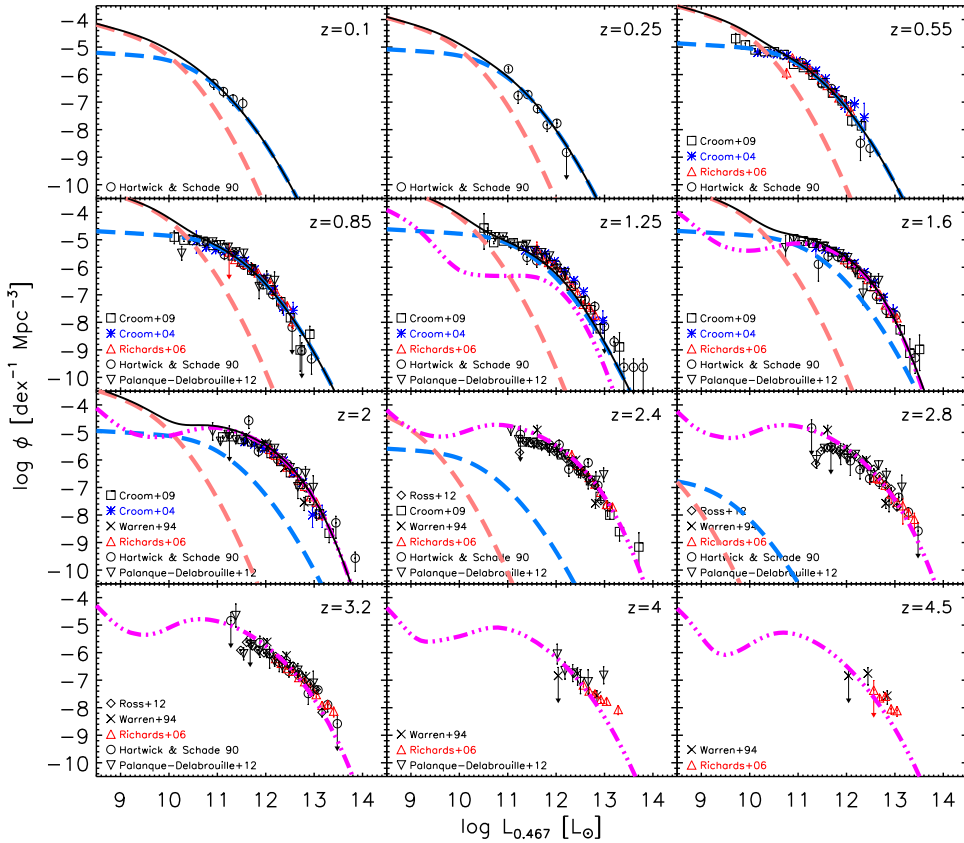


Figure 4.2: Comparison between model and observed *g*-band ($0.467\mu\text{m}$) AGN luminosity function at several redshifts. As in Figure 4.1, the long-dashed light-blue and pink lines refer to type 1 and type 2 AGNs, respectively, while the triple-dot-dashed magenta lines refer to AGNs associated with proto-spheroidal galaxies. At $z \lesssim 2$, the solid black line shows the sum of all the contributions. At higher z only proto-spheroids are considered. Data points are from Hartwick & Schade (1990; black open circles), Warren et al. (1994; black crosses), Croom et al. (2004; blue stars), Richards et al. (2006; red triangles), Croom et al. (2009; black open squares), Ross et al. (2012; black diamonds), and Palanque-Delabrouille et al. (2013; black downward triangles). The data by Hartwick & Schade (1990), given in terms of M_B in the Vega system, were converted to M_g adopting the $B - g \simeq 0.14$ color estimated by Fukugita et al. (1996) and were further corrected for the different cosmology. The UV magnitudes of Warren et al. (1994) were first converted to B magnitudes ($M_B = M_{C,1216\text{\AA}} + 1.39\alpha_\nu + 0.09$, with $\alpha_\nu = -0.5$) following Pei (1995) and then to M_g as before. The data by Ross et al. (2012) were converted from $M_i(z = 2)$ to M_g following Richards et al. (2006) with spectral index $\alpha_\nu = -0.5$. The correction for the different cosmology was also applied. Finally, the conversion from M_g to $\nu L_\nu(0.467\mu\text{m})$ is given in Section 4.1.2.

the dips at intermediate luminosities around $\sim 10^{10} L_\odot$ indicate the transition of the dominant AGN population from unobscured to obscured AGNs. Due to the larger dust extinction at shorter wavelengths, this transition is quicker and smoother in the *J*-band than in the *g*-band. A simple critical gas fraction $f_{\text{gas}} = 0.03$ (corresponding to the “visibility time” $\Delta_{\text{vis}} = 5 \times 10^7$ yr inferred from high- z AGN data by Lapi et al. 2006; see Section 3.1.2) has been adopted to set the beginning of the optical bright phase.

At $z \lesssim 1.5$ we have used the *g*-band data on the redshift dependent LF of type 1 AGNs to constrain their evolution. An extrapolation using the adopted mean SED was found to be in nice agreement with the *J*-band data at $z \gtrsim 0.8$. The extrapolations to the *J* band however exceed the observational estimates by Assef et al. (2011) at the faint end and the discrepancy increases with increasing z . Unless low-luminosity type 1 AGNs have strongly anomalous colours, this suggests that the Assef et al. (2011) sample is increasingly incomplete at low luminosity. At variance with what we saw at far-IR wavelengths, in the optical the bright end of low- z LFs is dominated by unobscured AGNs.

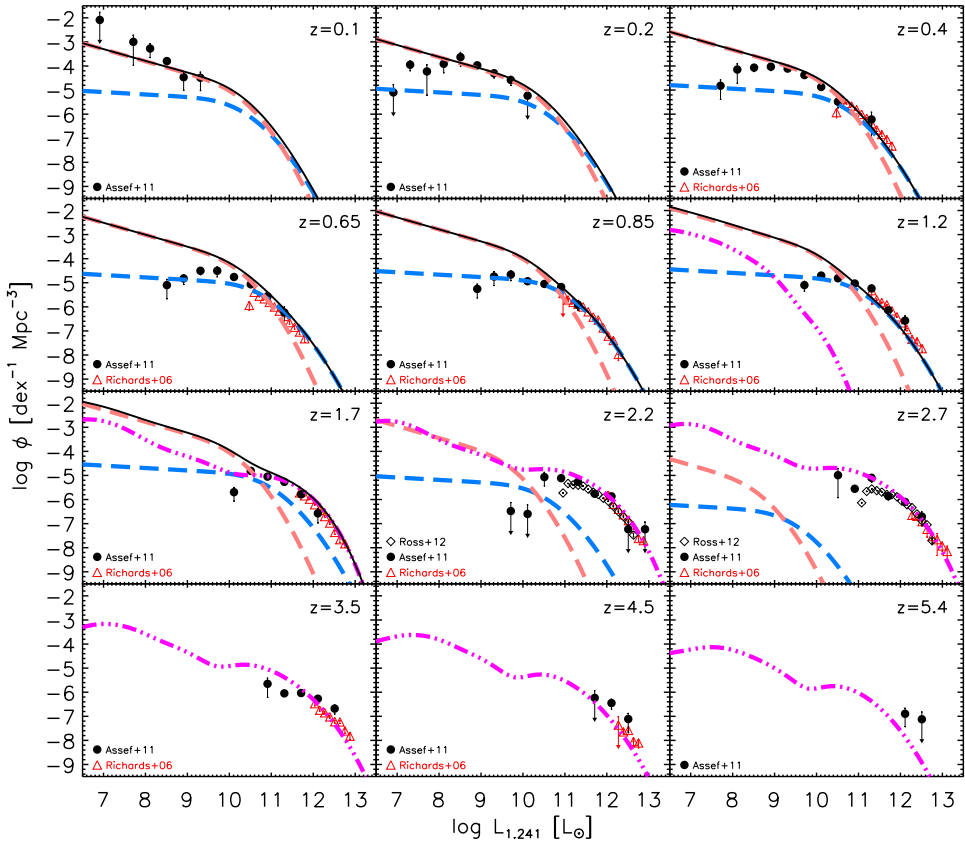


Figure 4.3: Comparison between model and observed J -band ($1.24\mu\text{m}$) AGN luminosity function at several redshifts. The lines have the same meaning as in Figure 4.2. There are clear signs of substantial incompleteness at the lowest luminosities. Data are from Richards et al. (2006; red triangles), Assef et al. (2011; black filled circles), and Ross et al. (2012; black diamonds). The data by Assef et al. (2011), given in terms of M_J in the Vega system, were converted to $\nu L_\nu(1.241\mu\text{m})$ using the relation $(L_\nu(1.241\mu\text{m}) = 1623 \times 10^{-0.4M_J} \text{ Jy})$ by Rieke et al. (2008). The i -band data by Richards et al. (2006) and Ross et al. (2012) were converted to $M_{J,\text{AB}}$ assuming spectral index $\alpha_\nu = -0.5$.

The type 1/type 2 space density ratio yielded by the model increases with luminosity, consistent with observations (e.g., Burlon et al. 2011) and with the receding torus model (Lawrence 1991). In the framework of the standard unified model of AGNs, type 1 and type 2 AGNs differ only in terms of the angle which the observers' line of sight makes with the axis of a dusty torus. If the line of sight to the central region is blocked by the torus, the AGN is seen as a type 2. According to the receding torus model the opening angle of the torus (measured from the torus axis to the equatorial plane) is larger in more luminous objects, implying that obscuration is less common in more luminous AGNs. Since our model implies that type 1 AGNs (but not type 2's) are evolving in luminosity, they become increasingly dominant with increasing redshift.

4.1.3 Monochromatic luminosity functions from IR to radio wavelengths

With the assumed empirical SEDs for star-forming galaxies and associated AGNs, the monochromatic LFs of each population can be obtained from the IR bolometric LFs illustrated in Figure 4.1. The comparisons between the global (stellar plus AGN components) LFs yielded by the model and those observationally determined at several redshifts and wavelengths from $8\mu\text{m}$ to $250\mu\text{m}$ are shown in Figures 4.4–4.12.

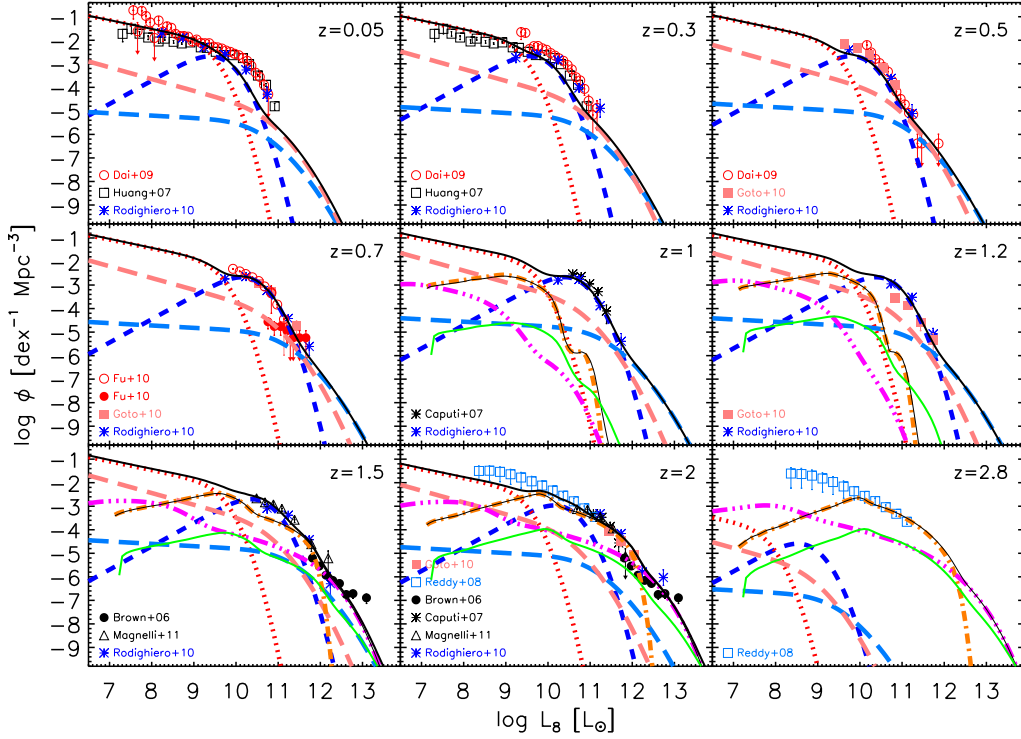


Figure 4.4: Comparison between model and observed $8\mu\text{m}$ global (galaxies plus AGNs) luminosity function at several redshifts. The lines have the same definition as in Figure 4.1. Data are from Brown et al. (2006; QSO data), Huang et al. (2007), Caputi et al. (2007), Reddy et al. (2008), Dai et al. (2009), Rodighiero et al. (2010), Goto et al. (2010), Fu et al. (2010); red open circles for star formation and red filled circles for AGNs), and Magnelli et al. (2011).

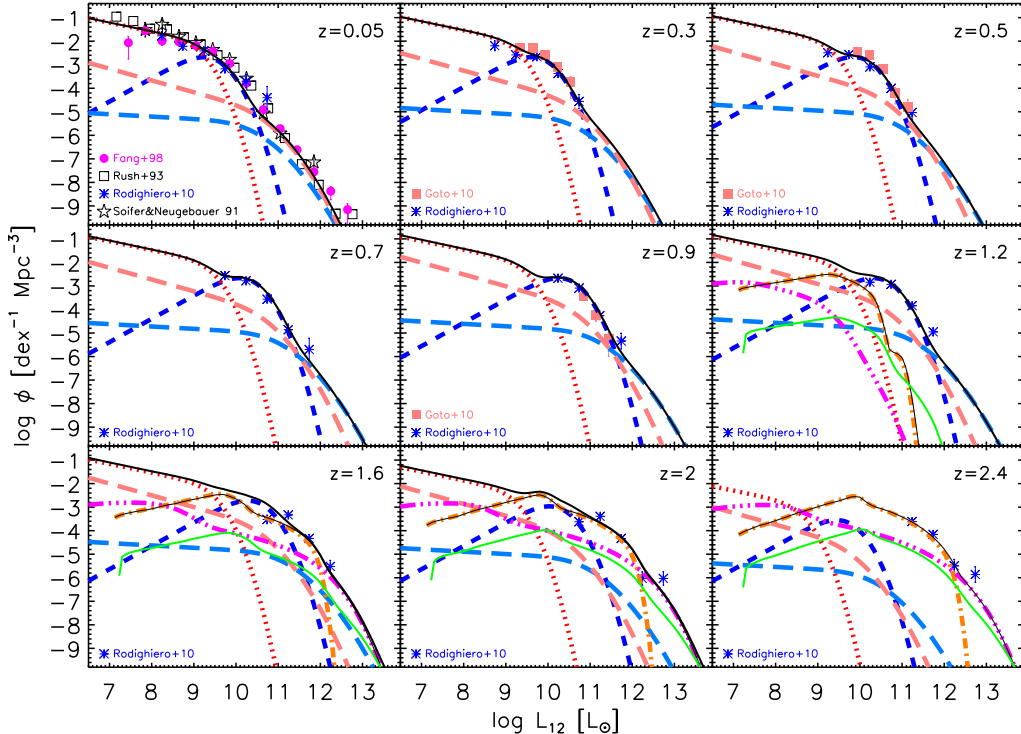


Figure 4.5: Comparison between model and observed $12\mu\text{m}$ global (galaxies plus AGNs) luminosity function at several redshifts. The lines have the same definition as in Figure 4.1. Data are from Soifer & Neugebauer (1991), Rush et al. (1993), Fang et al. (1998), Goto et al. (2010), and Rodighiero et al. (2010).

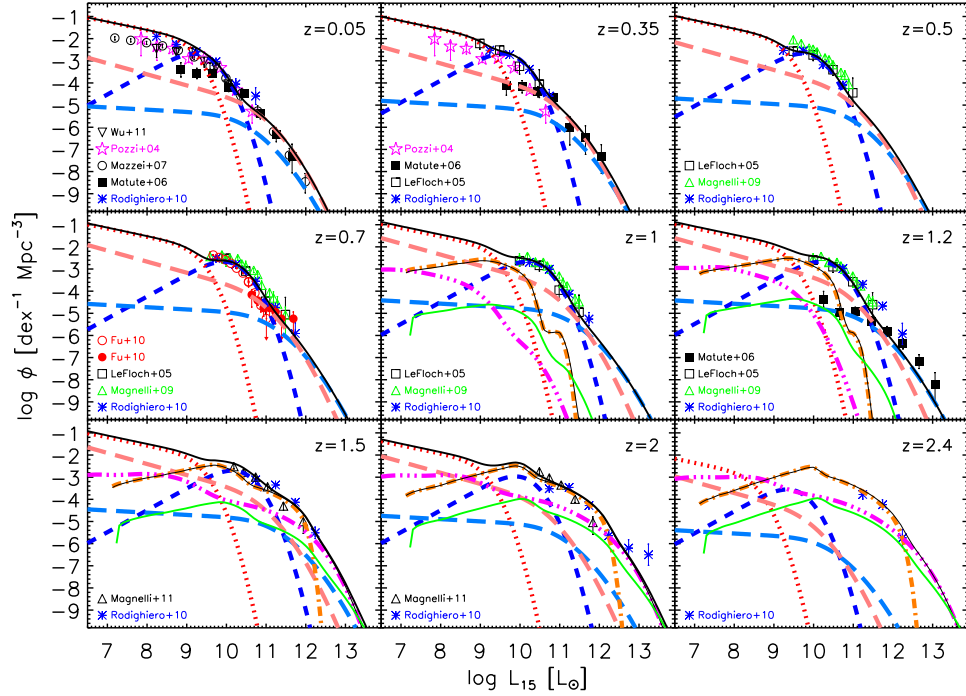


Figure 4.6: Comparison between model and observed $15\mu\text{m}$ global (galaxies plus AGNs) luminosity function at several redshifts. Data are from [Pozzi et al. \(2004\)](#), [Le Floc'h et al. \(2005\)](#), [Mature et al. \(2006\)](#), [Mazzei et al. \(2007\)](#), [Magnelli et al. \(2009, 2011\)](#), [Rodighiero et al. \(2010\)](#), [Fu et al. \(2010\)](#); red open circles for star formation and red filled circles for AGNs, and [Wu et al. \(2011\)](#). The black filled squares in the panels at $z = 0.05$ and 0.35 show observational estimates of the luminosity function of type 2 AGNs only, while the red filled circles at $z = 0.7$ and the black filled squares at $z = 1.2$ refer to AGN of both types and at $z = 1.2$ refer to type 1 only. The lines have the same definition as in Figure 4.1.

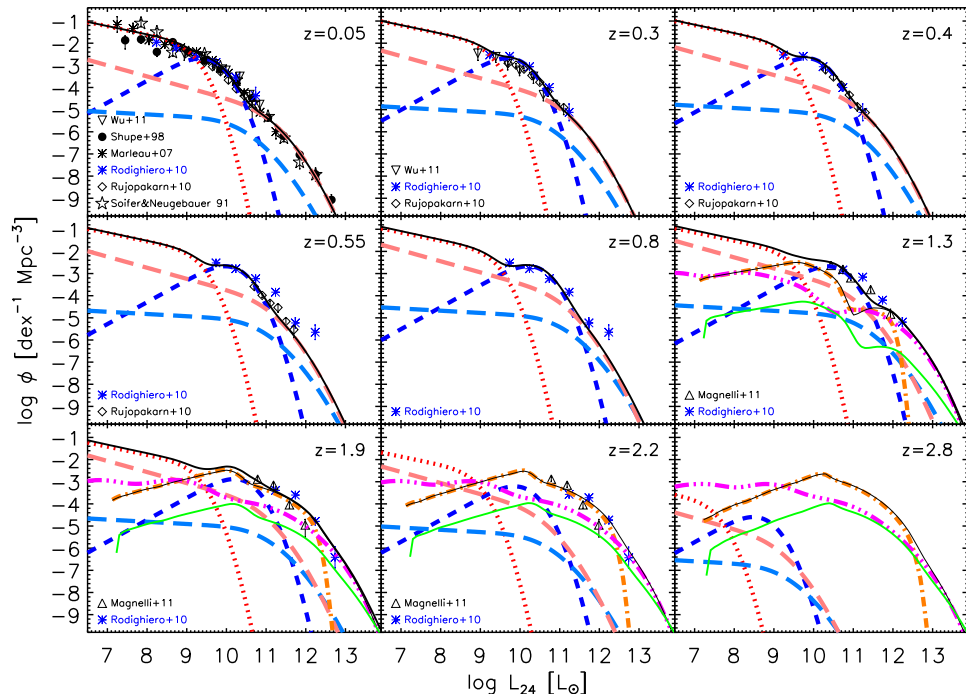


Figure 4.7: Comparison between model and observed $24\mu\text{m}$ global (galaxies plus AGNs) luminosity function at several redshifts. The lines have the same definition as in Figure 4.1. Data are from [Soifer & Neugebauer \(1991\)](#), [Shupe et al. \(1998\)](#), [Marleau et al. \(2007\)](#), [Rodighiero et al. \(2010\)](#), [Rujopakarn et al. \(2010\)](#), [Magnelli et al. \(2011\)](#), and [Wu et al. \(2011\)](#).

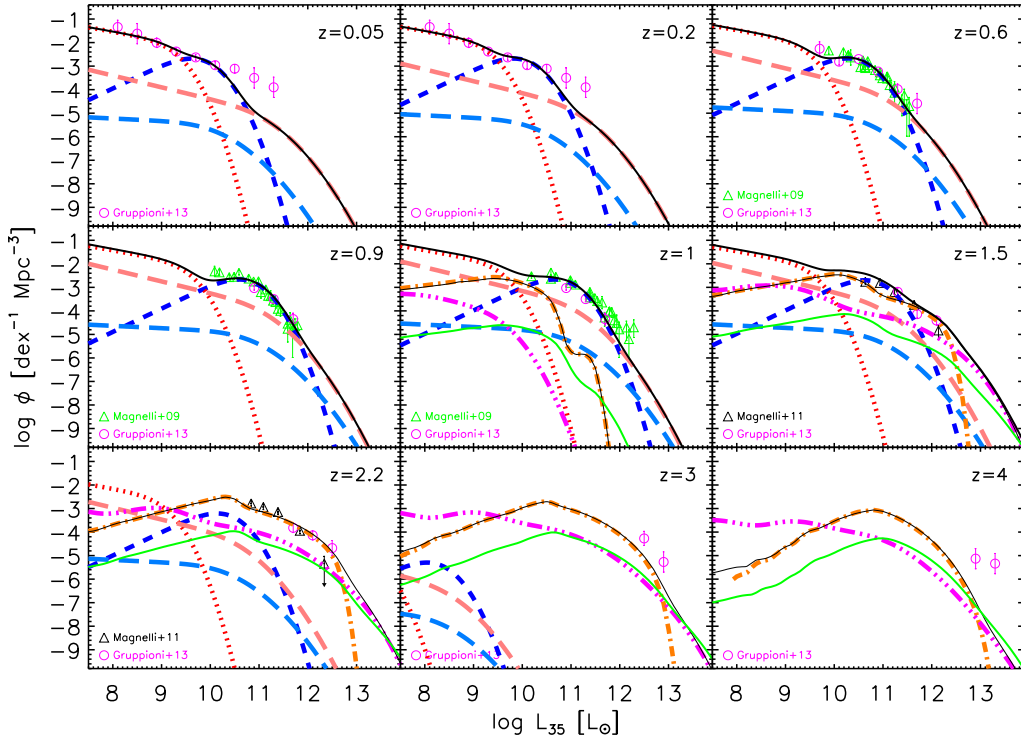


Figure 4.8: Comparison between model and observed 35 μm global (galaxies plus AGNs) luminosity function at several redshifts. The lines have the same definition as in Figure 4.1. Data are from Magnelli et al. (2009, 2011) and Gruppioni et al. (2013).

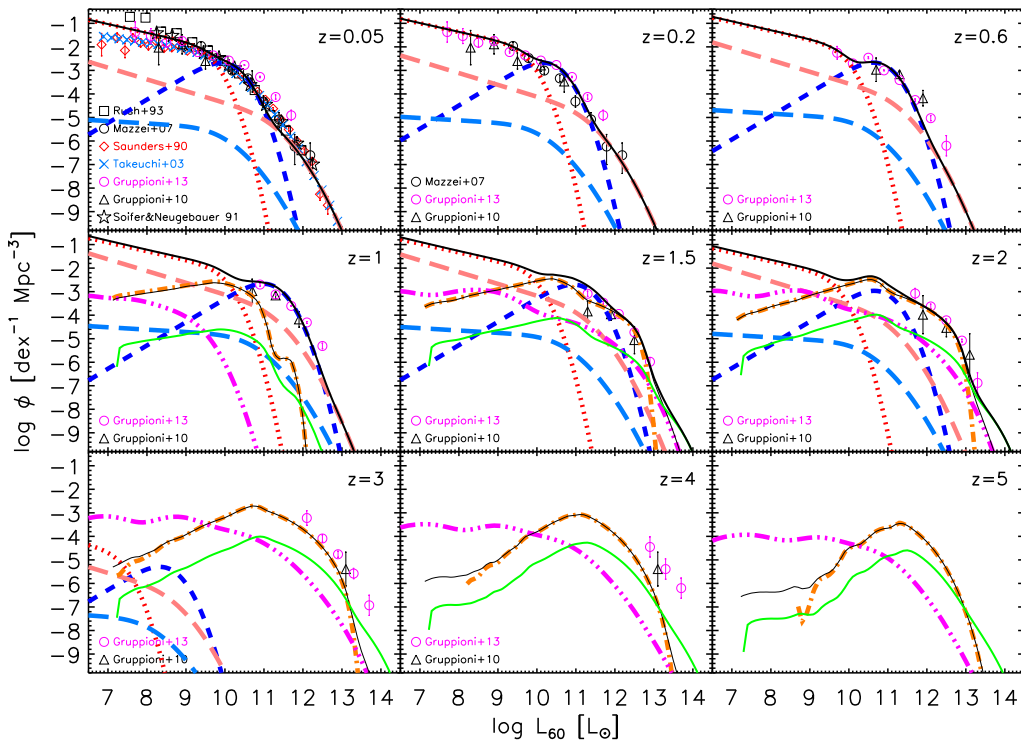


Figure 4.9: Comparison between model and observed 60 μm global (galaxies plus AGNs) luminosity function at several redshifts. The lines have the same definition as in Figure 4.1. Data are from Saunders et al. (1990), Soifer & Neugebauer (1991), Rush et al. (1993), Takeuchi et al. (2003), Mazzei et al. (2007), and Gruppioni et al. (2010, 2013).

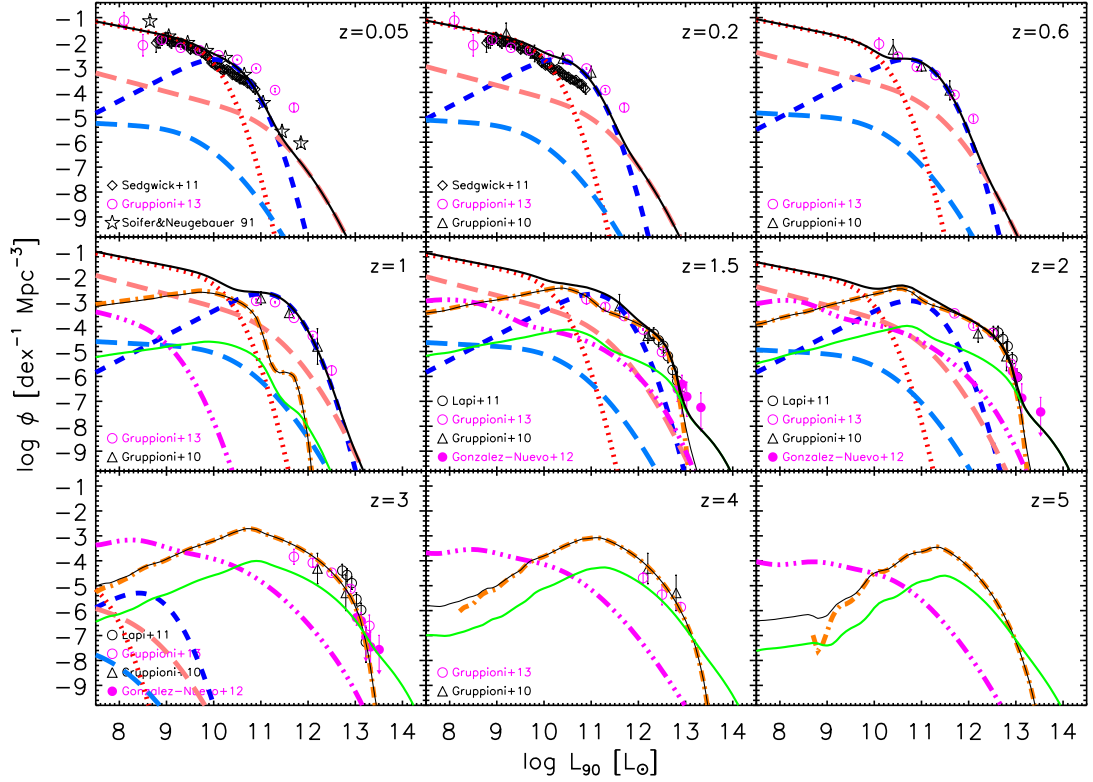


Figure 4.10: Comparison between model and observed 90 μm global (galaxies plus AGNs) luminosity function at several redshifts. The lines have the same definition as in Figure 4.1. Data are from Soifer & Neugebauer (1991; 100 μm), Gruppioni et al. (2010), Sedgwick et al. (2011), Lapi et al. (2011; 100 μm), González-Nuevo et al. (2012; 100 μm ; based on the parent sample of strongly lensed candidates, see Section 4.1.4), and Gruppioni et al. (2010, 2013).

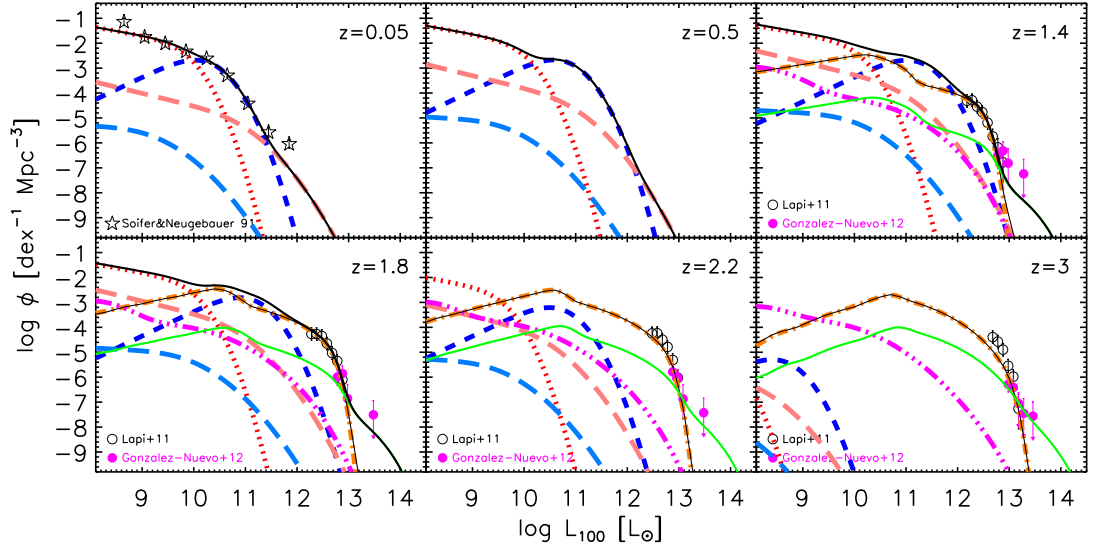


Figure 4.11: Comparison between model and observed 100 μm global (galaxies plus AGNs) luminosity function at several redshifts. The lines have the same definition as in Figure 4.1. Data are from Soifer & Neugebauer (1991), Lapi et al. (2011), and González-Nuevo et al. (2012; based on the parent sample of strongly lensed candidates, see Section 4.1.4).

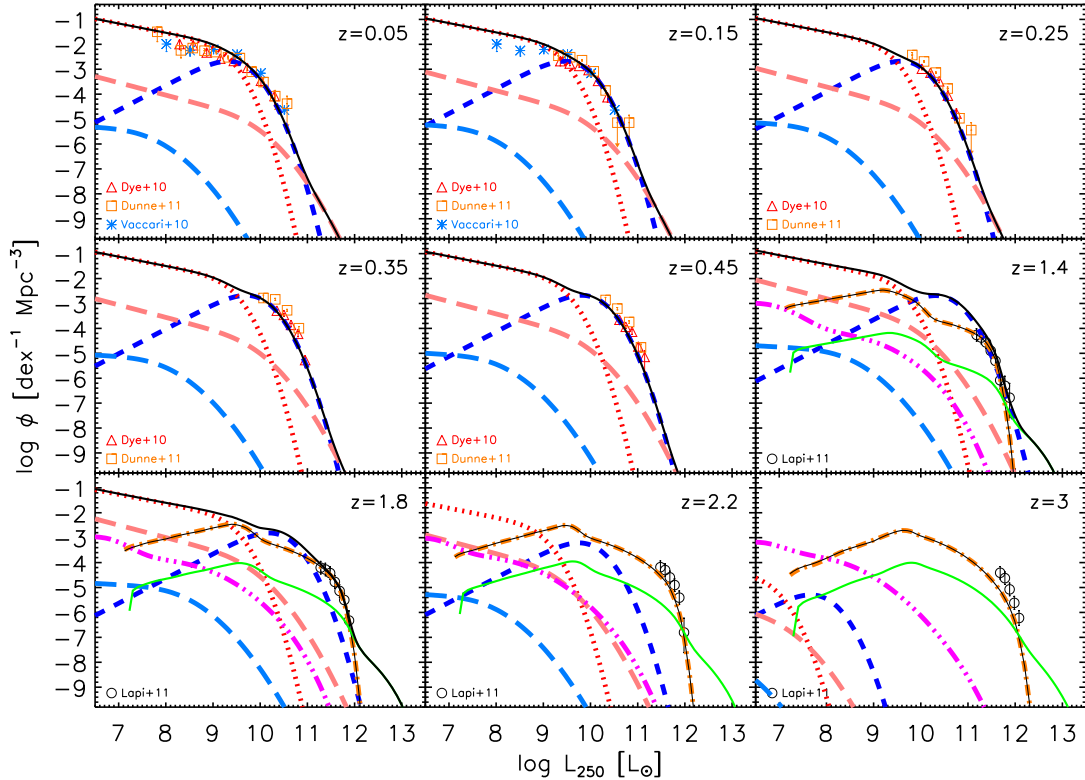


Figure 4.12: Comparison between model and observed 250 μm global (galaxies plus AGNs) luminosity function at several redshifts. The lines have the same definition as in Figure 4.1. Data are from Dye et al. (2010), Vaccari et al. (2010), Dunne et al. (2011), and Lapi et al. (2011).

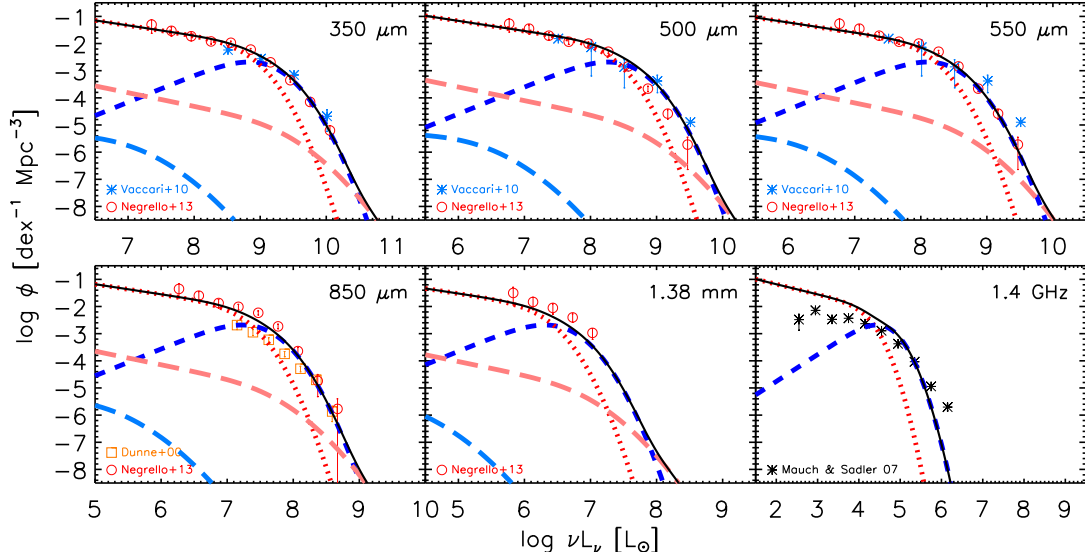


Figure 4.13: Local luminosity functions of star-forming galaxies at (sub-)millimeter wavelengths and at 1.4 GHz. As in the other figures the short-dashed blue lines refer to “warm” galaxies, the dotted red lines to “cold” galaxies, the long-dashed pink lines to type 2 AGNs, and the long-dashed light-blue lines to type 1 AGNs. Data are from Dunne et al. (2000), Mauch & Sadler (2007), Vaccari et al. (2010; 350 and 500 μm), and Negrello et al. (2013; 350, 550, 850, and 1380 μm).

The global agreement between model predictions and observational estimations suggests that the assumed empirical SED is reasonably typical for each population over the redshift range of interest, even though we have made the simplifying assumption that it is luminosity-independent. The adopted SEDs, based on a combination of those by Dale & Helou (2002) and Smith et al. (2012), for “warm” and “cold” star-forming galaxies have been discussed in Section 3.2.2.

However, the agreement between the model and the data is not equally good at all wavelengths. At $8 \mu\text{m}$ and $z \lesssim 0.5$, the model under-predicts the observed LFs and the disagreement becomes more prominent with decreasing redshift. At longer wavelengths, however, the model fits the data quite well also at these redshifts (cf. Figure 4.5–Figure 4.7 for $12\text{--}24 \mu\text{m}$). Since the $8 \mu\text{m}$ emission is more sensitive to the delicate PAH contribution, the data could imply that lower redshift galaxies, whose IR luminosities are typically $L_{\text{IR}} < 10^{11} L_{\odot}$, have a relatively stronger $8 \mu\text{m}$ emission than typical star-forming galaxies with $L_{\text{IR}} > 10^{11} L_{\odot}$ at higher redshift (cf. Figure 4.1).

At $8 \mu\text{m}$ and $z \gtrsim 2$, the decline at low luminosities is an artifact due to the adopted lower limit to the proto-spheroid halo masses (see Section 3.1.4). However an extension of the model to lower luminosities is beyond the scope of the present work.

At $35 \mu\text{m}$ and $z \lesssim 0.1$, the data seems to suggest that the model underestimates the number density of bright sources. However the difference can be due to the fact that the model refers precisely to this redshift while the data refer to a large redshift bin ($0 \leq z \leq 0.4$; see the improved comparison at $z = 0.2$). At 35 and $60 \mu\text{m}$, the high- z data by Gruppioni et al. (2013) are higher than the model predictions, while agreement is found at $90 \mu\text{m}$. Although a warmer SED at higher redshift would reduce this discrepancy, more reliable data will be required to assess this possibility since currently only few sources at $z > 2$ have spectroscopic redshifts (Berta et al. 2011).

The top-left panel in Figures 4.4–4.12 shows the corresponding local LFs from $8 \mu\text{m}$ to $250 \mu\text{m}$, while local LFs at some other (sub-)millimeter wavelengths from $350 \mu\text{m}$ to $1380 \mu\text{m}$ and at 1.4 GHz are shown in Figure 4.13. To calculate the 1.4 GHz luminosities, the SEDs of “warm” and “cold” populations have been tentatively extended to radio wavelengths assuming the well-known IR-radio correlation (Condon 1992) with the updated calibration for sources at $z \lesssim 0.5$ by Jarvis et al. (2010)

$$\frac{L_{1.4\text{GHz}}}{\text{erg s}^{-1} \text{ Hz}^{-1}} = 1.06 \times 10^{-15} \frac{L_{\text{IR}}}{\text{erg s}^{-1}}, \quad (4.2)$$

and assuming a power-law radio spectrum $L_{\nu} \propto \nu^{-\alpha}$ with $\alpha \simeq 0.7$. The resulting local 1.4 GHz LF are more or less consistent with the data except for the over-prediction at the faint end, due to the known fact (see, e.g., Massardi et al. 2010) that galaxies with $\log(L_{60}/L_{\odot}) \lesssim 9$ or $\log(L_{\text{IR}}/L_{\odot}) \lesssim 10$ are found to have radio to far-IR luminosity ratios systematically lower than those given by Equation (4.2). A possible explanation for this fact is that the IR luminosity of these faint galaxies is not entirely due to newly formed stars while the radio emission is a more direct proxy of the SFR. To extend the SED to radio wavelengths we need to add another contribution, i.e., the free-free emission, which can dominate the total emission around 100 GHz (see Figure 1 of Condon 1992). Preliminary predictions of radio counts of star-forming galaxies at radio to mm wavelengths are presented in Section 4.2.4.

4.1.4 High- z luminosity functions including strongly lensed galaxies

As stressed by Treu (2010) most of the applications of strong gravitational lensing to address major astrophysical and cosmological issues are currently limited by sample size. Substantial progress will be made only with future samples of thousands of strongly lensed systems observed by wide field optical (see, e.g., Oguri & Marshall 2010) and radio surveys (e.g., Koopmans et al. 2004). However, as predicted by Blain (1996), Perrotta et al. (2002, 2003), Negrello et al. (2007), Paciga et al. (2009), and Lima et al. (2010), among others, and demonstrated by Negrello et al. (2010), millimeter and submillimeter surveys are an especially effective route to reach this goal because the extreme steepness of number counts of unlensed high- z galaxies implies a strong magnification bias so that they are easily exceeded by those of strongly lensed galaxies at the bright end (see Figure 4.18 and Section 4.2.3 for more discussion on lensed counts). Consequently, the selection of strongly lensed galaxies (SLGs) is particularly easy for relatively shallow large area (sub-)millimeter surveys.

Negrello et al. (2010) demonstrated that, for $S_{500} \geq 100$ mJy, the surface density of high- z strongly lensed (sub-)millimeter galaxies (SMGs) plus a handful of radio sources (mostly blazars), easily identified in low-frequency radio catalogs, is comparable to that of low- z ($z \leq 0.1$) late-type galaxies, with far-IR emission above the *IRAS* detection limit and easily identified in the optical. Instead, the surface density of unlensed high- z galaxies is small at such flux density limit. The predicted (and observed) surface density of SLGs with $S_{500} \geq 100$ mJy is $\simeq 0.3$ deg 2 . A similar surface density of candidate SLGs was found by Vieira et al. (2010) at the detection limit of their 87 deg 2 survey with the South Pole Telescope (SPT) at 1.4 and 2 mm ($S_{1.4\text{mm}} \gtrsim 11$ mJy and $S_{2\text{mm}} \gtrsim 4.4$ mJy). This means that the SPT, which plans to cover some 2500 deg 2 , may yield a sample of $\simeq 750$ SLGs. The *Herschel* Astrophysical Terahertz Large Area Survey ¹ (H-ATLAS; Eales et al. 2010), the largest area survey carried out by the *Herschel Space Observatory* (Pilbratt et al. 2010), covering ~ 550 deg 2 with PACS (Poglitsch et al. 2010) and SPIRE (Griffin et al. 2010), will easily provide a sample of about 150–200 SLGs with $S_{500} \geq 100$ mJy.

Many more lensed objects may be found at fainter flux densities, but singling them out is difficult because they are mixed with high- z unlensed galaxies. In order to efficiently select these SLGs with submillimeter flux densities as faint as possible González-Nuevo et al. (2012) devised a two-step strategy allowing us to reach candidate SLG surface densities of $\sim 1.5\text{--}2$ deg 2 that would imply a total of up to ~ 1000 SLGs in the full H-ATLAS survey.

Selection of strongly lensed galaxies with $S_{500} < 100$ mJy

The selection of the parent sample appeals to the fact that SLGs inevitably dominate the highest apparent luminosity tail of the high- z LF. We have selected an initial sample of 74 objects in the H-ATLAS SDP field of $\simeq 14.4$ deg 2 based on the following criteria: $S_{350} \geq 85$ mJy, $S_{250} \geq 35$ mJy, $S_{350}/S_{250} > 0.6$, and $S_{500}/S_{350} > 0.4$. The flux limit at 250 μm is slightly larger than the 5 σ detection limit for H-ATLAS SDP galaxies (33.5 mJy). The flux density limit of 85 mJy at 350 μm is such that, based on the results by (Lapi et al. 2011), the expected ratio of lensed to unlensed high- z galaxies is of order unity; yet, due

¹<http://www.h-atlas.org>

to the steepness of the counts, the expected surface density of strongly lensed sources is substantially higher than that for $S_{500} \geq 100$ mJy. The colour criteria imply that $z \geq 1.2$ based on some representative SEDs of ultraluminous dusty galaxies (Arp 220; SMM J2135-0102 at $z = 2.3$, [Ivison et al. 2010](#); [Swinbank et al. 2010](#); H-ATLAS J142413.9+022304 at $z = 4.24$, [Cox et al. 2011](#)). After having carefully rejected intruders of various types, the parent sample contains 64 objects, listed in Table 4.1.

Exploiting the classical [Schmidt \(1968\)](#) $1/V_{\max}$ estimator, together with redshift estimates and K -corrections computed with the reference SED (the one of SMM J2135-0102), we used the parent sample to estimate the bright end of the $100 \mu\text{m}$ LFs in the same redshift bins as in [Lapi et al. \(2011\)](#). The results are shown in Figures 4.10 and 4.11. The estimates join smoothly with those of [Lapi et al. \(2011\)](#) at the lowest apparent (i.e., uncorrected for the effect of gravitational lensing) luminosities but show an indication of a flattening at the highest apparent luminosities. This flattening is expected as the effect of strong lensing, in analogy to what happens with the source counts. It was not present in [Lapi et al. \(2011\)](#) because all objects with SDSS counterparts were removed from their sample. SLGs unavoidably dominate the highest apparent luminosity (or flux density) tail of the observed LFs (or number counts), where the space (or surface) density of unlensed galaxies drops very rapidly. The flattening induced by these objects reflects the flatter slope of the sub- L_* LF (or the flattening of faint counts). The five SLGs identified by [Negrello et al. \(2010\)](#) fall on this part of the LF. Although there is a clear analogy between the behavior of the LFs and that of the source counts, the latter are integrated quantities. As a consequence, even in the case of modestly accurate photometric redshifts, the LFs in redshift bins are a much stronger discriminator of SLGs than the number counts in flux density bins. This is the basis of our approach for extending the selection of candidate SLGs to fainter flux densities.

In Figures 4.10 and 4.11 the estimated LFs including strongly lensed galaxies are compared with model predictions using the lensing probability of [Lapi et al. \(2012\)](#) with a maximum amplification $\mu_{\max} = 30$ (see Section 3.3.2). The agreement is generally good. Predictions for a broad range of IR/(sub-)millimeter wavelengths are shown in Figures 4.4–4.12. We find that only at $\lambda_{\text{obs}} \gtrsim 60 \mu\text{m}$ the number densities of strongly lensed galaxies can be larger than that of obscured AGNs associated with proto-spheroidal galaxies at the highest luminosities.

Strongly lensed candidates exploiting VIKING data

An additional criterion to select strongly lensed candidates from the parent sample is based on the fact that frequently (but not always, as demonstrated by the SWELLS survey; [Treu et al. 2011](#)) the lenses are passive elliptical galaxies ([Auger et al. 2009](#); [Negrello et al. 2010](#)) and therefore have optical/near-IR SEDs incompatible with them being the identifications of the far-IR/submillimeter ultra-luminous H-ATLAS objects (see Figure 4.14 for an example). We thus looked for optical/near-IR galaxies with small angular separations from the H-ATLAS sources, but with redshifts much lower than those of the latter.

Using a search radius of $10''$, 106 possible VIKING counterparts to 58 of our 64 objects were found ($\sim 91\%$). When there is more than one possible counterpart, the one closest to the SPIRE position was selected. Considering the ratio between the mean surface densities of VIKING galaxies in 0.5 arcsec wide annuli, centered on the position of objects in our parent sample, and the mean surface density of

Table 4.1: The parent sample

H-ATLAS	SDP ID	S(mJy) (500 μm)	S(mJy) (350 μm)	S(mJy) (250 μm)	z_{source} (SMM)	$\log(L_{100 \mu\text{m}})$ (SMM)	z_{lens}	$(g - r)$ (SDSS)	$(Z - H)$ (VIKING)	Δ_{pos} (arcsec)
J090740.0-004200	9 ^N	183 (9)	358 (8)	507 (7)	1.58 (0.01)	27.38 (0.30)	0.69 (0.13) _V	1.33	1.11	0.34
J091043.0-000321	11 ^N	249 (10)	403 (8)	462 (7)	1.79 (0.01)	27.59 (0.31)	0.72 (0.37) _V	1.93	1.23	0.98
J090302.9-014127	17 ^N	230 (9)	342 (8)	343 (7)	3.04 (0.01)	27.60 (0.28)	0.68 (0.40) _V	0.72	1.31	1.77
J091331.3-003642	44	89 (10)	151 (8)	187 (7)	1.50 (0.30)	27.03 (0.30)	0.30 (0.01) _S	1.45	0.88	1.79
J090051.0+015049	53	54 (10)	120 (8)	177 (7)	1.32 (0.28)	26.92 (0.32)	1.01 (0.09) _H	—	1.79	1.40
J090952.9-010811	60	90 (9)	131 (8)	159 (7)	1.54 (0.40)	26.99 (0.38)	0.22 (0.02) _V	1.09	0.94	3.03
J091341.4-004342	62	72 (9)	124 (8)	159 (7)	1.53 (0.30)	26.98 (0.28)	1.07 (0.09) _H	—	1.53	3.85
J090957.6-003619	72 ^{a,b}	83 (9)	129 (8)	132 (7)	1.91 (0.46)	27.09 (0.39)	0.47 (0.18) _V	0.91	0.70	1.91
J090749.7-003807	79	69 (9)	113 (8)	140 (7)	1.48 (0.34)	26.90 (0.34)	1.05 (0.08) _H	—	1.41	2.50
J090311.6+003906	81 ^N	173 (10)	202 (8)	135 (7)	2.63 (0.01)	27.60 (0.31)	0.30 (0.01) _S	1.67	0.82	0.73
J090356.8+002310	87	64 (9)	115 (8)	131 (7)	1.42 (0.36)	26.84 (0.37)	0.42 (0.05) _V	2.22	1.71	4.21
J090448.8+021646	98 ^b	52 (9)	97 (8)	126 (7)	1.47 (0.29)	26.85 (0.29)	0.63 (0.07) _H	—	—	3.10
J090033.8+001957	103	44 (9)	94 (8)	125 (7)	1.33 (0.28)	26.77 (0.31)	0.55 (0.16) _V	1.58	1.37	5.97
J090459.3+020837	104	66 (9)	102 (8)	111 (7)	1.79 (0.41)	26.96 (0.39)	0.34 (0.06) _V	0.53	0.04	9.43
J091056.5-002919	122	54 (9)	98 (8)	116 (7)	1.68 (0.31)	26.93 (0.29)	1.04 (0.14) _H	—	1.95	2.35
J091521.5-002443	126	82 (9)	106 (8)	116 (7)	2.19 (0.42)	27.15 (0.31)	1.01 (0.36) _H	—	—	0.98
J090542.0+020733	127	58 (10)	100 (8)	112 (7)	1.82 (0.33)	26.98 (0.31)	0.87 (0.32) _V	0.39	—	1.02
J091304.9-005343	130 ^N	112 (9)	141 (8)	110 (7)	2.30 (0.01)	27.39 (0.29)	0.26 (0.01) _S	1.28	0.80	2.35
J090626.6+022612	132	71 (9)	99 (8)	113 (7)	2.01 (0.42)	27.06 (0.34)	0.84 (0.14) _H	0.36	0.97	1.11
J090459.9+015043	153	62 (9)	88 (8)	110 (7)	1.74 (0.42)	26.93 (0.40)	0.36 (0.03) _V	1.27	1.05	6.57
J090408.6+012610	180	46 (10)	95 (8)	103 (7)	1.79 (0.36)	26.93 (0.34)	1.29 (0.20) _H	—	—	2.51
J090403.9+005619	183	50 (9)	87 (8)	104 (7)	1.69 (0.31)	26.88 (0.30)	0.31 (0.02) _V	1.04	0.88	4.08
J090653.3+023207	189	64 (9)	95 (8)	102 (7)	2.08 (0.37)	27.05 (0.29)	1.02 (0.10) _H	1.25	1.88	5.16
J090707.9-003134	191	56 (10)	95 (8)	102 (7)	1.94 (0.34)	26.99 (0.30)	1.11 (0.06) _H	—	—	2.01
J091305.1-001409	194	62 (9)	97 (8)	95 (7)	2.18 (0.37)	27.06 (0.27)	0.47 (0.04) _V	2.50	1.06	7.31
J090732.3-005207	217	52 (9)	103 (8)	91 (7)	2.13 (0.47)	27.02 (0.35)	1.13 (0.16) _H	—	1.62	2.78
J091354.6-004539	219	50 (9)	87 (8)	92 (7)	1.95 (0.34)	26.95 (0.30)	0.42 (0.10) _V	1.50	0.72	5.67
J090504.8+000800	225	71 (9)	97 (8)	97 (7)	2.18 (0.46)	27.07 (0.33)	—	—	—	—
J090308.3-000420	227	55 (10)	95 (8)	99 (7)	1.98 (0.35)	26.99 (0.29)	0.88 (0.07) _H	—	1.44	7.47
J090705.7+002128	237	64 (10)	92 (8)	90 (7)	2.28 (0.38)	27.08 (0.27)	1.37 (0.23) _H	—	—	2.56
J090433.4-010740	238	70 (9)	104 (8)	84 (7)	2.52 (0.44)	27.17 (0.33)	0.15 (0.12) _{VH}	0.61	0.19	7.58
J090239.0+002819	249	48 (9)	85 (8)	97 (7)	1.81 (0.32)	26.91 (0.31)	0.43 (0.16) _H	—	1.04	8.03
J090931.8+000133	257 ^{a,b}	56 (10)	88 (8)	92 (7)	1.91 (0.54)	26.93 (0.45)	0.34 (0.21) _V	0.46	0.51	2.37
J090459.0-012911	265	44 (9)	88 (8)	92 (7)	1.87 (0.37)	26.91 (0.34)	0.97 (0.07) _H	—	1.32	2.30
J091148.2+003355	290 ^b	72 (9)	102 (8)	90 (7)	2.45 (0.40)	27.16 (0.29)	0.74 (0.20) _V	1.41	—	3.05
J090319.6+015635	301	61 (9)	89 (8)	87 (7)	2.26 (0.38)	27.06 (0.27)	0.82 (0.07) _H	—	1.30	2.20
J090405.3-003331	302	76 (10)	98 (8)	85 (7)	2.57 (0.41)	27.19 (0.31)	0.66 (0.08) _{VH}	0.67	1.04	4.42
J085751.3+013334	309	64 (10)	90 (8)	88 (7)	2.29 (0.38)	27.08 (0.28)	1.78 (0.10) _H	—	—	2.11
J085900.3+001405	312	50 (10)	92 (8)	89 (7)	2.06 (0.39)	26.98 (0.31)	—	—	—	—
J091351.7-002340	327	48 (10)	89 (8)	90 (7)	1.99 (0.37)	26.95 (0.31)	0.88 (0.42) _V	0.47	1.19	1.89
J090446.4+022218	329	61 (9)	86 (8)	87 (7)	2.24 (0.38)	27.05 (0.28)	0.26 (0.05) _V	0.67	0.67	9.09
J091003.5+021028	340	46 (9)	86 (8)	87 (7)	1.97 (0.37)	26.93 (0.31)	—	—	—	—
J090429.6+002935	354 ^c	60 (10)	86 (8)	85 (7)	2.18 (0.60)	27.01 (0.44)	0.18 (0.01) _V	3.32	0.62	3.16
J090032.7+004316	383	50 (10)	85 (8)	85 (7)	2.08 (0.36)	26.97 (0.28)	0.52 (0.14) _V	0.98	1.24	3.85
J090613.7-010044	390	69 (9)	86 (8)	79 (7)	2.52 (0.41)	27.14 (0.31)	—	—	—	—
J090453.2+022018	392	88 (9)	107 (8)	83 (7)	2.80 (0.44)	27.28 (0.29)	0.66 (0.11) _V	2.01	1.02	1.97
J085855.3+013728	393	68 (9)	92 (8)	80 (7)	2.51 (0.40)	27.14 (0.30)	1.48 (0.17) _H	—	2.35	1.43
J090346.1+013428	396	68 (9)	91 (8)	79 (7)	2.53 (0.41)	27.15 (0.30)	—	—	—	—
J090954.6+001754	407	76 (10)	111 (8)	83 (7)	2.67 (0.48)	27.23 (0.33)	0.68 (0.25) _V	—	1.09	2.11
J090440.0-013439	414	76 (9)	98 (8)	76 (7)	2.75 (0.44)	27.22 (0.30)	—	—	—	—
J090950.8+000427	419 ^a	68 (9)	92 (8)	81 (7)	2.50 (0.40)	27.14 (0.30)	0.62 (0.31) _V	0.69	0.37	2.46
J090204.1-003829	436	61 (9)	87 (8)	79 (7)	2.40 (0.39)	27.08 (0.29)	—	—	—	—
J090930.4+002224	462	57 (9)	85 (8)	76 (7)	2.39 (0.40)	27.06 (0.29)	1.00 (0.10) _H	—	1.71	4.89
J090409.4+010734	476	55 (10)	86 (8)	79 (7)	2.29 (0.39)	27.03 (0.28)	0.92 (0.09) _{VH}	0.22	1.54	2.76
J090310.6+015149	503	71 (9)	105 (8)	77 (7)	2.69 (0.49)	27.20 (0.34)	1.00 (0.07) _H	—	1.66	4.26
J085859.2+002818	512	52 (9)	85 (8)	77 (7)	2.28 (0.41)	27.01 (0.29)	0.43 (0.03) _V	1.56	1.04	2.96
J090530.4+012800	514	65 (9)	90 (8)	78 (7)	2.51 (0.41)	27.13 (0.30)	0.49 (0.07) _V	2.84	1.01	5.38
J090818.9+023330	515	57 (10)	92 (8)	77 (7)	2.42 (0.44)	27.08 (0.32)	—	—	—	—
J090441.5+015154	545 ^c	70 (10)	87 (8)	76 (7)	2.60 (0.42)	27.16 (0.31)	-0.02 (0.02) _H	—	0.29	3.21
J090739.1-003948	639 ^a	81 (9)	99 (8)	73 (7)	2.89 (0.45)	27.25 (0.28)	0.39 (0.15) _H	—	0.64	0.82
J091257.2+000300	700	87 (10)	96 (8)	69 (7)	3.03 (0.46)	27.29 (0.27)	—	—	—	—
J090819.1-002026	751	66 (10)	93 (8)	69 (7)	2.71 (0.47)	27.16 (0.32)	—	—	—	—
J090813.0-003657	775	65 (10)	88 (8)	66 (7)	2.74 (0.45)	27.16 (0.31)	—	—	—	—
J085908.5+011320	910	70 (10)	87 (8)	67 (7)	2.81 (0.44)	27.19 (0.29)	0.94 (0.08) _H	—	1.50	5.47

Notes. The 100 μm luminosity, $L_{100 \mu\text{m}}$, is in W/Hz. The 31 SLG candidates are shown in boldface. Errors in parentheses. The subscript next to the lens redshift indicates its origin: “V” for VIKING, “H” for H-ATLAS (this work), “VH” for galaxies whose redshifts were re-estimated by us because the VIKING estimate has exceedingly large errors ($z = 1.83 \pm 1.25$, 1.86 ± 1.42 , 1.56 ± 1.35 for SDP.238, SDP.302, and SDP.476, respectively), and “S” for spectroscopic measurements.

^aThe optical counterpart has colors compatible with those of a late-type galaxy; ^bTentative lens probability $< 30\%$;

^cThe optical counterpart is local, $z < 0.2$; ^NConfirmed strongly lensed galaxy (Negrello et al. 2010).

VIKING galaxies ($\simeq 1.19 \times 10^{-3}$ arcsec $^{-2}$) as a function of the angular distance from the objects, there is a clear overdensity for radii smaller than 3.5 arcsec,

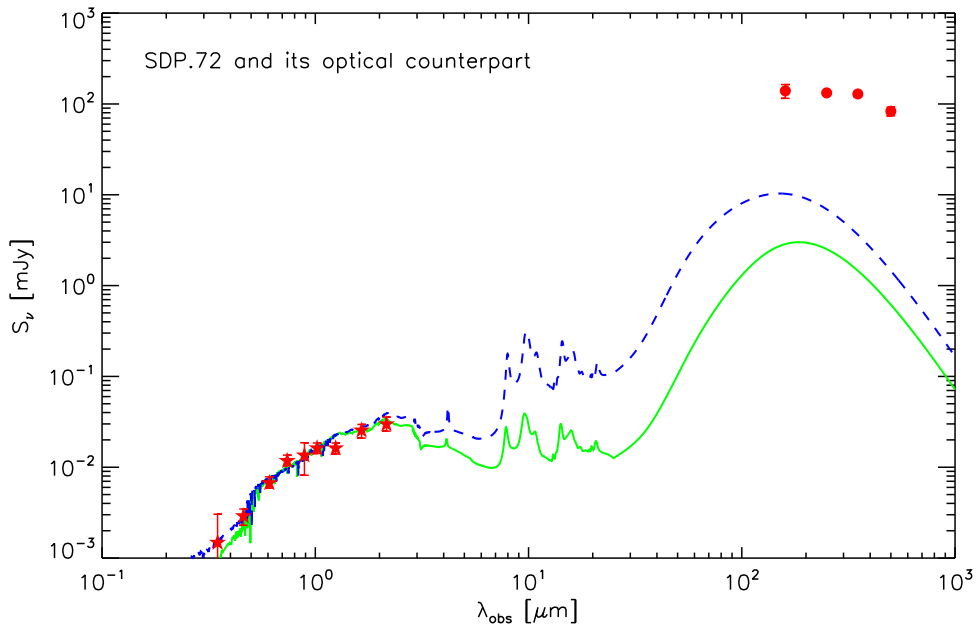


Figure 4.14: Photometric data of a lensed candidate, SDP.72, (PACS and SPIRE; filled red circles) and of its optical/near-IR counterpart (SDSS and VIKING; filled red stars). The optical/near-IR photometry of the optical counterpart of SDP.72 is fitted with mean (solid green line; $\log(L_{\text{IR}}/L_{\odot}) \simeq 10.5$) and high far-IR luminosity (dashed blue line; $\log(L_{\text{IR}}/L_{\odot}) \gtrsim 11.5$) SEDs of low- z H-ATLAS galaxies (Smith et al. 2012). SDP.72 is an example of objects whose far-IR to optical luminosity ratios are too large to be accounted for by a cold far-IR SED of the kind observed for $z \lesssim 0.5$ galaxies with moderate SFRs, and therefore its optical counterpart is likely to be a foreground galaxy that may act as gravitational lens.

lensing. Since 3.5 arcsec is roughly the angular distance between the lens and the lensed images where the separation distribution drops (Kochanek 2006), we have selected as candidate SLGs the objects in the parent sample with a VIKING association within this separation. We found 34 objects satisfying this criterion. The counterpart of the object SDP.180 was conservatively dropped since it has photometric data in only two bands (J and K_s). The VIKING survey has provided the $z - H$ colors for 19 candidate lenses in our sample. With five exceptions (SDP.72, SDP.132, SDP.257, SDP.419, and SDP.639), the colors of candidate lenses are consistent with them being passive early-type galaxies.

New photometric redshift estimates were made for the 23 objects in the parent sample without VIKING redshift and for three additional objects with VIKING redshift but exceedingly large errors (see Table 4.1; Fleuren et al. 2012), using a library of 16 SEDs of early-type galaxies computed with GRASIL (Silva et al. 1998) with updated stellar populations. We ran two chemical models suitable for a typical early type galaxy, i.e., with an efficient SFR for the first Gyr, and passively evolving thereafter. The two chemical evolution models have a different metal enrichment history with a SFR-averaged metallicity $\langle Z \rangle \sim 0.05$ and $\langle Z \rangle \sim 0.03$, respectively. For each chemical evolution model we have then computed a series of synthetic SEDs at eight selected ages, between 2 Gyr and 9 Gyr. For each SED template the redshift was estimated through a minimum χ^2 fit of the SDSS (available only for 5 of the 23+3 objects) and VIKING photometric data (including upper limits). The adopted photometric redshift is the median value obtained with the different SEDs and the associated error is the rms difference from the median (typically ~ 0.1). After having estimated the photometric redshifts, two other candidate SLGs with $z < 0.2$ were conservatively dropped because both theoretical expectations for objects in the

redshift range considered here and observational data from surveys with a source redshift distribution similar to ours, namely the Cosmic Lens All-Sky Survey (CLASS; Browne et al. 2003), the SDSS Quasar Lens Search (SQLS; Oguri et al. 2006, 2008), and the COSMOS survey (Faure et al. 2008; Jackson 2008; see Figure 7 of Treu 2010), indicate a cutoff at $z_{\text{lens}} \simeq 0.2$ in the redshift distribution of *lenses* though this cutoff could be due to an observational bias.

Although we have been as conservative as possible in the selection of the candidate SLGs, some contamination of the sample is unavoidable. Firstly, given the wide variety of galaxy SEDs, we cannot be absolutely sure that the VIKING counterparts of *all* our 31 strong candidates are foreground galaxies and not the identifications of sources themselves. Second, given the uncertainties on the redshifts of candidate sources and lenses, on the mass and density profiles of the candidate lenses and, especially, on source positions, even if the VIKING sources are foreground galaxies they may not yield a strong (i.e., a factor of at least 2) gravitational amplification. Therefore, the “lens probabilities”, i.e., the probability of a “strong” gravitational amplification ($\mu \geq 2$), of individual candidate SLGs were estimated adopting the photometric or measured redshifts of the candidate sources and lenses. For the latter we adopted a singular isothermal sphere profile (see Section 3.3.2). The halo masses of the lenses are estimated using $M_{\star}/L_K = 1$ (Williams et al. 2009) and $M_{\text{halo}}/M_{\star}$ from Moster et al. (2010) and Shankar et al. (2006). The distribution of angular separations between the source and the lens is modeled as a Gaussian with mean equal to the nominal separation and dispersion $\sigma_{\text{sep}} = 2.4''[5/(S/N)]$, where S/N is the signal-to-noise ratio of the source. The lens probability of individual candidate SLGs was then obtained as the area of the Gaussian over the range of angular separations yielding $\mu \geq 2$.

We defined the “purity” of the sample as a function of S_{350} or of the angular separation, as the ratio between the sum of lens probabilities and the number of lensed candidates within each flux density or angular separation bin. As expected the “purity” declines with increasing angular separation and with decreasing flux density. The global “purity” of the sample is 72%. Four (eight) out of 31 candidate SLGs with lens probability < 30% (50%) are specified in Table 4.1. The objects that will eventually turn out not to be SLGs would be in any case interesting targets for follow-up: Figure 4.1 shows that all our SLG candidates have apparent SFRs of thousands $M_{\odot} \text{ yr}^{-1}$, i.e., apparent far-IR luminosities of a few to several times $10^{13} L_{\odot}$. Therefore if their emission is not amplified by a factor ≥ 2 , they would be among the brightest ultraluminous infrared galaxies.

The redshift distribution of the candidate lensed sources is close to that reported for most previous surveys for lensed galaxies (e.g., CLASS, SQLS, COSMOS, and SLACS (Auger et al. 2009) as given in Figure 7 of Treu 2010), while that of candidate lenses extends to substantially higher redshifts than found in the other surveys. If confirmed (and the agreement with theoretical expectations is quite reassuring in this respect), this result implies that our selection allows one to substantially extend the redshift range over which gravitational lensing can be exploited to study the lens galaxy structure and its evolution. We note, in particular, that there is observational evidence of a strong size evolution of massive early type galaxies from $z \sim 1$ (e.g., Trujillo et al. 2011 and references therein). The interpretation of this evolution is still controversial, however (e.g., Oser et al. 2012; van Dokkum et al. 2010; Fan et al. 2008, 2010). Different models imply different predictions for the evolution of gravitational potential in the inner parts

of the galaxies; gravitational lensing will provide a test for such predictions.

Strongly lensed candidates based on SPIRE data alone

As discussed above, the VIKING data play a key role in the selection of our SLG candidates, since they allow us to identify the associated candidate lenses. Although the VIKING survey plans to cover $\simeq 1500 \text{ deg}^2$, it will not cover the H-ATLAS North Galactic Pole field, and near-IR surveys to the same depth of the missing areas are not foreseen. However, a high efficiency selection of candidate strongly lensed sources fainter than $S_{500} = 100 \text{ mJy}$ is possible using only SPIRE data. This is readily apparent from the previous results: almost 50% of objects selected with the criteria $S_{350} \geq 85 \text{ mJy}$, $S_{250} \geq 35 \text{ mJy}$, $S_{350}/S_{250} > 0.6$, and $S_{500}/S_{350} > 0.4$ turn out to be strong candidate SLGs, in close agreement with the predictions of the [Lapi et al. \(2011\)](#) model. This is already an impressively high fraction, especially in consideration of how easily it is achieved. However, the selection efficiency can be further improved by exploiting the fact that SLGs dominate the highest apparent luminosity tail of the high- z far-IR/submillimeter LF (Figure 4.11).

To investigate the potential of an approach relying only on *Herschel*/SPIRE photometry, we have computed, using the SED of SMM J2135-0102, the photometric redshifts of SDP objects with $S_{250} \geq 35 \text{ mJy}$ and S_{350} above the 4σ limit ($\simeq 30 \text{ mJy}$), a sample almost completely overlapping the one defined by [Lapi et al. \(2011\)](#), except that the reliability $R > 0.8$ SDSS associations are not removed. The redshifts were split in bins of $\delta z_{\text{source}} = 0.1$, and within each bin we have selected the objects with $S_{350} > 85 \text{ mJy}$, $z_{\text{source}} > 1.2$ and apparent luminosity above a given percentile. In order to moderate the dependence of the results on a particular SED, we have repeated the procedure using the three SEDs mentioned before (local Arp 220; SMM J2135-0102; H-ATLAS J142413.9+022304) and considered only the candidates selected by all the SEDs. As expected the percentage (total number) of SLG candidates decreases (increases) with increasing top luminosity percentile. A slightly lower surface density ($\simeq 1.45 \text{ deg}^2$) can be reached with a $\sim 70\%$ efficiency: about 70% of objects having apparent $100 \mu\text{m}$ luminosity in the top 2% (21 objects) were previously identified as strong SLG candidates.

4.1.5 Redshift distributions

In Figure 4.15, we compare model and observed redshift distributions at various mid- to far-IR wavelengths and flux density limits. Note that a substantial fraction of sources have only photometric redshifts. For example, the fraction of photometric redshifts is 91% for the VVDS-SWIRE survey with $S_{24 \mu\text{m}} > 0.4 \text{ mJy}$ ([Rodighiero et al. 2010](#)), 67.5% for the GOODS-N, and 36% for the GOODS-S samples with $S_{24 \mu\text{m}} > 0.08 \text{ mJy}$ ([Rodighiero et al. 2010](#)). Only few sources at $z > 2$ have spectroscopic redshifts ([Berta et al. 2011](#)). Note that photometric redshift errors tend to moderate the decline of the distributions at high- z . The effect is analogous to the Eddington bias on source counts: errors move more objects from the more populated lower z bins to the less populated higher z bins than in the other direction. Thus the observed distributions may be overestimated at the highest redshifts. In addition, optical identifications are not always complete. On the whole, observational estimates of LFs and of redshift distributions may

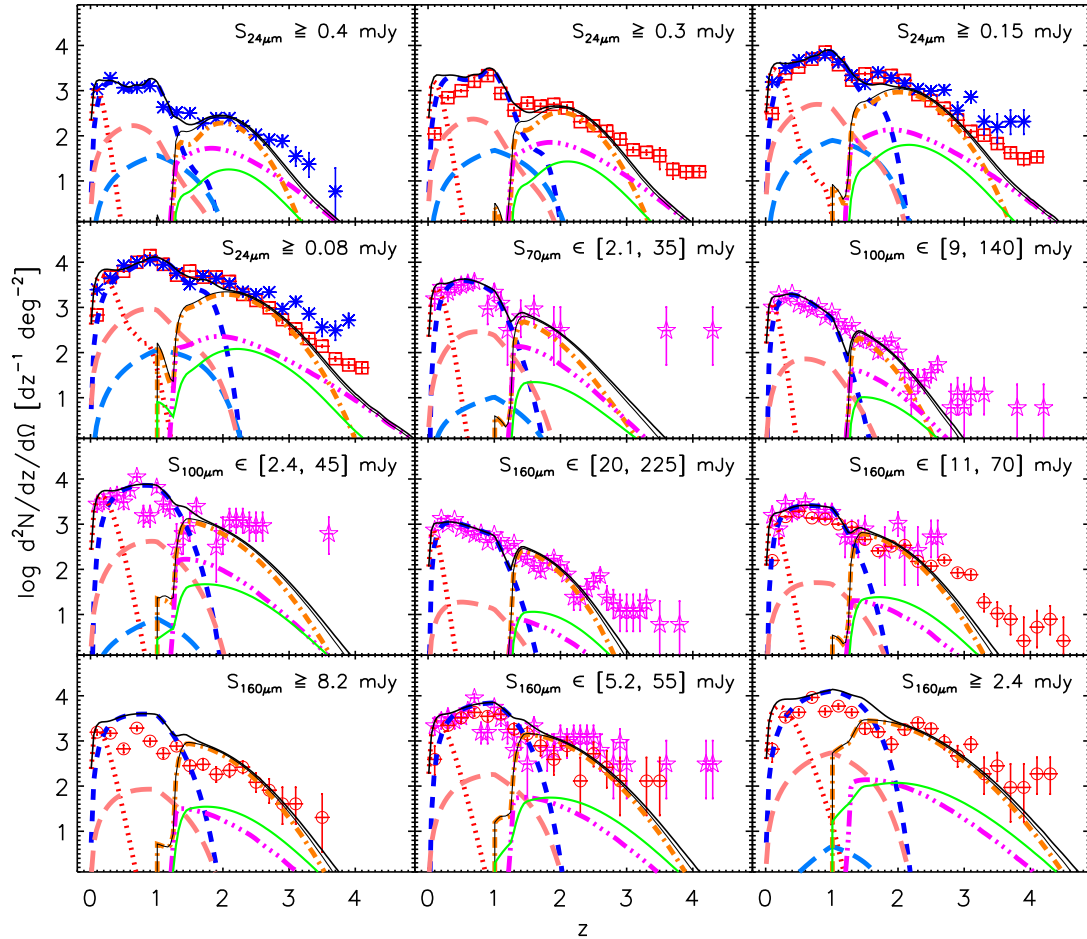


Figure 4.15: Comparison between model and observed redshift distributions at mid- and far-IR wavelengths for several flux density limits. The lines have the same definition as in Figure 4.1. Data are from Le Floc'h et al. (2009; red open squares, 24 μm), Rodighiero et al. (2010; blue stars, 24 μm), Berta et al. (2011; magenta open asterisks, 70, 100, and 160 μm), and Gruppioni et al. (2013; red open circles, 160 μm). Note that a substantial fraction of sources have only photometric redshifts and only few $z > 2$ redshifts are spectroscopic. Photometric redshift errors tend to moderate the decline of the distributions at high- z ; thus the observed distributions may be overestimated at the highest redshifts (see Section 4.1.5). The dip around $z \simeq 1.5$ in the redshift distributions yielded by the model signals the transition from the phenomenological approach adopted for low- z sources to the physical approach for high- z proto-spheroidal galaxies and associated AGNs. Such artificial discontinuity is a weakness of the model that needs to be cleared by further work.

be affected by systematic effects difficult to quantify and the true uncertainties may be larger than the nominal values. The Poisson errors of data shown in Figure 4.15–4.17 are calculated following Gehrels (1986) if they were not provided in the original paper (e.g., Chapman et al. 2005; Chapin et al. 2009, 2011; Smolčić et al. 2012; Yun et al. 2012; Gruppioni et al. 2013; Weiß et al. 2013).

Figure 4.16 compares model and observed redshift distributions at various submillimeter wavelengths and flux density limits. The data of Chapin et al. (2011) are directly derived from their catalog with the effective area of $\simeq 0.2 \text{ deg}^2$ and the completeness correction of 66% for all three wavelengths, while the data of Chapman et al. (2005) are normalized to the model at $z = 2.5$ since the effective area is unknown for their 73 spectroscopically confirmed SMGs. Compared to samples selected at mid- to far-IR wavelengths, submillimeter-selected samples show larger mean redshift and wider distributions thanks to the strongly negative K -correction making the flux corresponding to a given luminosity essentially

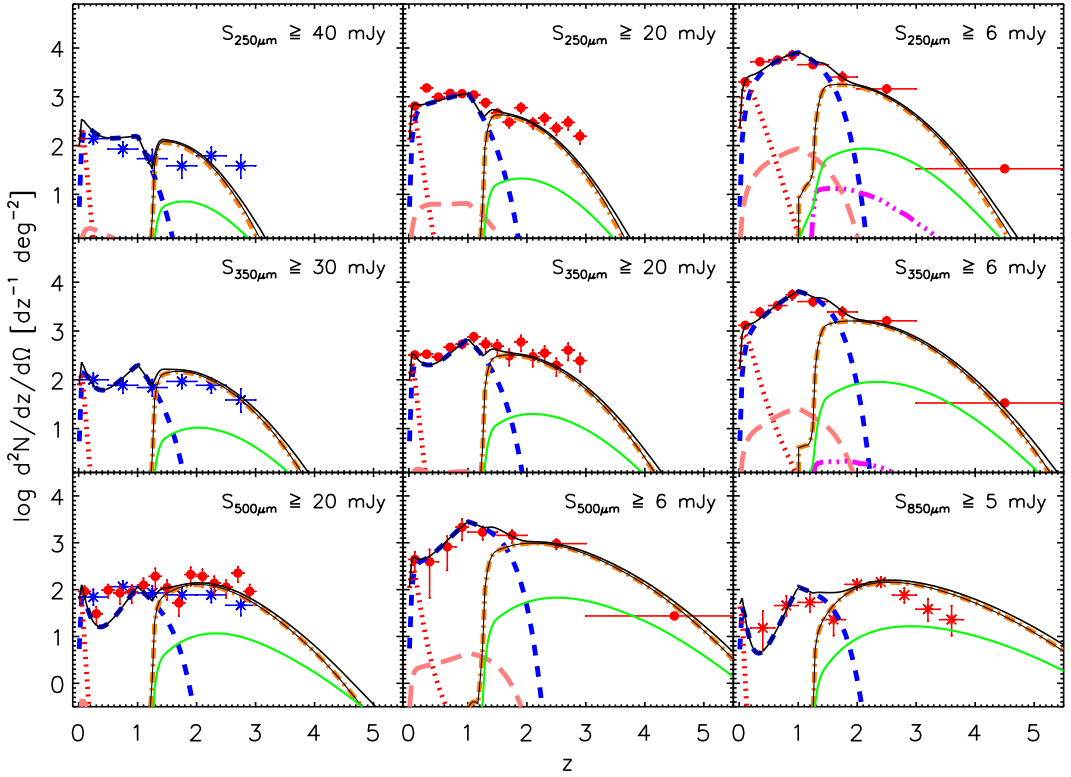


Figure 4.16: Comparison between model and observed redshift distributions at submillimeter wavelengths for several flux density limits. The lines have the same definition as in Figure 4.1. Data are from Chapin et al. (2011; blue stars, 250, 350, and 500 μ m), Béthermin et al. (2012b; red filled circles, 250, 350, and 500 μ m), and Chapman et al. (2005; red stars, 850 μ m). The dip at $z \simeq 1.5$ in the observed redshift distribution of sources with $S_{850\mu\text{m}} > 5$ mJy is due to the “redshift desert”, i.e., to the lack of strong spectral features within the observational window and the fast decline at $z > 2.5$ is due to the lack of radio identifications (Chapman et al. 2005).

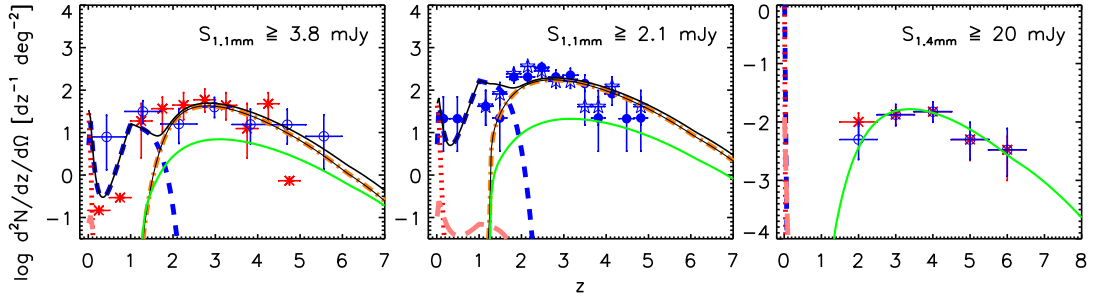


Figure 4.17: Comparison between model and observed redshift distributions at millimeter wavelengths and for several flux density limits. The lines have the same definition as in Figure 4.1. Data are from Chapin et al. (2009; 1.1 mm, red stars), Smolčić et al. (2012; 1.1 mm, blue open circles), Yun et al. (2012; 1.1 mm, blue open asterisks based on the optical photo-z and blue filled circles based on millimetric photo-z), and Weiß et al. (2013; 1.4 mm, red stars and blue open circles for strongly lensed SPT galaxies including and excluding three sources without CO line detection, respectively). The three galaxies without CO line detection are likely at $z > 4$ (J. Vieira, personal communication).

independent of distance.

This effect is more prominent at millimeter wavelengths as shown in Figure 4.17. For the 1.1 mm data of Chapin et al. (2009), Smolčić et al. (2012), and Yun et al. (2012) we have adopted effective areas of $\simeq 245$ arcmin 2 , $\simeq 0.15$ deg 2 , and $\simeq 0.143$ deg 2 , respectively. For the 1.4 mm SPT data of Weiß et al. (2013) we have estimated an effective area of $\simeq 600$ deg 2 . The intrinsic unlensed flux densities of these lensed galaxies are about $\sim 1\text{--}10$ mJy. The surface density of unlensed high- z galaxies drops

rapidly with increasing flux density above 10 mJy; therefore these galaxies are not represented in the SPT sample which has a flux density limit of 20 mJy. The other detected sources are either local galaxies (see Section 4.2.1 and Figure 4.18) or flat-spectrum radio sources. The agreement between the model and the data is remarkably good.

In Figures 4.16–4.17, there are prominent dips around $z \sim 0.5$. The dip becomes more prominent with increasing flux density limit at the same observed wavelength or with increasing observed wavelength at the same flux density limit. The dips are due in part to the decline/emergence of different populations and in part to the combination of the effects of the large positive luminosity evolution of the “warm” population and of the negative K -correction. At low redshifts, when the latter effects are small, the number of sources declines with increasing cosmic distance until the two effects “switch on” reversing this trend. At mid-/far-IR wavelengths these dips are not present because the K -correction is positive.

4.2 Number counts

4.2.1 IR/(sub-)millimeter counts

The differential number counts, i.e., the number density of sources as a function of the flux density, are the most classical and most easily available tool to investigate the cosmological evolution of the galaxy LF, without redshift information. A distinctive feature of the present model is that we have attempted to fit simultaneously the data over a broad wavelength range, from mid-IR to millimeter waves. As mentioned in several papers, this presents several challenges. First, the data come from different instruments and the relative calibration is sometimes problematic (see the discussion in [Béthermin et al. 2011](#)). Systematic calibration offsets may hinder simultaneous fits of different data sets. For example, [Marsden et al. \(2011\)](#) pointed out that there is considerable tension between the SCUBA 850 μm counts and the AzTEC counts at 1.1 mm, and indeed the 850 μm and millimeter-wave counts have been repeatedly corrected (generally downwards) as biases were discovered and better data were acquired. Also, the very complex SEDs in the mid-IR, where strong polycyclic aromatic hydrocarbon (PAH) emission features show up, make the counts exceedingly sensitive to the details of the spectral response function of the specific instrument and introduce large uncertainties in the conversion from broadband measurements to monochromatic flux densities giving rise to strong discrepancies among data sets nominally referring to the same wavelength. In fact, large discrepancies are present among different determinations of 15 μm source counts and are clearly visible in Figure 4.18.

Comparisons between the counts yielded by the model and the data at other wavelengths from 8 μm to 2 mm are presented in Figure 4.18. At wavelengths $\geq 350 \mu\text{m}$, where, in the present framework, proto-spheroidal galaxies are most important, the model provides a simple physical explanation of the steeply rising portion of the counts, that proved to be very hard to account for by other both physical ([Hayward et al. 2013; Niemi et al. 2012; Lacey et al. 2010](#)) and phenomenological (e.g., [Béthermin et al. 2012a; Gruppioni et al. 2011](#)) models. In our model the sudden steepening of the (sub-)millimeter counts is due to the appearance of proto-spheroidal galaxies that show up primarily at $z \gtrsim 1.5$ and are mostly

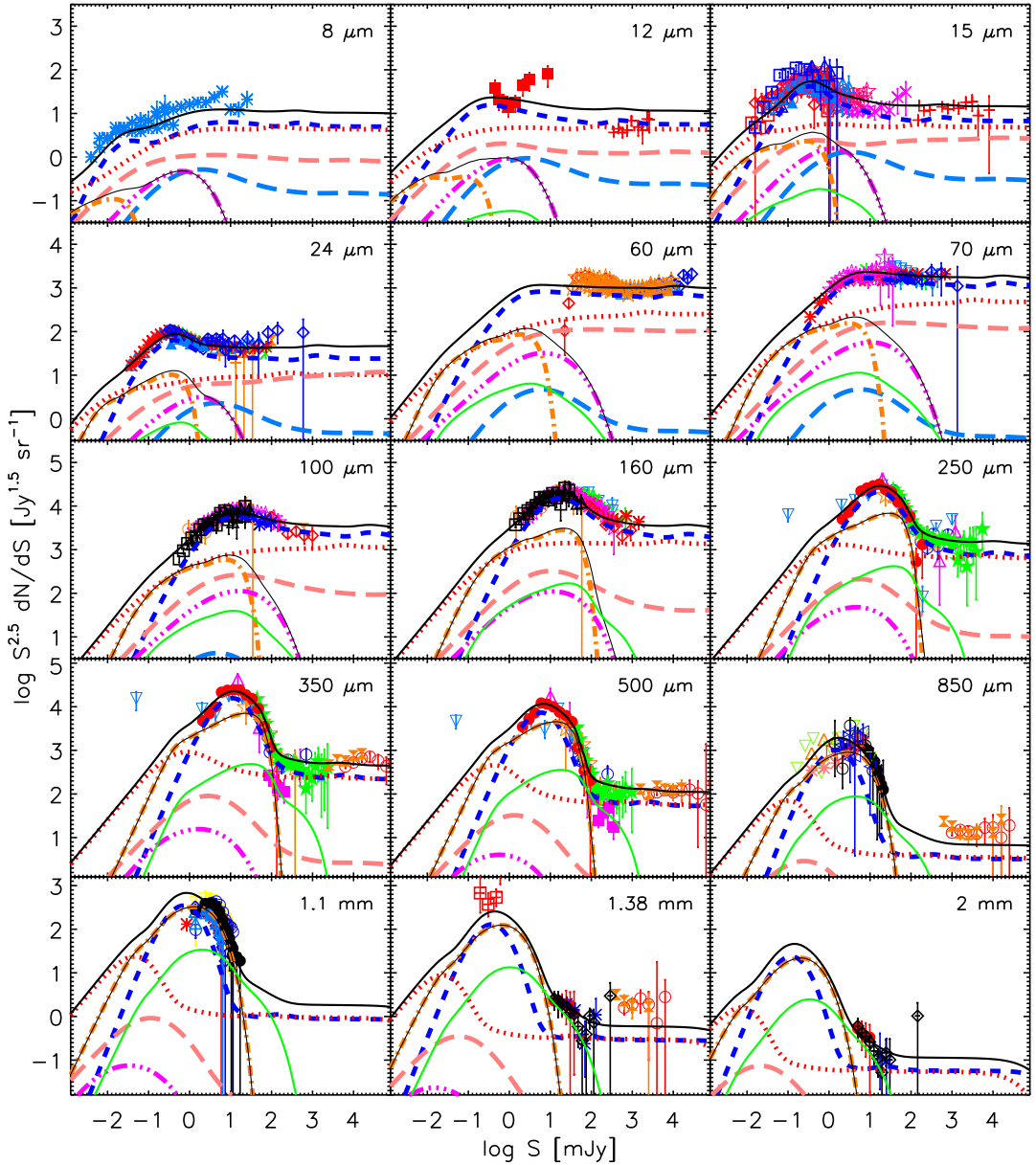


Figure 4.18: Euclidean normalized differential number counts at wavelengths from $8 \mu\text{m}$ to 2 mm . The thick solid lines are the sum of contributions from: “cold” late-type galaxies (dotted red lines), “warm” (starburst) late-type galaxies (dashed blue lines), type 1 AGNs (long-dashed light-blue lines), type 2 AGNs (long-dashed pink lines), stellar component of proto-spheroids (dot-dashed orange lines), AGN component of proto-spheroids (triple-dot-dashed magenta lines), strongly lensed ($\mu \geq 2$) proto-spheroids (solid green lines; only significant at $\lambda \geq 250 \mu\text{m}$). The thin solid black lines show the counts of unlensed proto-spheroids, including both the stellar and the AGN components; at $\lambda \geq 250 \mu\text{m}$ these counts essentially coincide with the counts of the stellar component only. The purple filled squares in the $350 \mu\text{m}$ and $500 \mu\text{m}$ panel show the estimated counts of strongly lensed galaxies (González-Nuevo et al. 2012; Lapi et al. 2012). The bright counts at 1.38 and 2 mm are also generally interpreted as due to strongly lensed galaxies (Vieira et al. 2010; Greve et al. 2010; Mocanu et al. 2013; Marsden et al. 2013). References for all the data points are given in Table 4.2. The model provides a physical explanation of the sudden steepening of the (sub-)millimeter counts: it is due to the appearance of proto-spheroidal galaxies that show up primarily at $z \gtrsim 1.5$, being mostly in passive evolution at lower redshifts. The passive evolving galaxies have been neglected in the current model and will become significant at $\lambda \lesssim 8 \mu\text{m}$ as indicated by the slightly under-prediction of $8 \mu\text{m}$ counts by the model.

in passive evolution at lower redshifts. Their counts are extremely steep because, due to the strongly negative K -correction, the submillimeter flux densities corresponding to a given luminosity are only

Table 4.2: References for Data on IR/(sub-)millimeter Number Counts (See Figure 4.18)

Wavelength (μm)	Instrument	Field	Symbol	Reference
8	<i>Spitzer</i> /MIPS	GOODS-N+S (AGN)	Filled blue circles	Treister et al. (2006)
8	<i>Spitzer</i> /IRAC	Bootes, EGS, QSO 1700	Blue stars	Fazio et al. (2004)
12	<i>ISO</i> /ISOCAM	Four high galactic latitude fields	Filled red squares	Clements et al. (1999)
12, 15	<i>IRAS</i>	All sky $ b \geq 25^\circ$	Red pluses	Rush et al. (1993)
15, 24	<i>AKARI</i> /IRC	NEP-deep	Filled light-blue triangles	Takagi et al. (2012)
15	<i>AKARI</i> /IRC	De-lensed A2218	Open red squares	Hopwood et al. (2010)
15	<i>AKARI</i> /IRC	NEP-deep+wide	Open pink asterisks	Pearson et al. (2010)
15	<i>AKARI</i> /IRC	CDFS	Open blue squares	Burgarella et al. (2009)
15	<i>AKARI</i> /IRC	NEP-deep	Open red diamonds	Wada et al. (2007)
15	<i>ISO</i> /ISOCAM	ELAIS-S	Magenta crosses	Gruppioni et al. (2002)
15	<i>ISO</i> /ISOCAM	ISOCAM deep surveys	Open red circles	Elbaz et al. (1999)
16	<i>Spitzer</i> /IRS	GOODS-N+S	Open light-blue triangles	Teplitz et al. (2011)
16	<i>Spitzer</i> /IRS	GOODS-N+S (AGN)	Filled red circles	Teplitz et al. (2011)
16	<i>Spitzer</i> /IRS	HDF-N	Open blue triangles	Teplitz et al. (2005)
24, 70	<i>Spitzer</i> /MIPS	ADF-S	Open blue diamonds	Clements et al. (2011)
24, 70, 160 ^a	<i>Spitzer</i> /MIPS	<i>Spitzer</i> legacy fields	Red stars	Béthermin et al. (2010)
24	<i>Spitzer</i> /MIPS	COSMOS	Orange pluses	Le Floc'h et al. (2009)
24	<i>Spitzer</i> /MIPS	SWIRE fields	Green crosses	Shupe et al. (2008)
24	<i>Spitzer</i> /MIPS	NDWFS Bootes (AGN)	Open red circles	Brown et al. (2006)
24	<i>Spitzer</i> /MIPS	GOODS-N (AGN)	Filled blue circles	Treister et al. (2006)
24	<i>Spitzer</i> /MIPS	Deep <i>Spitzer</i> fields	Open light-blue triangles	Papovich et al. (2004)
60	<i>IRAS</i>	<i>IRAS</i> fields	Open orange asterisks	Bertin et al. (1997)
60	<i>IRAS</i>	<i>IRAS</i> deep fields	Open red diamonds	Gregorich et al. (1995)
60	<i>IRAS</i>	All sky $ b > 10^\circ$	Open light-blue triangles	Rowan-Robinson et al. (1991)
60	<i>IRAS</i>	All sky $ b > 50^\circ$	Open blue diamonds	Lonsdale et al. (1990)
70, 100, 160	<i>Herschel</i> /PACS	GOODS, LH, COSMOS	Open magenta asterisks	Berta et al. (2011)
70, 160	<i>Spitzer</i> /MIPS	xFLS	Green crosses	Frayer et al. (2006)
70, 160	<i>Spitzer</i> /MIPS	Bootes, Marano, CDF-S	Open light-blue downward triangles	Dole et al. (2004)
100, 160	<i>Herschel</i> /PACS	GOODS-S	Open squares	Magnelli et al. (2013)
100, 160	<i>Herschel</i> /PACS	GOODS-S+N	Open triangles	Magnelli et al. (2013)
100	<i>Herschel</i> /PACS	DEBRIS	Blue stars	Sibthorpe et al. (2013)
100, 160	<i>Herschel</i> /PACS	GAMA-9	Open red diamonds	Rigby et al. (2011)
100, 160	<i>Herschel</i> /PACS	A2218	Open orange circles	Altieri et al. (2010)
250, 350, 500	<i>Herschel</i> /SPIRE	H-ATLAS	Filled green asterisks	E. Rigby et al. (in preparation)
250, 350, 500	<i>Herschel</i> /SPIRE	HerMES	Filled red circles	Béthermin et al. (2012b)
250, 350, 500	<i>Herschel</i> /SPIRE	H-ATLAS	Open blue circles	Clements et al. (2010)
250, 350, 500	<i>Herschel</i> /SPIRE	HerMES	Open orange circles	Oliver et al. (2010)
250, 350, 500	<i>Herschel</i> /SPIRE	HerMES P(D)	Open light-blue downward triangles	Glenn et al. (2010)
250, 350, 500	BLAST	BGS P(D)	Open magenta triangles	Patanchon et al. (2009)
350, 550, 850, 1382	<i>Planck</i>	ERCSC	Open orange circles	Negrello et al. (2013)
350, 550, 850, 1382	<i>Planck</i>	<i>Planck</i> all-sky survey (dusty)	Filled orange hourglass	Planck Collaboration et al. (2013)
350	<i>Herschel</i> /SPIRE	H-ATLAS (lensed)	Filled magenta squares	González-Nuevo et al. (2012)
500	<i>Herschel</i> /SPIRE	H-ATLAS (lensed)	Filled magenta squares	Lapi et al. (2012)
850	SCUBA	Clusters	Open blue leftfacing triangles	Noble et al. (2012)
850	SCUBA	A370 and A2390	Open black circles	Chen et al. (2011)
850	SCUBA	Clusters	Pink stars	Zemcov et al. (2010)
850	SCUBA	Clusters and NTT-DF	Open green downward triangles	Knudsen et al. (2008)
850	SCUBA	SHADES	Filled black circles	Coppin et al. (2006)
850	SCUBA	Clusters	Open orange triangles	Smail et al. (2002)
870	APEX/LABOCA	Clusters	Open red rightfacing triangles	Johansson et al. (2011)
1100	ASTE/AzTEC	AzTEC blank-field survey	Filled black circles	Scott et al. (2012)
1100	ASTE/AzTEC	COSMOS	Open blue circles	Aretxaga et al. (2011)
1100	ASTE/AzTEC	ADF-S, SXDF, and SSA22	Open light-blue triangles	Hatsukade et al. (2011)
1100	ASTE/AzTEC	GOODS-S	Red stars	Scott et al. (2010)
1100	JCMT/AzTEC	SHADES	Open blue diamonds	Austermann et al. (2010)
1100	JCMT/AzTEC	COSMOS	Open green downward triangles	Austermann et al. (2009)
1300	ALMA	SXDS	Open red squares	Hatsukade et al. (2013)
1364, 2000	SPT	SPT survey (dusty, lensed)	Open black diamonds	Mocanu et al. (2013)
1376, 2027	ACT	ACT survey (dusty, lensed)	Blue crosses	Marsden et al. (2013)
1400, 2000	SPT	SPT survey (dusty, lensed)	Filled red circles	Vieira et al. (2010)

^a The 24, 70, and 160 μm flux densities of counts in Béthermin et al. (2010) for a constant νS_ν color correction have been converted to the 10 000 K convention as Béthermin et al. (2011) by multiplying a factor of 0.961, 0.918, and 0.959, respectively.

weakly dependent on the source redshift. Then, since the far-IR luminosity is roughly proportional to the halo mass, the counts mirror the high- z LF whose bright end reflects, to some extent, the exponential decline of halo mass function at high masses.

This situation results in a very strong magnification bias due to gravitational lensing (Blain 1996; Perrotta et al. 2002, 2003; Negrello et al. 2007). The counts of strongly lensed galaxies depend on the redshift distribution of the unlensed ones. Thus, the good agreement between the model and the observed

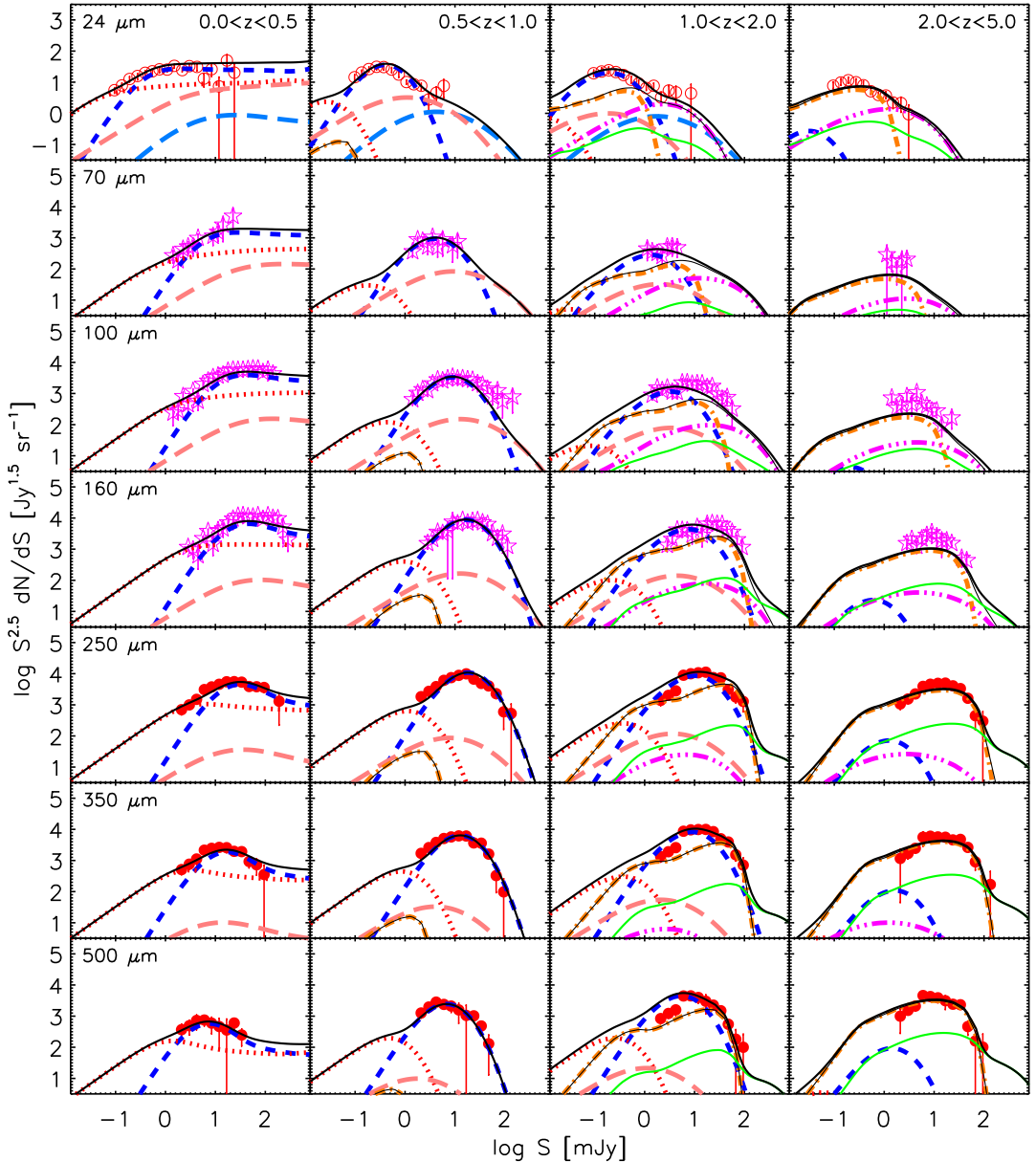


Figure 4.19: Euclidean normalized differential number counts per redshift slices. Lines have the same meaning as in Figure 4.18. Data are from Le Floc'h et al. (2009; red open circles, 24 μm), Berta et al. (2011; magenta open asterisks, 70, 100, and 160 μm), and Béthermin et al. (2012b; red filled circles, 250, 350 and 500 μm).

counts of strongly lensed galaxies (see the 350 μm , 500 μm , 1.28 mm, and 2 mm panels of Figure 4.18) indicates that the model passes this test on the redshift distribution (see also Section 4.1.5). Low- z “warm” and “cold” star-forming galaxy populations become increasingly important with decreasing wavelength. At $\lambda \leq 160 \mu\text{m}$, proto-spheroidal galaxies yield only a minor contribution to the counts.

Another test on the redshift distribution is provided by the estimated counts in different redshift slices (Figure 4.19), although we caution that the true uncertainties may be larger than the nominal ones since the observational estimates are partly based on photometric redshifts and on stacking. The consistency between the model and the data is reasonably good.

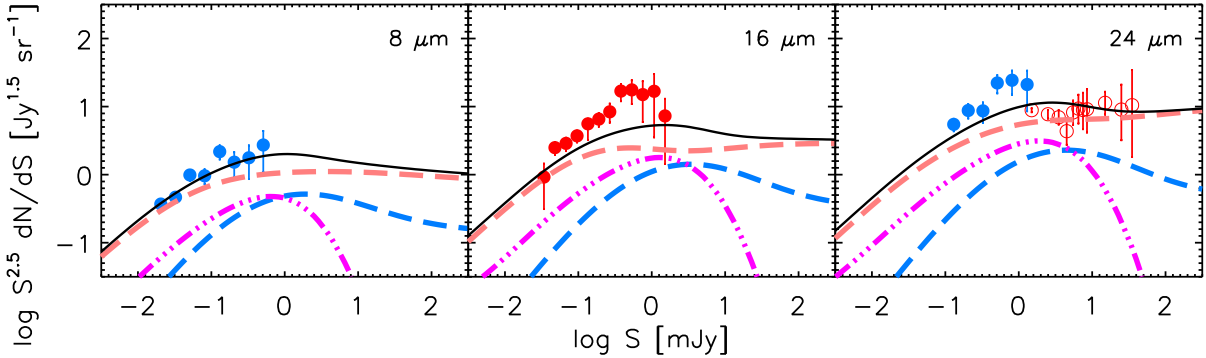


Figure 4.20: Euclidean normalized differential AGN number counts at 8, 16, and 24 μm . The long-dashed light-blue and pink lines refer to type 1 and type 2 AGNs, respectively, while the triple-dot-dashed magenta lines refer to AGNs (obscured, or type 3, and unobscured) associated with proto-spheroidal galaxies. The solid black line shows the sum of all the contributions. The filled blue circles at 8 and 24 μm have been converted from the cumulative counts of Treister et al. (2006) and associated with Poisson errors according to the inferred number of AGNs within the effective area (320 arcmin^2 for GOODSS-N+S at 8 μm and 160 arcmin^2 for GOODSS-S at 24 μm), while the filled red circles at 16 μm and open red circles at 24 μm are from Teplitz et al. (2011) and Brown et al. (2006), respectively.

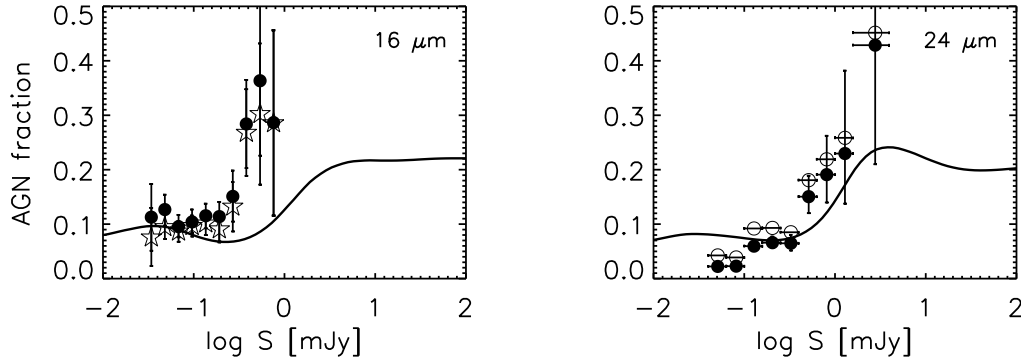


Figure 4.21: Fraction of sources classified as AGNs (type 1 + type 2 + type 3) as a function of the flux density at 16 and 24 μm . Data are from Teplitz et al. (2011; 16 μm , open asterisks for 16 μm sources with hard X-ray detection and filled circles including about 10% more AGNs identified by a power-law SED in IRAC+16 μm bands) and Treister et al. (2006; 24 μm , filled circles for sources with hard X-ray detection and open circles including hard X-ray undetected sources estimated using the AGN population synthesis model).

4.2.2 Mid-IR AGN counts

As mentioned in Section 3.2.3 the mid-IR AGN counts have been used to constrain the evolution of AGN LFs. Figure 4.20 compares the model predictions with observational estimates of AGN counts at mid-IR wavelengths. The AGN (mostly type 2) contribution to the total counts implied by the model is always sub-dominant. Figure 4.21 shows the comparison between model predicted AGN fraction, defined as the total AGN number counts (type 1 + type 2 + type 3) over the total number counts (AGNs + galaxies) as a function of flux density, and the observed fraction at 16 and 24 μm . At 16 μm it is $\simeq 8\%$ up to 1 mJy and then rapidly increases up to $\simeq 20\%$ above 10 mJy, while at 24 μm it is $\simeq 7\text{--}8\%$ up to 0.5 mJy and increases up to $\simeq 20\%$ above 2 mJy, in fair agreement with the observational estimates (Treister et al. 2006; Teplitz et al. 2011). It must be noted that these observational estimates are endowed with substantial uncertainties: on one side they may be too low because strongly obscured AGNs may be missed, and on the other side they may be too high because a significant fraction of the observed emission may come from the host galaxy.

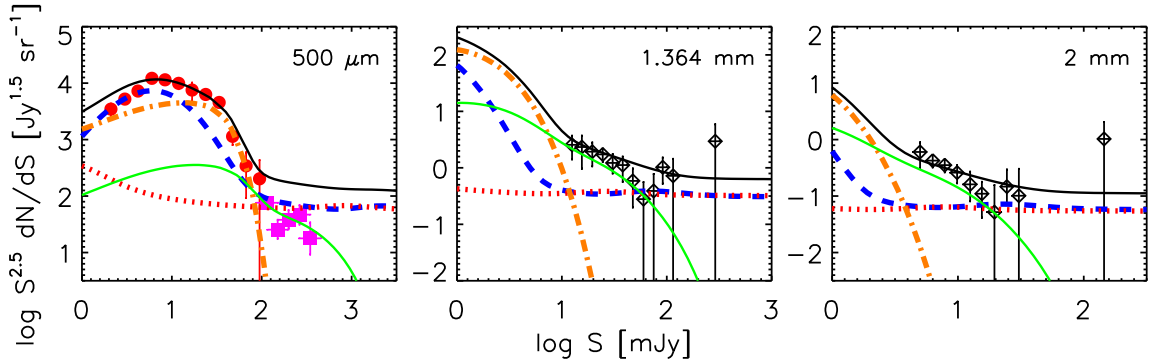


Figure 4.22: Euclidean normalized counts at 500 μm , 1.364 mm, and 2 mm to highlight the increasing importance of lensed counts with increasing wavelength. The solid line illustrates the total model counts comprising the contributions of unlensed (dot-dashed orange lines) and strongly lensed (solid green lines) high- z proto-spheroidal galaxies, and of low- z “warm” (dashed blue lines) and “cold” (dotted red lines) star-forming galaxies. At 500 μm , the filled red circles refer to unlensed counts of Béthermin et al. (2012b), while the filled magenta squares refer to the counts of the bright SDP lensed spectroscopically confirmed by Negrello et al. (2010; see also Lapi et al. 2012). At 1.364 and 2 mm (220 and 150 GHz), the total SPT dusty counts are from Mocanu et al. (2013).

4.2.3 (Sub-)millimeter lensed counts

As mentioned in Section 4.1.4, Negrello et al. (2010) has demonstrated that, for $S_{500} \geq 100$ mJy, the surface density of high- z strongly lensed SMGs is almost equal to that of low- z star-forming galaxies (cf. left panel of Figure 4.22), as predicted by Negrello et al. (2007). Figure 4.22 also shows that, at millimeter wavelengths, the surface density of strongly lensed high- z proto-spheroidal galaxies can even be larger than that of low- z late-type galaxies by a factor ≥ 2 .

A basic ingredient in the calculation of the counts of strongly lensed galaxies (see Section 3.3.2) is the lensing probability distribution $dP/d\mu$ that describes the probability for a source at redshift z to be amplified by factor μ . This distribution is cut-off at some maximum amplification that depends on the source size: larger source size means lower maximum amplification. We have adopted the lensing probability by Lapi et al. (2012) and tentatively assumed $\mu_{\max} = 100$ in Cai et al. (2013), implying very small source sizes. The recent SPT counts at 220 GHz (1.36 mm) of strongly lensed galaxies now allow much better constraints on μ_{\max} .

The effect of changing μ_{\max} is illustrated by Figure 4.23. The SPT counts indicate values around 20–40. A similar range has also been found from the H-ATLAS lensed counts at 500 μm (M. Negrello et al. in preparation). Interestingly, these values of μ_{\max} correspond to effective radii of high- z sources $R_e \simeq 2\text{--}5$ kpc.

4.2.4 Radio counts of star-forming galaxies

The counts shown in Figure 4.18 take into account only the thermal dust emission. However, star-forming galaxies emit also via synchrotron of relativistic electrons interacting with the galactic magnetic field and via free-free of their thermal plasma. Figure 4.24 shows contributions of different populations of star-forming galaxies and of radio-loud AGNs to the radio counts² from 150 GHz to 0.15 GHz. A preliminary estimate of the contributions of star-forming galaxies has been obtained from our IR model using the

²Tabulated counts at $\nu \leq 61$ GHz can be downloaded from http://web.oapd.inaf.it/rstools/srcnt/srcnt_tables.html.

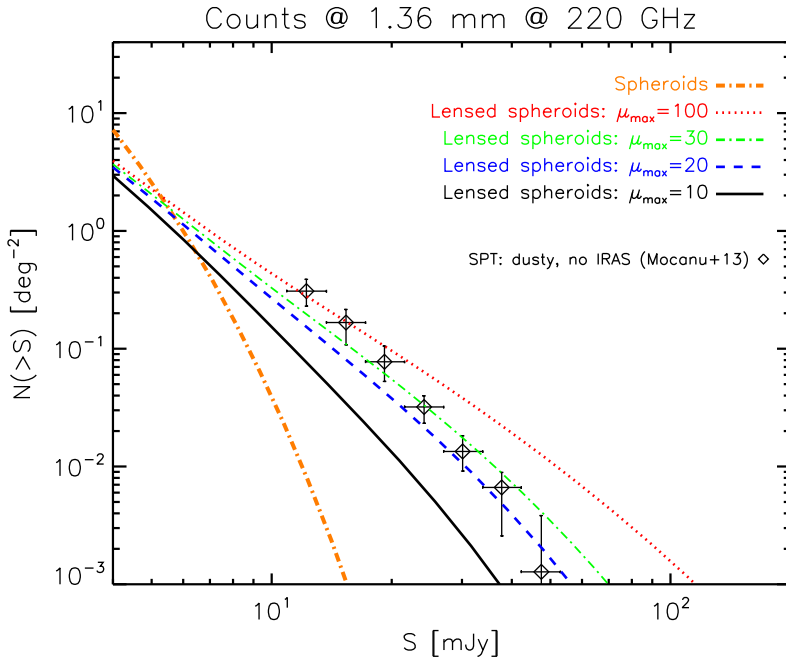


Figure 4.23: Cumulative SPT counts of high- z dusty galaxies, interpreted as strongly lensed, compared to the unlensed model counts (dot-dashed orange line) and to the lensed model counts for different maximum amplifications: $\mu_{\max} = 10$ (solid black line), 20 (dashed blue line), 30 (dot-dashed green line), and 100 (dotted red line).

IR-radio correlation, assuming power-law radio spectrum, $S_\nu \propto \nu^{-\alpha}$, as specified in Section 4.1.3. This confirms that, as discussed by [Massardi et al. \(2010\)](#), the upturn of radio sources counts at sub-mJy levels can be straightforwardly interpreted as due to dusty star-forming galaxies. Note that the preliminary results at frequencies around 100 GHz are more uncertain because the assumed single power-law spectrum for synchrotron emission neglects the possible contribution from free-free emission (with flatter power-law spectrum), which begins to dominate over synchrotron and thermal emission around 100 GHz (cf. Figure 1 in [Condon 1992](#)). Figure 4.25 shows a preliminary estimate of the 1.4 GHz redshift distribution of star-forming galaxies yielded by our model extended to radio wavelength.

The counts of radio-loud AGNs, shown for comparison, are modeled following [Massardi et al. \(2010\)](#), who interpreted the bright part of radio counts with three AGN populations having different evolutionary properties: two populations of flat-spectrum radio sources (flat-spectrum radio quasars and BL Lacs; $\alpha_{\text{FSRQ}} = \alpha_{\text{BL Lac}} = 0.1$) and one population of steep-spectrum radio AGNs ($\alpha_{\text{steep}} = 0.8$). The [Massardi et al. \(2010\)](#) model has been directly extended beyond the frequency range considered by [Massardi et al. \(2010\)](#), $\nu \leq 5 \text{ GHz}$ keeping the same spectral indices.

Current sensitivities of radio surveys require stacking analyses to examine galaxy populations at high redshift ([Ivison et al. 2007](#); [Pannella et al. 2009](#)). The future Square Kilometer Array (SKA; [Feretti et al. 2013](#)), with unprecedented spatial resolution, field-of-view, and sensitivity, will revolutionize the measurements of the SFR in star-forming galaxies via the radio continuum to extremely high redshift. These preliminary results give some hints on the potential of SKA to understand the formation and evolution of galaxies over comic time using the radio continuum observations to determine the integrated star formation history and supermassive black hole accretion history of the Universe. This problem has

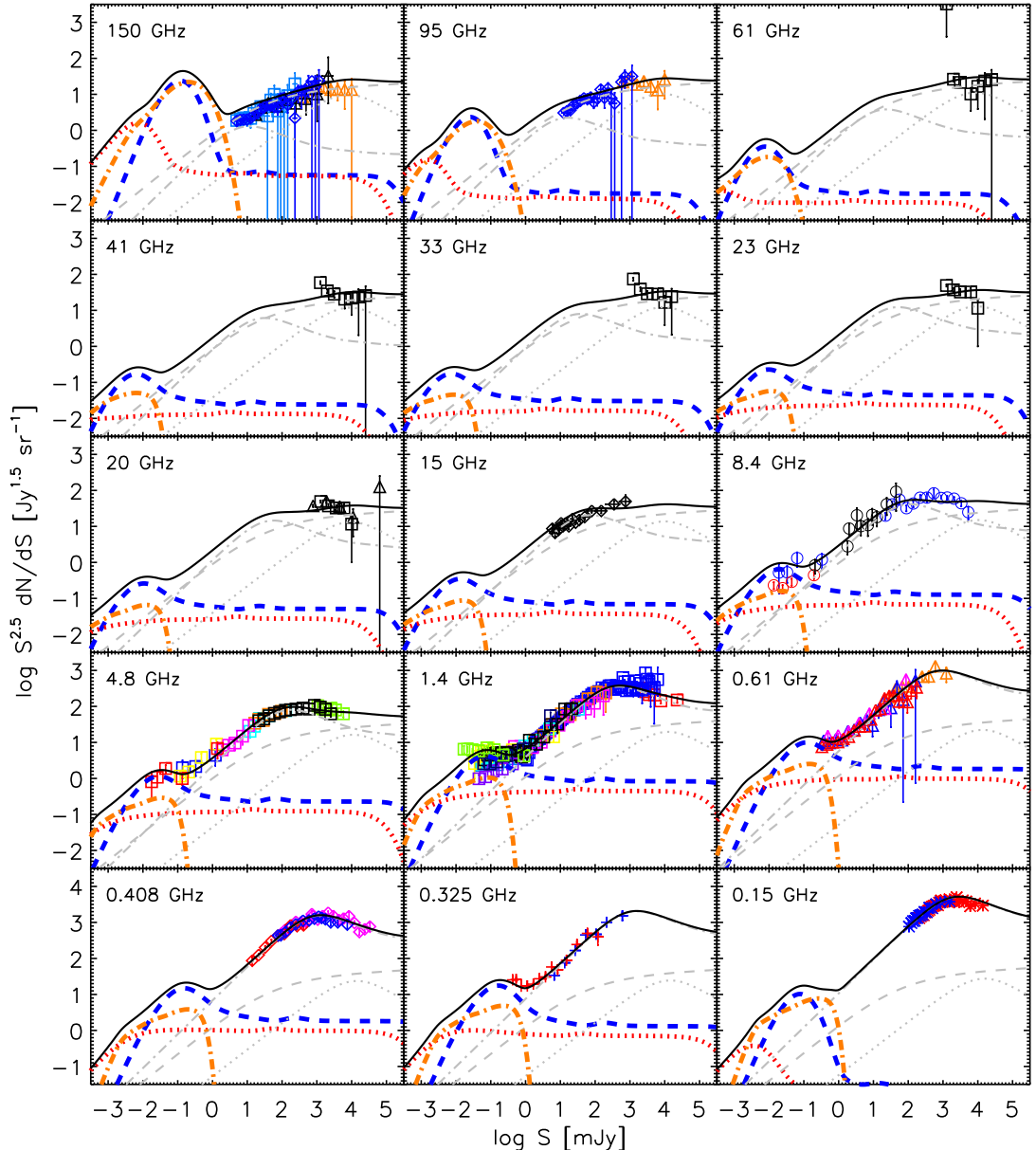


Figure 4.24: Euclidean normalized differential number counts at radio frequencies from 150 GHz to 0.15 GHz contributed by different populations of star-forming galaxies and radio-loud AGNs. A preliminary estimate of the radio counts of the “warm” (thick dashed blue lines) and “cold” (thick dotted red lines) low- z star-forming galaxies as well as of the high- z proto-spheroidal galaxies (thick dot-dashed orange lines) was obtained using the IR-radio correlation and assuming a power-law radio spectrum as specified in Section 4.1.3. The counts of three populations of radio-loud AGNs (flat-spectrum radio quasars, FSRQs, thin dotted gray lines; BL Lacs, thin dashed gray lines; steep-spectrum radio AGNs thin dot-dashed gray lines) modeled following Massardi et al. (2010) are also shown for comparison. Extrapolations to higher frequencies than considered by Massardi et al. (2010), i.e., to $\nu > 5$ GHz, were simply done assuming power-law spectra, $S_\nu \propto \nu^{-\alpha}$, with $\alpha = 0.1$ for FSRQs and BL Lacs and $\alpha = 0.8$ for steep spectrum sources. A complete list of references of the data points at frequencies smaller than 15 GHz can be found in de Zotti et al. (2010). Massardi et al. (2008; open triangles) gave the 20 GHz counts using the Australia Telescope 20-GHz survey and Massardi et al. (2009; open squares) provided the counts from 61 GHz to 20 GHz in WMAP 5-yr maps. The higher frequency data are from Vieira et al. (2010; 150 GHz, light-blue squares), Planck Collaboration et al. (2013; 150 and 95 GHz, orange triangles), Mocanu et al. (2013; 150 and 95 GHz, blue diamonds), and Marsden et al. (2013; 150 GHz, black triangles).

been addressed in the past by using optical and near-IR surveys or by IR/(sub-)millimeter measurements. The former is hampered by the large uncertainties in the correction for dust extinction, while the latter is

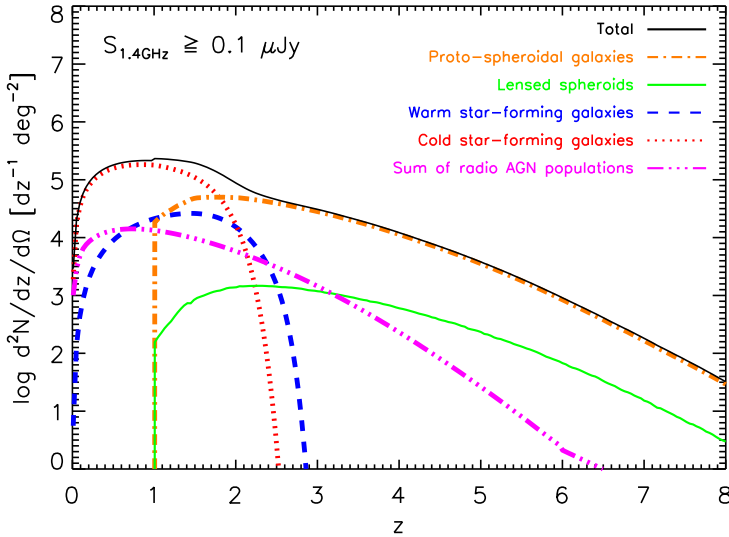


Figure 4.25: Contributions of different populations of star-forming galaxies and of radio-loud AGNs to the 1.4 GHz redshift distribution for the detection limit of SKA, i.e., $S_{1.4\text{GHz}} \geq 0.1\text{ }\mu\text{Jy}$. The various source components are indicated in the legends. Radio-loud AGNs are modeled following Massardi et al. (2010).

instead limited by the large IR beams (low spatial resolution) of the current diffraction-limited telescopes. Fortunately, the radio observations can overcome both limits and unbiasedly trace the star formation and AGN activity.

A key ingredient of modern galaxy formation models is the feedback from supernovae and from active nuclei (Kauffmann & Haehnelt 2000; Granato et al. 2004; Di Matteo et al. 2005; Hasinger et al. 2005; Ferrarese & Ford 2005; Bower et al. 2006). Feedback effects have a crucial role in shaping both the high-mass, high-luminosity and low-mass, low-luminosity tails of the galaxy distribution. Supernova feedback quenches the star formation in small halos, making the low-luminosity portion of the galaxy LF flatter than the mass function of dark matter halos. On the other hand, the AGN feedback quenches the star formation in the most massive galaxies, causing the LF to sink down, at high luminosities, much faster than the halo mass function. At least two different modes of AGN feedback can affect the galaxy evolution: a radiation-efficient fast accretion model (Silk & Rees 1998; “quasar model”) and a radiation-inefficient slow accretion model (Croton et al. 2006; also known as “radio model”).

Since the AGN activity has important effects on star formation and a higher radio to IR luminosity ratios is yielded by emission associated with AGN activity, one need to identity the contribution of accretion activity in bolometric surveys to quantity its impact on the evolution of star formation and to further test galaxy formation theories. A variety of diagnostic tools have been developed to distinguish star formation from AGN activity in radio sources. Such tools are mainly based on multi-wavelength analysis of the source properties or based on optical/IR SED fitting algorithms including both a starburst and an AGN component. However, recent studies have shown that radio-quiet AGN share many properties with star-forming galaxies, such as similar radio luminosities, optical- and IR-radio flux ratios, and even optical spectra (Prandoni et al. 2009; Padovani et al. 2011), and strongly suggest that the radio emission in such AGNs is actually triggered by star formation. In other words, a very careful analysis of the radio properties is needed in order to assess whether the radio emission in individual objects is due to

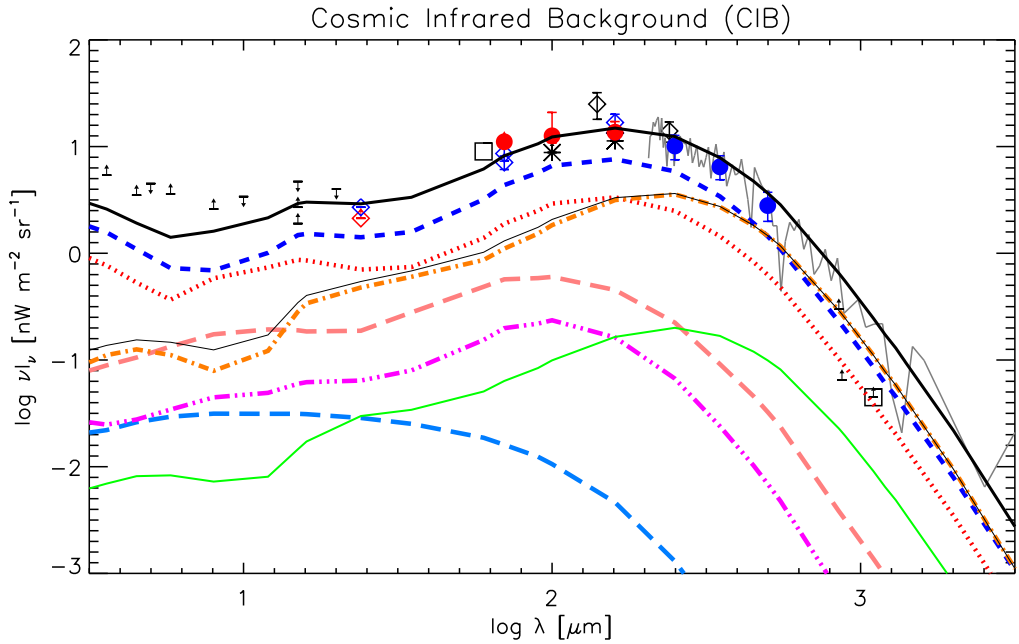


Figure 4.26: Contributions of the different populations to the cosmic infrared background. The lines have the same meaning as in Figure 4.18. Proto-spheroidal galaxies are the main contributors to the CIB above $\simeq 500 \mu\text{m}$. Data points are from Stecker & de Jager (1997, upper limit at $20 \mu\text{m}$), Lagache et al. (2000, gray line from $200 \mu\text{m}$ to $1200 \mu\text{m}$), Renault et al. (2001, upper limits at $5, 10$, and $15 \mu\text{m}$), Elbaz et al. (2002, lower limit at $15 \mu\text{m}$), Miville-Deschénes et al. (2002, open square at $60 \mu\text{m}$), Smail et al. (2002, lower limit at $850 \mu\text{m}$), Fazio et al. (2004, lower limits at $3.6, 4.5, 5.8$, and $8 \mu\text{m}$), Papovich et al. (2004, open red diamond at $24 \mu\text{m}$), Dole et al. (2006, open blue diamonds at $24, 70$, and $160 \mu\text{m}$), Hopwood et al. (2010, lower limit at $15 \mu\text{m}$), Greve et al. (2010, lower limit at $870 \mu\text{m}$), Scott et al. (2010, lower limit at 1.1 mm), Altieri et al. (2010, black stars at 100 and $160 \mu\text{m}$), Berta et al. (2011, filled red circles at $70, 100$, and $160 \mu\text{m}$), and Béthermin et al. (2012b, filled blue circles at $250, 350$, and $500 \mu\text{m}$).

star formation, AGN activity, or both. One of the most direct ways to pinpoint embedded radio-AGN cores in galaxies is the detection of high surface brightness ($T > 10^7 \text{ K}$) radio emission through high resolution - VLBI-like - observations. Examples have been shown by Biggs et al. (2010) and Chi et al. (2013) combining observations at two or more radio frequencies.

Therefore future deep high-resolution radio continuum observations, e.g., SKA, will provide the temperature and dust-obscuration-insensitive tool required to resolve and measure the star formation and nuclear activity in high-redshift galaxies, and so track the growth of their stellar populations and of the supermassive black hole at their center. These deep radio surveys will probably shed light on many physical processes, such as those involved in AGN feedback and those responsible for the radio emission in radio-quiet AGNs. The various scenarios proposed to explain the sub-mJy radio source counts will also be tested.

4.3 The cosmic infrared background (CIB)

4.3.1 CIB intensity

The cosmic infrared background (CIB) is the integrated IR/(sub-)millimeter emission of all sources not individually resolved. Figure 4.26 shows the contributions of the different populations to the CIB. The model accounts for the full CIB intensity over the whole wavelength range. Only at $\lambda \leqslant 10 \mu\text{m}$ other

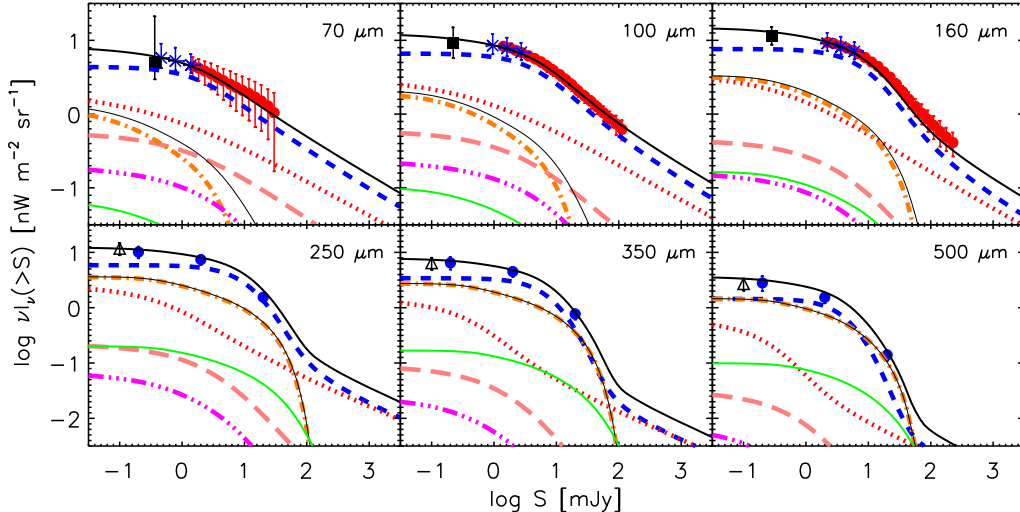


Figure 4.27: Cumulative contribution to the CIB as a function of the flux density limit from $70\ \mu\text{m}$ to $500\ \mu\text{m}$. The lines have the same meaning as in Figure 4.18. Data are from Berta et al. (2011, at 70 , 100 , and $160\ \mu\text{m}$, filled red circles for resolved *Herschel/PACS* sources, blue crosses for stacking $24\ \mu\text{m}$ counts, and filled black squares for P(D) analysis), Lagache et al. (2000, open triangles at 250 , 350 , and $500\ \mu\text{m}$), and Béthermin et al. (2012b, blue filled circles at 250 , 350 , and $500\ \mu\text{m}$).

galaxy populations, such as passively evolving galaxies, become important. According to the model, for $\lambda \geq 350\ \mu\text{m}$ the main contribution to the CIB comes from proto-spheroidal galaxies and the fraction contributed by these objects increases with increasing wavelengths. Below $\lambda = 350\ \mu\text{m}$ lower z “warm” galaxies take over, with “cold” galaxies adding a minor contribution. AGNs are always sub-dominant. The model gives a total (type 1 + type 2 + type 3) AGN contribution of 8.6% at $16\ \mu\text{m}$ and of 8.1% at $24\ \mu\text{m}$. For comparison, Teplitz et al. (2011) estimate a contribution of $\sim 15\%$ at $16\ \mu\text{m}$; Treister et al. (2006) and Ballantyne & Papovich (2007) find a contribution of $\sim 10\%$ at $24\ \mu\text{m}$. Given the good agreement with the observed counts at far-IR/submillimeter, the cumulative contributions to CIB as a function of flux density limit at these wavelengths are also found to be consistent with estimations as shown in Figure 4.27.

4.3.2 Clustering properties of dusty galaxies and CIB power spectrum

An important test of our physical model for the evolution of dusty proto-spheroidal galaxies is provided by their clustering properties that are informative on their halo masses. A specific prediction of our model is that proto-spheroidal galaxies are the main contributors to the CIB at (sub-)millimeter wavelengths with “warm” starburst galaxies becoming increasingly important with decreasing wavelength. Since, in our model, proto-spheroidal galaxies are much more strongly clustered than starburst galaxies, the variation in the mixture with wavelength translates in quantitative predictions on the frequency dependence of the amplitude of the CIB power spectra and on the level of correlations among the maps at different frequencies.

We have updated the analysis by Xia et al. (2012) taking into account the new auto- and cross-frequency power spectra obtained by Vieira et al. (2010) from *Herschel/SPIRE* measurements and the power spectrum at $100\ \mu\text{m}$ derived by Pénin et al. (2012). The latter authors actually give also an

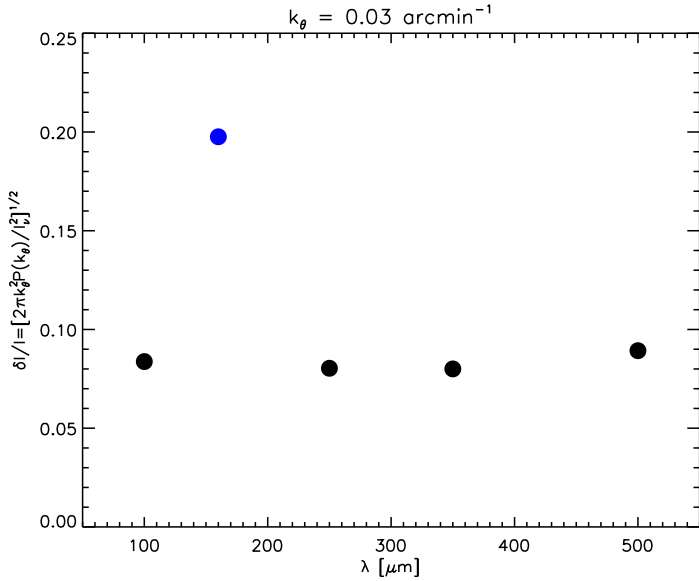


Figure 4.28: Normalized CIB anisotropy for the wave number $k_\theta = 0.03 \text{ arcmin}^{-1}$ at $\lambda = 100, 160, 250, 350$, and $500 \mu\text{m}$. See text for references.

estimate of the power spectrum at $160 \mu\text{m}$. However the amplitude of the latter is anomalously large. As an example, for the wave number $k_\theta = 0.03 \text{ arcmin}^{-1}$ we find that the amplitude normalized to the CIB intensity

$$\frac{\delta I}{I} = \frac{[2\pi k_\theta^2 P(k_\theta)]^{1/2}}{I_{\text{CIB}}}, \quad (4.3)$$

(Equation (13) of Vieira et al. 2010) is $\simeq 0.08\text{--}0.09$ at $100, 250, 350$, and $500 \mu\text{m}$ but jumps to $\simeq 0.2$ at $160 \mu\text{m}$ (see Figure 4.28). Since such a jump over a small wavelength range looks odd, we decided not to use the $160 \mu\text{m}$ power spectrum.

All the relevant details on the formalism for the power spectrum of the galaxy distribution are presented in Section 3.3.3. In the Xia et al. (2012) paper the only free parameters are the minimum halo mass, $M_{\text{min,protosph}}$, and the power-law index of the mean occupation function of satellites, $\alpha_{\text{sat,protosph}}$, of proto-spheroidal galaxies. This is because the contribution of late-type galaxies to the power spectra at $\lambda \geq 250 \mu\text{m}$ is always sub-dominant and therefore the parameters characterizing their clustering properties were poorly constrained. This is no longer true if we add the $100 \mu\text{m}$ power spectrum, which, however, still provides only weak constraints on $\alpha_{\text{sat,late-type}}$. We therefore fixed that parameter to $\alpha_{\text{sat,late-type}} = 1$. The fits to the *Herschel*/SPIRE power spectra determined by Viero et al. (2013) give $\log(M_{\text{min,protosph}}/M_\odot) = 12.15 \pm 0.04$ and $\alpha_{\text{sat,protosph}} = 1.55 \pm 0.05$ (1σ errors), close to the values found by Xia et al. (2012). The $100 \mu\text{m}$ data do not constrain these parameters further but yield $\log(M_{\text{min,later-type}}/M_\odot) = 11.0 \pm 0.06$. The nominal errors on each parameter have been computed marginalizing on the other and correspond to $\Delta\chi^2 = 1$. We caution that the true uncertainties are likely substantially higher than the nominal values, both because the model relies on simplifying assumptions that may make it too rigid and because of possible systematics affecting the data. Our value of $M_{\text{min,protosph}}$ implies an effective halo mass, i.e., Equation (3.64), at $z \simeq 2$ of proto-spheroidal galaxies, making up most of the CIB, $M_{\text{eff}} \simeq 4.5 \times 10^{12} M_\odot$. This value is close to the estimated halo mass of the

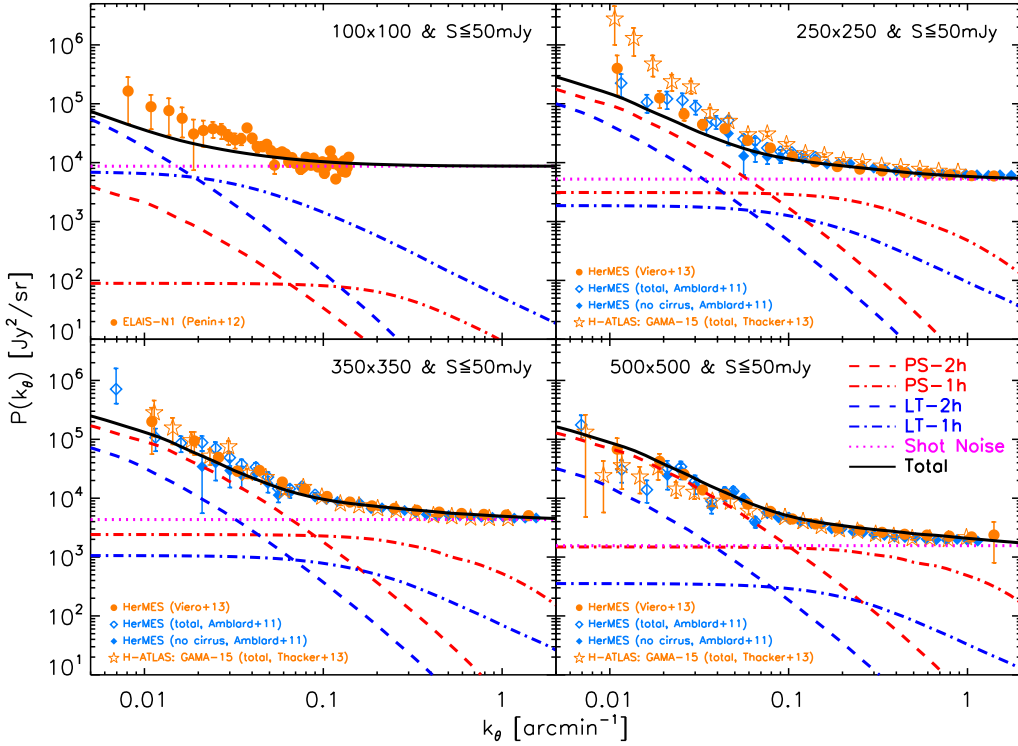


Figure 4.29: CIB angular power spectra excluding resolved sources brighter than 50 mJy at far-IR/submillimeter wavelengths. The 100 μm data are from Pépin et al. (2012, filled orange circles), those at longer wavelengths are from Amblard et al. (2011, open blue diamonds for the total power spectrum and filled blue diamonds for that corrected for Galactic cirrus), Thacker et al. (2013, open orange asterisks) and Viero et al. (2013, filled orange circles). The lines show the contributions of the one-halo and two-halo terms for the two populations considered here: late-type (LT) “warm” plus “cold” galaxies and proto-spheroidal (PS) galaxies. The horizontal dotted magenta lines denote the shot noise level. At $\lambda \geq 250 \mu\text{m}$, the signal is dominated by proto-spheroidal galaxies while late-type galaxies take over at shorter wavelengths.

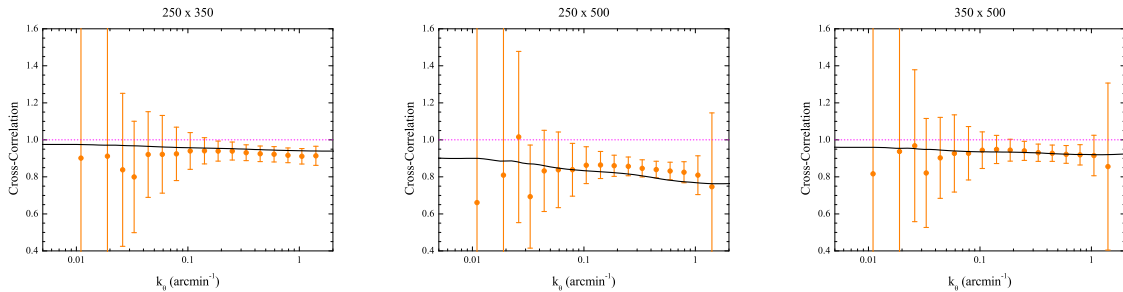


Figure 4.30: CIB cross-frequency power spectra at submillimeter wavelengths normalized according to Equation (14) of Viero et al. (2013). The solid line is the result from the model. The data are from Viero et al. (2013).

most effective star formers in the universe. Tacconi et al. (2008) estimated their mean comoving density at $z \sim 2$ to be $\sim 2 \times 10^{-4} \text{ Mpc}^{-3}$. For the standard ΛCDM cosmology, this implies that they are hosted by dark matter halos of $\sim 3.5 \times 10^{12} M_{\odot}$.

The best fit model power spectra are plotted in Figure 4.29 where the one- and two-halo contributions of proto-spheroidal and late-type galaxies are also shown. The relative contribution of the latter galaxy population increases with decreasing wavelength and becomes dominant at 100 μm . This trend implies a decrease of the level of correlations among the maps with increasing separation in wavelength. As illustrated by Figure 4.30, the model is in very good agreement with the cross-wavelength correlations

measured by [Viero et al. \(2013\)](#) according to Equation (3.67).

4.4 IR line luminosity functions

The rest-frame mid- to far-IR spectral region offers a rich suite of spectral lines that allow us to probe all phases of the interstellar medium (ISM): ionized, atomic and molecular. Measurements of these lines provide redshifts and key insight on physical conditions of dust obscured regions and on the energy sources controlling their temperature and pressure. This information is critically important for investigating the complex physics ruling the dust-enshrouded active star-forming phase of galaxy evolution and the relationship with nuclear activity.

A major progress in this field is therefore expected with forthcoming projects specifically devoted to mid- to far-IR spectroscopy such as the SSpace IR telescope for Cosmology and Astrophysics (SPICA) with its SpicA FAR infrared Instrument (SAFARI; [Roelfsema et al. 2012](#)). SAFARI is an imaging spectrometer designed to fully exploit the extremely low far-IR background environment provided by the SPICA observatory. In each integration it will take complete 34–210 μm spectra, spatially resolving the full $2' \times 2'$ field of view (FoV).

Predictions for SPICA-SAFARI spectroscopic surveys have been worked out by [Spinoglio et al. \(2012\)](#) using phenomenological models for the cosmological evolution of the IR luminosity of galaxies and AGNs and empirical correlations between line and continuum luminosities. Although this study is quite recent, it is now possible to substantially improve the analysis taking advantage of the fast progress in observational determinations of redshift dependent IR luminosity functions of different populations of extragalactic sources ([Lapi et al. 2011](#); [Gruppioni et al. 2013](#)). Moreover, we have carefully re-assessed the correlations between line and continuum IR luminosity, considering also differences among source populations, with the support of extensive simulations that take into account dust obscuration. Finally, updated predictions for the number counts and the redshift distributions of spectroscopically detectable star-forming galaxies were obtained (M. Bonato et al. 2013, in preparation).

4.4.1 Correlations between line and continuum IR luminosity

We have updated the relations between line and IR luminosities in several respects. First we have found and collected from the literature additional measurements for the PAH 11.25 μm , H₂ 17.03 μm , [O I] 63.18 μm and [C II] 157.7 μm lines (see Figure 4.31). When far-IR luminosities over rest-frame wavelength ranges different from the one (8–1000 μm) adopted here were given, we applied the following conversions, from [Stacey et al. \(2010\)](#) and [Graciá-Carpio et al. \(2008\)](#), respectively

$$L_{\text{FIR}}(40 - 500 \mu\text{m}) = 1.5 \times L_{\text{FIR}}(42 - 122 \mu\text{m}), \quad (4.4)$$

$$L_{\text{IR}}(8 - 1000 \mu\text{m}) = 1.3 \times L_{\text{FIR}}(40 - 500 \mu\text{m}). \quad (4.5)$$

The correlations between luminosities in these lines and L_{IR} are shown in Figure 4.31. In this figure we have included all objects for which no evidence for a substantial AGN effect on the strength of the lines

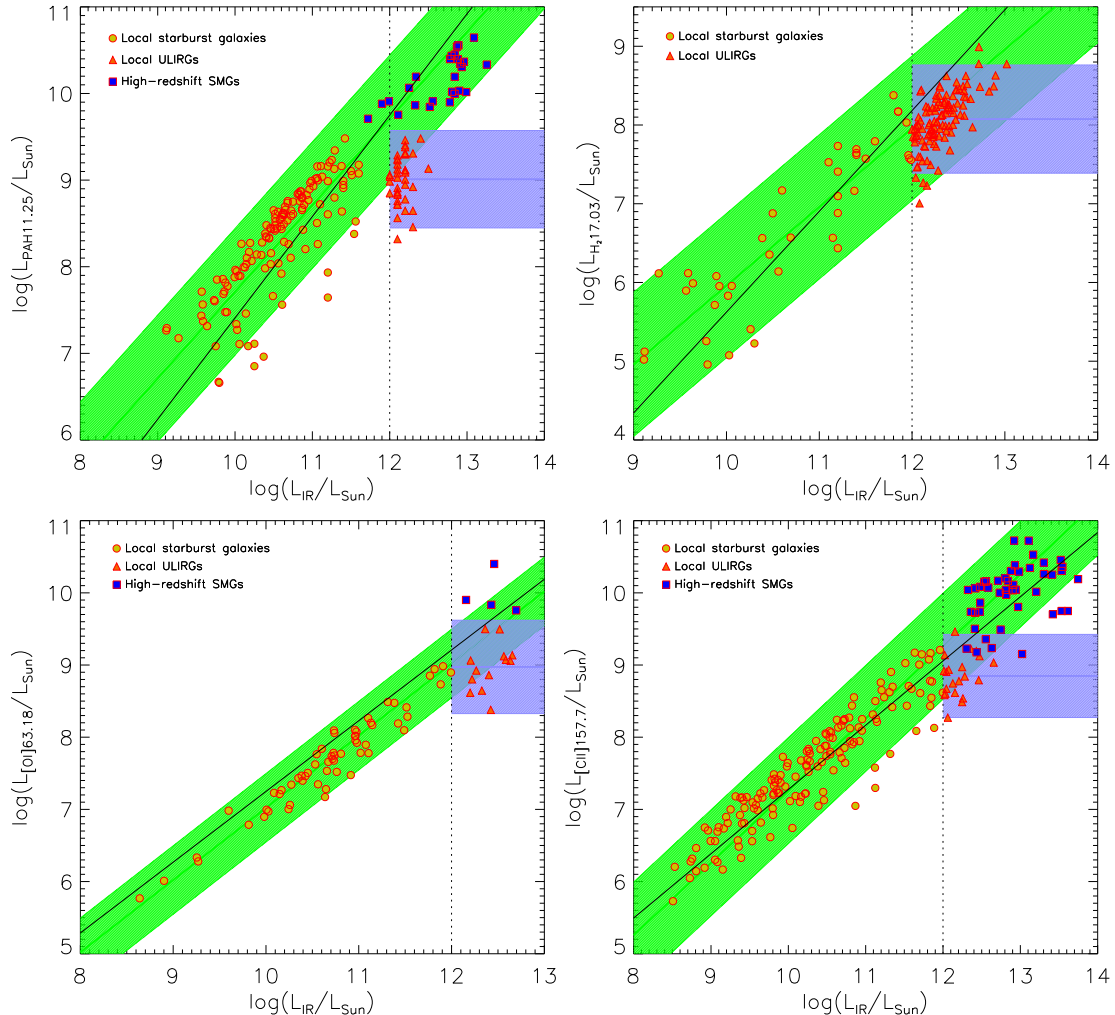


Figure 4.31: Luminosity of the PAH $11.25\mu\text{m}$ (top-left panel), $\text{H}_2\ 17.03\mu\text{m}$ (top-right panel), $[\text{O}\ \text{I}]\ 63.18\mu\text{m}$ (bottom-left panel) and $[\text{C}\ \text{II}]\ 157.7\mu\text{m}$ (bottom-right panel) lines, versus continuum IR luminosity. The green band shows the 2σ range around the mean linear relation $\log(L_\ell) = \log(L_{\text{IR}}) + c$ for local star-forming galaxies with $L_{\text{IR}} < 10^{12} L_\odot$ (circles) and high-redshift SMGs (squares); the values of $c \equiv \langle \log(L_\ell/L_{\text{IR}}) \rangle$ are given in Table 4.3. The azure band shows the 2σ spread around the mean line luminosity for the sample of local ULIRGs (triangles) whose line luminosities appear to be uncorrelated with L_{IR} and are generally lower than expected from the linear relation holding for the other sources. The mean line luminosities ($\log L_\ell$) of these objects are given in Table 4.3. The vertical dotted black line at $L_{\text{IR}} = 10^{12} L_\odot$ marks the lower boundary of ULIRG luminosities. References for data points are as follows. PAH $11.25\mu\text{m}$ line: Bernard-Salas et al. (2009), Brandl et al. (2006, 2009), O'Dowd et al. (2009, 2011), and Pereira-Santaella et al. (2010) for local star-forming galaxies; Imanishi (2009) and Imanishi et al. (2007, 2010) for local ULIRGs; Sajina et al. (2007), Yan et al. (2005, 2007), Pope et al. (2008), and Fiolet et al. (2010) for high- z SMGs. $\text{H}_2\ 17.03\mu\text{m}$ line: Bernard-Salas et al. (2009), Veilleux et al. (2009), Cormier et al. (2012), Rousset et al. (2006), Devost et al. (2004), Farrah et al. (2007), Pereira-Santaella et al. (2010), and Brandl et al. (2009) for local star-forming galaxies; Higdon et al. (2006), Veilleux et al. (2009), and Farrah et al. (2007) for local ULIRGs. $[\text{O}\ \text{I}]\ 63.18\mu\text{m}$ line: Colbert et al. (1999), Malhotra et al. (2001), Negishi et al. (2001), Cormier et al. (2012), and Graciá-Carpio et al. (2011) for local star-forming galaxies; Fischer et al. (2010), Graciá-Carpio et al. (2011), and Luhman et al. (2003) for local ULIRGs; Coppin et al. (2012), for high- z SMGs. $[\text{C}\ \text{II}]\ 157.7\mu\text{m}$ line: Graciá-Carpio et al. (2011), Negishi et al. (2001), Carral et al. (1994), Colbert et al. (1999), Unger et al. (2000), Malhotra et al. (2001), Cormier et al. (2012), and Swinbank et al. (2012) for local star-forming galaxies; Graciá-Carpio et al. (2011), Luhman et al. (1998, 2003), and Swinbank et al. (2012) for local ULIRGs; Wagg et al. (2010), Ivison et al. (2010), Hailey-Dunsheath et al. (2010), Maiolino et al. (2009), Colbert et al. (1999), Graciá-Carpio et al. (2011), Stacey et al. (2010), De Breuck et al. (2011), Swinbank et al. (2012), Cox et al. (2011), Walter et al. (2012), Riechers et al. (2013), and Carilli & Walter (2013) for high- z SMGs.

was reported.

A common property of these lines is that they are not (or not only) produced in H II regions but in

Table 4.3: Mean values of the log of line to IR (8-1000 μm) continuum luminosities, $\langle \log(L_\ell/L_{\text{IR}}) \rangle$, and associated dispersions σ . For the PAH 11.25 μm , H₂ 17.03 μm , [O I] 63.18 μm and [C II] 157.7 μm lines, $\langle \log(L_\ell/L_{\text{IR}}) \rangle$ has been computed excluding local ULIRGs, for which the luminosity in these lines was found to be uncorrelated with L_{IR} . For the latter objects the last column gives the mean values of $\log(L_\ell)$ in these lines and their dispersions.

Spectral line	$\langle \log(L_\ell/L_{\text{IR}}) \rangle$ (σ)	$\langle \log(L_\ell) \rangle$ (σ)
PAH 11.25 μm	-2.29 (0.36)	9.01 (0.28)
[Ne II] 12.81 μm	-3.11 (0.45)	-
[Ne III] 15.55 μm	-3.69 (0.47)	-
H ₂ 17.03 μm	-4.04 (0.46)	8.07 (0.34)
[S III] 18.71 μm	-3.49 (0.48)	-
[O IV] 25.89 μm	-4.38 (0.40)	-
[S III] 33.48 μm	-3.05 (0.31)	-
[Si II] 34.82 μm	-2.91 (0.28)	-
[O III] 51.81 μm	-2.84 (0.44)	-
[N III] 57.32 μm	-3.26 (0.16)	-
[O I] 63.18 μm	-2.99 (0.24)	8.97 (0.32)
[O III] 88.36 μm	-2.87 (0.47)	-
[N II] 121.9 μm	-3.49 (0.36)	-
[O I] 145.5 μm	-3.80 (0.43)	-
[C II] 157.7 μm	-2.74 (0.37)	8.85 (0.29)

(or also in) neutral and ionized ISM and in photo-dissociation regions (PDRs). In fact, as pointed out by Panuzzo et al. (2003), because carbon has a ionization potential (11.26 eV) which is lower than H, the C II ion is present in PDRs and in neutral medium illuminated by far-UV stellar radiation. Indeed, the [C II] 157.7 μm line is the most important coolant of the warm neutral medium. The excitation temperature of the [O I] 63.2 μm line is of 228 K (Kaufman et al. 1999) so that it can be easily produced in the neutral medium. The H₂ 17.03 μm line is the strongest molecular hydrogen line used to give information on the conditions of the warm component in the PDRs. Polycyclic aromatic hydrocarbon (PAH) molecules are found to be ubiquitous in the ISM but apparently do not survive in the ionized gas (Tielens 2008). An important consequence is that these lines suffer from much less extinction than those produced inside the dense, dust enshrouded stellar birth clouds.

Moreover, these lines are less directly linked to the SFR (and therefore to L_{IR}) than lines originated deep in stellar birth clouds. This difference may have to do with the steep drop in the $L_{[\text{C II}]}/L_{\text{IR}}$ ratio at high luminosities observed in local galaxies (Luhman et al. 2003; Graciá-Carpio et al. 2011) but not at high redshifts (Maiolino et al. 2009; Stacey et al. 2010). The estimated duration of the star formation episode in local ULIRGs, generally triggered by interactions/mergers, is ~ 0.1 Gyr, i.e., of the same order as the typical time (as estimated by Silva et al. 1998) for hot stars to leave the dense birth clouds, where UV photons capable of ionizing C atoms have a short mean free path for absorption. Thus PDRs are necessarily small and $L_{[\text{C II}]}$ correspondingly low. When the birth clouds begin to dissolve and larger PDRs can be produced, the SFR is declining in many cases below the threshold for the classification as ULIRGs.

In high- z galaxies the star formation is galaxy-wide and, as shown by Lapi et al. (2011), the data on LFs indicate a longer duration (~ 0.7 Gyr) of the intense star formation phase. Thus a significant fraction of hot stars have the time to leave the birth clouds and to migrate to less dense regions where they can generate extended PDRs while the SFR is still very high. This can explain their larger $L_{[\text{C II}]}/L_{\text{IR}}$ ratios.

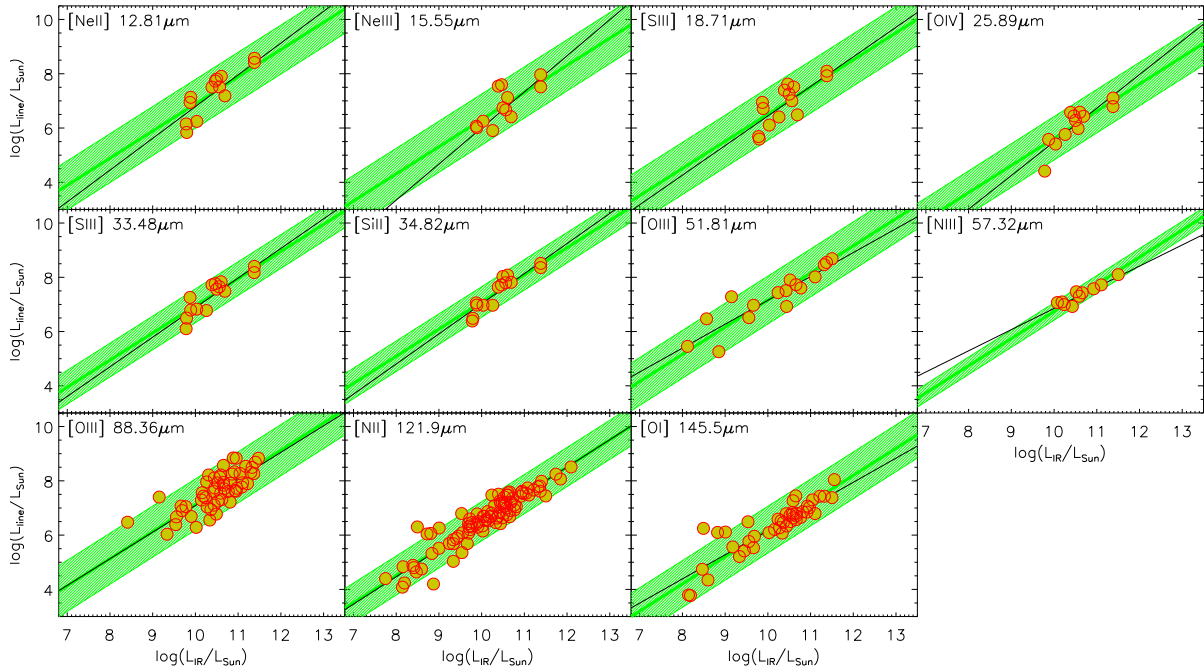


Figure 4.32: Log of the line luminosity as a function of $\log(L_{\text{IR}})$, in solar units, for all the IR lines studied in the present work, except for the four lines (PAH 11.25 μm , H₂ 17.03 μm , [O I] 63.18 μm and [C II] 157.7 μm) considered separately (see Figure 4.31). Data for $\lambda \leq 34.82 \mu\text{m}$ refer to the local starburst galaxies from the [Bernard-Salas et al. \(2009\)](#) catalogue. Data at longer wavelengths are from the heterogeneous sample of [Brauher et al. \(2008\)](#). The green band shows the 2σ spread around the mean linear relation $\log(L_\ell) = \log(L_{\text{IR}}) + c$ (represented by the green line). The black lines show the best-fit relations derived by [Spinoglio et al. \(2012\)](#). Our simulations favor a direct proportionality between line and continuum luminosity.

The same argument holds for non-ULIRG low- z galaxies whose star formation is long lived. Alternative explanations are discussed by [Carilli & Walter \(2013\)](#).

Anyway, the luminosity of low- z ULIRGs in these lines appears to be essentially uncorrelated with L_{IR} . For these objects we have therefore adopted Gaussian distributions of $\log(L_\ell)$ around mean values, $\langle \log(L_\ell) \rangle$, independent of L_{IR} . On the contrary, the mean line luminosities for the other low- and high- z galaxies, and for all galaxies in the cases of the other lines considered in this paper, are found to be tightly correlated with, and essentially proportional to L_{IR} (Figures 4.31 and 4.32). Again we have adopted Gaussian distributions around $\langle \log(L_\ell/L_{\text{IR}}) \rangle$.

4.4.2 Simulations of line and continuum IR luminosity

The data on line and continuum luminosities refer to heterogeneous samples of galaxies, affected by unknown selection effects and unknown and variable amounts of dust extinction. They may therefore not be representative of the true distributions of line-to-IR luminosity ratios. To estimate the distribution of the line-to-IR luminosity ratios and identify possible biases, we simulated the spectral energy distribution (SED) of star-forming galaxies in the absence of dust extinction and derived both the line luminosities, using the [Panuzzo et al. \(2003\)](#) library³, and the continuum IR luminosity, assuming an extinction law. The SED was generated using GALAXEV, the library of evolutionary stellar population synthesis of

³<http://pasquale.panuzzo.free.fr/hii/>

Bruzual & Charlot (2003).

The continuum emission at the time t_{obs} of a stellar population characterized by a star formation rate $\text{SFR}(t)$ is written as (e.g., Charlot & Fall 2000)

$$L_{\lambda}^{\text{SED}}(t_{\text{obs}}) = \int_0^{t_{\text{obs}}} \text{SFR}(t_{\text{obs}} - t) L_{\lambda}^{\text{SSP}}(t) T_{\lambda}(t) dt, \quad (4.6)$$

where $L_{\lambda}^{\text{SSP}}(t)$ is the power radiated per unit interval of frequency and of initial mass by the single stellar population (SSP) of age t , and $T_{\lambda}(t)$ is the “transmission function” defined as the fraction of the radiation, produced at wavelength λ and at the time t , that escapes from the galaxy. To get $L_{\lambda}^{\text{SSP}}(t)$ within GALAXEV, we adopt the SSP model computed with the evolutionary tracks and isochrones by Bertelli et al. (1994), with solar metallicity (i.e., $Z = Z_{\odot} = 0.02$) and a Chabrier (2003) Initial Mass Function (IMF). The fraction absorbed by dust in the galaxy is therefore $1 - T_{\lambda}(t)$. The transmission function is written as $T_{\lambda}(t) = \exp[-\tau_{\lambda}(t)]$, where $\tau_{\lambda}(t)$ being the effective absorption optical depth at wavelength λ seen by stars at age t . Stars are born in dense molecular clouds, which dissipate typically on a time-scale $t_{\text{BC}} \sim 10^7$ yr. This implies that the emission from stars younger than t_{BC} is more attenuated than that from older stars. Charlot & Fall (2000) write the transmission function as

$$T_{\lambda}(t) = \begin{cases} T_{\lambda}^{\text{BC}} \times T_{\lambda}^{\text{ISM}} & \text{for } t \leq t_{\text{BC}} \\ T_{\lambda}^{\text{ISM}} & \text{for } t > t_{\text{BC}} \end{cases}, \quad (4.7)$$

where T_{λ}^{BC} and T_{λ}^{ISM} are the fractions of radiation transmitted by the birth clouds and by the ambient ISM, respectively, here assumed (for simplicity) to be independent of time. We model the effective optical depths of the birth clouds and of the ISM, $\tau_{\lambda}^{\text{BC}}$ and $\tau_{\lambda}^{\text{ISM}}$, as in da Cunha et al. (2008), respectively,

$$\tau_{\lambda}^{\text{BC}} = (1 - \mu) \tau_V \left(\frac{\lambda}{5500 \text{\AA}} \right)^{-1.3} \quad \text{and} \quad \tau_{\lambda}^{\text{ISM}} = \mu \tau_V \left(\frac{\lambda}{5500 \text{\AA}} \right)^{-0.7}, \quad (4.8)$$

where τ_V being the total effective V -band absorption optical depth of the dust seen by young stars inside the birth clouds and $\mu = \tau_V^{\text{ISM}} / (\tau_V^{\text{BC}} + \tau_V^{\text{ISM}})$ the fraction of this contributed by dust in the ambient ISM. We assume an exponentially declining star formation rate, $\text{SFR}(t) = (A_{\text{SFR}}/\tau) \exp(-t/\tau)$, with $\tau = 10^7$ yr ($= t_{\text{BC}}$). The normalization, A_{SFR} , corresponds to the stellar mass assembled by the time $t \gg \tau$.

The total luminosity absorbed by dust in the birth clouds and re-radiated at far-IR/submillimeter wavelengths is (da Cunha et al. 2008)

$$L_{\text{dust}}^{\text{BC}}(t_{\text{obs}}) = \int_0^{\infty} d\lambda (1 - T_{\lambda}^{\text{BC}}) \int_0^{t_{\text{BC}}} dt \text{SFR}(t_{\text{obs}} - t) L_{\lambda}^{\text{SSP}}(t), \quad (4.9)$$

while the total luminosity absorbed by the *ambient* ISM is

$$L_{\text{dust}}^{\text{ISM}}(t_{\text{obs}}) = \int_0^{\infty} d\lambda (1 - T_{\lambda}^{\text{ISM}}) \int_{t_{\text{BC}}}^{t_{\text{obs}}} dt \text{SFR}(t_{\text{obs}} - t) L_{\lambda}^{\text{SSP}}(t). \quad (4.10)$$

Therefore the total luminosity absorbed and re-radiated by dust is

$$L_{\text{dust}}(t_{\text{obs}}) = L_{\text{dust}}^{\text{BC}}(t_{\text{obs}}) + L_{\text{dust}}^{\text{ISM}}(t_{\text{obs}}). \quad (4.11)$$

We take this as the total infrared luminosity L_{IR} .

The luminosity of a nebular line of wavelength λ_ℓ is given by

$$L_{\lambda_\ell}(t_{\text{obs}}) = \int_0^{t_{\text{BC}}} \text{SFR}(t_{\text{obs}} - t) L_{\lambda_\ell}^{\text{SSP}}(t) T_{\lambda_\ell}(t) dt, \quad (4.12)$$

where $L_{\lambda_\ell}^{\text{SSP}}(t)$ is the luminosity of the line produced in the H II regions by a stellar generation of age t . The Panuzzo's library provides line luminosities for 60 nebular emission lines, at wavelengths from the UV to the far-IR, and for 54 H and He recombination lines. There are 12 lines in common with those considered by [Spinoglio et al. \(2012\)](#). Eight of them are generated in star formation/H II regions while the others may be associated with PDRs. The library was produced interfacing version 94 of the photo-ionization code Cloudy ([Ferland 2000](#)) with the SSP model of [Bressan et al. \(1994\)](#) which provides the spectrum of the ionizing sources. The analysis by [Panuzzo et al. \(2003\)](#) showed that the emission line spectrum of an H II region with fixed gas properties (metallicity, density, and geometry) is described with reasonable precision by only three quantities: the production rates of photons capable of ionizing H I, He I, and O II:

$$Q_{\text{H}}(t) = \int_{\nu_{\text{H}}}^{\infty} \frac{L_{\nu}^{\text{SSP}}(t)}{h\nu} d\nu, \quad Q_{\text{He}}(t) = \int_{\nu_{\text{He}}}^{\infty} \frac{L_{\nu}^{\text{SSP}}(t)}{h\nu} d\nu, \quad Q_{\text{O}}(t) = \int_{\nu_{\text{O}}}^{\infty} \frac{L_{\nu}^{\text{SSP}}(t)}{h\nu} d\nu, \quad (4.13)$$

where $L_{\nu}^{\text{SSP}}(t)$ is monochromatic continuum luminosity of the SSP (in units of $\text{erg s}^{-1} \text{Hz}^{-1}$) and $\lambda_{\text{H}} = c/\nu_{\text{H}} = 911.76 \text{ \AA}$, $\lambda_{\text{He}} = c/\nu_{\text{He}} = 504.1 \text{ \AA}$, and $\lambda_{\text{O}} = c/\nu_{\text{O}} = 350.7 \text{ \AA}$ are the photo-ionization threshold frequencies for H I, He I, and O II, respectively. Therefore, different ionizing sources that provide the same values of Q_{H} , Q_{He} , and Q_{O} produce the same emission line spectra, with reasonable accuracy. The [Panuzzo et al. \(2003\)](#) library provides line luminosities for a grid of values of Q_{H} , Q_{He} , and Q_{O} , and a range of values of the gas density, ρ_{gas} , inside the star birth clouds, the gas metallicity, Z_{gas} , and the gas filling factor, ϵ_{gas} . According to the authors, the range of parameters covered by their library is fully adequate to describe the emission properties of the majority of star-forming and starburst galaxies. They do not consider line emission from PDRs and from diffuse warm neutral/low ionized medium, although some fine structure IR lines are efficiently produced in these media. As a consequence their luminosities for these lines should be taken as lower limits. GALAXEV was used to compute the SSP continuum luminosity, $L_{\lambda}^{\text{SSP}}(t)$, from which the Q -values are derived as a function of the SSP age and used to get the line luminosities, $L_{\lambda_\ell}^{\text{SSP}}(t)$, from Panuzzo's library. Line luminosities were simulated for different values of t_{obs} , A_{SFR} , ρ_{gas} , ϵ_{gas} , τ_V , and μ within the range specified below, assuming uniform distributions,

- $\log(t_{\text{obs}}/\text{yr}) \in [5.0 - 8.0]$,
- $\log(A_{\text{SFR}}/M_{\odot}) \in [7.0 - 11.0]$,

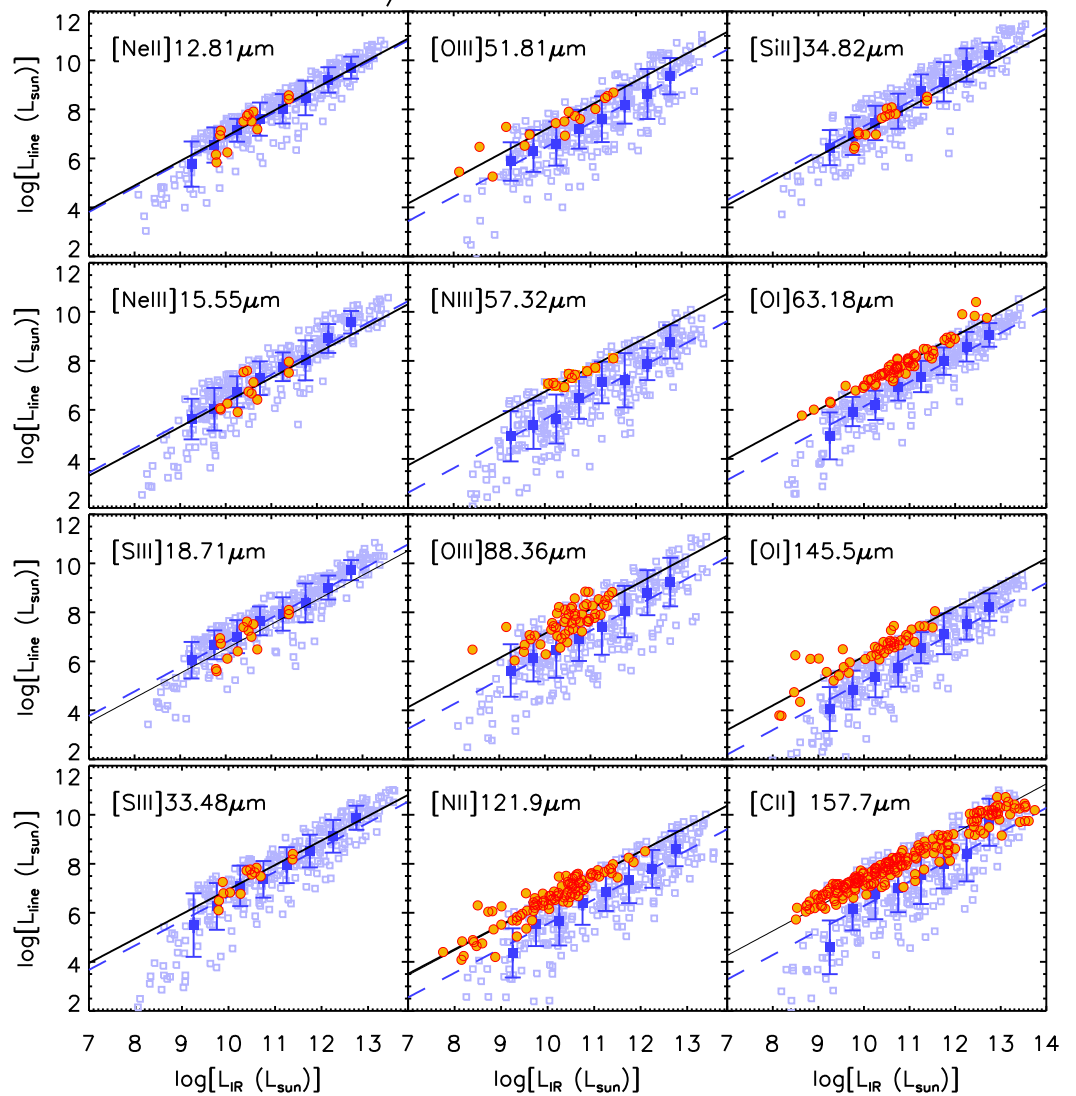


Figure 4.33: Simulated line versus IR luminosity (open squares) for some fine structure lines produced in stellar/H II regions (left and central panels) and in PDRs (right panels). Only purely star-forming galaxies (no AGN contributions) are considered in the simulations. The dashed blue lines correspond to the average ratios $c = \langle \log(L_\ell/L_{\text{IR}}) \rangle$, i.e., to a direct proportionality between $\log(L_\ell)$ and $\log(L_{\text{IR}})$, for the simulated data points after binning them in steps of 0.25 in $\log L_{\text{dust}}$ (filled squares with error bars). The solid black lines correspond to the average ratios for the real data points. The data points are the same as in Figures 4.31 and 4.32. The simulations are systematically low for longer wavelength lines ($\lambda > 50 \mu\text{m}$) as expected since they do not include the emission from outside H II regions.

- $\rho_{\text{gas}} \in [10 - 10000]$ and $\epsilon_{\text{gas}} \in [0.001 - 1.0]$ ⁴,
- $\log(\tau_V) \in [\log 2 - 2]$ as in da Cunha et al. (2010),
- $\mu\tau_V \in [0 - 2]$ as in da Cunha et al. (2010).

We made 300 simulations for each line. The derived line luminosities are shown in Figure 4.33 as a function of the continuum IR luminosity and compared with the available data. The solid black lines and the dashed blue lines correspond to a direct proportionality between $\log(L_\ell)$ and $\log(L_{\text{IR}})$, i.e., to the

⁴As these are the intervals considered by Panuzzo et al. (2003).

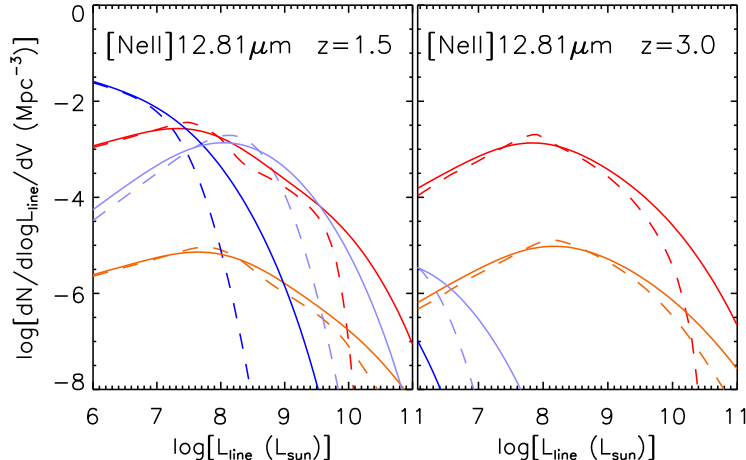


Figure 4.34: Effect of the dispersion in the line-to-IR luminosity ratio on the predicted luminosity function of the [Ne II] $12.81\mu\text{m}$ line. Solid lines: including dispersion; dashed lines: no dispersion. The colors identify the contributions of different source populations: blue and cyan for cold and warm late-type galaxies, respectively; red and orange for unlensed and strongly lensed proto-spheroids, respectively.

average ratios $c = \langle \log(L_\ell/L_{\text{IR}}) \rangle$ for real and simulated data, respectively. For simulated data the ratios were computed after binning them in steps of 0.25 in $\log L_{\text{dust}}$.

Overall, we find a good agreement between observed and simulated distributions of luminosities for lines with $\lambda < 50\mu\text{m}$. For these lines the simulations are consistent with a direct proportionality between L_ℓ and L_{IR} and the derived values of $c = \langle \log(L_\ell/L_{\text{IR}}) \rangle$ are consistent with the determinations directly based on the data. On the other hand, the luminosities of longer wavelength lines found from simulations fall systematically below the observed luminosities as expected, since, as mentioned above, the Panuzzo et al. (2003) library refers to the emission line spectrum of H II regions only.

Based on these results, we have adopted the mean $\log(L_\ell/L_{\text{IR}})$ (or the mean $\log(L_\ell)$ in the case of low- z ULIRGs) and the associated dispersions derived from observations, buying from simulations the indication of a direct proportionality between line and IR luminosity.

4.4.3 Predictions for the SPICA reference survey

The line LFs were derived from the IR ones allowing for the effect of the dispersion in the line-to-IR luminosity ratios. In practice, for each line, we generated 1000 simulations, each one corresponding to a random selection of $\log(L_\ell/L_{\text{IR}})$ or of $\log(L_\ell)$, drawn from Gaussian distributions with the mean values and the dispersions given in Table 4.3. The simulated line LFs were then averaged over bins of $\log(L_\ell)$. In Figure 4.34 we show, as an example, the effect of the dispersion on the predicted LF for the [Ne II] $12.81\mu\text{m}$ line. Since dispersions are substantial, they result in a vast increase, compared to the case without dispersion, of the density of the most luminous sources and, correspondingly, of the bright portion of source counts.

The differential number counts can be obtained by integrating the line LFs over redshift (see Equation (3.28)). The limits in redshift are set by the wavelength range covered by the instrument, $[\lambda_{\min}, \lambda_{\max}]$, and by the rest-frame wavelength, λ_ℓ , of the considered spectral line: $z_{\min,\max} = \lambda_{\min,\max}/\lambda_\ell - 1$.

The integral counts predicted by our model are shown, for all the 15 lines considered in this work, in

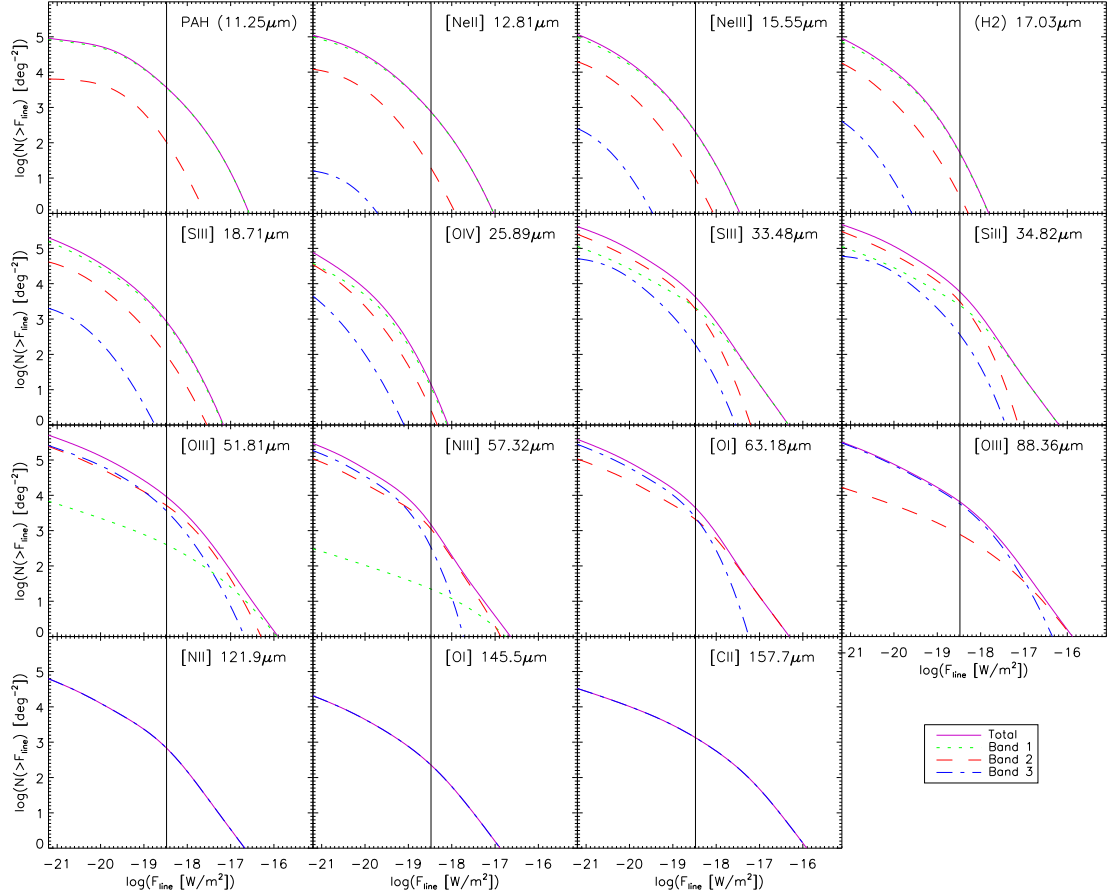


Figure 4.35: Integral counts of star-forming galaxies as a function of line fluxes over the full SPICA-SAFARI wavelength range (black solid line) and in each of its three bands. The vertical lines correspond to the average detection limit in the 3 bands for the reference survey.

Figure 4.35. According to B. Sibthorpe 2013 (private communication), the reference 5σ detection limits for an integration of 1 hr per FoV are $3.7 \times 10^{-19} \text{ W/m}^2$ for the first band ($34-60 \mu\text{m}$), $3.4 \times 10^{-19} \text{ W/m}^2$ for the second band ($60-110 \mu\text{m}$), and $2.9 \times 10^{-19} \text{ W/m}^2$ for the third band ($110-210 \mu\text{m}$). The expected surface density of sources detected at these limits, summing over the 3 bands, range from a few to several thousands of sources. With the exception of 4 lines ([Ne III] $15.55 \mu\text{m}$, H₂ $17.03 \mu\text{m}$, [S III] $18.71 \mu\text{m}$, and [O IV] $25.89 \mu\text{m}$) out of 15, the slope of the integral counts just below the detection limits of the reference survey is < 2 so that the number of detections for given observing time increases more with the surveyed area than with survey depth.

The predicted numbers of sources detected in each line by the survey considered by Spinoglio et al. (2012), covering 0.5 deg^2 with a 1 hr integration/FoV (hereafter “the reference survey”) are given in the last column of Table 4.4. The other columns detail the redshift distributions of detected sources. Examples of such redshift distributions are displayed, for 4 lines, in Figure 4.36, were the redshift ranges covered by the different bands are identified by different colors. Obviously, only the shortest wavelength lines can be detected up to very high redshifts. According to our model, the reference survey can detect the PAH $11.25 \mu\text{m}$ line in some galaxies at redshifts up to $\simeq 6$.

Figure 4.37 illustrates the luminosity and redshift distributions of sources for which the reference

Table 4.4: Predicted redshift distributions of star-forming galaxies detectable by the reference survey in each of the 15 emission lines considered in this paper.

Spectral line	0.00 – 0.75	0.75 – 1.25	1.25 – 1.75	1.75 – 2.25	2.25 – 2.75	2.75 – 4.00	4.00 – 6.00	All z
PAH 11.25 μm	0	0	0	375	574	547	82	1578
[Ne II] 12.81 μm	0	0	47	148	73	49	4	321
[Ne III] 15.55 μm	0	8	47	21	9	5	0	90
H ₂ 17.03 μm	0	7	9	4	2	1	0	23
[S III] 18.71 μm	0	200	109	48	26	15	1	399
[O IV] 25.89 μm	4	1	1	0	0	0	0	6
[S III] 33.48 μm	885	652	290	125	76	43	2	2073
[Si II] 34.82 μm	1176	952	440	189	116	68	3	2944
[O III] 51.81 μm	1655	1454	1061	422	219	155	0	4966
[N III] 57.32 μm	478	220	91	49	18	4	0	860
[O I] 63.18 μm	1038	874	373	161	78	4	0	2528
[O III] 88.36 μm	1802	1574	1009	0	0	0	0	4385
[N II] 121.9 μm	412	108	0	0	0	0	0	520
[O I] 145.5 μm	182	0	0	0	0	0	0	182
[C II] 157.7 μm	1312	0	0	0	0	0	0	1312

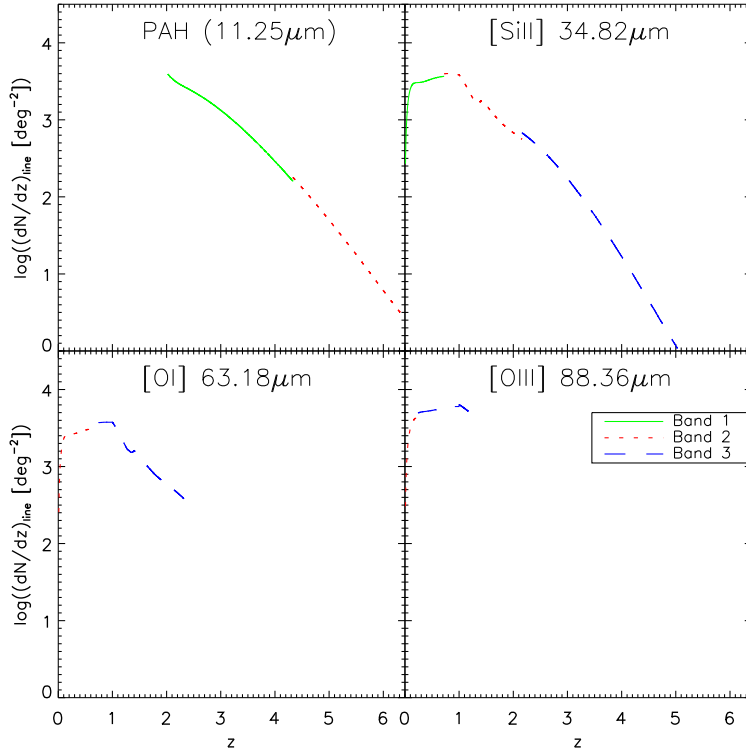


Figure 4.36: Examples of the predicted redshift distributions of sources detected by SPICA/SAFARI for a 1 hr exposure per FoV. The different colors correspond to the 3 spectral bands.

survey will detect 2, 3, or 4 lines. From our model we expect about 4740 sources detected in two lines, about 2900 in 3 lines, and about 1890 in 4 lines. The numbers of proto-spheroids among these are about 965, 510, and 310, respectively.

Figure 4.38 compares the present predictions of the redshift distributions of sources detected by the reference survey in 4 lines with those from the 3 models used by Spinoglio et al. (2012). The main differences concern the PAH 11.25 μm line, for which our predictions are substantially higher than those from all the other models. On the contrary, our results are generally lower for the [O I] 63.18 μm line. Most differences are within a factor ~ 2 ; the largest are those with the Valiante et al. (2009) model in the low redshift bins of the [O I] 63.18 μm and [O III] 88.36 μm lines.

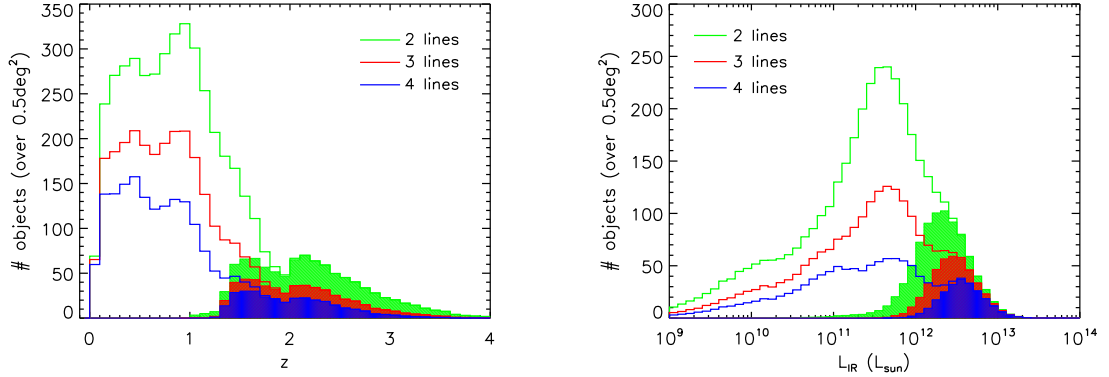


Figure 4.37: Predicted redshift (left) and luminosity (right) distributions of star-forming galaxies detectable in two (green histogram), three (red), and four (blue) spectral lines, by the reference survey with SPICA/SAFARI. The shaded areas represent the contributions of proto-spheroids.

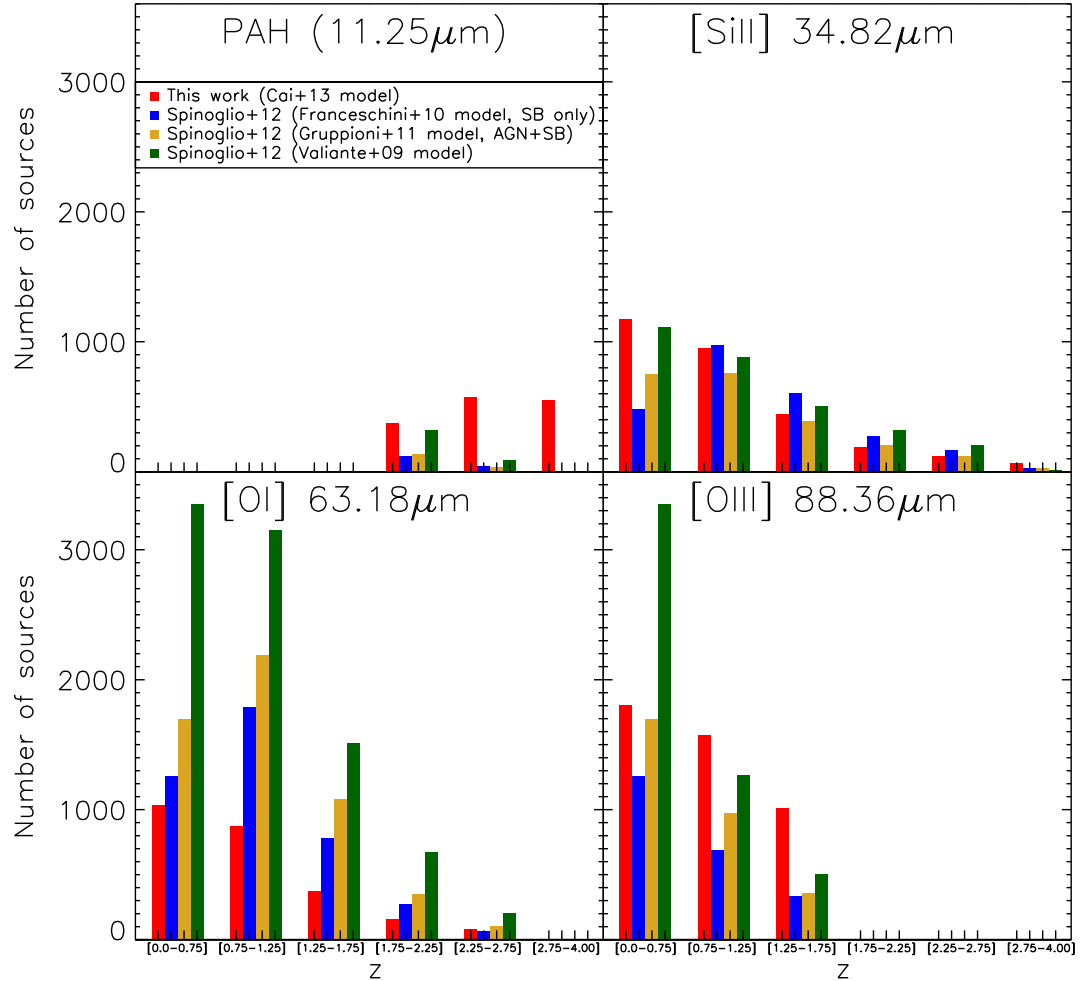


Figure 4.38: Redshift distributions of star-forming galaxies detectable in the each of the 4 lines considered in the previous figures by the reference survey. The predictions of our model (red bars) are compared with those of the 3 models used by Spinoglio et al. (2012): Franceschini et al. (2010), Gruppioni et al. (2011), and Valiante et al. (2009); see the legend in the top left panel.

Chapter 5

Early UV–bright star formation and reionization

5.1 Ingredients of the model

We adopt the same values of the parameters as for the IR model discussed in the previous Chapter with only one exception, due to the fact that Cai et al. (2013) dealt with relatively high halo masses ($M_{\text{vir}} \gtrsim 10^{11.3} M_{\odot}$) while, at the high redshifts of interest here, the masses of interest are substantially lower. As pointed out by Shankar et al. (2006), the data indicate that the star formation efficiency in low-mass halos must be lower than implied by the SN feedback efficiency gauged for higher halo masses. In other words, as extensively discussed in the literature, external (UV background) or internal (SN explosions, radiation from massive low-metallicity stars and, possibly, stellar winds) heating processes can reduce the star formation rate in low-mass halos (e.g. Hambrick et al. 2011; Krumholz & Dekel 2012; Pawlik et al. 2013; Sobacchi & Mesinger 2013) and completely suppress it below a critical halo mass, M_{crit} .

We take this into account by increasing the SN feedback efficiency with decreasing halo mass and introducing a low-mass cutoff, i.e., considering only galaxies with $M_{\text{vir}} \geq M_{\text{crit}}$. The rate of cold gas mass loss due to SN feedback is parameterized as in Equation (3.7) in terms of the star formation rate \dot{M}_{\star} and of the effective efficiency of gas removal β_{SN} , which depends on the number, N_{SN} , of SNe per unit solar mass of condensed stars, on the energy per SN, ϵ_{SN} , available to remove the cold gas, on the kinetic energy, E_{SN} , released per SN, and on the halo binding energy E_{bind} . For our low-mass halos we set:

$$\epsilon_{\text{SN}} = 0.05 \{3 + \text{erf}[-\log(M_{\text{vir}}/10^{11} M_{\odot})/0.5]\}/2, \quad (5.1)$$

that converges, for $M_{\text{vir}} \geq 10^{11} M_{\odot}$, to the constant value, $\epsilon_{\text{SN}} = 0.05$, used by Cai et al. (2013).

The critical halo mass can be estimated equating the gas thermal speed in virialized halos to the escape velocity to find $M_{\text{crit}} \simeq 2 \times 10^8 (T/2 \times 10^4 \text{ K})^{3/2} M_{\odot}$ (Hambrick et al. 2011), where $2 \times 10^4 \text{ K}$ corresponds to the peak of the hydrogen cooling curve. If the balance between heating and cooling processes results in

higher gas temperatures, M_{crit} can increase even by a large factor. An accurate modeling of the physical processes involved is difficult and numerical simulations yield estimates of $M_{\text{crit}}/M_{\odot}$ in the range from 4×10^8 to $\gtrsim 10^9$ (Hambrick et al. 2011; Krumholz & Dekel 2012; Pawlik et al. 2013; Sobacchi & Mesinger 2013), with a trend towards lower values at $z > 6$ when the intensity of the UV background is expected to decrease.

If, on one side, heating properties can decrease the star formation rate (SFR) in small galactic halos, the production of UV photons per unit stellar mass is expected to substantially increase with redshift, at least at $z \gtrsim 3$. Padoan et al. (1997) argued that the characteristic stellar mass, corresponding to the peak in the initial stellar mass function (IMF) per unit logarithmic mass interval, scales as the square of the temperature, T_{mc} , of the giant molecular clouds within which stars form. But the typical local value of T_{mc} (~ 10 K) is lower than the cosmic microwave background temperature at $z \gtrsim 3$, implying a rapid increase with z of the characteristic stellar mass, hence of the fraction of massive stars producing UV photons. On the other hand, a higher fraction of massive stars also implies a more efficient gas heating, hence a stronger quenching of the SFR. This complex set of phenomena tend to counterbalance each other. Therefore in the following we adopt, above M_{crit} , the SFR given by the model and the UV (ionizing and non-ionizing) photon production rate appropriate to the Chabrier (2003) IMF, allowing for the possibility of a correction factor to be determined by comparison with the data.

5.2 Non-ionizing UV photons and cosmic star formation rate history

5.2.1 Luminosity functions of Lyman break galaxies

The model allows us to compute the evolution with galactic age of the SFR, of the mass in stars, of the metal abundance of the gas, and of dust extinction as a function of the halo mass and of the halo formation redshift. Illustrative examples are shown in Figure 5.1. A few points are worth noting: i) the active star formation phase in the most massive halos ($M_{\text{vir}} \gtrsim 10^{12} M_{\odot}$) is abruptly terminated by the AGN feedback, while in less massive halos, where the feedback is dominated by stellar processes, the SFR declines more gently; ii) at fixed halo mass, the SFR is initially higher at higher redshifts (because the higher densities imply faster cooling of the gas) and declines earlier; iii) the stellar to halo mass ratio and the metallicity are higher for galaxies that formed at higher redshifts; iv) the UV extinction is always low for the least massive galaxies ($M_{\text{vir}} \leq 10^{11} M_{\odot}$), but increases with increasing z paralleling the increase in the gas metallicity.

The absolute magnitude of a galaxy at our reference UV wavelength, $\lambda \approx 1350$ Å, in the AB system, is related to its star formation rate and to dust extinction A_{λ} as

$$M_{1350} = 51.59 - 2.5 \frac{\log \bar{L}_{1350}}{\text{erg s}^{-1} \text{Hz}^{-1}} + A_{1350}, \quad (5.2)$$

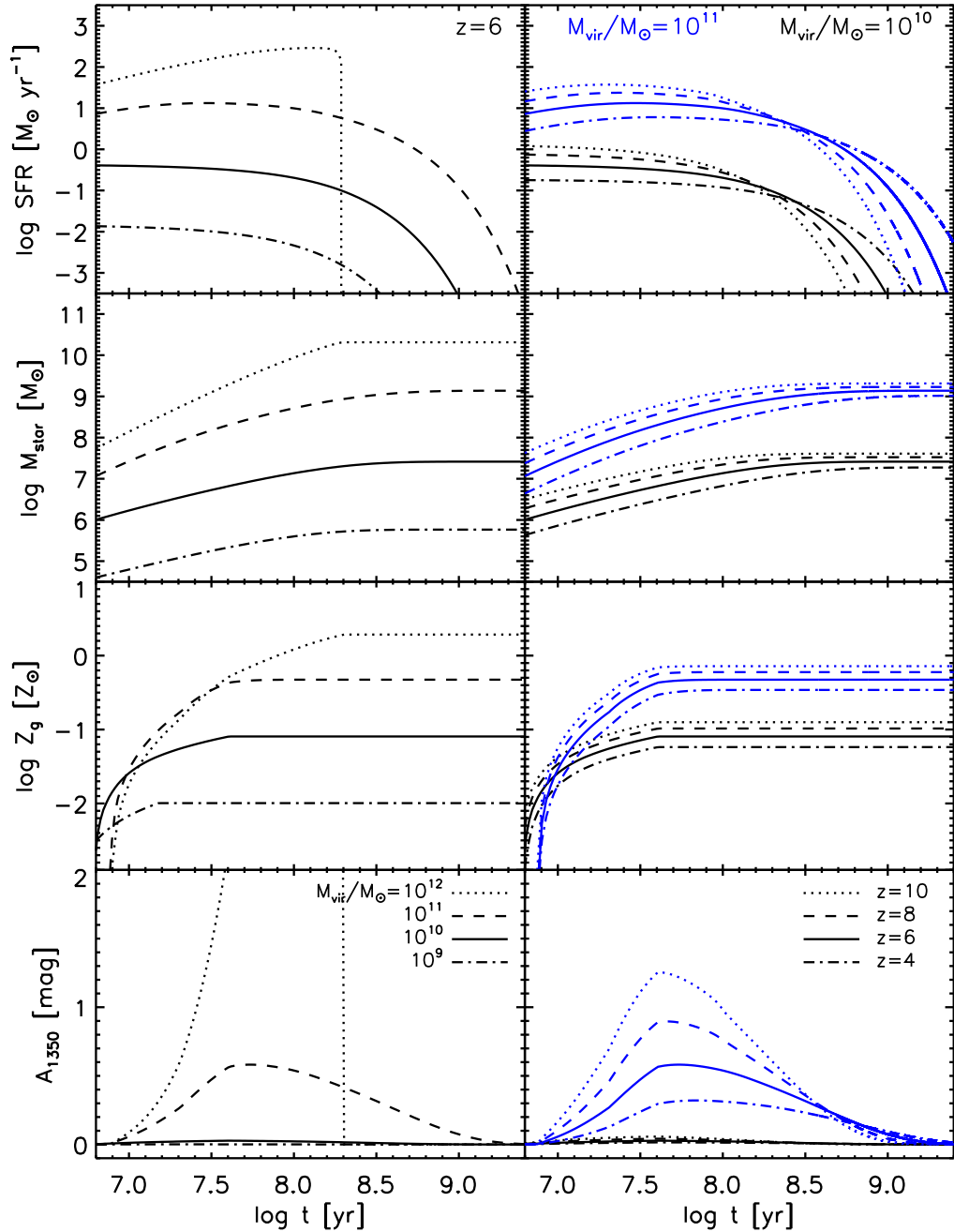


Figure 5.1: Left panels: Evolution with galactic age of the SFR, of the stellar mass M_{star} , of the gas metallicity Z_g , and of the dust extinction A_{1350} (from top to bottom) for halo masses of $M_{\text{vir}} = 10^9$ (dot-dashed lines), 10^{10} (solid lines), 10^{11} (dashed lines), and $10^{12} M_{\odot}$ (dotted lines) virialized at $z = 6$. Right panels: Evolution of the quantities on the left panels at fixed halo mass ($M_{\text{vir}} = 10^{10} M_{\odot}$ and $10^{11} M_{\odot}$, black and blue lines, respectively) for different redshifts: $z = 4$ (dot-dashed lines), 6 (solid lines), 8 (dashed lines), and 10 (dotted lines).

with

$$\frac{\bar{L}_{1350}}{\text{erg s}^{-1} \text{Hz}^{-1}} = k_{\text{UV}} \frac{\dot{M}_{\star}}{M_{\odot} \text{yr}^{-1}}, \quad (5.3)$$

where \bar{L}_{1350} is the monochromatic luminosity at the frequency corresponding to 1350 Å. On account of the uncertainties on the IMF at high z , mentioned above, we treat the normalization factor k_{UV} ($\text{erg s}^{-1} \text{Hz}^{-1} M_{\odot}^{-1} \text{yr}$) as an adjustable parameter and adopt as reference values those found for a Chabrier (2003) IMF.

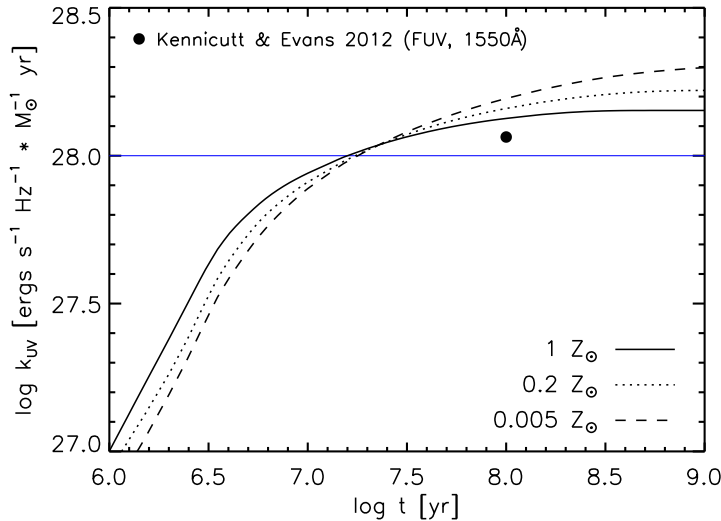


Figure 5.2: Evolution with galactic age of the coefficient k_{UV} (Equation (5.3)) for a constant SFR, a Chabrier (2003) IMF, and three gas metallicities: $Z_g = 0.005$ (dashed line), 0.02 (dotted line), and $1 Z_\odot$ (solid line). The far-UV/SFR calibration by Kennicutt & Evans (2012) for solar metallicity and a Kroupa IMF is also shown (filled circle at $\log(t/\text{[yr]}) = 8$). The horizontal blue line corresponds to the value adopted in the present paper.

Using the evolutionary stellar models of Fagotto et al. (1994a,b) we find that k_{UV} varies with galactic age and gas metallicity as illustrated by Figure 5.2. Most of the contributions to the UV luminosity function come from galactic ages $\geq 10^7$ yr, when $\log k_{\text{UV}} \geq 27.8$ and is somewhat higher for lower metallicity. We remind that the relationship between the absolute AB magnitude at the effective frequency ν , M_ν , and the luminosity is $\log[(\nu L_\nu)/L_\odot] = 2.3995 - \log(\lambda/1350 \text{ \AA}) - 0.4 M_\nu$ where $L_\odot = 3.845 \times 10^{33} \text{ erg s}^{-1}$.

We adopt the standard “dust screen” model for dust extinction, so that the observed luminosity is related to the intrinsic one by

$$L_{\text{obs}}(\lambda) = L_{\text{int}}(\lambda) 10^{-0.4 A_\lambda}, \quad (5.4)$$

with the Calzetti et al. (2000) reddening curve for $0.12 \mu\text{m} \leq \lambda \leq 0.63 \mu\text{m}$:

$$A_\lambda/E_s(B-V) \equiv k(\lambda) \simeq 2.659(-2.156 + 1.590/\lambda - 0.198/\lambda^2 + 0.011/\lambda^3) + R_V \quad (5.5)$$

where $E_s(B-V)$ is the color excess of the galaxy stellar continuum and $R_V = 4.05$. This gives $A_{1350}/E_s(B-V) \simeq 11.0$ and $A_{1216} \simeq 1.08 A_{1350}$. If Equation (5.5) is approximately valid up to 912 Å we further have $A_{912} \simeq 1.59 A_{1350}$.

The dust extinction is proportional to the dust column density which, in turn, is proportional to the gas column density, N_{gas} , times the metallicity to some power reflecting the fraction of metals locked into dust grains. As discussed by Mao et al. (2007), according to our model we have, approximately, $N_{\text{gas}} \propto M_{\text{cold}}^{1/3} \propto \dot{M}_*^{1/3}$. We thus expect that $A_{1350} \propto \dot{M}_*^\alpha Z_g^\beta$. Mao et al. (2007) found that a relationship of this kind

$$A_{1350} \approx 0.35 \left(\frac{\dot{M}_*}{M_\odot \text{ yr}^{-1}} \right)^{0.45} \left(\frac{Z_g}{Z_\odot} \right)^{0.8}, \quad (5.6)$$

does indeed provide a good fit of the luminosity-reddening relation found by Shapley et al. (2001). This

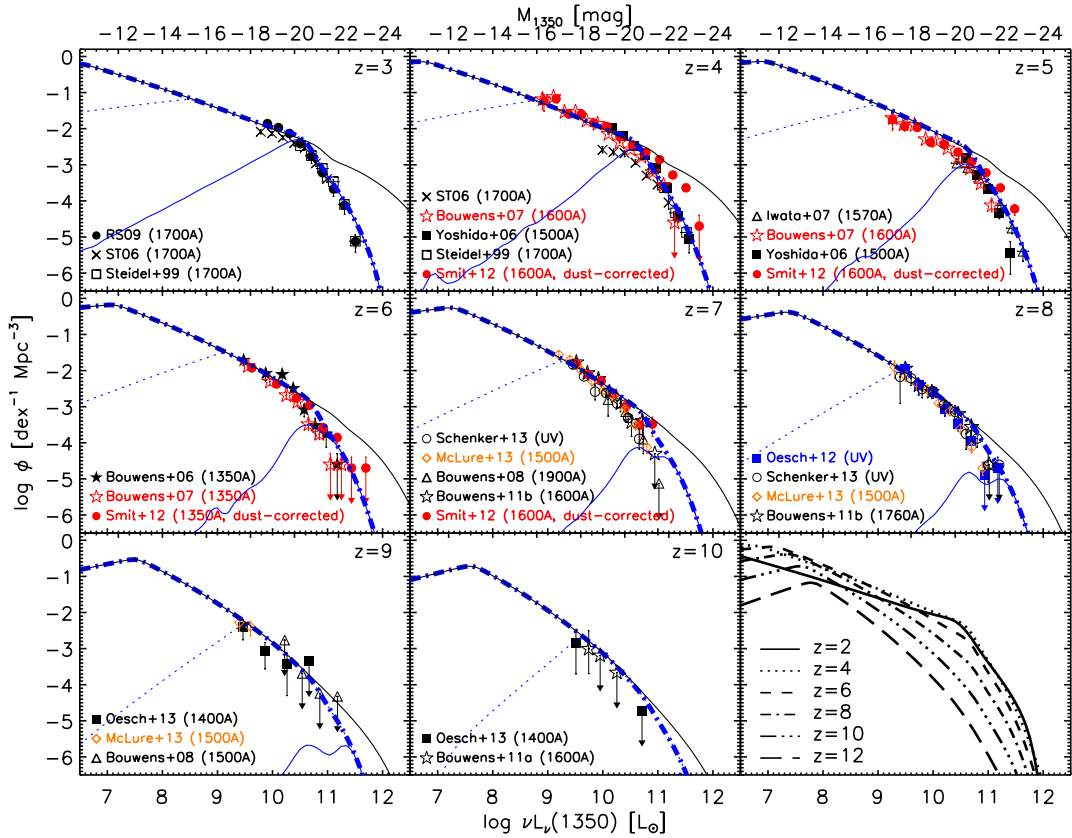


Figure 5.3: Luminosity functions at 1350 Å at several redshifts, specified in the upper right corner of each panel. The upper scale gives the UV magnitudes corresponding to the UV luminosities at 1350 Å. The solid black lines show the predicted luminosity function neglecting extinction while the dot-dashed blue lines include the effect of extinction. The low luminosity break corresponds to $M_{\text{crit}} = 10^{8.5} M_{\odot}$. The thin dotted and solid blue lines show the effect of increasing the minimum halo mass to $10^{9.8} M_{\odot}$ and $10^{11.2} M_{\odot}$, respectively, including extinction. The extinction affects mostly the highest luminosities, associated to the most massive objects which have the fastest chemical enrichment (see Figure 5.1). As illustrated by the bottom right panel, showing the evolution of the luminosity function, its faint portion is predicted to steepen with increasing redshift. The model implies a weak evolution of the luminosity function from $z = 2$ to $z = 6$. The data are from Steidel et al. (1999), Sawicki & Thompson (2006a, ST06), Yoshida et al. (2006), Iwata et al. (2007), Reddy & Steidel (2009, RS09), Bouwens et al. (2006, 2007, 2008, 2011a,b), Smit et al. (2012), Schenker et al. (2013), McLure et al. (2013), and Oesch et al. (2012, 2013). Only the estimates by Smit et al. (2012) include an (uncertain) correction for dust extinction, based on the slope of the UV continuum.

relation will be adopted in the following.

Coupling the halo formation rate with the relationship between halo mass and SFR as a function of cosmic time, τ , and with the relationship between SFR and UV luminosity (Equation (5.2)), the comoving differential UV luminosity function $\Phi(\log L_{1350}, z)$, i.e., the number density of galaxies per unit $\log L_{1350}$ interval at redshift z , can then be computed following Equation (3.22), where we set $z_{\text{vir}}^{\max} = 16$, $M_{\text{vir}}^{\max} = 10^{13.3} M_{\odot}$, and $M_{\text{vir}}^{\min} = M_{\text{crit}}$.

Figure 5.3 shows that the model is nicely consistent with observational estimates of the UV luminosity function over the full redshift range from $z \sim 3$ to $z \sim 10$, without any adjustment of the parameters and adopting a value of $k_{\text{UV}} = 1.0 \times 10^{28} \text{ erg s}^{-1} \text{ Hz}^{-1} M_{\odot}^{-1} \text{ yr}$ (Equation (5.3), see also Figure 5.2).

Observational determinations of UV luminosity functions were made at various rest-frame wavelengths. However, since the UV continuum slope, β ($f_{\lambda} \propto \lambda^{\beta}$), of high- z galaxies is close to $\beta = -2$ (Bouwens et al. 2012; Castellano et al. 2012), the color correction $M_{\text{AB},\lambda_1} - M_{\text{AB},\lambda_2} = -2.5(\beta +$

2) $\log(\lambda_1/\lambda_2)$ is small and will be neglected. A few points are worth noting:

- The effect of dust extinction is highly differential in luminosity as is clearly seen comparing the solid black lines (no extinction) with the dot-dashed blue lines (extinction included). This follows from the faster metal enrichment in the more massive objects (see Figure 5.1), where the SN and radiative feedbacks are less effective in depressing the SFR.
- Figure 5.1 also shows that the least massive galaxies have low extinction throughout their lifetime. This means that, in the present framework, their UV luminosity function can be linked to the halo formation rate without the complication of uncertain extinction corrections. Since the luminosity function is increasingly dominated by lower mass halos at higher and higher redshifts, the difference between the luminosity functions with and without extinction becomes increasingly small.
- The luminosity function has, at the faint end, a break corresponding to M_{crit} , the mass below which the star formation is suppressed by external and internal heating processes (see Section 5.1). In Figure 5.3 $M_{\text{crit}} = 10^{8.5} M_{\odot}$ but in the panels comparing the model with the data at various redshifts the thin dotted and solid blue lines show the effect of increasing M_{crit} to $10^{9.8} M_{\odot}$ and $10^{11.2} M_{\odot}$, respectively. This shows that the data only constrain M_{crit} to be $\leq 10^{9.8} M_{\odot}$, consistent with estimates from simulations.
- The higher feedback efficiency for less massive halos (Equation (5.1)) makes the slope of the faint end of the luminosity function (above the break) flatter than that of the low mass end of the halo formation rate function (illustrated by Figure 2.2). However the former slope reflects to some extent the steepening with increasing redshift of the latter. The dust extinction, differential with halo mass, further steepens the bright end of the observed UV luminosity function.
- As shown by the bottom right panel of Figure 5.3, the model implies that the evolution of the luminosity function from $z = 2$ to $z = 6$ is weak. In particular the fast decrease with increasing redshift of the high mass halo formation rate (Figure 2.2) is not mirrored by the bright end of the luminosity function. This is partly due, again, to the fast metal enrichment of massive galaxies that translates into a rapid increase of dust extinction and, consequently, in a short duration of their UV bright phase (Figure 5.1). Thus the contribution to the UV luminosity function of galaxies in halos more massive than $\sim 10^{11.2} M_{\odot}$ (thin solid blue line in Figure 5.3) decreases rapidly with increasing redshift and galaxies with $M_{\text{vir}} \gg 10^{11.2} M_{\odot}$ contribute very little. The UV luminosity function at high z is therefore weakly sensitive to the rapid variation of formation rate of the latter galaxies. The milder decrease of the formation rates of less massive galaxies is largely compensated by the increase of the star formation efficiency due to the faster gas cooling. At $z > 6$ however, the decrease of the formation rate even of intermediate mass galaxies prevails and determines a clear negative evolution of the UV luminosity function.
- The average properties, weighted by the halo formation rate, of galaxies at $z = 3, 6$, and 12 are shown, as a function of the observed luminosity, in the left panels of Figure 5.4. Ages are, on average,

substantially younger for the brighter galaxies, which are associated to the most massive halos and may reach SFR $\sim 100 M_\odot \text{ yr}^{-1}$. At $z \sim 3$ the range of stellar masses of galaxies in the luminosity interval covered by observations ($-18 \lesssim M_{1350} \lesssim -23$) is remarkably narrow, around few $\times 10^9 M_\odot$. At $z \simeq 6$ the stellar masses in the observed luminosity interval range from $\simeq 10^9 M_\odot$ to $\simeq 3 \times 10^9 M_\odot$.

5.2.2 Cosmic star formation rate history

The fact that the star formation in massive galaxies is dust enshrouded over most of its duration implies that these galaxies show up primarily at far-IR/(sub-)millimeter wavelengths. Thus the present framework predicts a continuity between the high- z galaxy SFR function derived from the UV luminosity function (dominated by low-mass galaxies) and that derived from the infrared (IR; 8–1000 μm) luminosity function (dominated by massive galaxies), investigated by Lapi et al. (2011) and Cai et al. (2013). In Figure 5.5 this prediction is tested against observational data at $z = 2$ and 3. Once proper allowance for the effect of dust attenuation is made, the model accurately matches the IR and the UV luminosity functions and, as predicted, UV and IR data cover complementary SFR ranges.

The SFR histories inferred from UV and far-IR data are compared in Figure 5.6. This figure shows that the ratio of dust-obscured to unobscured SFR increases with increasing redshift until it reaches a broad maximum at $z \sim 2$ –3 and decreases afterwards. This entails a prediction for the evolution of the IR luminosity density, ρ_{IR} , beyond $z \simeq 3.5$, where it cannot yet be determined observationally. According to the present model, at these redshifts, ρ_{IR} decreases with increasing z faster than the UV luminosity density, ρ_{UV} . In other words, the extinction correction needed to determine the SFR density from the observed ρ_{UV} is increasingly small at higher and higher redshifts. This is because the massive halos, that can reach high values of dust extinction, become increasingly rare at high z .

5.3 Ionizing photons and cosmic reionization

5.3.1 Luminosity functions of Lyman alpha emitters

The ionizing photons ($\lambda \leq 912 \text{ \AA}$) can be absorbed by both dust and neutral hydrogen. About 2/3 of those absorbed by HI are converted into Ly α photons (Osterbrock 1989; Santos 2004), so that the luminosity functions of Ly α emitters (LAEs) provide information on their production rate. The Ly α line luminosity before extinction is then

$$L_{\text{Ly}\alpha}^{\text{int}} = \frac{2}{3} \dot{N}_{912}^{\text{int}} f_{912}^{\text{dust}} (1 - f_{912}^{\text{HI}}) h\nu_{\text{Ly}\alpha} \quad (5.7)$$

where $\dot{N}_{912}^{\text{int}}$ is the production rate of ionizing photons while $f_{912}^{\text{dust}} = \exp(-A_{912}/1.08)$ and $f_{912}^{\text{HI}} = \exp(-\tau_{\text{HI}})$ are the fractions of them that escape absorption by dust and by HI, respectively. In analogy to Equation (5.6) we set

$$\tau_{\text{HI}} = \tau_{\text{HI}}^0 \left(\frac{\dot{M}_*}{M_\odot \text{ yr}^{-1}} \right)^{\alpha_{\text{HI}}} . \quad (5.8)$$

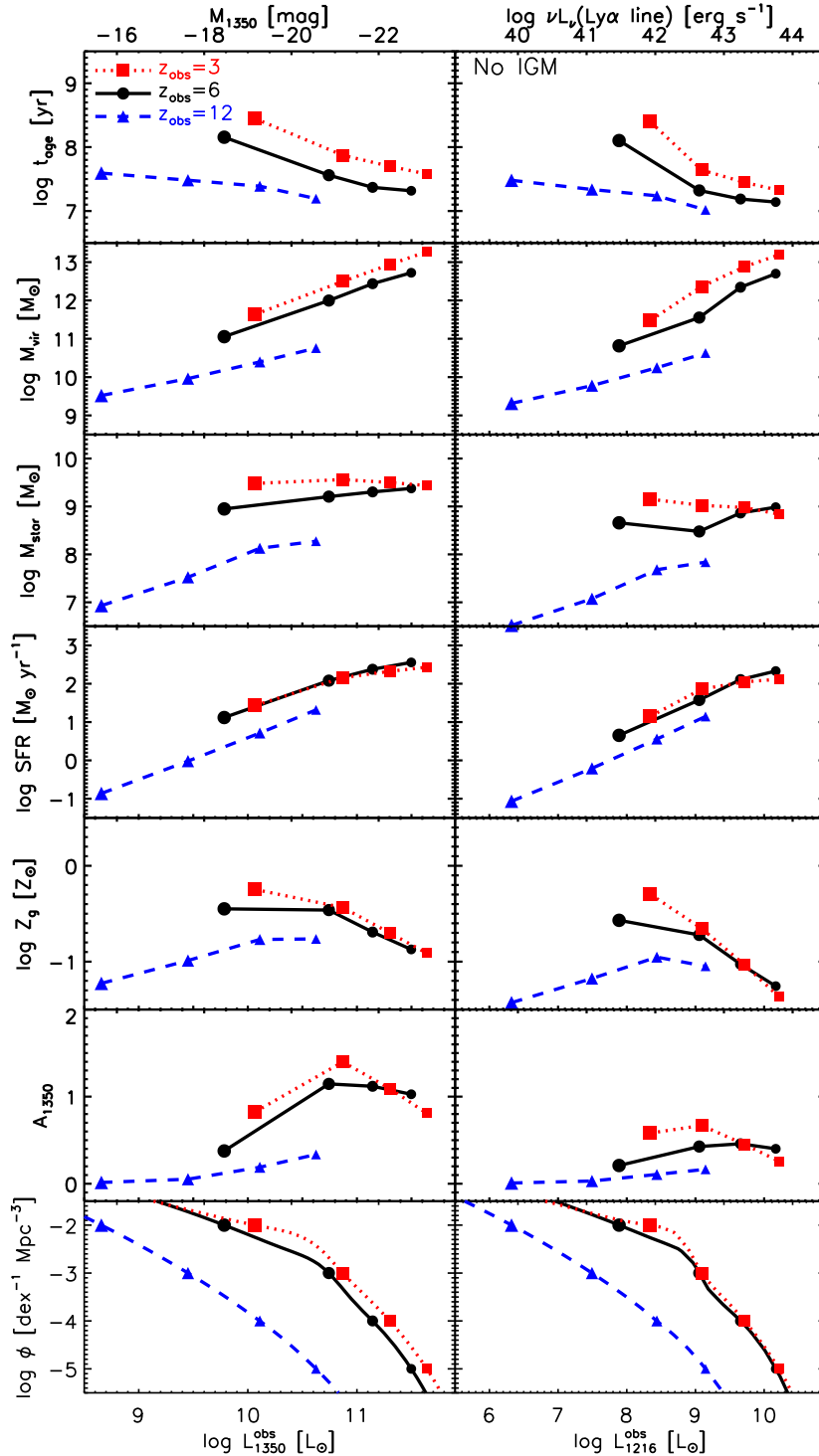


Figure 5.4: Average properties, weighted by the halo formation rate, of modeled galaxies at $z_{\text{obs}} = 3, 6$, and 12 (filled red squares, black circles, and blue triangles, respectively) as a function of the UV luminosity (left panels) and of the observed Ly α luminosity without the IGM attenuation (right panels). Larger symbols correspond to more numerous objects.

The evolution with galactic age of $\dot{N}_{912}^{\text{int}}$, for a Chabrier (2003) IMF, a constant SFR of $1 M_{\odot} \text{ yr}^{-1}$, and three values of the gas metallicity is illustrated by Figure 5.7. We adopt an effective ratio $k_{\text{ion}} \equiv \dot{N}_{912}^{\text{int}} / \dot{M}_{\star} (M_{\odot} \text{ yr}^{-1}) \simeq 4.0 \times 10^{53} \text{ photons s}^{-1}$, appropriate for the typical galactic ages and metallicities

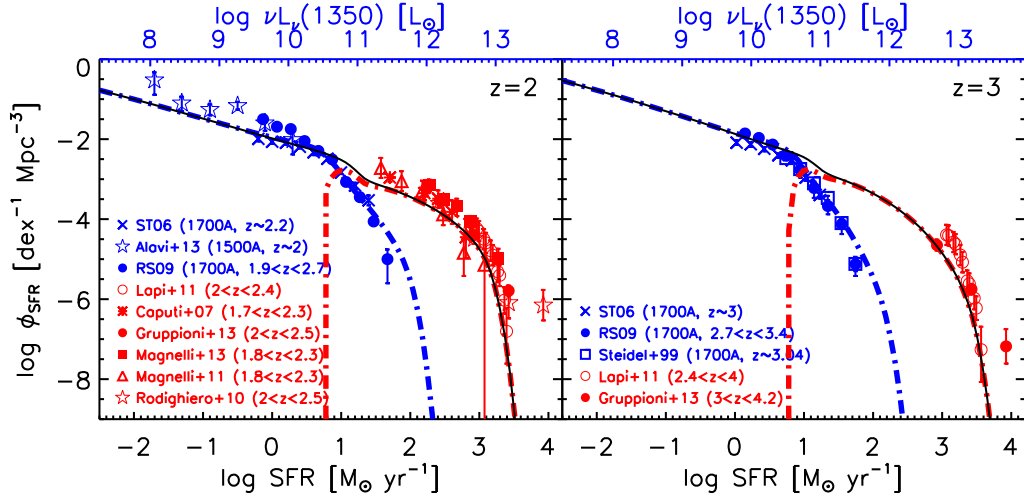


Figure 5.5: Comparison of the SFR functions yielded by the model at $z = 2$ and 3 with those inferred from IR ($8\text{--}1000\,\mu\text{m}$, red data points; Caputi et al. 2007; Rodighiero et al. 2010; Lapi et al. 2011; Gruppioni et al. 2013; Magnelli et al. 2011, 2013) and UV (blue data points; Steidel et al. 1999; Sawicki & Thompson 2006b; Reddy & Steidel 2009; Alavi et al. 2013) luminosity functions. The conversion of IR luminosities into SFRs was done using the Kennicutt & Evans (2012) calibration. The SFR function from IR data can be directly compared to the SFR function yielded by the model (solid black line) because the star formation in these IR-bright galaxies is almost entirely dust-obscured and the contribution of older stars to dust heating is negligible. The dot-dashed blue lines show the model SFR functions as determined from eq. (5.3) with $k_{\text{UV}} = 1.0 \times 10^{28}\,\text{erg s}^{-1}\,\text{Hz}^{-1}\,M_{\odot}^{-1}\,\text{yr}$, applied to “observed” (i.e., attenuated by dust) UV luminosities, and therefore these curves can be directly compared with the observed UV data, uncorrected for attenuation. The dot-dashed blue lines converge to the black lines at low SFRs, for which the dust attenuation is small.

of our sources. The figure also shows the evolution of the intrinsic ratio of Lyman continuum ($\lambda \leq 912\,\text{\AA}$; $L_{912}^{\text{int}} = \dot{N}_{912}^{\text{int}} h \text{ erg s}^{-1} \text{ Hz}^{-1}$) to UV luminosity at $1350\,\text{\AA}$, $R_{\text{int}} \equiv L_{912}^{\text{int}} / L_{1350}^{\text{int}}$. For our choice of k_{ion} and k_{UV} (Equation (5.3)) we have $R_{\text{int}} \simeq 0.265$.

The interstellar dust attenuates $L_{\text{Ly}\alpha}^{\text{int}}$ by a further factor $f_{\text{Ly}\alpha}^{\text{dust}} = \exp(-\tau_{\text{Ly}\alpha}^{\text{dust}})$, where $\tau_{\text{Ly}\alpha}^{\text{dust}}$ is the dust optical depth at the Ly α wavelength ($1216\,\text{\AA}$). The physical processes governing the escape of Ly α photons from galaxies are complex; dust content, neutral gas kinematics, and the geometry of the neutral gas seem to play the most important roles. For objects with low dust extinction, such as those relevant here, the detailed calculations of the Ly α radiation transfer by Duval et al. (2013, see their Figs. 18 and 19) show that the Ly α is more attenuated than the nearby UV continuum by a factor $\simeq 2$, consistent with the observational result (e.g., Gronwall et al. 2007) that the star formation rates derived from the Ly α luminosity are $\simeq 3$ times lower than those inferred from the rest-frame UV continuum. With reference to the latter result, it must be noted that part of the attenuation of the Ly α luminosity must be ascribed to the IGM (see below) and that the discrepancy between Ly α and UV continuum star formation rates may be due, at least in part, to uncertainties in their estimators. Fits of the Ly α line luminosity functions (see below) indicate $f_{\text{Ly}\alpha}^{\text{dust}} \simeq f_{1216}^{\text{dust}} / 1.6$, where $f_{1216}^{\text{dust}} = \exp(-A_{1216}/1.08) \simeq f_{1350}^{\text{dust}}$.

The fraction $f_{\text{Ly}\alpha}^{\text{IGM}} = \exp(-\tau_{\text{Ly}\alpha}^{\text{IGM}})$ of Ly α photons that survive the passage through the IGM was computed following Madau (1995), taking into account only the absorption of the blue wing of the line

$$f_{\text{Ly}\alpha}^{\text{IGM}} = 0.5 \{1 + \exp[-0.0036(1+z)^{3.46}]\}. \quad (5.9)$$

The strong attenuation by dust within the galaxy and by HI in the IGM implies that estimates of the

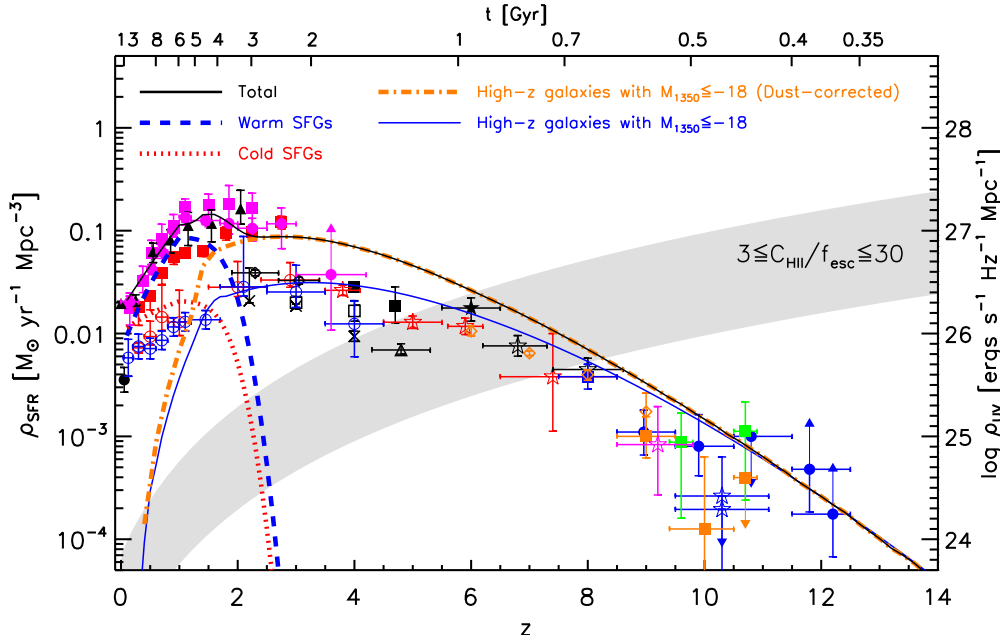


Figure 5.6: History of cosmic SFR density. The solid black line shows the global value, sum of the contributions of warm (dashed blue line) and cold (dotted red line) late-type galaxies and of proto-spheroidal galaxies with intrinsic $M_{1350} \leq -18$ (dot-dashed orange line, that overlaps the solid black line for $z > 2$). The SFR density of late-type galaxies was computed using the Cai et al. (2013) model; that of proto-spheroidal galaxies was computed with the present model, including halo masses $\log(M_{\text{vir}}/M_\odot) \geq 8.5$. The solid blue line shows the evolution, as given by our model, of the SFR density of galaxies with observed (i.e., attenuated by dust) magnitudes brighter than $M_{1350} = -18$, already represented in the observed UV luminosity functions. The gray region illustrates the minimum SFR densities required to keep the universe fully ionized if $3 \lesssim C_{\text{HII}}/f_{\text{esc}} \lesssim 30$ (Madau et al. 1999). Observational estimates of SFR densities from UV data are from Wyder et al. (2005, filled black circles), Schiminovich et al. (2005, open red circles), Cucciati et al. (2012, open blue circles), Sawicki & Thompson (2006b, black crosses), Steidel et al. (1999, open black squares), Yoshida et al. (2006, filled black squares), Iwata et al. (2007, open black triangle), Reddy & Steidel (2009, open black diamonds), Bouwens et al. (2006, 2007, 2011a,b, 2013, filled black star, open red stars, open blue star, open black stars, and open magenta star, respectively), Oesch et al. (2012, 2013, filled blue and orange square, respectively), Coe et al. (2013, filled green squares), McLure et al. (2013, open orange diamonds), and Ellis et al. (2013, filled blue circles). For completeness we also show SFR densities inferred from far-IR/sub-mm (Rodighiero et al. 2010; Gruppioni et al. 2013; Magnelli et al. 2013, filled magenta squares, filled magenta circles, and filled black triangles, respectively) and radio (Karim et al. 2011, filled red squares) data.

SFR of high-\$z\$ LBGs and LAEs from the observed Ly\$\alpha\$ luminosity require careful corrections and are correspondingly endowed with large uncertainties. Vice versa, the statistics of LAEs and LBGs at high redshifts are sensitive absorption/extinction probes.

All in all, the observed Ly\$\alpha\$ line luminosity writes

$$L_{\text{Ly}\alpha}^{\text{obs}} \simeq 4.36 \times 10^{42} \left(\frac{\dot{M}_\star}{M_\odot \text{ yr}^{-1}} \right) f_{912}^{\text{dust}} (1 - f_{912}^{\text{HI}}) f_{\text{Ly}\alpha}^{\text{dust}} f_{\text{Ly}\alpha}^{\text{IGM}} \text{ erg s}^{-1}. \quad (5.10)$$

Nestor et al. (2013) measured the ratios of non-ionizing UV to Lyman-continuum flux density corrected for IGM attenuation, η_{obs} , for a sample of Lyman break galaxies (LBGs) and a sample of LAEs, both at $z \sim 3$. Such ratios were found to be $\eta_{\text{LBG}} = 18.0^{+34.8}_{-7.4}$ for LBGs (rest frame UV absolute magnitudes $-22 \leq M_{\text{AB}} \leq -20$) and $\eta_{\text{LAE}} = 3.7^{+2.5}_{-1.1}$ for LAEs ($-20 < M_{\text{AB}} \leq -18.3$). The observed ratios are equal to the intrinsic ones $\eta_{\text{int}} \simeq R_{\text{int}}^{-1}$ attenuated by dust and HI absorption (the latter only for ionizing photons)

$$\eta_{\text{obs}} = \eta_{\text{int}} \frac{f_{1350}^{\text{dust}}}{f_{912}^{\text{dust}} \cdot f_{912}^{\text{HI}}}. \quad (5.11)$$

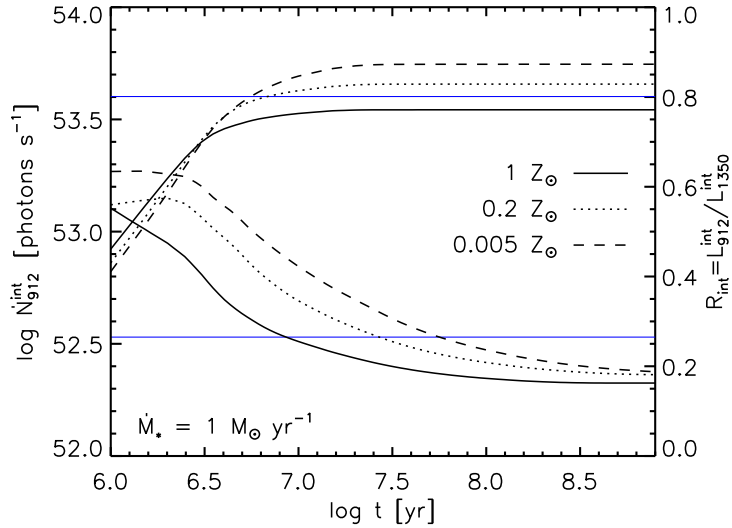


Figure 5.7: Evolution with galactic age of the production rate of ionizing photons, N_{912}^{int} (curves raising with increasing $\log t$; left y -scale), and of the intrinsic ratio of Lyman continuum to UV luminosity, $R_{\text{int}} \equiv L_{912}^{\text{int}}/L_{1350}^{\text{int}}$ (curves declining with increasing $\log t$; right y -scale) for a constant SFR, $\dot{M}_{\star} = 1 M_{\odot} \text{ yr}^{-1}$, a Chabrier (2003) IMF, and three metallicities: $Z_g = 0.005$ (dashed line), 0.02 (dotted line), and $1 Z_{\odot}$ (solid line). The chosen reference values, $N_{912}^{\text{int}} = 4.0 \times 10^{53}$ and $R_{\text{int}} = 0.265$, are indicated by the upper and lower horizontal lines, respectively.

The intrinsic ratio $\eta_{\text{int}} \simeq R_{\text{int}}^{-1} \simeq 3.77$ is within the range measured for LAEs in the Nestor et al. (2013) sample, implying that the attenuation both by dust and by HI is small, as expected in the present framework (cf. Figure 5.4). The luminosities of LBGs correspond to SFRs in the range 50–250 M_{\odot}/yr and metallicities in the range 0.5–0.2 Z_{\odot} . Inserting in Equation (5.6) the average SFR and metallicity appropriate for each UV luminosity, we get an almost luminosity independent value of $\ln(f_{1350}^{\text{dust}}/f_{912}^{\text{dust}}) \simeq (A_{912,\text{LBG}} - A_{1350,\text{LBG}})/1.08 \simeq 0.55 A_{1350,\text{LBG}} \simeq 0.64$. Then, Equation (5.11) gives $\tau_{\text{HI,LBG}} \simeq 1.0(+1, -0.6)$.

Additional constraints on the parameters of the optical depth for HI absorption (Equation (5.8)) come from the Ly α line luminosity functions, through Equation (5.10). There is however a degeneracy between the values of τ_{HI}^0 and of α_{HI} . To break it we have set $\alpha_{\text{HI}} = 0.45$, in analogy to Equation (5.6). We have then obtained $\tau_{\text{HI}}^0 = 0.2$. This choice of the parameters yields, for the UV luminosity range of Nestor et al. (2013), $\tau_{\text{HI,LBG}}$ in the range 1.1–2.4, with a substantial overlap with the range inferred from measurements.

The bottom right panel of Figure 5.8 shows that the *intrinsic* evolution of the Ly α luminosity function is remarkably weak from $z = 2$ to $z = 6$, even weaker than in the UV case (Figure 5.3), and similarly to the latter case, its faint portion is predicted to steepen with increasing redshift. The *observed* evolution at high- z is more strongly negative than the *intrinsic* one due to the increasing attenuation by the IGM. The figure also demonstrates that, at $z \geq 5.7$, observational estimates based on photometric samples (open symbols), only partially confirmed in spectroscopy, tend to be systematically higher than those based on purely spectroscopic samples (filled symbols). Therefore, more extensive spectroscopic confirmation is necessary before firm conclusions on the high- z evolution of the Ly α luminosity function can be drawn.

The average properties, weighted by the halo formation rate, of LAEs at $z = 3, 6$, and 12 are shown, as a function of the observed luminosity, in the right-hand panels of Figure 5.4. Compared to LBGs (left

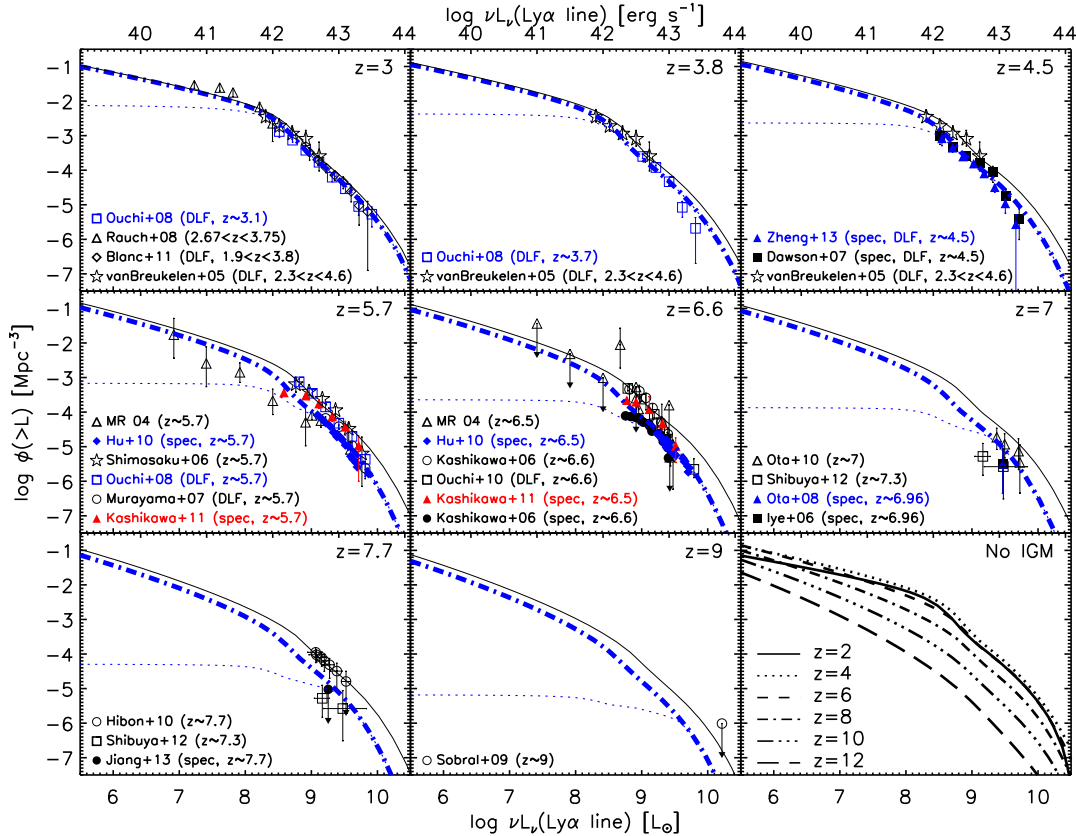


Figure 5.8: Model cumulative Ly α luminosity functions at several redshifts, specified in the upper right corner of each panel corrected (solid black lines) and uncorrected (dot-dashed blue lines) for attenuation by the IGM computed following Madau (1995). We have adopted a minimum halo mass of $10^{8.5} M_{\odot}$. The dotted blue lines give the contributions of halo masses $\geq 10^{11} M_{\odot}$. The bottom right panel illustrates the *intrinsic* evolution of the Ly α line luminosity function (i.e., without attenuation by the IGM). The data are from Ouchi et al. (2003), Malhotra & Rhoads (2004, MR 04), van Breukelen et al. (2005), Shimasaku et al. (2006), Iye et al. (2006), Kashikawa et al. (2006, 2011), Dawson et al. (2007), Murayama et al. (2007), Rauch et al. (2008), Ouchi et al. (2008, 2010), Ota et al. (2008, 2010), Sobral et al. (2009), Hibon et al. (2010), Hu et al. (2010), Blanc et al. (2011), Shibuya et al. (2012), Zheng et al. (2013), and Jiang et al. (2013). The data based on spectroscopic samples are shown by filled symbols and the references within panels are labeled “spec”. Those based on photometric samples are shown by open symbols. The label “DLF” associated to references means that the original papers gave the differential luminosity functions.

panels of the same figure), LAEs have somewhat younger ages, implying somewhat lower stellar masses, SFRs and metallicities at given M_{vir} . The latter two factors combine to give substantially lower dust extinction.

5.3.2 Cosmic reionization

The injection rate of ionizing photons into the IGM is

$$\dot{N}_{912}^{\text{int}} f_{912}^{\text{esc}} = k_{\text{ion}} \frac{\dot{M}_{\star}}{M_{\odot} \text{ yr}^{-1}} f_{912}^{\text{esc}} \text{ photons s}^{-1}, \quad (5.12)$$

where $f_{912}^{\text{esc}} \equiv f_{912}^{\text{dust}} \times f_{912}^{\text{HI}}$ is the fraction of ionizing photons emerging at the galaxy boundary. The dependences on UV magnitude and redshift of f_{912}^{dust} , f_{912}^{HI} , and f_{912}^{esc} , weighted by the halo formation rate, are illustrated in Figure 5.9. The escape fractions are substantially higher, and weakly dependent

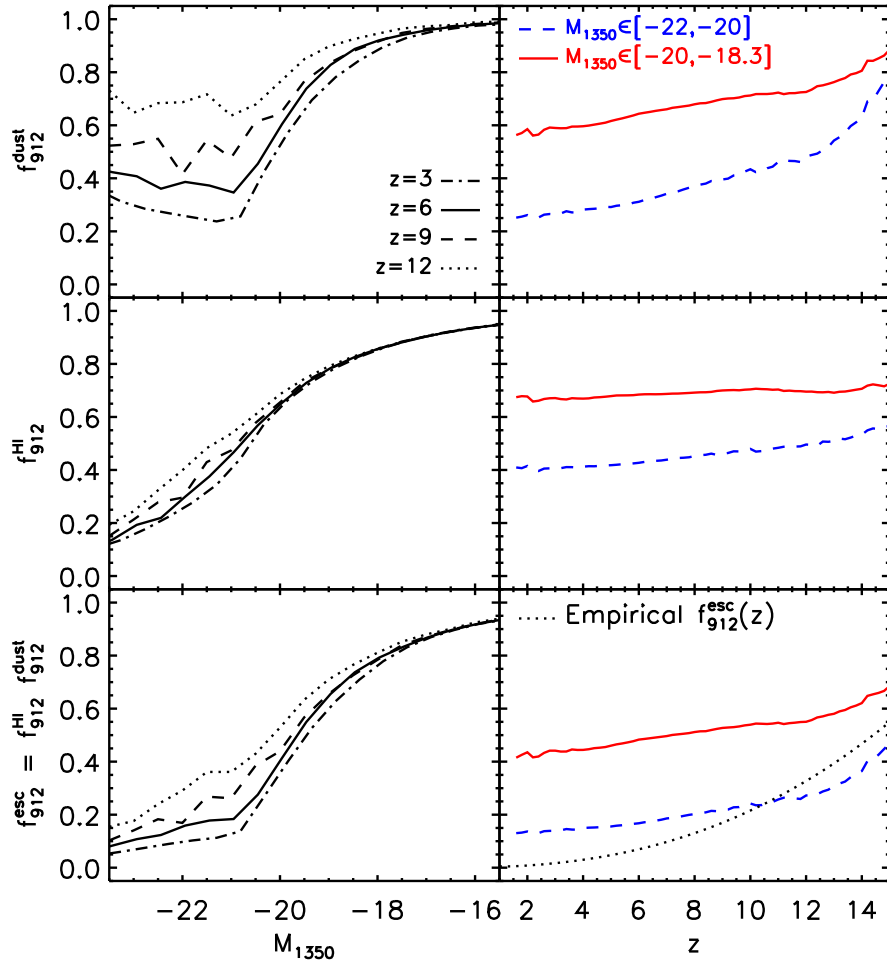


Figure 5.9: Left panels: fractions of ionizing photons surviving dust, HI and both absorptions (f_{912}^{dust} , f_{912}^{HI} and f_{912}^{esc} , from top to bottom), weighted by the halo formation rate, yielded by our model for $z_{\text{obs}} = 3$ (dot-dashed line), 6 (solid line), 9 (dashed line), and 12 (dotted line) as a function of the attenuated UV luminosity M_{1350} . Right panels: escape fractions given by the model as a function of z for two luminosity bins, i.e., $M_{1350} \in [-22, -20]$ (dashed blue line) and $M_{1350} \in [-20, -18.3]$ (solid red line). The dotted line shows the empirical redshift dependence, $f_{912}^{\text{esc}}(z) = 0.03[(1+z)/5]^{2.5}$, that may attenuate the tension between observational indications of a rapid drop of the ionization degree at $z \gtrsim 6.5$ and the relatively high electron scattering optical depth determined by WMAP that would imply substantial ionization degrees up to much higher redshifts (see Figure 5.10).

on redshift, for the lower luminosity galaxies. For the brighter galaxies the fraction that escapes dust absorption increases with increasing z , while the fraction escaping HI absorption is essentially redshift independent at all luminosities.

The redshift-dependent emission rate function, $\phi(\log \dot{N}_{912}^{\text{esc}}, z)$, can be constructed in the same way as the UV luminosity function (Section 5.2.1). The average injection rate of ionizing photons into the IGM per unit comoving volume at redshift z is

$$\langle \dot{N}_{912}^{\text{esc}}(z) \rangle = \int \dot{N}_{912}^{\text{esc}} \phi(\log \dot{N}_{912}^{\text{esc}}, z) d \log \dot{N}_{912}^{\text{esc}}. \quad (5.13)$$

The reionization of the IGM is described in terms of the evolution of the volume filling factor of HII

regions, $Q_{\text{HII}}(t)$, which is ruled by (Madau et al. 1999)

$$\frac{dQ_{\text{HII}}}{dt} \simeq \frac{\langle \dot{N}_{912}^{\text{esc}} \rangle}{\bar{n}_{\text{H}}} - \frac{Q_{\text{HII}}}{\bar{t}_{\text{rec}}}, \quad (5.14)$$

where $\bar{n}_{\text{H}} = X\rho_{\text{c}}\Omega_{\text{b}}/m_{\text{p}} \simeq 2.5 \times 10^{-7}X(\Omega_{\text{b}}h^2/0.022) \text{ cm}^{-3}$ is the mean comoving hydrogen number density in terms of the primordial mass fraction of hydrogen $X = 0.75$, of the present-day critical density $\rho_{\text{c}} = 1.878h^2 \times 10^{-29} \text{ g cm}^{-3}$, of the mean baryon density Ω_{b} , of the Hubble constant h , and of the proton mass $m_{\text{p}} = 1.67 \times 10^{-24} \text{ g}$. The mean recombination time is given by (Madau et al. 1999; Kuhlen & Faucher-Giguère 2012)

$$\begin{aligned} \bar{t}_{\text{rec}} &= \frac{1}{f_e \bar{n}_{\text{H}} (1+z)^3 \alpha_{\text{B}}(T_0) C_{\text{HII}}} = \\ &= \frac{0.51}{f_e} \left(\frac{\Omega_{\text{b}}}{0.049} \right)^{-1} \left(\frac{1+z}{7} \right)^{-3} \left(\frac{T_0}{2 \times 10^4 \text{ K}} \right)^{0.7} \left(\frac{C_{\text{HII}}}{6} \right)^{-1} \text{ Gyr}, \end{aligned} \quad (5.15)$$

where f_e is the number of free electrons per hydrogen nucleus in the ionized IGM, assumed to have a temperature $T_0 = 2 \times 10^4 \text{ K}$, and $C_{\text{HII}} \equiv \langle \rho_{\text{HII}}^2 \rangle / \langle \rho_{\text{HII}} \rangle^2$ is the clumping factor of the ionized hydrogen. f_e depends on the ionization state of helium; we assumed it to be doubly ionized ($f_e = 1 + Y/2X \simeq 1.167$) at $z < 4$ and singly ionized ($f_e = 1 + Y/4X \simeq 1.083$) at higher redshifts (Robertson et al. 2013).

Additional constraints on the re-ionization history are set by the electron scattering optical depth τ_{es} measured by Cosmic Microwave Background (CMB) anisotropy experiments. The optical depth up to redshift z is given by

$$\tau_{\text{es}}(< z) = \int_0^z dz' \left| \frac{dt}{dz'} \right| c \sigma_{\text{T}} n_e(z') = \int_0^z dz' \frac{c(1+z')^2}{H_0 \sqrt{\Omega_{\Lambda} + \Omega_{\text{m}}(1+z')^3}} f_e Q_{\text{HII}}(z') \sigma_{\text{T}} \bar{n}_{\text{H}}, \quad (5.16)$$

where $n_e \simeq f_e Q_{\text{HII}} \bar{n}_{\text{H}} (1+z)^3$ is the mean electron density, c is the speed of light, and $\sigma_{\text{T}} \simeq 6.65 \times 10^{-25} \text{ cm}^2$ is the Thomson cross section. WMAP 9-yr data alone give $\tau_{\text{es}} = 0.089 \pm 0.014$, slightly decreasing to $\tau_{\text{es}} = 0.081 \pm 0.012$ when they are combined with external data sets (Hinshaw et al. 2012). The combination of the *Planck* temperature power spectrum with a WMAP polarisation low-multipole likelihood results in an estimate closely matching the WMAP 9-yr value, $\tau_{\text{es}} = 0.089^{+0.012}_{-0.014}$ (Planck collaboration et al. 2013b). However, replacing the WMAP polarised dust template with the far more sensitive *Planck*/HFI 353 GHz polarisation map lowers the best fit value to $\tau_{\text{es}} = 0.075 \pm 0.013$ (Planck collaboration et al. 2013a); this result has however to be taken as preliminary.

The evolution of $Q_{\text{HII}}(t)$ and the electron scattering optical depth $\tau_{\text{es}}(< z)$ yielded by the model adopting the critical halo mass $M_{\text{crit}} = 10^{8.5} M_{\odot}$, the effective escape fraction f_{912}^{esc} laid down before and the evolutionary law of the IGM clumping factor C_{HII} by Iliev et al. (2007), are shown by the thick solid black lines in the main panel of Figure 5.10. Although this model gives a τ_{es} consistent with determinations by Hinshaw et al. (2012) and Planck collaboration et al. (2013b), it yields a more extended fully ionized phase than indicated by the constraints on Q_{HII} at $z \geq 6$ collected by Robertson et al. (2013) who, however, cautioned that they are all subject to substantial systematic or modeling uncertainties. We now discuss different choices for M_{crit} , $f_{912}^{\text{esc}}(z)$ and $C_{\text{HII}}(z)$ that may attenuate the tension between

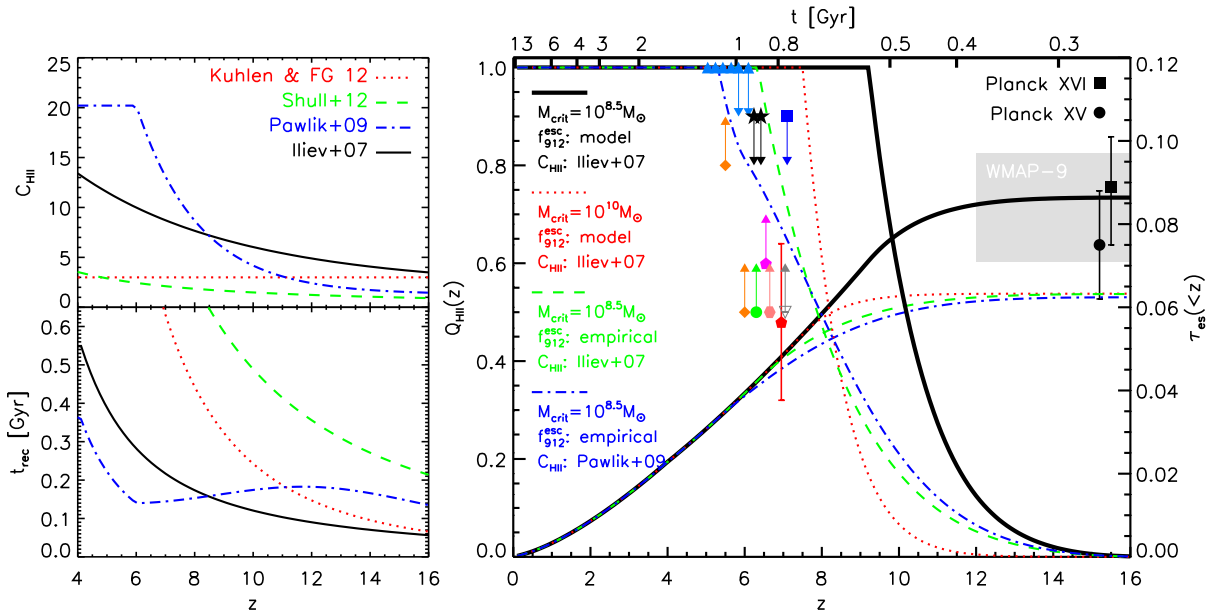


Figure 5.10: Left panels: evolutionary laws for the IGM clumping factor C_{HII} (upper panel) proposed in the literature and the corresponding recombination timescales t_{rec} (lower panel). Solid black line: $C_{\text{HII}}(z) = 26.2917 \exp(-0.1822z + 0.003505z^2)$ (Iliev et al. 2007); dotted red line: $C_{\text{HII}}(z) = 3$ (Kuhlen & Faucher-Giguère 2012); dashed green line: $C_{\text{HII}}(z) = 2.9[(1+z)/6]^{-1.1}$ (Shull et al. 2012); dot-dashed blue line: $C_{\text{HII}}(z) = \min[C_{\text{HII}}(z=6), \exp(-0.47z + 5.76) + 1.29]$, corresponding to the C_{-1} L6N256 reheating simulation by Pawlik et al. (2009) covering the range $6 \leq z \leq 20$. Main figure: evolution with redshift of the volume filling factor Q_{HII} (left y -scale) and of the electron optical depth τ_{es} (right y -scale). The thick solid black lines correspond to the fiducial model with $C_{\text{HII}}(z)$ by Iliev et al. (2007) and $M_{\text{crit}} = 10^{8.5} M_{\odot}$. The dotted red lines correspond to the same model but with $M_{\text{crit}} = 10^{10} M_{\odot}$. The dashed green lines and the dot-dashed blue lines show the results for the empirical dependence of the escape fraction of ionizing photons (see Fig. 5.9 and text) combined with the $C_{\text{HII}}(z)$ by Iliev et al. (2007) and by Pawlik et al. (2009), respectively, for $M_{\text{crit}} = 10^{8.5} M_{\odot}$. The observational constraints on the volume filling factor are from a collection of literature data made by Robertson et al. (2013). The 9-year WMAP constraint on electron optical depth, $\tau_{\text{es}} = 0.084 \pm 0.013$ (Hinshaw et al. 2012), is represented by the gray region while the filled square and the filled circle with error bars represent the preliminary estimates by Planck collaboration et al. (2013b) and Planck collaboration et al. (2013a), respectively.

measurements of $\tau_{\text{es}}(< z)$ and constraints on $Q_{\text{HII}}(z)$.

As we have seen before, the observed UV luminosity functions imply $M_{\text{crit}} \gtrsim 10^{10} M_{\odot}$. Adopting the latter value and keeping our baseline $f_{912}^{\text{esc}}(z)$ and $C_{\text{HII}}(z)$ shortens the fully ionized phase that now extends up to $z \sim 7.5$ (dotted red line in the main figure of Figure 5.10), substantially lessening the discrepancy with constraints on Q_{HII} at the cost of τ_{es} dropping $\simeq 1.6\sigma$ below the best fit WMAP value, but within 1σ of the best fit value of Planck collaboration et al. (2013a). This conclusion is unaffected by different choices for $C_{\text{HII}}(z)$, illustrated in the upper panel of Figure 5.10, as long as we keep our baseline $f_{912}^{\text{esc}}(z)$. This is because the production rate of ionizing photons (first term on the right-hand side of Equation (5.14)) is always substantially larger than the recombination rate. Consideration of Equation (5.14) shows that, if $f_{912}^{\text{esc}}(z)$ is kept fixed, the insensitivity of the re-ionization history to the choice of $C_{\text{HII}}(z)$ holds for any $M_{\text{crit}} \leq 10^{10} M_{\odot}$.

Consistency with data on Q_{HII} requires an escape fraction of ionizing photons much lower than the effective escape fraction yielded by the model, which is dominated by the contribution of low luminosity galaxies. But to have a fully ionized IGM up to $z \simeq 6$ and an acceptable τ_{es} value, the lower escape fraction must be compensated by a higher production rate, i.e., by a lower M_{crit} . The dashed green line in the main figure of Figure 5.10 shows that consistency with the data at $z \simeq 6-7$ can be achieved

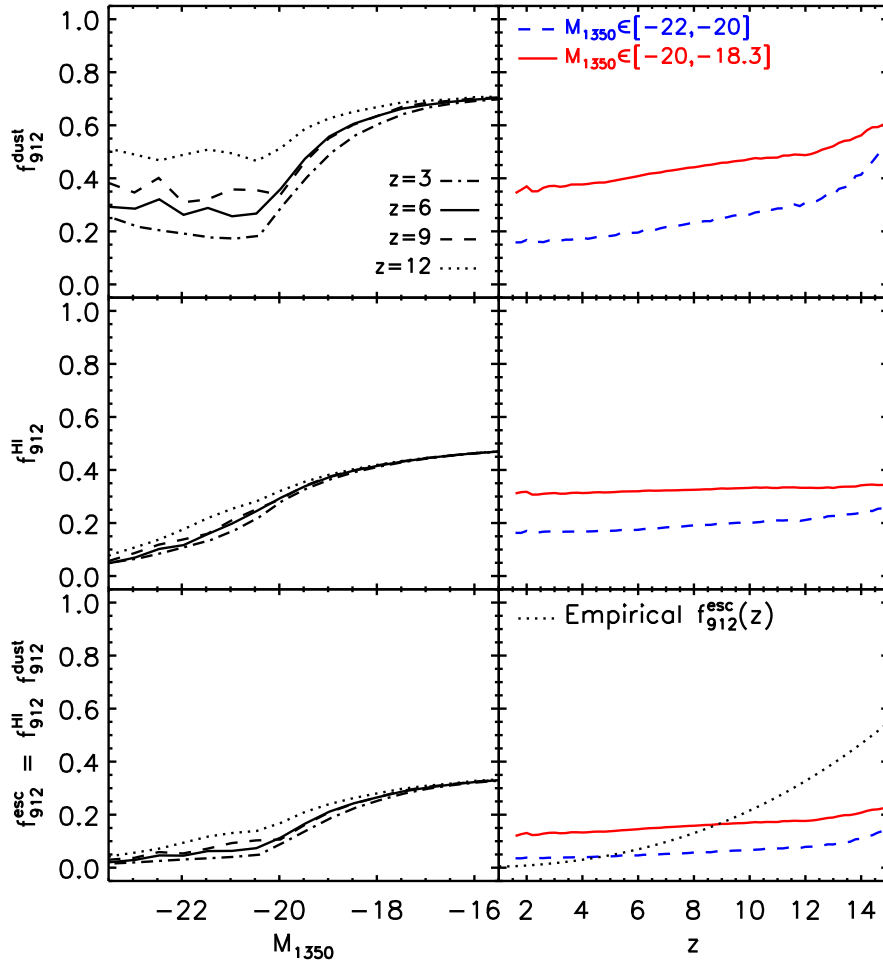


Figure 5.11: The same escape fractions as in Figure 5.9 but the model effective escape fraction, f_{912}^{esc} , is simply reduced by a single factor to be close to the empirical one while keeping good fits to the UV and Ly α luminosity functions (see Figures 5.12 and 5.13): f_{912}^{dust} and f_{912}^{HI} , compared to those in Figure 5.9, are reduced by a factor of 1.4 and 2, respectively.

replacing the redshift dependence of the escape fraction of ionizing photons given by the model with the empirical formula $f_{912}^{\text{esc}}(z) = 0.03[(1+z)/5]^{2.5}$ and assuming $M_{\text{crit}} = 10^{8.5} M_{\odot}$ (marginally consistent with the results of hydrodynamical simulations) together with the $C_{\text{HII}}(z)$ given by Iliev et al. (2007). The $C_{\text{HII}}(z)$ can be further replaced with that given by the C_{-1} L6N256 reheating simulation by Pawlik et al. (2009) to achieve an even better agreement with data on Q_{HII} (dot-dashed blue line in the main figure of Figure 5.10). On the other hand, with this empirical escape fraction there is no way to get within 1σ of the WMAP τ_{es} unless additional sources of ionizing photons at high- z (pop. III stars? decaying dark matter particles?) are advocated.

We can comparatively produce an effective escape fraction close to the empirical one in the framework of the present model (see Figure 5.11), salvaging the good fits to the UV and Ly α luminosity functions, by decreasing both f_{912}^{dust} and f_{912}^{HI} compared to the values given by Equations (5.6) and (5.8). Decreasing f_{912}^{dust} means increasing the amount of dust extinction, which implies a shift to lower luminosities of the observed UV luminosity function. A fit of similar quality to that shown in Figure 5.3 can be recovered decreasing f_{912}^{dust} by a factor of 1.4 and, at the same time, increasing k_{UV} by 20%. It is not necessary

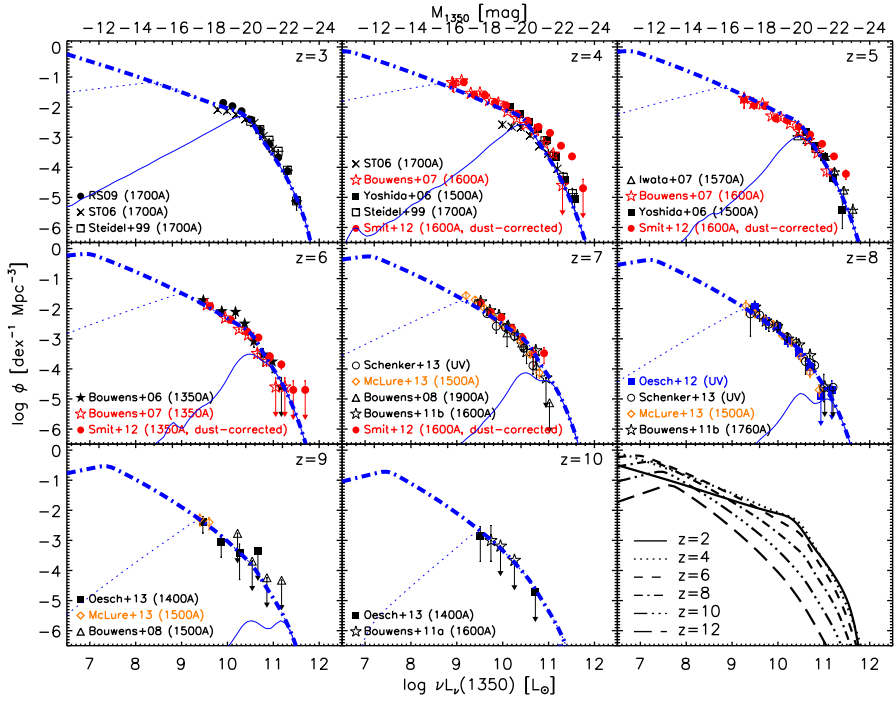


Figure 5.12: Luminosity functions at 1350 Å at several redshifts for increasing dust extinction via decreasing f_{912}^{dust} by a factor of 1.4. Lines and references are the same as in Figure 5.3.

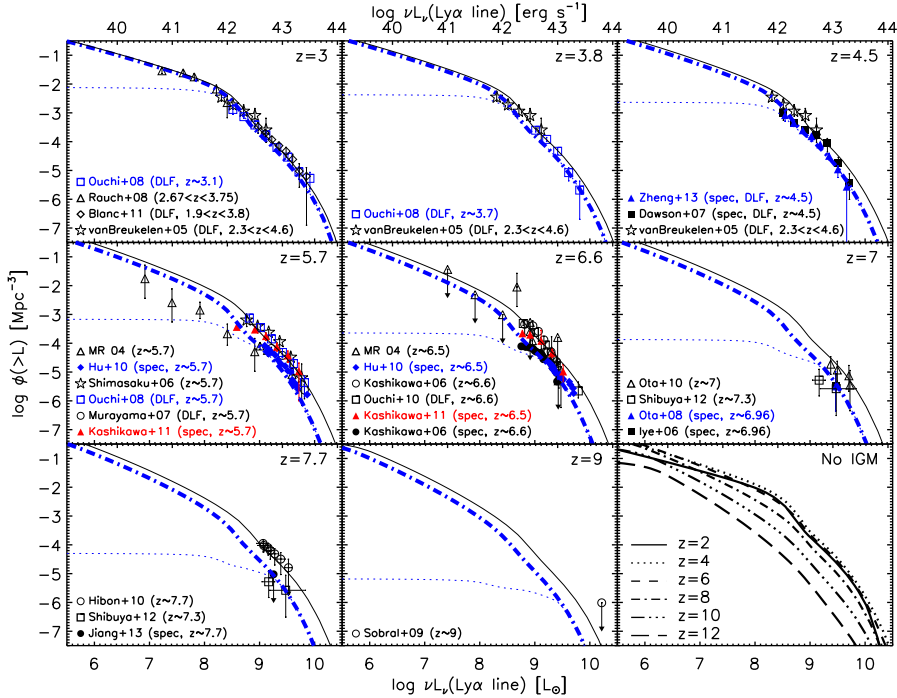


Figure 5.13: Cumulative Ly α luminosity functions at several redshifts for increasing dust extinction as in Figure 5.12 and decreasing f_{912}^{HI} by a factor of 2. Lines and references are the same as in Figure 5.8.

to increase k_{UV} by the same factor by which f_{912}^{dust} is decreased because Equation (5.6) leads to a slight over-prediction of the UV luminosity function (see Figure 5.12). To get close to the empirical $f_{912}^{\text{esc}}(z)$ we further need to decrease f_{912}^{HI} by a factor of 2. This leads to an increase of the Ly α luminosity, which is

proportional to $(1 - f_{912}^{\text{HI}})$ (Equation (5.10)), but this is compensated by the decrease of f_{912}^{dust} . On the whole, the fit of the Ly α luminosity functions shown in Figure 5.13 turns out to be qualitatively similar to that in Figure 5.8. There is some tension between these choices for f_{912}^{dust} and f_{912}^{HI} and the data by Nestor et al. (2013), but there is a better consistency with those by Mostardi et al. (2013) who find $\eta_{\text{obs}, \text{LBG}} = 82 \pm 45$.

The minimum SFR density required to keep the universe fully ionized at the redshift z is (Madau et al. 1999)

$$\dot{\rho}_* \simeq 8.2 \times 10^{-4} \left(\frac{C_{\text{HII}}}{f_{\text{esc}}} \right) \left(\frac{\Omega_b h^2}{0.022} \right)^2 \left(\frac{1+z}{7} \right)^3 M_\odot \text{ yr}^{-1} \text{ Mpc}^{-3}. \quad (5.17)$$

It is shown in Figure 5.6 (grey area) for $3 \lesssim C_{\text{HII}}/f_{\text{esc}} \lesssim 30$.

The present data do not allow us to draw any firm conclusion because they may be affected by substantial uncertainties. Those on data at $z = 6\text{--}7$ are discussed by Robertson et al. (2013). Those on τ_{es} are illustrated by the finding (Planck collaboration et al. 2013a) that different corrections for the contamination by polarised foregrounds may lower the best fit value by about 1σ .

Chapter 6

Conclusions

Current theories of galaxy and active galactic nucleus (AGN) formation and evolution from primordial density perturbations are still not fully able to catch up with the challenges set by the wealth of observational data that have been accumulating in recent years. Three main scenarios for the early evolution of galaxies have been discussed in the literature: merger driven evolution ([Baugh et al. 2005](#)); star formation fueled by cold flows ([Dekel et al. 2009](#)); or self-regulated by baryon processes ([Granato et al. 2004](#); [Lapi et al. 2006, 2011](#); [Cai et al. 2013](#)). In this thesis, we have investigated the predictions of the latter scenario for the cosmic star formation history as traced by IR and UV data (see Chapter 4 and Chapter 5, respectively).

A large fraction of the thesis work was devoted to elaborating the predictions of the self-regulated scenario for the dust-enshrouded phase of the evolution of massive proto-spheroidal galaxies and of the active nuclei at their centers, and to testing them against a broad variety of data, from near-IR to radio wavelengths. The physical model by [Granato et al. \(2004\)](#) has been upgraded working out, for the first time, the epoch-dependent luminosity functions (LFs) of sources as a whole (stellar plus AGN component), taking into account in a self-consistent way the variation with galactic age of the global spectral energy distribution (SED).

To make possible a full comparison with the multi-frequency data, the physical model was complemented with a phenomenological backward model for late-type galaxies and for the later AGN evolution at $z \lesssim 2$ (see Chapter 3). Great care was taken to define appropriate broad-band SEDs for the considered galaxy and AGN populations: proto-spheroids, “warm” and “cold” late-type galaxies, AGNs co-evolving with star-forming proto-spheroids (dubbed “type 3”), and canonical type 1 and type 2 AGNs. The “hybrid” model built in this way was successfully compared with a broad variety of data: total IR LFs (see Section 4.1.1) and monochromatic LFs (see Section 4.1.3) at different redshifts, redshift distributions at various detection limits (see Section 4.1.5), and number counts (both global and per redshift slices; see Sections 4.2.1 and 4.2.2).

The model naturally accounts for the observed positive evolution of both galaxies and AGNs up to $z \simeq 2.5$ and for the negative evolution at higher redshifts. This is the result of the combination of two competing effects. On one side cooling and free-fall timescales shorten with increasing redshift because

of the increase of the matter density and this yields higher star formation rates, i.e., higher galaxy luminosities at given halo mass. The higher gas densities are also responsible for a delay of the AGN switch-off time by feedback implying positive luminosity and density evolution of these objects. These effects are thwarted by the decrease in the comoving density of massive halos that prevails above $z \simeq 2.5$ causing a decline of the bolometric LFs of both galaxies and AGNs.

The model also provides a simple physical explanation for the steeply rising portion of the (sub-)millimeter counts (see Section 4.2.1), that proved to be very hard to account for by other physical and phenomenological models. The sharp steepening is due to the sudden appearance of proto-spheroidal galaxies that do not have, in this spectral band, an evolutionary connection with nearby galaxies because their descendants are in passive evolution at $z \lesssim 1.5$. Their (sub-)millimeter counts are extremely steep because, due to the strongly negative K -correction, the flux densities corresponding to a given luminosity are only weakly dependent on the source redshift. Then, since the far-IR luminosity is roughly proportional to the halo mass, the counts reflect, to some extent, the exponential decline of halo mass function at high masses.

The steepness of the counts imply a strong magnification bias due to gravitational lensing. The counts of strongly lensed sources depend on the redshift distribution that determines the distribution of lensing optical depths. In fact, this model was the only one that correctly predicted (Negrello et al. 2007) the strongly lensed counts at $500\,\mu\text{m}$ and the correct redshift distribution of bright ($S_{500\,\mu\text{m}} \geq 100\,\text{mJy}$) submillimeter sources (Negrello et al. 2010; González-Nuevo et al. 2012, see Sections 4.1.4 and 4.2.3).

There is a systematic variation with wavelength of the populations dominating the counts and the contributions to the extragalactic background intensity (see Section 4.3.1). Above $350\,\mu\text{m}$ the main contributors to the cosmic infrared background (CIB) are proto-spheroidal galaxies. In this wavelength range, late-type galaxies dominate the counts only at the brightest (where normal “cold” star-forming galaxies prevail) and at the faintest flux densities (where “warm” starburst galaxies outnumber the protospheroids). Proto-spheroidal galaxies become increasingly important with decreasing wavelength but are always sub-dominant below $250\,\mu\text{m}$. This strong variation with wavelength in the composition of IR sources implies specific predictions for the auto- and cross-power spectra of the source distribution, which may help discriminating between different models. Essentially, all the alternative models have all source populations present over the full relevant redshift range. This implies a high correlation between the CIB intensity fluctuations at different frequencies. On the contrary, the present model predicts a high (close to unity) cross-correlation only at the longest wavelengths ($\geq 500\,\mu\text{m}$). At shorter wavelengths the cross-correlation progressively weakens and we expect little cross-correlation between CIB fluctuations at, say, 100 and $500\,\mu\text{m}$. No observational determination is available for correlations among these wavelengths, but in the *Herschel*/SPIRE wavelength range, where cross-correlations have been measured, the model results are in good agreement with observations (see Section 4.3.2).

According to our model, the AGN contribution to the CIB is always sub-dominant (see Section 4.3.1). It is maximal in the mid-IR where it reaches 8.6% at $16\,\mu\text{m}$ and 8.1% at $24\,\mu\text{m}$. These contributions are close to, but somewhat lower than, most observation-based estimates which, however, are complicated by the difficulty of separating the AGN emission from that of the host galaxy. The AGN contribution to

the counts is also always sub-dominant. We find a maximum contribution in the mid-IR where the model gives AGN fractions in fair agreement with the observational estimates ([Treister et al. 2006](#); [Teplitz et al. 2011](#)).

Several applications of the model have been developed. In Section 4.4 we have presented predictions for the number counts and the redshift distributions of star-forming galaxies detectable through IR spectroscopy by future missions such as SPICA. The predictions are based on a re-assessment of the correlation between line and total IR luminosity, made with the help of extensive simulations. In Section 4.2.4 we have presented preliminary estimates of radio counts of star-forming galaxies, based on the well-known IR-radio correlation. These estimates were made for the Italian SKA White Book ([Feretti et al. 2013](#)), and were meant to illustrate the potential of the SKA to investigate dust-enshrouded star formation. Furthermore, the model was exploited to compute the confusion limits for the PRISM White Paper ([PRISM Collaboration et al. 2013](#)). Moreover, the model was used to upgrade the Planck Sky Model, that now simulates the three-dimensional distribution of dusty galaxies, consistent with observed counts, redshift distributions and clustering properties (Castex et al., in preparation).

Another important fraction of the thesis work was devoted to the earliest phases of galaxy evolution, before the interstellar medium (ISM) was strongly metal enriched and large amounts of dust could form, so that galaxies were bright in the UV. We have extended to this phase the physical model for protospheroidal galaxies. According to this model, the LF is directly linked to the formation rate of virialized halos and to the cooling and heating processes governing the star formation. For the low halo masses and young galactic ages of interest here it is not enough to take into account SN and AGN feedback, as usually done for halo masses $M_{\text{vir}} \gtrsim 10^{11} M_{\odot}$, because other heating processes such as the radiation from massive low-metallicity stars, stellar winds, and the UV background can contribute to reducing and eventually quenching the star formation rate (SFR). We have modeled this by increasing the efficiency of cold gas removal and introducing a lower limit, M_{crit} , to halo masses that can host active star formation.

Another still open issue is the production rate of UV photons per unit halo mass at high- z , which is influenced by two competing effects. On one side, the expected increase with redshift of the Jeans mass, hence of the characteristic stellar mass, entails a higher efficiency in the production of UV photons. On the other side, more UV photons imply more gas heating, i.e., a decrease of the SFR. We find that the observed UV LFs up to the highest redshifts are very well reproduced with the SFRs yielded by the model and the extinction law derived by [Mao et al. \(2007\)](#) for a production rate of UV photons corresponding to a [Chabrier \(2003\)](#) IMF.

We have found that the observed UV LFs (Lyman break galaxies; LBGs) constrain M_{crit} to be $\leq 10^{9.8} M_{\odot}$, consistent with estimates from simulations. The main features of the model are: i) dust extinction is higher for higher luminosities, associated to more massive halos which have a faster metal enrichment; ii) the higher feedback efficiency in less massive halos makes the slope of the faint end of the LF flatter than that of the halo formation rate; yet the former reflects to some extent the steepening with increasing z of the latter; this has important implications for the sources of the ionizing background at high z ; iii) the evolution of the LF from $z = 2$ to $z = 6$ is weak because the decrease with increasing redshift of the halo formation rate in the relevant range of halo masses is largely compensated by the

increase of the star formation efficiency due to the faster gas cooling.

Another key property of the model is the fast metal enrichment of the more massive galaxies that translates into a rapid increase of dust obscuration. Therefore these galaxies show up mostly at far-IR/(sub-)millimeter wavelength, a prediction successfully tested against observational data. The ratio of dust-obscured to unobscured star formation has a broad maximum at $z \simeq 2\text{--}3$. The decrease at lower redshifts is due to the decreasing amount of ISM in galaxies, that at higher redshifts is related to the fast decrease of the abundance of massive halos where the metal enrichment and, correspondingly, the dust extinction grow fast.

Similarly good fits are obtained for the Ly α line LF (Lyman alpha emitters; LAEs) that provide information on the production rate of ionizing photons and on their absorption by neutral interstellar hydrogen. Further constraints on the attenuation by dust and H I are provided by measurements of the observed ratios of non-ionizing UV to Lyman-continuum flux densities for LAEs and LBGs. These data have allowed us to derive a simple relationship between the optical depth for H I absorption and SFR. Taking this relation into account, the model reproduces the very weak evolution of the Ly α line LF between $z = 2$ and $z = 6$, even weaker than in the UV.

Having obtained the injection rate of ionizing photons into the intergalactic medium (IGM) as a function of halo mass and redshift, to reconstruct the ionization history of the universe, we further need the evolution of the clumping factor of the IGM, for which we have considered several possibilities, discussed in the literature. With our recipe for the escape fraction of ionizing photons we find that galaxies already represented in the observed UV LF, i.e., with $M_{\text{UV}} \leq -18$, can account for a complete ionization of the IGM up to $z \simeq 7.5$. This differs from the conclusions of other analyses (e.g. [Robertson et al. 2013](#)) according to which, to fully re-ionize the universe, the population of star-forming galaxies at $z \sim 7\text{--}9$ must extend in luminosity to $M_{\text{UV}} \sim -13$ or fainter. The reason of the difference is that our model implies substantially higher escape fractions for low-mass galaxies.

A complete IGM ionization up to $z \simeq 7.5$ is disfavored by some (admittedly uncertain) data at $z \simeq 6\text{--}7$ collected by [Robertson et al. \(2013\)](#), that point to a fast decline of the ionization degree at $z \gtrsim 6.5$. On the other hand, the electron scattering optical depth determined from CMB data point to an even more extended ionized phase. We have presented an empirical redshift dependence of the effective escape fraction of ionizing photons that yields a better overall agreement to these data sets and discussed how we can at the same time salvage the good fits to the UV and Ly α LFs. Since all these constraints on the re-ionization history are affected by substantial uncertainties any firm conclusion is premature. Better data are needed to resolve the issue.

Although the presented comprehensive “hybrid” model provides a good fit to the multi-wavelength (from IR to mm-waves and high- z UV) observational estimates, it relies on a phenomenological approach for the evolution of low- z late-type galaxies and associated AGNs and its validity is currently limited within the IR to mm wavelength range where the relative uniformity of dust emission ensures the simplicity of the IR model for the IR extragalactic background unlike the UV/optical wavelength range suffered to delicate dust extinction. On one hand, based on the well-known IR-radio relation, the current IR model of dusty galaxies complemented with a new empirical radio AGN model is being upgraded for

the radio extragalactic background. On the other hand, to further understand the cosmic co-evolution of star formation of host galaxy and central activity of AGN, a physical model including the evolution of low- z late-type galaxies and associated AGNs will be explored and developed for the panchromatic extragalactic background.

Bibliography

- Alavi, A., Siana, B., Richard, J., et al. 2013, ArXiv e-prints, [arXiv:1305.2413 \[astro-ph.CO\]](https://arxiv.org/abs/1305.2413)
- Altieri, B., Berta, S., Lutz, D., et al. 2010, [A&A, 518, L17](#)
- Amblard, A., Cooray, A., Serra, P., et al. 2011, [Nature, 470, 510](#)
- Angulo, R. E., Springel, V., White, S. D. M., et al. 2012, [MNRAS, 426, 2046](#)
- Aretxaga, I., Hughes, D. H., Coppin, K., et al. 2007, [MNRAS, 379, 1571](#)
- Aretxaga, I., Wilson, G. W., Aguilar, E., et al. 2011, [MNRAS, 415, 3831](#)
- Arrigoni, M., Trager, S. C., Somerville, R. S., & Gibson, B. K. 2010, [MNRAS, 402, 173](#)
- Assef, R. J., Kochanek, C. S., Ashby, M. L. N., et al. 2011, [ApJ, 728, 56](#)
- Auger, M. W., Treu, T., Bolton, A. S., et al. 2009, [ApJ, 705, 1099](#)
- Austermann, J. E., Aretxaga, I., Hughes, D. H., et al. 2009, [MNRAS, 393, 1573](#)
- Austermann, J. E., Dunlop, J. S., Perera, T. A., et al. 2010, [MNRAS, 401, 160](#)
- Ballantyne, D. R., & Papovich, C. 2007, [ApJ, 660, 988](#)
- Bardeen, J. M., Bond, J. R., Kaiser, N., & Szalay, A. S. 1986, [ApJ, 304, 15](#)
- Baugh, C. M., Lacey, C. G., Frenk, C. S., et al. 2005, [MNRAS, 356, 1191](#)
- Benson, A. J. 2010, [Phys. Rep., 495, 33](#)
- Bernard-Salas, J., Spoon, H. W. W., Charmandaris, V., et al. 2009, [ApJS, 184, 230](#)
- Bernardeau, F., Colombi, S., Gaztañaga, E., & Scoccimarro, R. 2002, [Phys. Rep., 367, 1](#)
- Bernardi, M., Shankar, F., Hyde, J. B., et al. 2010, [MNRAS, 404, 2087](#)
- Berta, S., Magnelli, B., Nordon, R., et al. 2011, [A&A, 532, A49](#)
- Bertelli, G., Bressan, A., Chiosi, C., Fagotto, F., & Nasi, E. 1994, [A&AS, 106, 275](#)
- Bertin, E., Dennefeld, M., & Moshir, M. 1997, [A&A, 323, 685](#)
- Béthermin, M., Dole, H., Beelen, A., & Aussel, H. 2010, [A&A, 512, A78](#)
- Béthermin, M., Dole, H., Lagache, G., Le Borgne, D., & Penin, A. 2011, [A&A, 529, A4](#)
- Béthermin, M., Daddi, E., Magdis, G., et al. 2012a, [ApJ, 757, L23](#)
- Béthermin, M., Le Floc'h, E., Ilbert, O., et al. 2012b, [A&A, 542, A58](#)
- Biggs, A. D., Younger, J. D., & Ivison, R. J. 2010, [MNRAS, 408, 342](#)
- Blain, A. W. 1996, [MNRAS, 283, 1340](#)
- Blanc, G. A., Adams, J. J., Gebhardt, K., et al. 2011, [ApJ, 736, 31](#)
- Bond, J. R., Cole, S., Efstathiou, G., & Kaiser, N. 1991, [ApJ, 379, 440](#)
- Bouwens, R. J., Illingworth, G. D., Blakeslee, J. P., & Franx, M. 2006, [ApJ, 653, 53](#)
- Bouwens, R. J., Illingworth, G. D., Franx, M., & Ford, H. 2007, [ApJ, 670, 928](#)
- . 2008, [ApJ, 686, 230](#)
- Bouwens, R. J., Illingworth, G. D., Labbe, I., et al. 2011a, [Nature, 469, 504](#)
- Bouwens, R. J., Illingworth, G. D., Oesch, P. A., et al. 2011b, [ApJ, 737, 90](#)
- . 2012, [ApJ, 754, 83](#)
- Bouwens, R., Bradley, L., Zitrin, A., et al. 2013, ArXiv e-prints, [arXiv:1211.2230 \[astro-ph.CO\]](https://arxiv.org/abs/1211.2230)
- Bower, R. G., Benson, A. J., Malbon, R., et al. 2006, [MNRAS, 370, 645](#)
- Bower, R. G., Lucey, J. R., & Ellis, R. S. 1992, [MNRAS, 254, 601](#)
- Boylan-Kolchin, M., Springel, V., White, S. D. M., Jenkins, A., & Lemson, G. 2009, [MNRAS, 398, 1150](#)
- Bracewell, R. N. 2000, The Fourier transform and its applications (McGRAW-HILL)
- Brandl, B. R., Bernard-Salas, J., Spoon, H. W. W., et al. 2006, [ApJ, 653, 1129](#)
- Brandl, B. R., Snijders, L., den Brok, M., et al. 2009, [ApJ, 699, 1982](#)
- Brauher, J. R., Dale, D. A., & Helou, G. 2008, [ApJS, 178, 280](#)
- Bressan, A., Chiosi, C., & Fagotto, F. 1994, [ApJS, 94, 63](#)
- Bressan, A., Granato, G. L., & Silva, L. 1998, [A&A, 332, 135](#)

- Brown, M. J. I., Brand, K., Dey, A., et al. 2006, [ApJ](#), **638**, 88
- Browne, I. W. A., Wilkinson, P. N., Jackson, N. J. F., et al. 2003, [MNRAS](#), **341**, 13
- Bruzual, G., & Charlot, S. 2003, [MNRAS](#), **344**, 1000
- Bryan, G. L., & Norman, M. L. 1998, [ApJ](#), **495**, 80
- Bullock, J. S., Kolatt, T. S., Sigad, Y., et al. 2001, [MNRAS](#), **321**, 559
- Burgarella, D., Buat, V., Takeuchi, T. T., Wada, T., & Pearson, C. 2009, [PASJ](#), **61**, 177
- Burlon, D., Ajello, M., Greiner, J., et al. 2011, [ApJ](#), **728**, 58
- Buta, R. J. 2011, ArXiv e-prints, [arXiv:1102.0550 \[astro-ph.CO\]](#)
- Cai, Z.-Y., Lapi, A., Xia, J.-Q., et al. 2013, [ApJ](#), **768**, 21
- Calzetti, D., Armus, L., Bohlin, R. C., et al. 2000, [ApJ](#), **533**, 682
- Caputi, K. I., Lagache, G., Yan, L., et al. 2007, [ApJ](#), **660**, 97
- Carilli, C., & Walter, F. 2013, ArXiv e-prints, [arXiv:1301.0371 \[astro-ph.CO\]](#)
- Carral, P., Hollenbach, D. J., Lord, S. D., et al. 1994, [ApJ](#), **423**, 223
- Carroll, S. M., Press, W. H., & Turner, E. L. 1992, [ARA&A](#), **30**, 499
- Castellano, M., Fontana, A., Grazian, A., et al. 2012, [A&A](#), **540**, A39
- Chabrier, G. 2003, [PASP](#), **115**, 763
- Chapin, E. L., Pope, A., Scott, D., et al. 2009, [MNRAS](#), **398**, 1793
- Chapin, E. L., Chapman, S. C., Coppin, K. E., et al. 2011, [MNRAS](#), **411**, 505
- Chapman, S. C., Blain, A. W., Smail, I., & Ivison, R. J. 2005, [ApJ](#), **622**, 772
- Chapman, S. C., Helou, G., Lewis, G. F., & Dale, D. A. 2003, [ApJ](#), **588**, 186
- Charlot, S., & Fall, S. M. 2000, [ApJ](#), **539**, 718
- Chen, C.-C., Cowie, L. L., Wang, W.-H., Barger, A. J., & Williams, J. P. 2011, [ApJ](#), **733**, 64
- Chi, S., Barthel, P. D., & Garrett, M. A. 2013, [A&A](#), **550**, A68
- Cirasuolo, M., Shankar, F., Granato, G. L., De Zotti, G., & Danese, L. 2005, [ApJ](#), **629**, 816
- Clemens, M. S., Bressan, A., Nikolic, B., & Rampazzo, R. 2009, [MNRAS](#), **392**, L35
- Clements, D. L., Bendo, G., Pearson, C., et al. 2011, [MNRAS](#), **411**, 373
- Clements, D. L., Desert, F.-X., Franceschini, A., et al. 1999, [A&A](#), **346**, 383
- Clements, D. L., Rigby, E., Maddox, S., et al. 2010, [A&A](#), **518**, L8
- Coe, D., Zitrin, A., Carrasco, M., et al. 2013, [ApJ](#), **762**, 32
- Colavitti, E., Matteucci, F., & Murante, G. 2008, [A&A](#), **483**, 401
- Colbert, J. W., Malkan, M. A., Clegg, P. E., et al. 1999, [ApJ](#), **511**, 721
- Coleman, P. H., Pietronero, L., & Sanders, R. H. 1988, [A&A](#), **200**, L32
- Condon, J. J. 1992, [ARA&A](#), **30**, 575
- Conley, A., Guy, J., Sullivan, M., et al. 2011, [ApJS](#), **192**, 1
- Cook, M., Lapi, A., & Granato, G. L. 2009, [MNRAS](#), **397**, 534
- Cooray, A., & Sheth, R. 2002, [Phys. Rep.](#), **372**, 1
- Coppin, K. E. K., Danielson, A. L. R., Geach, J. E., et al. 2012, [MNRAS](#), **427**, 520
- Coppin, K., Chapin, E. L., Mortier, A. M. J., et al. 2006, [MNRAS](#), **372**, 1621
- Cormier, D., Lebouteiller, V., Madden, S. C., et al. 2012, [A&A](#), **548**, A20
- Cox, P., Krips, M., Neri, R., et al. 2011, [ApJ](#), **740**, 63
- Croom, S. M., Smith, R. J., Boyle, B. J., et al. 2004, [MNRAS](#), **349**, 1397
- Croom, S. M., Richards, G. T., Shanks, T., et al. 2009, [MNRAS](#), **399**, 1755
- Croton, D. J., Springel, V., White, S. D. M., et al. 2006, [MNRAS](#), **365**, 11
- Cucciati, O., Tresse, L., Ilbert, O., et al. 2012, [A&A](#), **539**, A31
- da Cunha, E., Charlot, S., Dunne, L., Smith, D., & Rowlands, K. 2012, in *IAU Symposium*, Vol. 284, *IAU Symposium*, ed. R. J. Tuffs & C. C. Popescu, 292
- da Cunha, E., Charlot, S., & Elbaz, D. 2008, [MNRAS](#), **388**, 1595
- da Cunha, E., Charmandaris, V., Díaz-Santos, T., et al. 2010, [A&A](#), **523**, A78
- Dai, X., Assef, R. J., Kochanek, C. S., et al. 2009, [ApJ](#), **697**, 506
- Dale, D. A., & Helou, G. 2002, [ApJ](#), **576**, 159
- Dale, D. A., Helou, G., Contursi, A., Silbermann, N. A., & Kolhatkar, S. 2001, [ApJ](#), **549**, 215
- Dawson, S., Rhoads, J. E., Malhotra, S., et al. 2007, [ApJ](#), **671**, 1227
- De Breuck, C., Maiolino, R., Caselli, P., et al. 2011, [A&A](#), **530**, L8
- de Vaucouleurs, G. 1948, *Annales d' Astrophysique*, **11**, 247
- de Zotti, G., Massardi, M., Negrello, M., & Wall, J. 2010, [A&A Rev.](#), **18**, 1
- Dekel, A., Sari, R., & Ceverino, D. 2009, [ApJ](#), **703**, 785
- Devost, D., Brandl, B. R., Armus, L., et al. 2004, [ApJS](#), **154**, 242
- Di Matteo, T., Springel, V., & Hernquist, L. 2005, [Nature](#), **433**, 604

- Dole, H., Le Floc'h, E., Pérez-González, P. G., et al. 2004, [ApJS](#), **154**, 87
- Dole, H., Lagache, G., Puget, J.-L., et al. 2006, [A&A](#), **451**, 417
- Dufresne, D. 2004, [Adv. in Appl. Probab.](#), **36**, 747
- Dunne, L., Eales, S., Edmunds, M., et al. 2000, [MNRAS](#), **315**, 115
- Dunne, L., Gomez, H. L., da Cunha, E., et al. 2011, [MNRAS](#), **417**, 1510
- Duval, F., Schaefer, D., Östlin, G., & Laursen, P. 2013, ArXiv e-prints, [arXiv:1302.7042 \[astro-ph.GA\]](#)
- Dye, S., Dunne, L., Eales, S., et al. 2010, [A&A](#), **518**, L10
- Eales, S., Dunne, L., Clements, D., et al. 2010, [PASP](#), **122**, 499
- Eggen, O. J., Lynden-Bell, D., & Sandage, A. R. 1962, [ApJ](#), **136**, 748
- Einstein, A. 1916, [Annalen der Physik](#), **354**, 769
- Eisenstein, D. J., & Hu, W. 1998, [ApJ](#), **496**, 605
- Eke, V. R., Cole, S., & Frenk, C. S. 1996, [MNRAS](#), **282**, 263
- Elbaz, D., Cesarsky, C. J., Chamaud, P., et al. 2002, [A&A](#), **384**, 848
- Elbaz, D., Cesarsky, C. J., Fadda, D., et al. 1999, [A&A](#), **351**, L37
- Elbaz, D., Dickinson, M., Hwang, H. S., et al. 2011, [A&A](#), **533**, A119
- Ellis, R. S., McLure, R. J., Dunlop, J. S., et al. 2013, [ApJ](#), **763**, L7
- Fagotto, F., Bressan, A., Bertelli, G., & Chiosi, C. 1994a, [A&AS](#), **104**, 365
- . 1994b, [A&AS](#), **105**, 29
- Fan, L. 2011, PhD thesis, SISSA
- Fan, L., Lapi, A., Bressan, A., et al. 2010, [ApJ](#), **718**, 1460
- Fan, L., Lapi, A., De Zotti, G., & Danese, L. 2008, [ApJ](#), **689**, L101
- Fang, F., Shupe, D. L., Xu, C., & Hacking, P. B. 1998, [ApJ](#), **500**, 693
- Farrah, D., Bernard-Salas, J., Spoon, H. W. W., et al. 2007, [ApJ](#), **667**, 149
- Faure, C., Kneib, J.-P., Covone, G., et al. 2008, [ApJS](#), **176**, 19
- Fazio, G. G., Ashby, M. L. N., Barmby, P., et al. 2004, [ApJS](#), **154**, 39
- Feretti, L., Prandoni, I., Brunetti, G., et al. 2013, Italian SKA White Book, 4th edn.
- Ferland, G. J. 2000, Hazy, A Brief Introduction to Cloudy 94
- Ferrarese, L., & Ford, H. 2005, [Space Sci. Rev.](#), **116**, 523
- Fiolet, N., Omont, A., Lagache, G., et al. 2010, [A&A](#), **524**, A33
- Fischer, J., Sturm, E., González-Alfonso, E., et al. 2010, [A&A](#), **518**, L41
- Fixsen, D. J. 2009, [ApJ](#), **707**, 916
- Fleuren, S., Sutherland, W., Dunne, L., et al. 2012, [MNRAS](#), **423**, 2407
- Fontanot, F., De Lucia, G., Monaco, P., Somerville, R. S., & Santini, P. 2009, [MNRAS](#), **397**, 1776
- Franceschini, A., Rodighiero, G., Vaccari, M., et al. 2010, [A&A](#), **517**, A74
- Frayer, D. T., Fadda, D., Yan, L., et al. 2006, [AJ](#), **131**, 250
- Fu, H., Yan, L., Scoville, N. Z., et al. 2010, [ApJ](#), **722**, 653
- Fukugita, M., Ichikawa, T., Gunn, J. E., et al. 1996, [AJ](#), **111**, 1748
- Gehrels, N. 1986, [ApJ](#), **303**, 336
- Gerhard, O., Kronawitter, A., Saglia, R. P., & Bender, R. 2001, [AJ](#), **121**, 1936
- Glenn, J., Conley, A., Béthermin, M., et al. 2010, [MNRAS](#), **409**, 109
- González-Nuevo, J., Lapi, A., Fleuren, S., et al. 2012, [ApJ](#), **749**, 65
- Goto, T., Takagi, T., Matsuhara, H., et al. 2010, [A&A](#), **514**, A6
- Graciá-Carpio, J., García-Burillo, S., Planesas, P., Fuente, A., & Usero, A. 2008, [A&A](#), **479**, 703
- Graciá-Carpio, J., Sturm, E., Hailey-Dunsheath, S., et al. 2011, [ApJ](#), **728**, L7
- Granato, G. L., & Danese, L. 1994, [MNRAS](#), **268**, 235
- Granato, G. L., De Zotti, G., Silva, L., Bressan, A., & Danese, L. 2004, [ApJ](#), **600**, 580
- Granato, G. L., Silva, L., Lapi, A., et al. 2006, [MNRAS](#), **368**, L72
- Gregorich, D. T., Neugebauer, G., Soifer, B. T., Gunn, J. E., & Herter, T. L. 1995, [AJ](#), **110**, 259
- Greve, T. R., Weiβ, A., Walter, F., et al. 2010, [ApJ](#), **719**, 483
- Griffin, M. J., Abergel, A., Abreu, A., et al. 2010, [A&A](#), **518**, L3
- Gronwall, C., Ciardullo, R., Hickey, T., et al. 2007, [ApJ](#), **667**, 79
- Gruppioni, C., Lari, C., Pozzi, F., et al. 2002, [MNRAS](#), **335**, 831
- Gruppioni, C., Pozzi, F., Zamorani, G., & Vignali, C. 2011, [MNRAS](#), **416**, 70
- Gruppioni, C., Pozzi, F., Andreani, P., et al. 2010, [A&A](#), **518**, L27
- Gruppioni, C., Pozzi, F., Rodighiero, G., et al. 2013, [MNRAS](#), **432**, 23
- Haehnelt, M. G., & Rees, M. J. 1993, [MNRAS](#), **263**, 168
- Hailey-Dunsheath, S., Nikola, T., Stacey, G. J., et al. 2010, [ApJ](#), **714**, L162
- Hambrick, D. C., Ostriker, J. P., Johansson, P. H., & Naab, T. 2011, [MNRAS](#), **413**, 2421

- Hartwick, F. D. A., & Schade, D. 1990, *ARA&A*, **28**, 437
- Hasinger, G., Miyaji, T., & Schmidt, M. 2005, *A&A*, **441**, 417
- Hatsukade, B., Ohta, K., Seko, A., Yabe, K., & Akiyama, M. 2013, *ApJ*, **769**, L27
- Hatsukade, B., Kohno, K., Arétxaga, I., et al. 2011, *MNRAS*, **411**, 102
- Hawkins, E., Maddox, S., Branchini, E., & Saunders, W. 2001, *MNRAS*, **325**, 589
- Hayward, C. C., Narayanan, D., Kereš, D., et al. 2013, *MNRAS*, **428**, 2529
- Hibon, P., Cuby, J.-G., Willis, J., et al. 2010, *A&A*, **515**, A97
- Higdon, S. J. U., Armus, L., Higdon, J. L., Soifer, B. T., & Spoon, H. W. W. 2006, *ApJ*, **648**, 323
- Hinshaw, G., Larson, D., Komatsu, E., et al. 2012, ArXiv e-prints, [arXiv:1212.5226 \[astro-ph.CO\]](https://arxiv.org/abs/1212.5226)
- Hogg, D. W. 1999, ArXiv Astrophysics e-prints, [arXiv:astro-ph/9905116](https://arxiv.org/abs/astro-ph/9905116)
- Hopwood, R., Serjeant, S., Negrello, M., et al. 2010, *ApJ*, **716**, L45
- Hu, E. M., Cowie, L. L., Barger, A. J., et al. 2010, *ApJ*, **725**, 394
- Huang, J.-S., Ashby, M. L. N., Barmby, P., et al. 2007, *ApJ*, **664**, 840
- Hubble, E. 1929, *Proceedings of the National Academy of Science*, **15**, 168
- Hyde, J. B., & Bernardi, M. 2009, *MNRAS*, **396**, 1171
- Iliev, I. T., Mellema, G., Shapiro, P. R., & Pen, U.-L. 2007, *MNRAS*, **376**, 534
- Imanishi, M. 2009, *ApJ*, **694**, 751
- Imanishi, M., Dudley, C. C., Maiolino, R., et al. 2007, *ApJS*, **171**, 72
- Imanishi, M., Maiolino, R., & Nakagawa, T. 2010, *ApJ*, **709**, 801
- Ivison, R. J., Chapman, S. C., Faber, S. M., et al. 2007, *ApJ*, **660**, L77
- Ivison, R. J., Swinbank, A. M., Swinyard, B., et al. 2010, *A&A*, **518**, L35
- Iwata, I., Ohta, K., Tamura, N., et al. 2007, *MNRAS*, **376**, 1557
- Iye, M., Ota, K., Kashikawa, N., et al. 2006, *Nature*, **443**, 186
- Jackson, N. 2008, *MNRAS*, **389**, 1311
- Jain, B., & Lima, M. 2011, *MNRAS*, **411**, 2113
- Jarvis, M. J., Smith, D. J. B., Bonfield, D. G., et al. 2010, *MNRAS*, **409**, 92
- Jiang, L., Bian, F., Fan, X., et al. 2013, *ApJ*, **771**, L6
- Johansson, D., Sigurdarson, H., & Horellou, C. 2011, *A&A*, **527**, A117
- Karim, A., Schinnerer, E., Martínez-Sansigre, A., et al. 2011, *ApJ*, **730**, 61
- Kashikawa, N., Shimasaku, K., Malkan, M. A., et al. 2006, *ApJ*, **648**, 7
- Kashikawa, N., Shimasaku, K., Matsuda, Y., et al. 2011, *ApJ*, **734**, 119
- Kauffmann, G., Colberg, J. M., Diaferio, A., & White, S. D. M. 1999, *MNRAS*, **303**, 188
- Kauffmann, G., & Haehnelt, M. 2000, *MNRAS*, **311**, 576
- Kaufman, M. J., Wolfire, M. G., Hollenbach, D. J., & Luhman, M. L. 1999, *ApJ*, **527**, 795
- Kaviani, A., Haehnelt, M. G., & Kauffmann, G. 2003, *MNRAS*, **340**, 739
- Kaviraj, S., Khochfar, S., Schawinski, K., et al. 2008, *MNRAS*, **388**, 67
- Kawakatu, N., & Umemura, M. 2002, *MNRAS*, **329**, 572
- Kawakatu, N., Umemura, M., & Mori, M. 2003, *ApJ*, **583**, 85
- Kennicutt, R. C., & Evans, N. J. 2012, *ARA&A*, **50**, 531
- Kennicutt, Jr., R. C. 1998, *ARA&A*, **36**, 189
- Khochfar, S., & Silk, J. 2011, *MNRAS*, **410**, L42
- Kim, H.-S., Lacey, C. G., Cole, S., et al. 2012, *MNRAS*, **425**, 2674
- Kleinheinrich, M., Rix, H.-W., Erben, T., et al. 2005, *A&A*, **439**, 513
- Klypin, A. A., Trujillo-Gómez, S., & Primack, J. 2011, *ApJ*, **740**, 102
- Knudsen, K. K., van der Werf, P. P., & Kneib, J.-P. 2008, *MNRAS*, **384**, 1611
- Kochanek, C. S. 2006, in Saas-Fee Advanced Course 33: Gravitational Lensing: Strong, Weak and Micro, ed. P. Schneider, C. S. Kochanek, & J. Wambsganss, 91
- Kochanek, C. S., & White, M. 2001, *ApJ*, **559**, 531
- Komatsu, E., Smith, K. M., Dunkley, J., et al. 2011, *ApJS*, **192**, 18
- Koopmans, L. V. E., Browne, I. W. A., & Jackson, N. J. 2004, *New A Rev.*, **48**, 1085
- Kormendy, J., Fisher, D. B., Cornell, M. E., & Bender, R. 2009, *ApJS*, **182**, 216
- Kronawitter, A., Saglia, R. P., Gerhard, O., & Bender, R. 2000, *A&AS*, **144**, 53
- Krumholz, M. R., & Dekel, A. 2012, *ApJ*, **753**, 16
- Kuhlen, M., & Faucher-Giguère, C.-A. 2012, *MNRAS*, **423**, 862
- Lacey, C., & Cole, S. 1993, *MNRAS*, **262**, 627
- Lacey, C. G., Baugh, C. M., Frenk, C. S., et al. 2010, *MNRAS*, **405**, 2
- . 2008, *MNRAS*, **385**, 1155
- Lagache, G., Haffner, L. M., Reynolds, R. J., & Tufte, S. L. 2000, *A&A*, **354**, 247

- Lagattuta, D. J., Fassnacht, C. D., Auger, M. W., et al. 2010, [ApJ](#), **716**, 1579
- Lahav, O., Lilje, P. B., Primack, J. R., & Rees, M. J. 1991, [MNRAS](#), **251**, 128
- Lahav, O., & Suto, Y. 2004, [Living Reviews in Relativity](#), **7**, 8
- Lapi, A. 2004, PhD thesis, Università “Tor Vergata”
- Lapi, A., & Cavaliere, A. 2011, [ApJ](#), **743**, 127
- Lapi, A., Kawakatu, N., Bosnjak, Z., et al. 2008, [MNRAS](#), **386**, 608
- Lapi, A., Negrello, M., González-Nuevo, J., et al. 2012, [ApJ](#), **755**, 46
- Lapi, A., Salucci, P., & Danese, L. 2013, [ApJ](#), **772**, 85
- Lapi, A., Shankar, F., Mao, J., et al. 2006, [ApJ](#), **650**, 42
- Lapi, A., González-Nuevo, J., Fan, L., et al. 2011, [ApJ](#), **742**, 24
- Lawrence, A. 1991, [MNRAS](#), **252**, 586
- Le Borgne, D., Elbaz, D., Ocvirk, P., & Pichon, C. 2009, [A&A](#), **504**, 727
- Le Floc'h, E., Papovich, C., Dole, H., et al. 2005, [ApJ](#), **632**, 169
- Le Floc'h, E., Aussel, H., Ilbert, O., et al. 2009, [ApJ](#), **703**, 222
- Lewis, A., Challinor, A., & Lasenby, A. 2000, [ApJ](#), **538**, 473
- Lima, M., Jain, B., & Devlin, M. 2010, [MNRAS](#), **406**, 2352
- Lonsdale, C. J., Hacking, P. B., Conrow, T. P., & Rowan-Robinson, M. 1990, [ApJ](#), **358**, 60
- Luhman, M. L., Satyapal, S., Fischer, J., et al. 2003, [ApJ](#), **594**, 758
- . 1998, [ApJ](#), **504**, L11
- Madau, P. 1995, [ApJ](#), **441**, 18
- Madau, P., Haardt, F., & Rees, M. J. 1999, [ApJ](#), **514**, 648
- Magliocchetti, M., & Porciani, C. 2003, [MNRAS](#), **346**, 186
- Magnelli, B., Elbaz, D., Chary, R. R., et al. 2009, [A&A](#), **496**, 57
- . 2011, [A&A](#), **528**, A35
- Magnelli, B., Popesso, P., Berta, S., et al. 2013, [A&A](#), **553**, A132
- Magorrian, J., Tremaine, S., Richstone, D., et al. 1998, [AJ](#), **115**, 2285
- Maiolino, R., Caselli, P., Nagao, T., et al. 2009, [A&A](#), **500**, L1
- Malhotra, S., & Rhoads, J. E. 2004, [ApJ](#), **617**, L5
- Malhotra, S., Kaufman, M. J., Hollenbach, D., et al. 2001, [ApJ](#), **561**, 766
- Mancone, C. L., Gonzalez, A. H., Brodwin, M., et al. 2010, [ApJ](#), **720**, 284
- Mao, J. 2006, PhD thesis, SISSA
- Mao, J., Lapi, A., Granato, G. L., de Zotti, G., & Danese, L. 2007, [ApJ](#), **667**, 655
- Markwardt, C. B. 2009, in [Astronomical Data Analysis Software and Systems XVIII](#), ed. D. A. Bohlander, D. Durand, & P. Dowler, Vol. **411**, 251
- Marleau, F. R., Fadda, D., Appleton, P. N., et al. 2007, [ApJ](#), **663**, 218
- Marsden, D., Gralla, M., Marriage, T. A., et al. 2013, ArXiv e-prints, [arXiv:1306.2288 \[astro-ph.CO\]](#)
- Marsden, G., Chapin, E. L., Halpern, M., et al. 2011, [MNRAS](#), **417**, 1192
- Massardi, M., Bonaldi, A., Negrello, M., et al. 2010, [MNRAS](#), **404**, 532
- Massardi, M., López-Caniego, M., González-Nuevo, J., et al. 2009, [MNRAS](#), **392**, 733
- Massardi, M., Ekers, R. D., Murphy, T., et al. 2008, [MNRAS](#), **384**, 775
- Matteucci, F. 1994, [A&A](#), **288**, 57
- Matute, I., La Franca, F., Pozzi, F., et al. 2006, [A&A](#), **451**, 443
- Mauch, T., & Sadler, E. M. 2007, [MNRAS](#), **375**, 931
- Mazzei, P., Della Valle, A., & Bettoni, D. 2007, [A&A](#), **462**, 21
- Mazzei, P., Xu, C., & de Zotti, G. 1992, [A&A](#), **256**, 45
- McLure, R. J., Dunlop, J. S., Bowler, R. A. A., et al. 2013, [MNRAS](#), **432**, 2696
- Miville-Deschénes, M.-A., Lagache, G., & Puget, J.-L. 2002, [A&A](#), **393**, 749
- Mo, H. J., & Mao, S. 2004, [MNRAS](#), **353**, 829
- Mo, H. J., & White, S. D. M. 1996, [MNRAS](#), **282**, 347
- Mo, H., van den Bosch, F. C., & White, S. 2010, [Galaxy Formation and Evolution](#) (Cambridge University Press)
- Mocanu, L. M., Crawford, T. M., Vieira, J. D., et al. 2013, ArXiv e-prints, [arXiv:1306.3470 \[astro-ph.CO\]](#)
- Moré, J. 1978, in [Numerical Analysis](#), ed. G. A. Watson, Vol. **630** (Berlin: Springer), 105
- Mostardi, R. E., Shapley, A. E., Nestor, D. B., Steidel, C. C., & Reddy, N. A. 2013, ArXiv e-prints, [arXiv:1306.1535 \[astro-ph.CO\]](#)
- Moster, B. P., Somerville, R. S., Maulbetsch, C., et al. 2010, [ApJ](#), **710**, 903
- Mukhanov, V. 2005, [Physical Foundations of Cosmology](#) (Cambridge University Press)
- Murayama, T., Taniguchi, Y., Scoville, N. Z., et al. 2007, [ApJS](#), **172**, 523
- Nair, P. B., van den Bergh, S., & Abraham, R. G. 2010, [ApJ](#), **715**, 606
- Nakamura, T. T., & Suto, Y. 1997, [Progress of Theoretical Physics](#), **97**, 49

- Narayanan, D., Hayward, C. C., Cox, T. J., et al. 2010, *MNRAS*, **401**, 1613
- Navarro, J. F., Frenk, C. S., & White, S. D. M. 1996, *ApJ*, **462**, 563
- . 1997, *ApJ*, **490**, 493
- Negishi, T., Onaka, T., Chan, K.-W., & Roellig, T. L. 2001, *A&A*, **375**, 566
- Negrello, M. 2006, PhD thesis, SISSA
- Negrello, M., Perrotta, F., González-Nuevo, J., et al. 2007, *MNRAS*, **377**, 1557
- Negrello, M., Hopwood, R., De Zotti, G., et al. 2010, *Science*, **330**, 800
- Negrello, M., Clemens, M., Gonzalez-Nuevo, J., et al. 2013, *MNRAS*, **429**, 1309
- Nestor, D. B., Shapley, A. E., Kornei, K. A., Steidel, C. C., & Siana, B. 2013, *ApJ*, **765**, 47
- Niemi, S.-M., Somerville, R. S., Ferguson, H. C., et al. 2012, *MNRAS*, **421**, 1539
- Noble, A. G., Webb, T. M. A., Ellingson, E., et al. 2012, *MNRAS*, **419**, 1983
- O'Dowd, M. J., Schiminovich, D., Johnson, B. D., et al. 2009, *ApJ*, **705**, 885
- . 2011, *ApJ*, **741**, 79
- Oesch, P. A., Bouwens, R. J., Illingworth, G. D., et al. 2012, *ApJ*, **759**, 135
- . 2013, ArXiv e-prints, [arXiv:1301.6162 \[astro-ph.CO\]](https://arxiv.org/abs/1301.6162)
- Oguri, M., & Marshall, P. J. 2010, *MNRAS*, **405**, 2579
- Oguri, M., Inada, N., Pindor, B., et al. 2006, *AJ*, **132**, 999
- Oguri, M., Inada, N., Strauss, M. A., et al. 2008, *AJ*, **135**, 512
- Oliver, S. J., Wang, L., Smith, A. J., et al. 2010, *A&A*, **518**, L21
- Oser, L., Naab, T., Ostriker, J. P., & Johansson, P. H. 2012, *ApJ*, **744**, 63
- Osterbrock, D. E. 1989, *Astrophysics of gaseous nebulae and active galactic nuclei* (University Science Books)
- Ota, K., Iye, M., Kashikawa, N., et al. 2008, *ApJ*, **677**, 12
- . 2010, *ApJ*, **722**, 803
- Ouchi, M., Shimasaku, K., Furusawa, H., et al. 2003, *ApJ*, **582**, 60
- Ouchi, M., Shimasaku, K., Akiyama, M., et al. 2008, *ApJS*, **176**, 301
- Ouchi, M., Shimasaku, K., Furusawa, H., et al. 2010, *ApJ*, **723**, 869
- Paciga, G., Scott, D., & Chapin, E. L. 2009, *MNRAS*, **395**, 1153
- Padmanabhan, T. 2002, *Theoretical Astrophysics*, Volume III: Galaxies and Cosmology (Cambridge University Press)
- Padoan, P., Nordlund, A., & Jones, B. J. T. 1997, *MNRAS*, **288**, 145
- Padovani, P., Miller, N., Kellermann, K. I., et al. 2011, *ApJ*, **740**, 20
- Palanque-Delabrouille, N., Magneville, C., Yèche, C., et al. 2013, *A&A*, **551**, A29
- Pannella, M., Carilli, C. L., Daddi, E., et al. 2009, *ApJ*, **698**, L116
- Panuzzo, P., Bressan, A., Granato, G. L., Silva, L., & Danese, L. 2003, *A&A*, **409**, 99
- Papovich, C., Dole, H., Egami, E., et al. 2004, *ApJS*, **154**, 70
- Patanchon, G., Ade, P. A. R., Bock, J. J., et al. 2009, *ApJ*, **707**, 1750
- Pawlak, A. H., Milosavljević, M., & Bromm, V. 2013, *ApJ*, **767**, 59
- Pawlak, A. H., Schaye, J., & van Scherpenzeel, E. 2009, *MNRAS*, **394**, 1812
- Peacock, J. A. 1982, *MNRAS*, **199**, 987
- . 1999, *Cosmological Physics* (Cambridge University Press)
- Pearson, C. P., Oyabu, S., Wada, T., et al. 2010, *A&A*, **514**, A8
- Peebles, P. J. E. 1980, *The large-scale structure of the universe* (Princeton University Press)
- Peebles, P. J. E., & Nusser, A. 2010, *Nature*, **465**, 565
- Peebles, P. J., & Ratra, B. 2003, *Reviews of Modern Physics*, **75**, 559
- Pei, Y. C. 1995, *ApJ*, **438**, 623
- Pénin, A., Lagache, G., Noriega-Crespo, A., et al. 2012, *A&A*, **543**, A123
- Pereira-Santaela, M., Alonso-Herrero, A., Rieke, G. H., et al. 2010, *ApJS*, **188**, 447
- Perrotta, F., Baccigalupi, C., Bartelmann, M., De Zotti, G., & Granato, G. L. 2002, *MNRAS*, **329**, 445
- Perrotta, F., Magliocchetti, M., Baccigalupi, C., et al. 2003, *MNRAS*, **338**, 623
- Pilbratt, G. L., Riedinger, J. R., Passvogel, T., et al. 2010, *A&A*, **518**, L1
- Planck Collaboration, Ade, P. A. R., Aghanim, N., et al. 2011, *A&A*, **536**, A18
- Planck collaboration, Ade, P. A. R., Aghanim, N., et al. 2013a, ArXiv e-prints, [arXiv:1303.5075 \[astro-ph.CO\]](https://arxiv.org/abs/1303.5075)
- . 2013b, ArXiv e-prints, [arXiv:1303.5076 \[astro-ph.CO\]](https://arxiv.org/abs/1303.5076)
- Planck Collaboration, Ade, P. A. R., Aghanim, N., et al. 2013, *A&A*, **550**, A133
- Poglitsch, A., Waelkens, C., Geis, N., et al. 2010, *A&A*, **518**, L2
- Polletta, M., Tajer, M., Maraschi, L., et al. 2007, *ApJ*, **663**, 81
- Pope, A., Chary, R.-R., Alexander, D. M., et al. 2008, *ApJ*, **675**, 1171
- Pozzi, F., Gruppioni, C., Oliver, S., et al. 2004, *ApJ*, **609**, 122
- Prada, F., Klypin, A. A., Cuesta, A. J., Betancort-Rijo, J. E., & Primack, J. 2012, *MNRAS*, **423**, 3018

- Prandoni, I., Morganti, R., & Mignano, A. 2009, in Panoramic Radio Astronomy: Wide-field 1-2 GHz Research on Galaxy Evolution Press, W. H., & Schechter, P. 1974, [ApJ, 187, 425](#)
- PRISM Collaboration, Andre, P., Baccigalupi, C., et al. 2013, ArXiv e-prints, [arXiv:1306.2259 \[astro-ph.CO\]](#)
- Prugniel, P., & Simien, F. 1997, [A&A, 321, 111](#)
- Rahmati, A., & van der Werf, P. P. 2011, [MNRAS, 418, 176](#)
- Rauch, M., Haehnelt, M., Bunker, A., et al. 2008, [ApJ, 681, 856](#)
- Reddy, N. A., & Steidel, C. C. 2009, [ApJ, 692, 778](#)
- Reddy, N. A., Steidel, C. C., Pettini, M., et al. 2008, [ApJS, 175, 48](#)
- Reddy, N., Dickinson, M., Elbaz, D., et al. 2012, [ApJ, 744, 154](#)
- Renault, C., Barrau, A., Lagache, G., & Puget, J.-L. 2001, [A&A, 371, 771](#)
- Renzini, A. 2006, [ARA&A, 44, 141](#)
- Renzini, A., & Ciotti, L. 1993, [ApJ, 416, L49](#)
- Richards, G. T., Lacy, M., Storrie-Lombardi, L. J., et al. 2006, [ApJS, 166, 470](#)
- Riechers, D. A., Bradford, C. M., Clements, D. L., et al. 2013, [Nature, 496, 329](#)
- Rieke, G. H., Blaylock, M., Decin, L., et al. 2008, [AJ, 135, 2245](#)
- Riess, A. G., Strolger, L.-G., Casertano, S., et al. 2007, [ApJ, 659, 98](#)
- Rigby, E. E., Maddox, S. J., Dunne, L., et al. 2011, [MNRAS, 415, 2336](#)
- Robertson, B. E., Furlanetto, S. R., Schneider, E., et al. 2013, ArXiv e-prints, [arXiv:1301.1228 \[astro-ph.CO\]](#)
- Robertson, H. P. 1935, [ApJ, 82, 284](#)
- Rodighiero, G., Vaccari, M., Franceschini, A., et al. 2010, [A&A, 515, A8](#)
- Roelfsema, P., Giard, M., Najarro, F., et al. 2012, in Society of Photo-Optical Instrumentation Engineers (SPIE) Conference Series, Vol. 8442, Society of Photo-Optical Instrumentation Engineers (SPIE) Conference Series
- Rogers, B., Ferreras, I., Pasquali, A., et al. 2010, [MNRAS, 405, 329](#)
- Ross, N. P., McGreer, I. D., White, M., et al. 2012, ArXiv e-prints, [arXiv:1210.6389 \[astro-ph.CO\]](#)
- Roussel, H., Helou, G., Smith, J. D., et al. 2006, [ApJ, 646, 841](#)
- Rowan-Robinson, M. 2009, [MNRAS, 394, 117](#)
- Rowan-Robinson, M., Saunders, W., Lawrence, A., & Leech, K. 1991, [MNRAS, 253, 485](#)
- Rujopakarn, W., Eisenstein, D. J., Rieke, G. H., et al. 2010, [ApJ, 718, 1171](#)
- Rush, B., Malkan, M. A., & Spinoglio, L. 1993, [ApJS, 89, 1](#)
- Sajina, A., Yan, L., Armus, L., et al. 2007, [ApJ, 664, 713](#)
- Sanders, D. B., & Mirabel, I. F. 1996, [ARA&A, 34, 749](#)
- Santos, M. R. 2004, [MNRAS, 349, 1137](#)
- Sasaki, S. 1994, [PASJ, 46, 427](#)
- Saunders, W., Rowan-Robinson, M., Lawrence, A., et al. 1990, [MNRAS, 242, 318](#)
- Sawicki, M., & Thompson, D. 2006a, [ApJ, 642, 653](#)
—. 2006b, [ApJ, 648, 299](#)
- Schenker, M. A., Robertson, B. E., Ellis, R. S., et al. 2013, [ApJ, 768, 196](#)
- Schiminovich, D., Ilbert, O., Arnouts, S., et al. 2005, [ApJ, 619, L47](#)
- Schmidt, M. 1968, [ApJ, 151, 393](#)
- Schneider, P. 2006, Extragalactic Astronomy and Cosmology: An Introduction (Springer)
- Schneider, P., Ehlers, J., & Falco, E. E. 1992, Gravitational Lenses (Springer)
- Scott, K. S., Yun, M. S., Wilson, G. W., et al. 2010, [MNRAS, 405, 2260](#)
- Scott, K. S., Wilson, G. W., Arretxaga, I., et al. 2012, [MNRAS, 423, 575](#)
- Sedgwick, C., Serjeant, S., Pearson, C., et al. 2011, [MNRAS, 416, 1862](#)
- Shankar, F. 2005, PhD thesis, SISSA
- Shankar, F., Lapi, A., Salucci, P., De Zotti, G., & Danese, L. 2006, [ApJ, 643, 14](#)
- Shapley, A. E., Steidel, C. C., Adelberger, K. L., et al. 2001, [ApJ, 562, 95](#)
- Shen, S., Mo, H. J., White, S. D. M., et al. 2003, [MNRAS, 343, 978](#)
- Sheth, R. K., Mo, H. J., & Tormen, G. 2001, [MNRAS, 323, 1](#)
- Sheth, R. K., & Tormen, G. 1999, [MNRAS, 308, 119](#)
—. 2002, [MNRAS, 329, 61](#)
- Shi, Y., Helou, G., Armus, L., Stierwalt, S., & Dale, D. 2013, [ApJ, 764, 28](#)
- Shibuya, T., Kashikawa, N., Ota, K., et al. 2012, [ApJ, 752, 114](#)
- Shimasaku, K., Kashikawa, N., Doi, M., et al. 2006, [PASJ, 58, 313](#)
- Shimizu, I., Yoshida, N., & Okamoto, T. 2012, [MNRAS, 427, 2866](#)
- Shull, J. M., Harness, A., Trenti, M., & Smith, B. D. 2012, [ApJ, 747, 100](#)
- Shupe, D. L., Fang, F., Hacking, P. B., & Huchra, J. P. 1998, [ApJ, 501, 597](#)
- Shupe, D. L., Rowan-Robinson, M., Lonsdale, C. J., et al. 2008, [AJ, 135, 1050](#)

- Sibthorpe, B., Ivison, R. J., Massey, R. J., et al. 2013, *MNRAS*, **428**, L6
- Silk, J., & Rees, M. J. 1998, *A&A*, **331**, L1
- Silva, L., De Zotti, G., Granato, G. L., Maiolino, R., & Danese, L. 2004a, ArXiv Astrophysics e-prints, [arXiv:astro-ph/0403166](https://arxiv.org/abs/astro-ph/0403166)
- . 2005, *MNRAS*, **357**, 1295
- Silva, L., Granato, G. L., Bressan, A., & Danese, L. 1998, *ApJ*, **509**, 103
- Silva, L., Maiolino, R., & Granato, G. L. 2004b, *MNRAS*, **355**, 973
- Smail, I., Ivison, R. J., Blain, A. W., & Kneib, J.-P. 2002, *MNRAS*, **331**, 495
- Smit, R., Bouwens, R. J., Franx, M., et al. 2012, *ApJ*, **756**, 14
- Smith, D. J. B., Dunne, L., da Cunha, E., et al. 2012, *MNRAS*, **427**, 703
- Smolčić, V., Aravena, M., Navarrete, F., et al. 2012, *A&A*, **548**, A4
- Sobacchi, E., & Mesinger, A. 2013, *MNRAS*, **432**, L51
- Sobral, D., Best, P. N., Geach, J. E., et al. 2009, *MNRAS*, **398**, L68
- Soifer, B. T., & Neugebauer, G. 1991, *AJ*, **101**, 354
- Spinoglio, L., Dasyra, K. M., Franceschini, A., et al. 2012, *ApJ*, **745**, 171
- Spinoglio, L., & Malkan, M. A. 1989, *ApJ*, **342**, 83
- Springel, V., White, S. D. M., Jenkins, A., et al. 2005, *Nature*, **435**, 629
- Stacey, G. J., Hailey-Dunsheath, S., Ferkinhoff, C., et al. 2010, *ApJ*, **724**, 957
- Stanford, S. A., Eisenhardt, P. R., & Dickinson, M. 1998, *ApJ*, **492**, 461
- Stecker, F. W., & de Jager, O. C. 1997, *ApJ*, **476**, 712
- Steidel, C. C., Adelberger, K. L., Giavalisco, M., Dickinson, M., & Pettini, M. 1999, *ApJ*, **519**, 1
- Steinmetz, M., & Navarro, J. F. 2002, *New A*, **7**, 155
- Sugiyama, N. 1995, *ApJS*, **100**, 281
- Sutherland, R. S., & Dopita, M. A. 1993, *ApJS*, **88**, 253
- Swinbank, A. M., Smail, I., Longmore, S., et al. 2010, *Nature*, **464**, 733
- Swinbank, A. M., Karim, A., Smail, I., et al. 2012, *MNRAS*, **427**, 1066
- Tacconi, L. J., Genzel, R., Smail, I., et al. 2008, *ApJ*, **680**, 246
- Takagi, T., Matsuhara, H., Goto, T., et al. 2012, *A&A*, **537**, A24
- Takeuchi, T. T., Yoshikawa, K., & Ishii, T. T. 2003, *ApJ*, **587**, L89
- Teplitz, H. I., Charmandaris, V., Chary, R., et al. 2005, *ApJ*, **634**, 128
- Teplitz, H. I., Chary, R., Elbaz, D., et al. 2011, *AJ*, **141**, 1
- Thacker, C., Cooray, A., Smidt, J., et al. 2013, *ApJ*, **768**, 58
- Thomas, D., Gregg, L., & Bender, R. 1999, *MNRAS*, **302**, 537
- Thomas, D., & Kauffmann, G. 1999, in Astronomical Society of the Pacific Conference Series, Vol. 192, Spectrophotometric Dating of Stars and Galaxies, ed. I. Hubeny, S. Heap, & R. Cornett, 261
- Thomas, D., Maraston, C., Schawinski, K., Sarzi, M., & Silk, J. 2010, *MNRAS*, **404**, 1775
- Tielens, A. G. G. M. 2008, *ARA&A*, **46**, 289
- Tinker, J. L., & Wetzel, A. R. 2010, *ApJ*, **719**, 88
- Treister, E., Urry, C. M., Van Duyne, J., et al. 2006, *ApJ*, **640**, 603
- Treu, T. 2010, *ARA&A*, **48**, 87
- Treu, T., Dutton, A. A., Auger, M. W., et al. 2011, *MNRAS*, **417**, 1601
- Trujillo, I., Ferreras, I., & de La Rosa, I. G. 2011, *MNRAS*, **415**, 3903
- Tucker, D. L., Oemler, Jr., A., Kirshner, R. P., et al. 1997, *MNRAS*, **285**, L5
- Unger, S. J., Clegg, P. E., Stacey, G. J., et al. 2000, *A&A*, **355**, 885
- Vaccari, M., Marchetti, L., Franceschini, A., et al. 2010, *A&A*, **518**, L20
- Vale, A., & Ostriker, J. P. 2004, *MNRAS*, **353**, 189
- . 2006, *MNRAS*, **371**, 1173
- Valiante, E., Lutz, D., Sturm, E., Genzel, R., & Chapin, E. L. 2009, *ApJ*, **701**, 1814
- van Breukelen, C., Jarvis, M. J., & Venemans, B. P. 2005, *MNRAS*, **359**, 895
- van den Bergh, S. 1998, Galaxy Morphology and Classification (Cambridge University Press)
- van den Bosch, F. C., Tormen, G., & Giocoli, C. 2005, *MNRAS*, **359**, 1029
- van Dokkum, P. G., Whitaker, K. E., Brammer, G., et al. 2010, *ApJ*, **709**, 1018
- Veilleux, S., Rupke, D. S. N., Kim, D.-C., et al. 2009, *ApJS*, **182**, 628
- Vieira, J. D., Crawford, T. M., Switzer, E. R., et al. 2010, *ApJ*, **719**, 763
- Viero, M. P., Wang, L., Zemcov, M., et al. 2013, *ApJ*, **772**, 77
- Wada, T., Oyabu, S., Ita, Y., et al. 2007, *PASJ*, **59**, 515
- Wagg, J., Carilli, C. L., Wilner, D. J., et al. 2010, *A&A*, **519**, L1
- Walter, F., Decarli, R., Carilli, C., et al. 2012, *Nature*, **486**, 233
- Wang, J., Navarro, J. F., Frenk, C. S., et al. 2011, *MNRAS*, **413**, 1373

- Warren, S. J., Hewett, P. C., & Osmer, P. S. 1994, [ApJ, 421, 412](#)
- Weinberg, S. 2008, Cosmology (Oxford University Press)
- Weiβ, A., De Breuck, C., Marrone, D. P., et al. 2013, [ApJ, 767, 88](#)
- White, S. D. M., & Rees, M. J. 1978, [MNRAS, 183, 341](#)
- Williams, M. J., Bureau, M., & Cappellari, M. 2009, [MNRAS, 400, 1665](#)
- Wilman, D. J., Fontanot, F., De Lucia, G., Erwin, P., & Monaco, P. 2013, [MNRAS, arXiv:1305.7163 \[astro-ph.CO\]](#)
- Wu, Y., Shi, Y., Helou, G., et al. 2011, [ApJ, 734, 40](#)
- Wyder, T. K., Treyer, M. A., Milliard, B., et al. 2005, [ApJ, 619, L15](#)
- Xia, J.-Q., Negrello, M., Lapi, A., et al. 2012, [MNRAS, 422, 1324](#)
- Yan, L., Chary, R., Armus, L., et al. 2005, [ApJ, 628, 604](#)
- Yan, L., Sajina, A., Fadda, D., et al. 2007, [ApJ, 658, 778](#)
- Yoshida, M., Shimasaku, K., Kashikawa, N., et al. 2006, [ApJ, 653, 988](#)
- Yun, M. S., Scott, K. S., Guo, Y., et al. 2012, [MNRAS, 420, 957](#)
- Zemcov, M., Blain, A., Halpern, M., & Levenson, L. 2010, [ApJ, 721, 424](#)
- Zentner, A. R. 2007, [International Journal of Modern Physics D, 16, 763](#)
- Zhao, D. H., Mo, H. J., Jing, Y. P., & Börner, G. 2003, [MNRAS, 339, 12](#)
- Zheng, Z.-Y., Finkelstein, S. L., Finkelstein, K., et al. 2013, [MNRAS, 431, 3589](#)
- Zheng, Z., Berlind, A. A., Weinberg, D. H., et al. 2005, [ApJ, 633, 791](#)

